SOLUTE MIXING DUE TO SQUARE MANHOLES

by

Modupe Olufunmilayo, Jimoh

MEng

A thesis submitted in partial fulfilment of the requirements
for the degree of
Doctor of philosophy in Engineering

University of Warwick

July 2015

AUTHOR: MODUPE JIMOH DEGREE: PhD

TITLE: Pollutant Mixing Within Urban Drainage System

DATE OF DEPOSIT: . . . . . .

I agree that this thesis shall be available in accordance with the regulations governing the University of Warwick theses.

I agree that the summary of this thesis may be submitted for publication.

I agree that the thesis may be photocopied (single copies for study purposes).

Theses with no restriction on photocopying will also be made available to the British Library for microfilming. The British Library may supply copies to individuals or libraries subject to a statement from them that the copy is supplied for non-publishing purposes. All copies supplied by the British Library will carry the following statement:

“Attention is drawn to the fact that the copyright of this thesis rests with its author. This copy of the thesis has been supplied on the condition that anyone who consults it is understood to recognise that its copyright rests with its author and that no quotation from the thesis and no in- formation derived from it may be published without the author's written consent."

AUTHOR'S SIGNATURE: . . . . . .

USER'S DECLARATION

1. I undertake not to quote or make use of any information from this thesis without making acknowledgement to the author.

2. I further undertake to allow no-one else to use this thesis while it is in my care.

DATE SIGNATURE ADDRESS

. . . . . .

Contents

List of Figures

List of Tables

Notations

A	Cross sectional area
A_o	Area of orifice opening
a	Radius
C	Concentration
C1	Coefficient related to relative manhole size
C2	Coefficient related to water depth in a manhole
C3	Coefficient related to lateral flow, lateral angle and plunging flow
C4	Coefficient relates to relative pipe direction
C_d	Coefficient of discharge
C_{HDL}	Headloss-Dispersion constant
c	Solute concentration
D	Diameter
D_H	Hydraulic diameter of the pipe
D_L	Longitudinal dispersion coefficient
D_{L35}	Longitudinal dispersion coefficient due to 35 mm diameter orifice
D_{L35+P}	Longitudinal dispersion coefficient due to 35 mm diameter orifice and pipe
D_{L25}	Longitudinal dispersion coefficient due to 25 mm diameter orifice
D_{L25+P}	Longitudinal dispersion coefficient due to 25 mm diameter orifice and pipe
D_m	Manhole diameter
D_p	Pipe internal diameter
e_m	Molecular diffusion coefficient
ΔE	Energy Loss
Fr	Froude number
f_D	friction factor
g	Acceleration due to gravity
H	Headloss
H_{O35}	Headloss at 35 mm diameter orifice
H_{O25}	Headloss at 25 mm diameter orifice
H_r	Height of flow contraction

h_f	Frictional losses in pipe
J_x	Molecular diffusive flux parameter in x direction
K	Head loss coefficient
K_d	Derivative control coefficient
K_e	Energy loss coefficient
K_i	Integral control coefficient
K_p	Pressure loss coefficient
K_p	Proportionality control coefficient
L	Pipe length
L_m	Manhole side length
L_r	Recirculation length after orifice
M	Mass of tracer
MB	Mass balance
MF	Mass factor
P	Pressure
Q	Discharge or volumetric flow rate
R	Pipe radius
Re	Reynolds number
R^2	Goodness of fit parameter
R_t^2	Fitting parameter of an observed and predicted temporal downstream profile
S	Level difference between the upstream and downstream pipes
S	Slope
s	surcharge
s’	Threshold surcharge depth
s/L_m	Surcharge Ratio with respect to length of manhole
s/D_m	Surcharge Ratio with respect of diameter of manhole
s/D_p	Surcharge Ratio with respect of diameter of pipe
T	Thickness
t	time
$\bar{t}$	Travel time
t_n	Normalised time i.e. volume over discharge

U	Mean velocity
u*	Shear velocity
u’	Temporally fluctuating velocity component
V	Volume
V_d	Velocity in the downstream pipe
v	velocity
x, y, z	Three-dimensional co-ordinate directions
y	Water depth in a manhole

Greek

β	Contraction ratio (orifice diameter : pipe diameter)
Δ	Change or interval
γ	Integration variable
θ	Angle
ρ	Density
τ	Reach time delay
ζ	Manhole shape factor
Φ_m	Manhole diameter
Φ_p	Pipe diameter
μ	Dynamic viscosity
ν	Kinematic viscosity

Abbreviatioons

ADE	Advection Diffusion Equation
ADZ	Aggregated Dead Zone
CFD	Computational Fluid Dynamics
CRTD	Cumulative Residence Time Distribution
CSO	Combined Sewer Overflow
CSRT	Continuously-Stirred Tank Reactor
Fr	Froude number

LIF	Laser-Induced Fluorometry
PID	Proportional Integral Derivative
PIV	Particle Image Velocimetry
Re	Reynolds number
RTD	Residence Time Distribution
SWMM	Storm Water Management Model

Acknowledgements

I would like to express my gratitude to Professor Ian Guymer for his unstinting encouragement, apt to share his knowledge, patience, excellent supervision and endless guidance during my years at the University of Warwick. He gave me opportunity to learn new ways to further harness my potential. He also provided me opportunity to attend seminars and conferences that helped me in this research.

I would like to thank James Hart for giving guidance in the laboratory and help solve problems that emanated from my MATLAB programming. Mr Ian Baylis helped out with the setting up of the rig and was readily available for numerous technical glitches that developed, I am grateful.

I would like to express my appreciation to the Commonwealth scholarship board for the scholarship offered me which covered my tuition fees and other expenses. Special thanks go to the Vice chancellor of the University of Ilorin and the staffs of the Faculty of Engineering (most especially the Department of Civil Engineering) for allowing me take up this position.

My friends and colleagues in the School of Engineering, Warwick were awesome and helpful throughout the year. I would like to mention a few of such friends; Muyiwa Oyinlola who was always willing to help me and patient enough to always respond to my transportation call outs, Soroush Abolfathai for the intelligent discussions and Oluyemi Jegede for his constant effort in reminding me of the end goal. I also appreciate my friends back home in Nigeria for their

support, too many names to mention but they know themselves. Special honour goes to Pastor Eniiwaju Etomi of RCCG, Holy Ghost zone, Coventry for her spiritual and motherly support during my stay in the UK. The worship team and all members of the Church are highly appreciated for making me comfortable during my tenure as the Worship team director.

Mummy Orok, Sarah Roberts, Isaac Robert, Salome Oduebo, Loretta, Arinze Chianumba, Mummy Bunmi Majemite and all members of the African Christian Fellowship (ACF) were astounding with their love and prayers, I felt at home with them.

I would like to thank my parents, In-laws and siblings for their prayers and support throughout my program. My sons (Imoleoluwa and Olaoluwa) were supportive and understanding during my long hours away, while finalizing my thesis write-up, boys, I love you!!!!

Last but not the least; I would like to express my deepest gratitude to my charming and adorable husband, Bashir Jimoh (a.k.a. Bash). I appreciate your continuous tolerance, unconditional love, encouragement and support. Without you, I would have struggled to complete this thesis.

Finally, all this would not have been possible, if the King of kings had not ordained it. I give God all the glory for the life, strength, wisdom, favour, good health etc. during my Ph.D. program and beyond. Father, I hail your name.!!!!!!!!!!!!

Declaration

I declare that the work in this thesis has been composed by myself and no portion of the work has been submitted in support of an application for another degree or qualification of this or any other university or other institute of learning. The work has been my own except where indicated and all quotations have been distinguished by quotation marks and the sources of information have been acknowledged.

ABSTRACT

Dispersion in sewers affects the concentration of pollutants within urban drainage systems and the quest to understand it has led to extensive studies of the hydraulics within circular manholes. Since there are both circular and square manholes within the urban drainage system, it is important to understand the hydraulics within a square manhole, its similarities and/or differences. This research is aimed at describing the transportation and mixing of soluble pollutants through urban drainage systems and the effects of structures such as manholes. It also seeks to study the relationship between headloss and dispersion coefficient in a full flowing pipe. Laboratory solute transport studies were carried out on a straight pipe with two diameter sizes (35 mm and 25 mm) of orifice plate inserted. Two square manhole sizes (388 mm x 388 mm and 150 mm x 150 mm) with a straight through flow was also studied at surcharge and overflow conditions. A relationship between the total headloss along the length of the pipe and the dispersion coefficient was established. With the introduction of a new parameter, a relationship was also established between the headloss due to the orifice and the dispersion coefficient when an orifice plate is inserted along the line of flow. It was observed for the large manhole size that at low surcharge depths there was more mixing occurring while at high surcharge depths the dye travels in a straight jet with some tracer trapped at the upper manhole volume. There exists a transition zone between the low and high surcharge depths which is not evident in the small size manhole. These observations mirror the phenomena

that have already been observed in circular manholes. Manhole overflow studies was indicative of a completely mixed flow for the large manhole whereas for the small manhole it suggests a piston flow (sometimes referred to as plug flow) with some longitudinal dispersion occurring.

1 Introduction

1.1 Background

Urban drainage systems, originally designed simply as a means of conveying effluent from source to treatment, are increasingly becoming a subject of interest with regard to water quality processes. This is due to the possible impact on receiving waters, through discharge of material from surcharged or overflowing manhole structures.

The historical design of urban drainage systems focused on the capacity of the system and its ability to convey a maximum discharge. To evaluate the alternative ways of reducing pollutant load to the environment, for example through the improved design or operation of combined sewer overflows, it has become increasingly important that the in-sewer physical processes affecting the transport of pollutants are accurately modelled (Guymer and O'Brien, 2000). Recently, considerable efforts have been made to achieve effective management of urban pollution by the development of water quality sewerage network models (Stovin et al., 2010a). Computer programs for drainage design and analysis emerged in the 1970s, but complex models only became standard tools of drainage engineers when appropriate computing power became available. Some of the models are: United States Environmental Protection Agency storm water management model (SWMM), Wallingford packages; HydroWorks and InfoWorks and the more popular European package MOUSE (Butler and Davis, 2011). These models are based on accepted mathematical

relationships between physical parameters. They all involve some element of simplification and are deterministic and do not account for randomness. The ability of these models to accurately describe the contribution of the physical characteristics of a sewerage network on the mixing of solutes is limited by lack of measurements quantifying the dominant mechanisms (Guymer and O'Brien, 2000), hence the need for further studies on mixing processes within a sewer network, particularly manholes.

The presence of structures along the line of flow or changes in the shape of the channel can affect longitudinal dispersion. Manholes are incorporated within sewers to allow access for maintenance and at points of change; elevation or direction (Butler and Davis, 2011). At manholes, there are significant changes in shape, providing regions where soluble material may be retained and discharged later. Guymer and O'Brien (2000), showed that the presence of manhole structures within urban drainage systems has a significant effect in increasing both the travel time and dispersion of a solute over ranges of discharge and surcharge. Surcharge of a sewer is the situation in which the sewer entrance and exit are submerged and the pipe is flowing full and under pressure.

Research on how best to describe the hydraulics within a surcharged manhole has been continuous. Johnston and Volker (1990) studied the internal flow and head loss across surcharged manholes, while Pedersen and Mark (1990) presented an analytic technique for predicting head loss. Guymer and O'Brien (2000) studied longitudinal dispersion due to surcharged manhole, Guymer et

al. (2005) investigated the relationship between various diameters and surcharge effects on the longitudinal dispersion of solute tracer across circular surcharged manhole. Further studies in Stovin et al. (2010a) and Guymer and Stovin (2011) aimed at developing a One-Dimensional Mixing model for surcharged manhole by using a deconvolution approach, derived from systems theory, to identify from laboratory data, two dimensionless cumulative residence time distributions(CRTDs) associated with surcharged manholes.

In water engineering, the CRTD has been used to evaluate the performance of hydraulic structures. One potential advantage of the CRTD approach to modelling dispersion is that it is not reliant on any conceptual model being fitted to the data. The application of this alternative approach by Stovin *et al* (2010b), represented a more robust characterization of the system's response, which is scalable and so can be applied to full-scale structures. A validated Computational Fluid Dynamics (CFD) modelling approach by Stovin et al. (2013) and laboratory studies by Jones (2011), confirmed that these flow regions exist. At high surcharges, above a threshold depth, the jet entering the manhole assumes a straight, central position while at low surcharge conditions below this threshold, the incoming jet deviates from the pipe centreline and mixes with the water stored in the manhole.

This study attempts to identify the flow patterns within a surcharged square manhole of two sizes, relating the results to previous results on circular manholes.

1.2 Aims and Objectives

1.2.1 Aim

The aim of this study is to describe the transportation and mixing of solute pollutants through urban drainage systems and the effects of structures such as a square manhole.

1.2.2 Objectives

The objectives of this study are to:

- Contribute to the body of knowledge by relating the headloss to the dispersion coefficient within a pipe system and the effect of orifice plates;
- Investigate the flow within a square manhole in comparison to a circular manhole;
- Understand the effect of change in manhole size by presenting two configurations of manhole to pipe ratio;
- Investigate the flow field and concentration distributions occurring in an overflowing manhole;
- Provide a modelling tool for predicting how cumulative residence time distributions will vary with size, shape, flow rate and surcharge in flow systems.

2 Literature Review

2.1 Urban Drainage

2.1.1 Introduction

Combined drainage systems in developed urban areas are facilities to dispose of liquid wastes, examples of which are storm water, sewage or wastewater. Urban drainage systems primarily comprise lengths of pipes conveying flow between nodal structures, including manholes, settling tanks, storage chambers and combined sewer overflows (CSOs). Most common flow in drainage systems is a hybrid of pipe flow and open channel flow. It is mainly part-filled pipe flow in which liquid flows in a pipe by gravity, with a free surface (Butler and Davis, 2011).

Storm water originates during precipitation events. The term storm water refers to water that originates with snowmelt that enters the storm water system. Storm water that does not soak into the ground becomes surface runoff, which either flows directly into surface waterways or is channelled into storm sewers, which eventually discharge to surface waters. Storm water is of concern for two main issues: one related to the volume and timing of runoff water (flood control and water supplies) and the other related to potential contaminants that the water is carrying, i.e. water pollution.

Sewage or wastewater on the other hand is water that has served the purpose of supporting life, maintaining a standard of living and satisfying the needs of industry. If not properly disposed, it could cause pollution and create health

risks. A sanitary sewer (also called a foul sewer) is a separate underground conveyance system specifically for transporting sewage from houses and commercial buildings to treatment or disposal. Sanitary sewers are sized to carry the amount of sewage generated by the collection area and they are much smaller than combined sewers designed to also carry surface runoff. A combined sewer is a type of sewer system that collects sanitary sewage and storm water runoff in a single pipe system as shown in Fig. 2.1. This type of sewer design is no longer used in building new communities, but many older cities continue to operate combined sewers. As cities added sewage treatment plants, relief structures called regulators were installed in the collection system so that the flow could be discharged into a river or stream during large storm events when the capacity of the pipe exceeded the capacity of the wastewater treatment plant thereby preventing, sewer backups in homes and streets.

In the developed world, sewers are usually pipelines that begin with connecting pipes from buildings to one or more levels of larger underground trunk mains, which transport the sewage to sewage treatment facilities. Vertical shafts, called manholes, connect the mains to the surface. The manholes are used for access to the sewer pipes for inspection and maintenance, and as a means to vent sewer gases. They also facilitate vertical and horizontal angles in otherwise straight pipelines. Sewers are generally gravity powered, though pumps may be used if necessary.

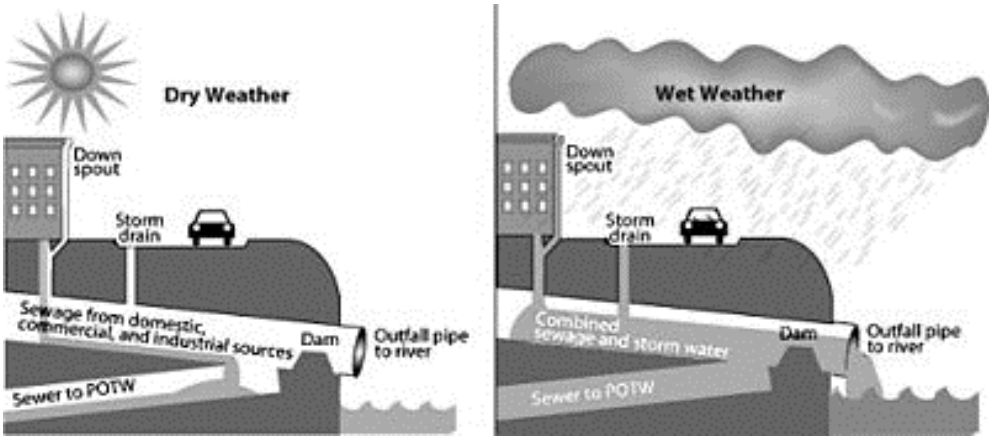

Figure 2.1: Schematic of the urban drainage system, (United States Environmental Protection Agency, 2004)

2.1.2 Urban drainage system failures

The sanitary sewer system is designed to carry sewage only. If storm water gets into the sanitary sewer system, the pipes can become full and spill over. These spills, called sanitary sewer overflows, usually occur at a manhole and overflow into a street or yard. Since these sanitary sewer overflows typically occur during heavy rains, they are considered "wet weather overflows" as shown in Fig. 2.2, (Clean Waterways Program of Frankfort & Franklin County Kentucky, 2008). On the other hand, a combined sewer overflow, occurs when the combined flow of wastewater and storm water exceeds the capacity of the sewer system and it is released directly into local waterways such as a river, stream, lake or ocean. Some CSO outfalls discharge infrequently, while others activate every time it rains. By far the most prevalent cause of CSOs stems from heavy rainfall events which can cause massive inflow of storm water into sewerage lines. Inadequate estimation of losses within the system can lead to the system being surcharged and such conditions often lead to basement flooding or sewage overflows. The

surcharging of sewers occurs for various reasons. For example, in combined and storm sewers, surcharging is caused by rare storms which produce higher-than-design peak flows (Marsalek and Greck, 1988).

Other modes of system failure can include power outage which may disable lift station pumps or parts of the treatment plant operations themselves; in fact, any mechanical system failure within a treatment plant can create a circumstance leading to overflow: breakdown of rotating arms of trickling filters, jamming of line gates, clogging of filters or grates etc. Furthermore, some forms of human error can infrequently lead to diversion of sewage and result in an overflow event. Decentralized failures in dry weather mainly occur from collection sewer line blockages, which can arise from a debris clog, line rupture or tree root intrusion into the line itself.

An example of the system failure occurred during a heavy rain event in the afternoon of 14 August 2010, when unusually intense rainfall hit the eastern parts of Denmark. Within eight hours the rain gauge measured 58 mm of rain corresponding to a return period of 20 years and 9.5% of the yearly rain in Copenhagen, Denmark. The rain intensity peaked between 16:00 and 18:00 and 19:00 to 19:30 to reach a maximum of 1.8 and 2.4 mm per 5 min as shown in Fig. 2.3. This overloaded the sewer system of the catchment and lead to a CSO event between 17:30 and 20:00 (Fig. 2.3). The maximum overflow intensity reached 2.84 m^3/s, corresponding to 41% of the maximal capacity of the overflow structure. In total 26,300 m^3 CSO water was discharged within a five hour period. Essentially no overflow events were recorded in the previous

period of 2007–2010, which demonstrates the extremity of this heavy rain event. The discharge into the water body used for bathing and recreation (more importantly the annual international ironman competition) prompted an epidemiological study to ascertain the safety of the water. It was discovered that during the competition, the bathing water contained about 0.13% of waste water with pathogen levels between 42 -50% (Anderson et al., 2013).

Figure 2.2 Overflow from a manhole, (Clean Waterways Program of Frankfort & Franklin County Kentucky, 2008)

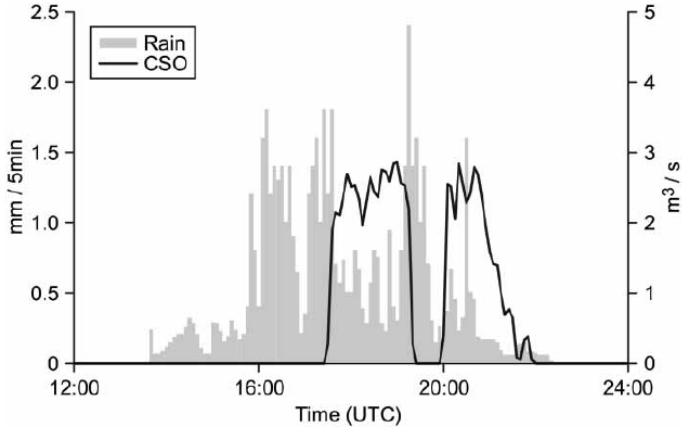

Figure 2.3: Measured volumes from the rain guage (mm/5 min) and the combined sewer overflow (CSO), (m^3/s), 14 August 2010, (Anderson et al., 2013)

2.1.3 Mechanisms within a drainage system

Flow within the urban drainage system is often driven by gravity. Since the drainage system consists of a large flow network, a detailed understanding of fluid flow in pipes is therefore required to achieve continuous transport of waste water from different points in the system. The various studies carried out have been able to identify and emphasis some of the dominant mechanisms within the mixing process as well as their importance and effects. Some of the mechanisms are:

2.1.3.1 Concentration/retention time

Important variables that must be properly understood are the time of travel of a pollutant in a pipe, the rate at which a pollutant spreads out, the decrease in its peak concentration and the resulting concentration patterns of the pollutant. Pollution may result if the capacity of a system to transport and disperse a contamination is overestimated. Underestimation on the other hand may result in valuable resources not being optimally utilised, resulting in unnecessary expenditure on treatment facilities (Hassan, 1993).

2.1.3.2 Pressure and energy loss

One of the most common problems in fluid mechanics is the estimation of pressure or energy loss. In a piping system, it results from a number of system characteristics which include among others; pipe friction, changes in direction of flow, obstructions in flow path, and sudden or gradual changes in the cross-section and shape of flow path. When a fluid flows through a pipe, the internal roughness of the pipe wall can create local eddy currents within the fluid adding

a resistance to flow of the fluid. The velocity profile in a pipe will show that the fluid elements in the centre of the pipe will move at a higher speed than those closer to the wall. Therefore friction will occur between layers within the fluid. This movement of fluid elements relative to each other is associated with pressure drop, called frictional losses. Pipes with smooth walls such as glass, copper, brass and polyethylene have only a small effect on the frictional resistance (PipeFlow.co.uk, 2007). Pipes with less smooth surfaces such as concrete, cast iron and steel have higher frictional factors which results in more loss due to friction.

The hydraulic design of sewer networks requires consideration of minor head losses at various appurtenances and special structures, among which the most common are sewer junctions. Marsalek (1984), wrote that in surcharged sewer systems (it is quite likely that), the minor losses caused by junctions, sewer inlets, house connections, and other appurtenances exceed the friction losses and reduce system capacity significantly.

2.1.3.3 Volume/sizing

Urban drainage system design is primarily based on conveyance requirements. Determining the maximum hydraulic conveyance for a particular drainage scheme entails the assessment of the head losses under both free flowing and surcharged conditions. Pipe size affects velocity. Given a constant flow rate, decreasing pipe size increases the velocity, which increases the friction. The friction losses are cumulative as the fluid travels through the length of the pipe. The greater the distance, the greater the friction losses will be.

2.1.3.4 Reynolds Number

In fluid mechanics, the Reynolds number (Re) is a dimensionless quantity that gives a measure of the ratio of inertial forces to viscous forces and consequently quantifies the relative importance of these two types of forces for given flow conditions (Falkovich, 2011).

$$\mathrm{Re} = \frac{\text{inertial forces}}{\text{viscous forces}} \qquad (2.1)$$

Reynolds numbers are also used to characterize different flow regimes, such as laminar or turbulent flow: laminar flow occurs at low Reynolds numbers, where viscous forces are dominant, and is characterized by smooth, constant fluid motion; turbulent flow occurs at high Reynolds numbers and is dominated by inertial forces, which tend to produce chaotic eddies, vortices and other flow instabilities. The flow is characterised as (Reynolds, 1883):

- laminar when $Re < 2300$
- transient when $2300 < Re < 4000$
- turbulent when $Re > 4000$

For flow in a pipe or tube, the Reynolds number is generally defined as:

$$Re = \frac{\rho \mathrm{V} D_H}{\mu} = \frac{\mathrm{V} D_H}{\nu} = \frac{Q D_H}{\nu A}$$

(2.2)

where:

- D_H is the hydraulic diameter of the pipe (m)
- Q is the volumetric flow rate (m^3/s)
- A is the pipe *cross-sectional* area (m^2)

- V is the mean velocity of the fluid (m/s)
- μ is the dynamic viscosity of the fluid (Pa·s or N·s/m^2 or kg(m·s))
- ν is the kinematic viscosity ($\nu=\mu/\rho$) (m^2/s)
- ρ is the density of the fluid (kg/m^3)

2.1.3.5 Structures

The presence of structures along the line of flow or the shape of the channel can affect longitudinal dispersion. Manholes are incorporated to allow access for maintenance and at points of change, elevation or direction, and are the most common structure, (Butler and Davis, 2011). At manholes and other structures, there are significant changes in shape, providing regions where soluble material may be retained and discharged later. Guymer and O'Brien (2000), showed that the presence of the manhole structures within urban drainage schemes has a significant effect in increasing both the travel time and dispersion of a solute over ranges of discharge and surcharge. Further studies in Guymer et al. (2005) indicated that as the circular manhole diameter increases, a greater proportion of the volume between measurements positions contributes to the dispersion of the tracer, suggesting more mixing throughout the volume. Study of these and other mechanisms is therefore necessary to properly and adequately model them in urban drainage network models.

2.1.3.6 Orifice Plate

An orifice plate is a thin plate with a hole in it, which is usually placed in a pipe. Due to the ease of duplication and the simple construction, the thin sharp edged orifice has been adopted as a standard. The minimum cross sectional area of the jet is known as the "vena contracta." As the fluid approaches the orifice the pressure increases slightly and then drops suddenly as the orifice is passed. It continues to drop until the "vena contracta" is reached and then gradually increases until, at approximately 5 to 8 diameters downstream, a maximum pressure point is reached that will be lower than the pressure upstream of the orifice. The decrease in pressure as the fluid passes through the orifice is a result of the increased velocity of the fluid passing through the reduced area of the orifice. When the velocity decreases as the fluid leaves the orifice the pressure increases and tends to return to its original level. All of the pressure loss is not recovered because of friction and turbulence losses in the stream, (Daniel Measurement and Control Inc, 2010).

From Bernoulli's equation the flow in a pipe with an orifice plate can be obtained from the equation 2.3

$$Q = C_d A_2 \sqrt{\frac{1}{1-\beta^4}} \sqrt{2(P_1 - P_2)/\rho} \qquad (2.3)$$

Where C_d = Coefficient of discharge, dimensionless

A_2 = cross- sectional area of orifice hole, m^2

β = Contraction ratio (orifice hole diameter to pipe diameter), dimensionless

P_1 = Fluid pressure upstream, kg/ $(m.s^2)$

P_2 = Fluid pressure downstream, kg (m.s^2)

ρ = fluid density, kg/m^3

Sharp-edged orifices have coefficients of discharge, C_d around 0.6 to 0.63, while the coefficients for conical entrance plates are in the range 0.73 to 0.734 and for quarter-circle plates 0.77 to 0.85. The coefficients of sharp-edged orifices vary more with fluids and flow rates than the coefficients of conical-entrance and quarter-circle plates, especially at low flows and high viscosities, (Bean, 1983).

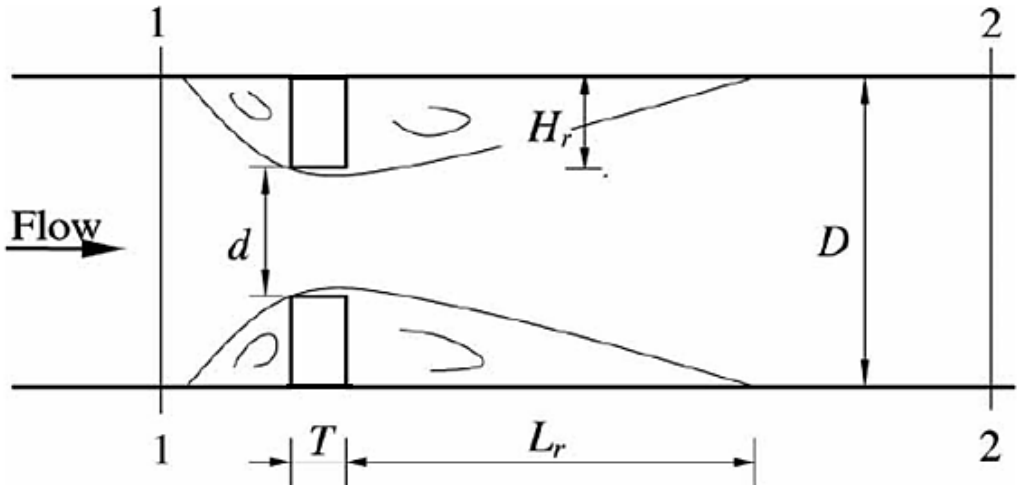

Figure 2.4: Flow through an orifice plate

The flow through an orifice plate is shown in Fig. 2.4, involving the vortex regions of ring form upstream and downstream of the orifice plate due to sudden cross-sectional changes. The recirculation length 'L_r' and height 'H_r' of the flow contraction determine the size of the vortex region, i.e. the energy dissipation region beyond the orifice plate. The orifice plate thickness 'T' has an effect on 'L_r' because of the length decrease with an increase in 'T'.

Experimental investigations by Hobbs and Humphreys (1990) suggested that the radius of the sharp edge of orifice plates has a marked effect upon the discharge coefficient. Gan and Riffat (1997), carried out tests to determine the pressure loss coefficient for square edged orifice plates for a range of Reynolds number. Computational fluid dynamics (CFD) was used to predict the loss coefficient, and the result was compared with experimental orifice measurements. The study showed that CFD can be used to predict the pressure loss coefficient for this type of plate. It concluded that for turbulent flow with Reynolds numbers of 1.6×10^5 to 3.7×10^5, the influence of Reynolds number on the pressure loss coefficient is negligible. It also found that by increasing the plate thickness to 1.5 times the orifice diameter, the pressure loss through an orifice plate can be reduced substantially.

A similar discovery was made by Jianhua et al. (2010), who showed that the head loss coefficient of an orifice plate energy dissipator and the dimensionless length of the recirculation region are functions of the contraction ratio (ratio of orifice plate diameter to the approach flow diameter), the ratio of orifice plate thickness to approach flow diameter and the approach flow Reynolds number. The latter effect was demonstrated to be negligible if $Re > 10^5$. The contraction ratio was the key factor in terms of head losses and recirculation length because the smaller the contraction ratio, the larger the head loss coefficient. Orifice plates as an effective energy dissipator have been used in hydropower projects such as the Xiaolangdi project in China (Jianhua et al., 2010). There an orifice plate energy dissipator, with a dissipation ratio of 44% was used due to their simplicity, convenient construction and high dissipation ratio.

2.2 Solute Transport

2.2.1 Tracers in Solute Transport Study

Smart and Laidlaw (1977), compared eight fluorescent dyes (amino G acid, photine CU, fluorescein, lissamine FE, pyranine, rhodamine B, rhodamine WT, and sulpho rhodamine B) in laboratory and field experiments to assess their utility in quantitative tracing work. The properties considered included sensitivity and minimum detectability, the effect of water chemistry on dye fluorescence, photochemical and biological decay rates, adsorption losses on equipment and sediments, toxicity to man and aquatic organisms. Tests conducted during the study by Smart and Laidlaw (1977) have shown that rhodamine WT is generally the most satisfactory dye tracer, while pyranine and photine CU have proved to have severe limitations.

Turner Designs (1994), published that Rhodamine WT has been approved as a tracer dye in potable water in the United States. It was developed to overcome a disadvantage of rhodamine B's absorption on suspended sediment. Rhodamine WT was an immediate success as a tracer in marine systems and in wastewater. On April 10, 1980, Dr. Joseph A. Cotruvo of the U.S.EPA issued a memo stating that the EPA does not anticipate any adverse health effects resulting from the use of Rhodamine WT as a fluorescent tracer in water flow studies when used within the stipulated guidelines (Turner Designs, 1994).

2.2.2 Mixing

Mixing can be defined as the intermingling of different materials (liquid, gas, solid) to produce a homogeneous mixture. Other processes, such as reaction, mass transfer (includes solubility and crystallization), heat transfer, and dispersion, are also promoted during mixing (McGraw-Hill concise encyclopedia of science & technology, 2005). The forces applicable during mixing develop overall circulation or bulk flow. Superimposed on this flow pattern, there is molecular diffusion, and if turbulence is present, also turbulent eddies. These provide micro mixing. The rate at which a tracer spreads into its surrounding environment is governed by a process called Molecular Diffusion (or Brownian Motion).

Mixing in pipe flows is often brought about by two process, molecular diffusion and dispersion. Dispersion is an effect in fluid mechanics in which a shear flow can increase the effective diffusivity of a species. Allen and Taylor (1923) conducted studies on dispersion measurements and conductivity along the length of a pipe, a further development in Taylor (1953) was able to establish (i) a distribution of velocity over the cross-section of a pipe, (ii) the connection between a the transfer of momentum in turbulent flow and the transfer of other properties and (iii) the distribution of concentration when one fluid follows another in a pipe. Essentially, the shear acts to smear out the concentration distribution in the direction of the flow, enhancing the rate at which it spreads in that direction (Taylor, 1953, Taylor, 1954). He therefore described the coefficient of dispersion D_L for turbulent pipe as follows:

$$D_L = 10.1\, au^* \qquad (2.4)$$

Where a is the radius (m) and u* is the shear velocity (m/s)

Coefficients from Taylors' studies have been applied to rivers and natural water courses and found to be insufficient in describing the mixing processes within these open channels. The quest to solve this challenge led to several mixing studies such as Fischer (1966) and the development of the one-dimensional Fickian's Diffusion model. Subsequently models such as Stefan and Demetracopoulos (1983)'s Cells-in-Series model, Beer and Young (1983) and Wallis et al. (1989)'s Aggregated Dead Zone model (ADZ), amongst others have been developed.

Longitudinal dispersion is the tendency for a cloud of soluble tracer travelling with a fluid flow to spread along the flow direction axis. This effect reduces the cross sectional averaged peak concentration of the tracer measured at locations downstream, and spreads the solute over a greater longitudinal distance, (Dennis, 2000). In urban drainage, the effects of dispersion may act to reduce or eliminate first foul flush effects or to moderate peak concentrations associated with intermittent discharges. Dispersion also implies that pollutant materials may be present a long time before and after predictions based on mean travel time would suggest (Stovin et al., 2010a).

2.2.3 Fick's first and second laws for molecular diffusion

Molecular diffusion was first identified by Fick in 1855. It was shown that a tracer moved from a high concentration to a low concentration at a rate proportional to the concentration gradient between the tracer and its surrounding environment. Molecular diffusion, often called simply diffusion, is the motion of all (liquid or gas) particles at temperatures above absolute zero. The rate of this movement is a function of temperature, viscosity of the fluid and the size (mass) of the particles. Diffusion explains the net flux of molecules from a region of higher concentration to one of lower concentration, but it is important to note that diffusion also occurs when there is no concentration gradient. The result of diffusion is a gradual mixing of material.

Fick (1985) deduced that the movement of the tracer in any one orthogonal direction could be defined in terms of a one dimensional diffusion equation often referred to as **the first law** of Fick (Rutherford, 1994).

$$J_x = -e_m\left(\frac{\partial c}{\partial x}\right) \tag{2.5}$$

where J_x = molecular diffusive flux in the x direction; c = solute concentration; and e_m = molecular diffusion coefficient, in which the sign is negative, since the molecules of the solute diffuse from the part of high concentration to the part of low concentration. Figure 2.5 shows the mass balance of the element which has volume ΔXΔYΔZ. Mass conservation is applied to consider the rate of change in

molecular diffusive flux per unit of time, referred to as **Fick's second law**. It can be written as Equation 2.6.

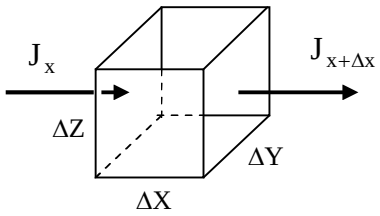

Figure 2.5: Mass Balance of Element

$$\frac{M_{t+\Delta t} - M_t}{\Delta t} = \left(J_x - J_{x+\Delta x}\right)\Delta Y \Delta Z \qquad (2.6)$$

where M_t and $M_{t+\Delta t}$ = tracer mass at time t and $t+\Delta t$, respectively; J_x = diffusive flux (averaged over the time interval Δt) entering the element; $J_{x+\Delta x}$ = diffusive flux (averaged over the time interval Δt) leaving the element; ΔX, ΔY, and ΔZ = dimensions of the fluid element.

Meanwhile, the mass balance compared with time is applied by a Taylor's series, ignoring terms greater than second order. That is

$$M_{t+\Delta t} = M_t + \frac{\partial M}{\partial t}\Delta t \qquad (2.7)$$

$$J_{x+\Delta x} = J_x + \frac{\partial J}{\partial x}\Delta x \qquad (2.8)$$

Then, both Equation 2.7 and Equation 2.8 are replaced in Equation 2.4, and it becomes

$$\frac{\left(M_t + \frac{\partial M}{\partial t}\Delta t\right) - M_t}{\Delta t} = \left(J_x - \left(J_x + \frac{\partial J}{\partial x}\Delta X\right)\right)\Delta Y \Delta Z$$

$$\frac{\partial M}{\partial t} = -\frac{\partial J_x}{\partial x}\Delta X\Delta Y\Delta Z \qquad (2.9)$$

When $c = M/\Delta x\Delta y\Delta z$, then the equation changes into Equation 2.10.

$$\frac{\partial c}{\partial t} = -\frac{\partial J_x}{\partial x} \qquad (2.10)$$

Molecular diffusive flux (Equation 2.5) is substituted into Equation 2.10 and reformed to be

$$\frac{\partial c}{\partial t} = -\frac{\partial\left(-e_m \frac{\partial c}{\partial x}\right)}{\partial x} \qquad (2.11)$$

When e_m is constant, Equation 2.11 becomes

$$\frac{\partial c}{\partial t} = e_m \frac{\partial^2 c}{\partial x^2} \qquad (2.12)$$

Equation 2.12 is the **Fick's second law** for one dimensional diffusion in stationary fluid and e_m is a constant. This equation is used to predict the spatial tracer concentration distribution at a time, rather than only predicted concentration along the distance as the Fick's first law.

2.2.4 Advection Dispersion Equation (ADE)

The advection dispersion equation (ADE) was presented by Taylor (1953) for flow in pipes. The depth and width average form of the equation for one dimension is given by

$$\frac{\partial(C)}{\partial t} + U\frac{\partial(C)}{\partial x} = \frac{\partial}{\partial x}\left[D_L \frac{\partial C}{\partial x}\right] \qquad (2.13)$$

In most practical situations the requirement is to make predictions of concentrations passing a fixed site of interest, such as an abstraction point. That is a temporal concentration profile at a fixed point. Under the assumption that U and D_L are constant, the solution of Equation 2.13 for an instantaneous point source is presented as Equation (2.12).

$$C(x,t) = \frac{M}{A\sqrt{4\pi D_L t}} \exp\left[-\frac{(x-Ut)^2}{4D_L t} \right] \qquad (2.14)$$

where M = mass of tracer injected at x = 0 and t = 0. Equation 2.14 is known as the Taylor Solution to the advection dispersion equation.

Temporal profile prediction

After Taylor's experiment with regard to the longitudinal dispersion in a pipe, the advection dispersion equation was adapted to deal with the solute transport between locations along a river (Fischer, 1966, Rutherford, 1994). However, observed temporal downstream concentration profiles within advective zone (which is defined as the distance it takes a tracer particle to sample the entire flow field) are more of a skew temporal concentration profile, than a Gaussian spatial concentration profile predicted by Equation 2.14. This is often attributed to the initial period where dispersion dominates diffusion, or dead zones and other trapping mechanisms. To predict such a profile, Equation 2.14 needs to be developed to deal with the skewness of the downstream profile. Many practical modelling situations require the prediction of a downstream temporal concentration distribution from a known upstream distribution. In such situations it is possible to use a routing procedure solution to the ADE,

converted to temporal distributions by the frozen cloud approximation. The frozen cloud approximation is the method that is used to convert between concentration-time and concentration-distance relationships.

The solution is:

$$C(x_2,t) = \int_{\gamma=-\infty}^{\infty} \frac{C(x_1,\gamma)U}{\sqrt{4\pi D_L \bar{t}}} exp\left(-\frac{U^2(\bar{t}-t-\gamma)^2}{4D_L\bar{t}}\right)d\gamma \qquad (2.15)$$

where $C(x_2,y)$ = predicted concentration as a function of time at location 2; $C(x_1,y)$ = observed concentration as a function of time at location 1; γ= integration variable on the time axis; $\bar{t}$ is travel time, the difference in time between the centroids of the upstream distributions, $\bar{t_1}$ and the downstream distribution $\bar{t_2}$; and U = mean velocity across the distributions.

This method effectively takes each individual upstream element of the temporal concentration distribution, advects it downstream by a fixed amount and spreads it assuming a Gaussian distribution. The downstream distributions can then be added to give the downstream concentration profile. The discretised routing form of equation 2.15 is shown in Fig 2.6

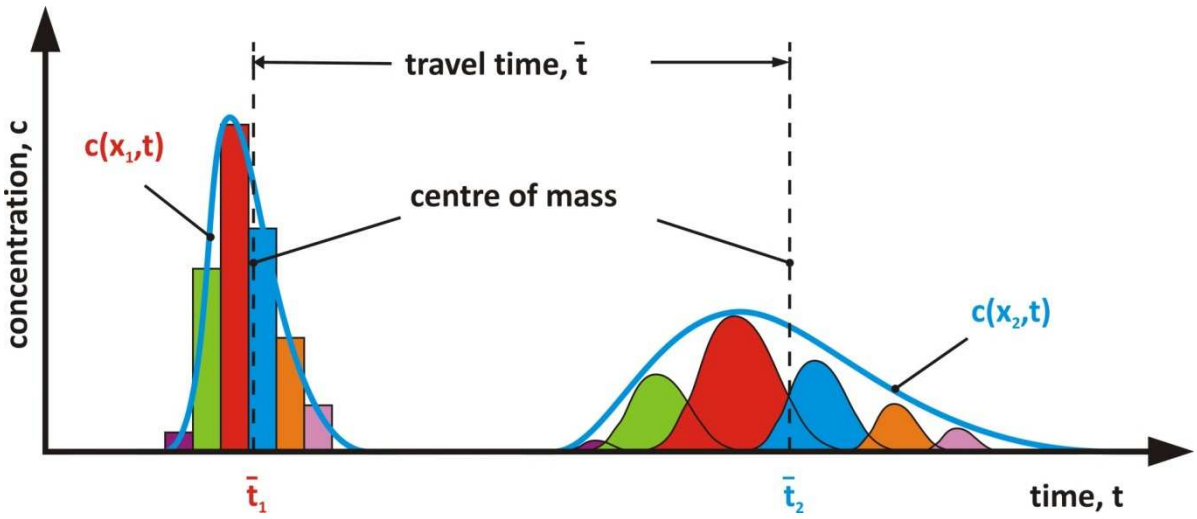

Figure 2.6: Sketch showing the process of the temporal routing procedure

2.2.5 Deconvolution

2.2.5.1 Cumulative Residence Time Distributions

Reactors such as continuous-stirred tank, and plug-flow reactors are used for modelling many complex chemical reactors, (Levenspiel, 1972). An alternative approach to modelling solute transport within complex engineered systems is to consider the system's retention (or residence) time distribution (RTD). In chemical engineering, the mixing characteristics of reactors are often described in terms of their RTDs. By definition, an RTD describes the system's response to an instantaneous upstream injection and so conceptually can only be derived from a pulse (or instantaneous injection) experiment. However, responses to other injection types—including the Gaussian-like distributions considered previously—may be converted to an RTD through numerical manipulation or deconvolution (Guymer and Stovin, 2011).

The residence-time distribution (RTD) of the reactor is one such characterization or measure of the flow pattern. The time spent by a particular tracer molecule in the reactor cannot be measured. A measurement of the concentration of tracer molecules in the effluent, however, can prove sufficient to determine the RTD. The effluent tracer concentration at some time, t is established by the combined exit of many tracer molecules with many different residence times, (Rawlings and Ekerdt, 2002). The RTD of a system represents its fundamental mixing response, i.e. the distribution of residence times experienced in response to an instantaneous upstream input.

Under laboratory conditions, the upstream temporal concentration profile will not be instantaneous because it is not physically possible to achieve full cross-sectional mixing instantaneously. Dye is usually injected some distance upstream to ensure that it is fully cross-sectionally mixed at the upstream end of the measurement section. The system's response to an arbitrary upstream injection will correspond to the convolution of the upstream input and the system's RTD.

The cumulative RTD (CRTD) represents the integral form of the RTD, which is usually normalized to sum to unity. In water engineering, the CRTD has been used to evaluate the performance of hydraulic structures (including ponds, storage tanks, wetlands and storage reservoirs). Various shapes of CRTDs have been derived to describe the hydraulic mixing within a structure as shown in Fig. 2.7. Ignoring any effects of longitudinal dispersion and assuming 'plug flow', the nominal retention time, t_n, within a body of fluid may be estimated from the

ratio of the storage volume (V) to the flow rate (Q), ($t_n = V/Q$), (Stovin et al., 2010b).

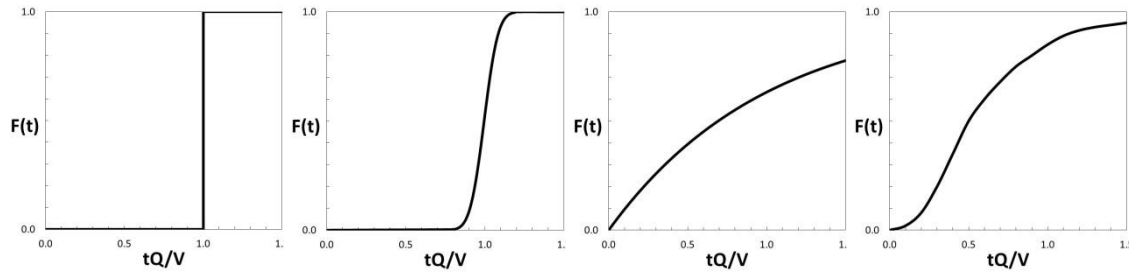

a) Piston Flow | b) Piston Flow with some Longitudinal Mixing | c) Complete Mixing | d) Dead Water

Figure 2.7: Example CRDTs (or F-diagrams) for four fundamental mixing regimes,(Danckwerts, 1953)

The solute transport performance of a surcharged manhole has been shown to be characterised by just two normalised CRTDs, one for pre- and the other for post-threshold surcharge depth. One potential advantage of the CRTD approach to modelling dispersion is that it is not reliant on any conceptual model being fine tuned to the data.(Stovin et al., 2010b, Guymer and Stovin, 2011, Lau et al., 2008).

2.2.5.2 Automated Deconvolution Tool

Stovin et al. (2010b), developed an automated deconvolution tool from Madden et al. (1996), to analyse previous laboratory data on dispersion within circular manhole by Guymer et al. (2005) based on system theory to identify the CRTDs associated with urban drainage systems. In the tool, the input/output

relationship of the system were considered in terms of a convolution integral between the upstream concentration and the RTD,

$$y(t) = \int_0^t x(t-\tau)E(\tau)d\tau \qquad (2.16)$$

where $y(t)$ is the output (downstream concentration), $x(t)$ the input (upstream concentration) and $E(\tau)$ the RTD. If $y(t)$and $x(t)$ are measured it is possible to deconvolve the unknown RTD, or, in systems theory nomenclature, the impulse response. Madden et al. (1996), identified that due to the noise present in the system the problem is ill-posed and direct methods, such Fourier Transformation and System Identification, are inappropriate. An alternative technique used was Regularisation where a single objective function is constructed that will yield an extremum (the maximum or minimum value of a function) when a simulated output is sufficiently close to the measured one, under a series of constraints encapsulating a priori knowledge regarding the function to be estimated, in this case E(τ). A standard technique for creation of the objective function is to use the Langrangian equation.

$$L(f, \lambda) = X^2(f) + \lambda S(f) \qquad (2.17)$$

where (f) is the N-discretised estimate of the system response, the Lagrange multiplier (λ) a discriminator between the two functions, $X^2(f)$ a weighted-least squares distance metric between measured and simulated output and $S(f)$ is the maximum-entropy constraint function that encourages smoothness and positivity on the estimated response. The local extremum of function (Equation

(2.17)) was found using standard optimisation routines to yield an estimate for the system impulse response, or RTD. The tool was implemented in MATLAB.

The deconvolution tool was applied to three different test cases. The first comprises a 'test' data set, in which the downstream concentration profile was synthesised from a known RTD and a given upstream profile. This was to confirm that the tool was capable of recovering a known RTD. The others are the tool's application to existing data on a surcharged manhole and an on-line storage tank. R_t^2, (Young et al., 1980) was used as a measure of the goodness-of-fit of the modelled profile compared with monitored data. An acceptable R_t^2 value of between 0.983 to 0.998 was achieved which was significantly better than that achieved with the ADE or ADZ models on the data (Guymer et al., 2005, Stovin et al., 2010a).

2.2.5.3 Improved Deconvolution Tool for Raw Solute Transport Data

Raw data are the information collected directly from instrumentation and recorded as-is during experimental laboratory and field work, e.g., voltage readings from a fluorometer. Due to differences in experimental set ups, raw data are often pre-processed before analysis. This process however can be time consuming and are prone to errors which affect the overall quality of the study. Saiyudthong (2003) and Jones (2011) described some of the pre-processes as a complex chain of operations consisting of calibration, subtraction of background concentration levels, filtering, and cropping the data record (reducing the length, or duration, of the record through data cut-off based on definitions of

experiment start and end times). Guymer and O'Brien (2000) provided a long and detailed description of fluorometer calibration, smoothing, and temporal averaging. Poor pre-processing, e.g., excessive smoothing or cropping, may introduce errors or remove useful information about the system.

Sonnenwald et al. (2015), sought to improve the quality of solute trace data analysis by incorporating ways of using raw trace data (skipping cropping and calibration before use) in the earlier described automated deconvolution tool (Section 2.2.5.2). He described a new interpolation function—linear interpolation with an automatic moving average (LAMA)—and demonstrated that, in combination with fewer sample points (e.g., 20), it enables smoother RTDs to be generated. A laboratory manhole solute transport data set was deconvolved with and without pre-processing using 40 sample points and linear interpolation. The raw data were also deconvolved using 20 sample points and LAMA interpolation, (Fig 2.8).

All three groups of CRTDs indicate the same bulk mixing characteristics however, there is variation between the groups that corresponds to differences in RTD shape. The two sets of RTDs deconvolved from the raw data show the same mixing trends as those deconvolved from pre-processed data. However, those deconvolved with LAMA interpolation and 20 sample points are significantly smoother. It therefore shows that using raw data for deconvolution and fewer sample points with LAMA interpolation both lead to improved quality of the deconvolved RTD (Sonnenwald et al., 2015).

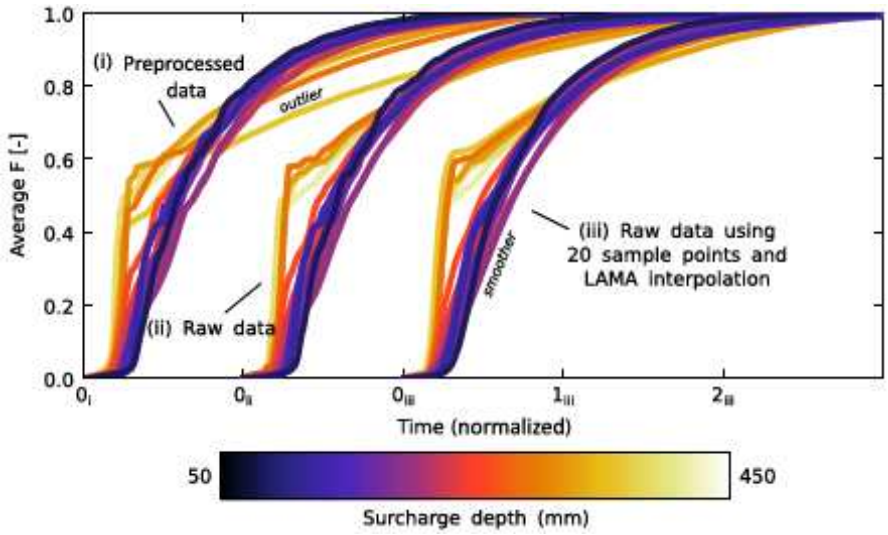

Figure 2.8: Comparison of CRTDs deconvolved with and without improvements from unbenched 30^0 outlet angle surcharged manhole data at 4 l/s, (Sonnenwald et al., 2015)

2.2.6 Goodness of Fit

A correlation value expresses the similarity between either two separate time-series

or two segments of the same time-series. They are frequently used to evaluate the goodness-of-fit for models. A measure of the goodness-of–fit of the one dimensional mixing model by Guymer and Stovin (2011) in predicting downstream temporal concentration profile, R_t^2 (Young et al., 1980) was obtained using the equation

$$R_t^2 = 1 - \left\{\frac{\sum_{t=1}^{n}[c(x_2,t)-p(x_2,t)]^2}{\sum_{t=1}^{n}[c(x_2,t)]^2}\right\} \qquad (2.17)$$

Where $c(x_2, t)$ is the measured downstream concentration data and $p(x_2, t)$ is the predicted downstream concentration profile.

A high R_t^2 value, usually higher than 0.95, indicates excellent model fit whereas any value less than 0.8 indicates that the model has a significant weakness in its practical predictive capacity (Guymer and Stovin, 2011).

Sonnenwald (2014), carried out a systematic comparison of twelve different correlation measures using three realistic solute concentration profiles to identify measures that show high sensitivity to profile shape but limited sensitivity to noise. Of these, the three non-dimensional measures, R^2 (Nash and Sutcliffe, 1970) , R_t^2 (Young et al., 1980) , and APE (Kashefipour and Falconer, 2000) produced correlation values that match visual interpretation of model fit, although at different levels of sensitivity. He noted that the measures might be suitable for different scenarios, with APE exaggerating small differences, R^2 exaggerating large differences, and R_t^2 being flexible about differences between concentration profiles. For the modified deconvolution tool (Sonnenwald et al., 2015), R^2 correlation measure was chosen for its high sensitivity to overall profile shape. With a perfect match, $R^2 = 1$, and for $R^2 = 0$ there is no correlation.

2.3 Manholes

2.3.1 Shapes and Sizing Considerations

Manholes are commonly constructed of precast concrete rings with exceptions to some countries that have rectangular or square shaped manholes. A typical circular and square manhole is shown in Fig. 2.9. They provide access in sewer systems and are different from inspection chambers in that they are deeper and can be entered if necessary. Manholes are often provided at changes in gradient,

changes in direction of pipes, changes in sizes of pipes, heads of runs, at major junctions with other sewers and at every 90m, (Butler and Davis, 2011). The structure size is a function of the number, size, elevation and entry angle of pipes connecting to the structure and must be large enough to accept the maximum size pipe. The normal practice is to ensure individual pipes between manholes have a constant gradient however there are many types of horizontal and vertical connection pattern in the connections of inflow and outflow pipes at a manhole.

Benching is commonly used to reduce sediment deposition within manholes at low flows. Benching arrangements differ, but may generally be described as open channels moulded into the base of manholes which flow between inlet and outlet pipes, as illustrated by Figure 2.10.

The use of square and rectangular manholes is becoming common, as more sizes of flat walled structures are created, promoted, and installed beneath street rights of way (Canadian Concrete Pipe Association, 2013). Square structures are typically used where pipes can intercept at 90 degrees or 180 degrees. Most roadways and some storm water site drainage systems employ these types of structures. This is because round manholes do not tolerate the intersection of large pipes at 90 degrees without a significant upsize required to maintain the structural arm between pipe openings. They can be more difficult to modify when cutting or coring onsite. Pipes are usually cut to be flush with the walls at the springline (the horizontal midpoint of a sewer pipe) instead of

flush with the wall at all points, thereby reducing the amount of working space within the manhole (Canadian Concrete Pipe Association, 2013).

a) Circular manhole b) Square manhole

Figure 2.9: Manhole Shapes, (New Civil Engineer, 2010)

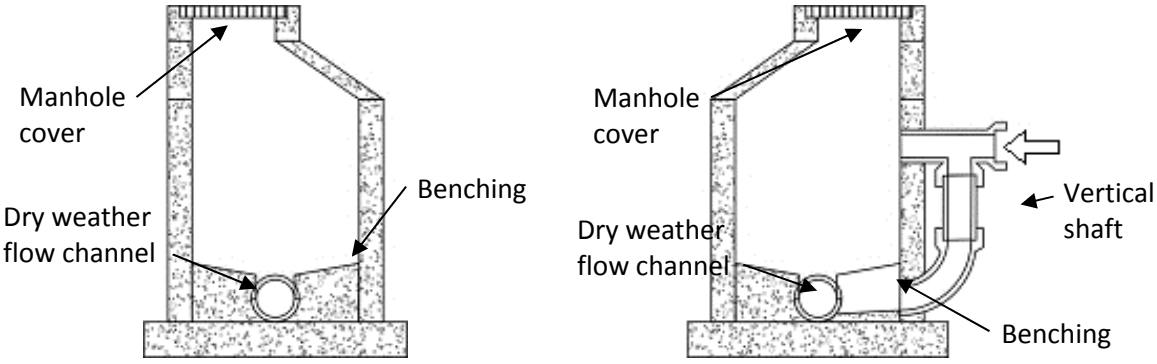

(a) – Sewer manhole (b) – Backdrop manhole

Figure 2.10: Typical Manhole Installation, (Lau, 2007)

Round structures allow more flexibility in the system design and layout. Various sizes of pipes entering at different angles can more easily be accommodated by a round structure, ensuring watertight connections are maintained. Local specifications and design handbooks may include minimum requirements and

design tables to assist in the sizing of manhole structures. Florida DOT Drainage Handbook: Storm Drains (Florida Department of Transportation, 2000) and The National Precast Concrete Association (2010) provides guide to manhole pipe sizing.

While studying the CFD modelling approach to explore the hydraulic behaviour and mixing processes in small-diameter surcharged manhole, Stovin et al. (2013) classified circular manholes into two in terms of the ratio of their diameter, Φ_m to the diameter of the inlet pipe, Φ_p. This is because previous research had focused on manholes with diameters that were at least 4.4 times greater than the pipe diameter. The classification is high Φ_m/Φ_p which refers to manholes where $\Phi_m/\Phi_p \geq 4.4$ and low Φ_m/Φ_p which refers to manholes where $\Phi_m/\Phi_p \leq 4.4$. For square manholes, the nomenclature will therefore be L_m/Φ_p.

2.3.2 Surcharge in Manholes

Surcharge of a sewer is the situation in which the sewer entrance and exit are submerged i.e the water level in the manhole rises above the soffit level of the inlet sewer and the pipe is flowing full and under pressure. Sewerage systems operate under surcharged conditions, i.e. pipe-full flows under pressurised conditions, relatively frequently. Storm sewer flow is time-varying (i.e., transient or unsteady) in nature because all rainstorms have finite durations and consequently the flood flow in the sewers changes with time. If the flood is small, none of the sewer pipes are completely filled and the flow remains as open-channel free-surface flow. However, for large floods, some or all of the sewer pipes may change from open-channel flow to pressurized-conduit flow

during and near the time of the flood peak. In comparison to what is often obtained, the return periods of storms used for their design are shorter, such as one year, and in some storm events, the amount of sewage, exceeds the designed capacity of the sewerage systems (Archer et al., 1978, Yen and Pansic, 1980).

Yen and Pansic (1980), further listed other causes of surcharge in sewers as follows:

(a) Under design resulting from inaccuracies in the design equations, coupled with uncertainty in design parameters (e.g., pipe roughness), can adversely affect system design.

(b) Hydrologic risk may cause surcharge because there is always a probability, no matter how small, that the design discharge may be exceeded one or more times during the service life of the sewer.

(c) Construction errors and material deviations (e.g., tolerance in the pipe dimensions), resulting in the sewer system in place not conforming to the design.

(d) In-line pumping stations that may be required due to system constraints.

(e) In-line detention or retention storage resulting in submergence of connecting pipes.

The flow in a sewer is affected by the hydraulic conditions at both its upstream and downstream ends. Reed (1983), suggested two possibilities in which the sewerage systems would become surcharged (Figure 2.11). It occurs when the

discharge along the pipe is greater than the just-full capacity at the pipe gradient (Figure 2.11a); or when the downstream drainage component imposes a backwater effect (Figure 2.11b).

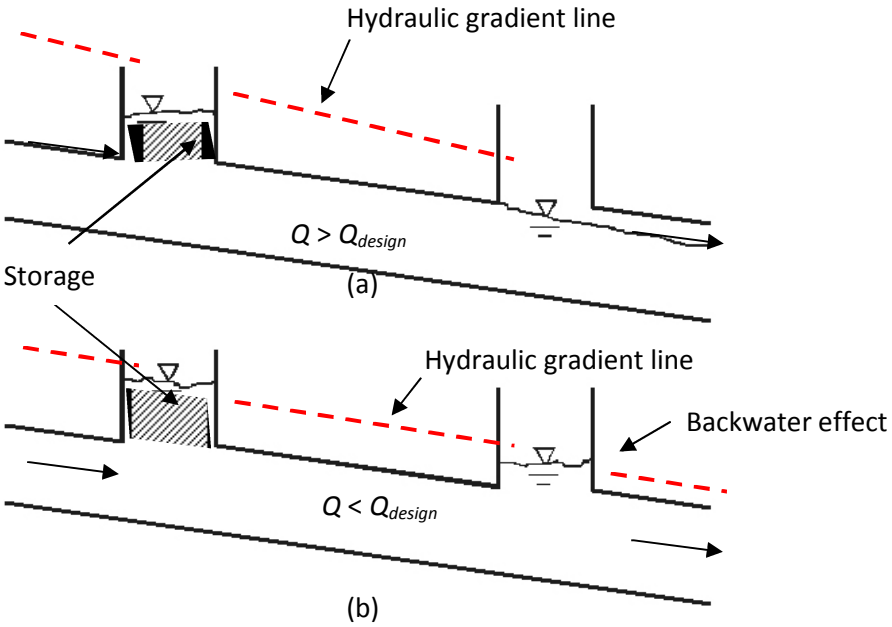

Figure 2.11: Conditions leading to surcharge in sewerage systems (Reed, 1983)

During surcharged conditions, a surcharged manhole can be seen to comprise two portions: a portion that allows water to flow through; and a storage compartment above the soffit. The storage compartment provides extra capacity to the sewerage systems by means of the provision of storage as well as the possibility to increase the hydraulic gradient in excess of the gradient of the sewers and hence increase the delivery flow rate (Figure 2.11a). (Reed, 1983, Lau, 2007, Butler and Davis, 2011).

2.3.3 Longitudinal Dispersion in Surcharged Manholes

In their study on longitudinal dispersion due to surcharged manholes, Guymer and O'Brien (2000) carried out laboratory experiments on both a straight pipe and a surcharged manhole in an attempt to describe the mixing processes occurring in a surcharged manhole structure. They discovered that the effect of a surcharged manhole structure increases the mean travel time by around twofold compared to the straight pipe. For the mixing of soluble material through a pipe, their results indicated that the dominant processes are dependent on discharge and to a less extent on surcharge. They also discovered that the presence of a surcharged manhole increases the longitudinal dispersion coefficient by fivefold compared to the straight pipe results, while observing that the greatest surcharge influences were at low surcharge elevations.

Further studies were carried out by Guymer et al. (2005) to quantify the effects of manhole diameter and surcharged level variations on the longitudinal dispersion of solutes over a range of discharges. They used manholes of diameters 400mm, 500mm, 600mm and 800mm with discharges of 0.87 l/s, 1.94 l/s, 3.33 l/s and 5.01 l/s. The results from this study however disproved the intuitive assumption that more surcharged volume leads to greater mixing; instead they indicated that different mechanisms are dominant within surcharged manhole flows at different surcharged values.

A surcharged threshold level was identified using tracing techniques and shown to be dependent on manhole diameter. At surcharge elevations below this threshold value solutes experience a large degree of mixing within the stored volume, while at surcharge elevations above the threshold value a large

proportion of the tracer is advected through the manhole, experiencing little mixing (Guymer et al., 2005, Jones, 2011). Values of the parameters required to predict the advection and dispersion were determined and their relationship quantified leading to a proposed regression equation for predicting the threshold surcharged depth.

$$\text{Threshold surcharged depth, } s' = 0.258\Phi_m \qquad (2.19)$$

CFD studies by Stovin et al. (2013) on different Φ_m/Φ_p ratios suggests that, at Φ_m/Φ_p ratios below 3.5, the jet is fully restrained by the geometry of the manhole, and the highly asymmetric (well-mixed) below-threshold flow regime cannot be established. The small manholes do not exhibit a large step in t_{50} times and the CRTDs do not show any evidence of below-threshold, well mixed, hydraulic regimes. It explained that the flow field is more comparable with that observed in high-surcharge conditions (above-threshold) in larger-diameter manholes. The study concluded that the hydraulic threshold previously identified for surcharged manholes is only evident in systems with large Φ_m/Φ_p ratios. In smaller-diameter manholes, the incoming jet will tend to bridge the distance across the manhole such that short-circuiting effects dominate, irrespective of surcharge level. The critical Φ_m/Φ_p ratio was found to be $\Phi_m/\Phi_p = 4.4$. Many manholes found in practice have Φ_m/Φ_p ratios of less than 4.4; their mixing characteristics can be assumed to be equivalent to a pipe,(Stovin et al., 2013).

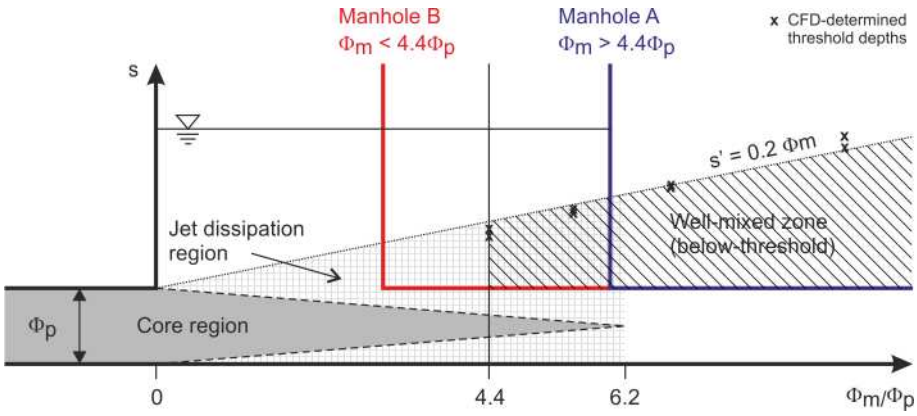

Figure 2.12: Hydraulic conditions associated with well-mixed flow in surcharged circular manholes, Stovin et al. (2013)

2.3.4 Dead Zones

Wallis et al. (1989), described a dead zone as a region in the flow with zero or relatively low velocity compared with that in the main flow. Dead zones are usually found in regions where water is stagnant or in recirculation zones. In natural rivers, because of geometrical irregularity, dead zones are a fairly common feature. Although it implies a form of pocket that is separated from the main flow, it should be considered in a wider context as a bulk parameter that not only describes the effect of segregated regions of flow, but also other dispersive catalysts such as eddies, viscose sub layers and velocity profile (Wallis et al., 1989, O'Brien, 2000). Dead zones also exist in sewerage systems; for example, significant change in geometrical shape at surcharged manholes provides an extraneous volume for dynamic storage of sewage. In highly surcharge manholes, dead zones are often created at the top of the manhole volume, temporarily accommodating a portion of the tracer while majority of the input tracer passes below it in a straight jet.

Dead zones have a significant impact on the overall mixing process. In contrast to the differential advection dispersion which gradually spreads the solute, a dead zone can attenuate the peak concentration of a solute travelling through the dead zone by a considerable amount. Fig. 2.13 shows an example of dead zone effects at a surcharged manhole. At time = t_0, the tracer disperses longitudinally due to differential advection; at time = t_1, some of the tracer is entrained in the dead zone of the manhole and some form of mixing takes place in the storage volume; at time = t_2, as the majority of the tracer has passed the manhole, the tracer which has been trapped in the storage volume is gradually released (Lau, 2007). Since the rate of release is slow, the downstream profile is often impacted resulting in a skewed profile with a considerable long tail as described in Guymer et al. (2005)

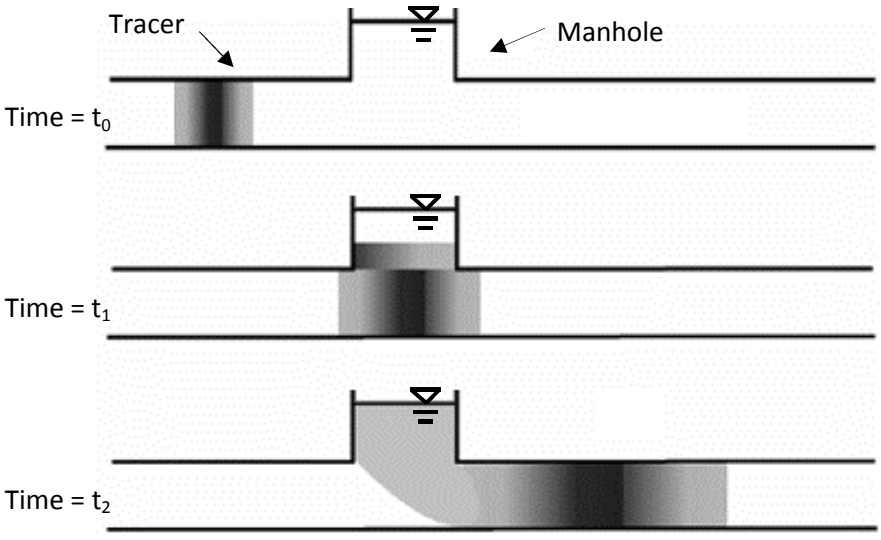

Figure 2.13 : Dead zone effects at a surcharged manhole, (Lau, 2007)

2.3.5 Pipe Directions

Saiyudthong (2003), investigated the effects of varying outlet angle (0°, 30°, 60° and 90°) in benched and unbenched surcharged manholes on solute transport and head loss. It was observed that the average head loss coefficients (K) of benched manholes were smaller than those of the unbenched manholes which might have been caused by the benching which confines almost three quarters of the jet flow and reduces the mixing zone in the manholes (Mark et al., 1996, Pedersen and Mark, 1990). Nevertheless, the influence of benching did not seem as important when the plane angle increased as shown in Table 2.1. The head loss coefficient clearly increased when the plane angle increased, especially for the benched manholes, but not for all plane angles of the unbenched manholes.

Table 2.1: Head loss coefficient (K) (Saiyudthong, 2003)

Plane angle (θ)	Head loss coefficient (K)	
	Benched	Unbenched
0°	0.27	0.51*
30°	1.24	2.22
60°	1.49	2.02
90°	1.50	1.97

* Dennis (2000)

The study (Fig. 2.14) shows that for a benched manhole, travel time was not related to surcharge when the plane angles were smaller than 60°. However, when the plane angle was either 60° or 90°, the relationship changed to be almost a linear increase before approximately 400 mm surcharge and afterwards it showed a slight reduction at low flow rate. Unlike the benched manholes, the linear relationship between the travel time and the surcharge

level took place at all plane angles for unbenched manholes, as shown in Fig 2.14. The travel time, however, rose linearly until a peak; afterwards, it dropped and remained almost constant. A surcharge threshold, in which a peak occurs and travel time starts decreasing when surcharge increases, varied when the plane angles changed. It was clear that the surcharge threshold was very small while the plane angle changed a little and the threshold increased when the plan angle increased. For instance, the threshold for the plane angles of 0°, 30° and 60° were about 50, 275 and 325 mm, respectively.

Sonnenwald et al. (2011), used the CRTD/deconvolution approach to investigate both the elevation of the threshold as well as how the mixing changes with outlet angle, by quantifying the fraction of the flow short circuiting the surcharge volume. He used the shape of the CRTD to provide some insight as to what might be occurring within the manhole. Fig 2.15 shows the potential path of jet as a result of the pipe direction studied by Sonnenwald et al. (2011). At the 0° outlet angle case, most of the jet passed straight through the manhole with the edges of the jet recirculating in the horizontal, while in the vertical, some of the flow goes into surcharged volume mixing. Most of the flow continues straight through the manhole, corresponding to the observed high proportion of short-circuiting. Meanwhile as the angle of pipe direction increases, there is less direction of the jet towards the exit rather it impacts the wall. Correspondingly the main body of the jet also goes into vertical storage mixing and reduces the short-circuiting further. He concluded that as the pipe direction angle increases, more recirculation occurs resulting in a reduction in short-circuiting.

(a)

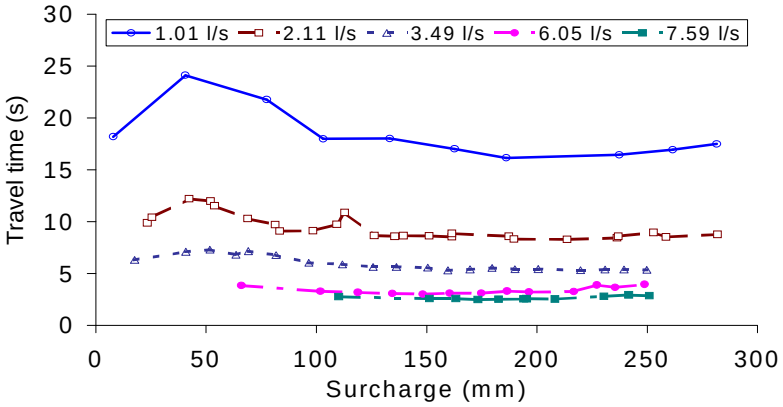

(b)

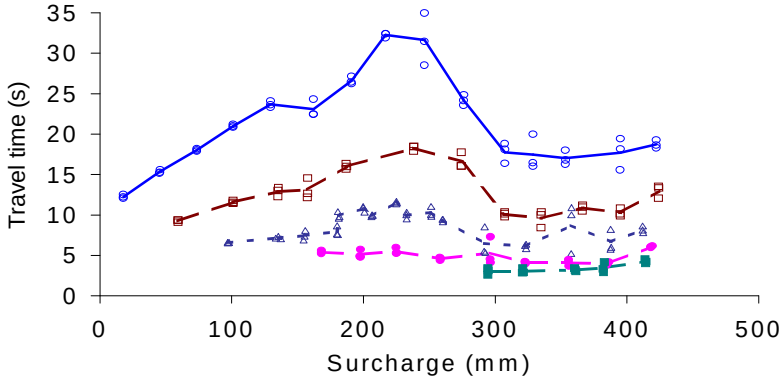

(c)

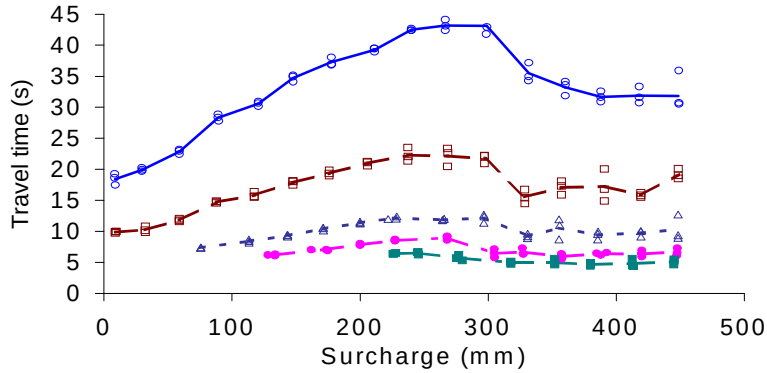

(d)

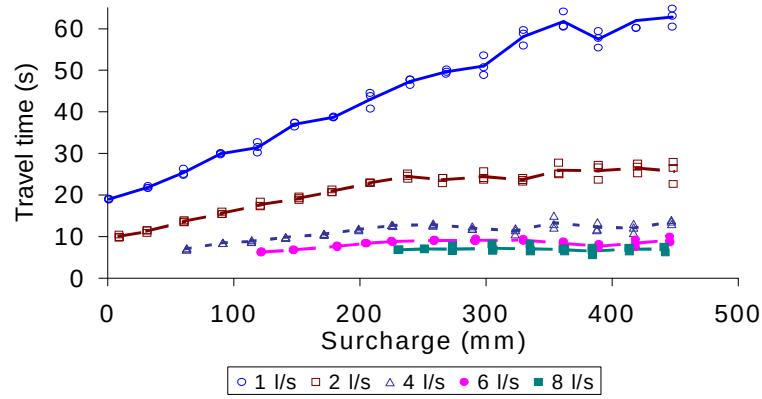

Figure 2.14: Travel time from unbenched manholes: (a) 0° (after Dennis, 2000), (b) 30°, (c) 60° and (d) 90° (Saiyudthong, 2003)

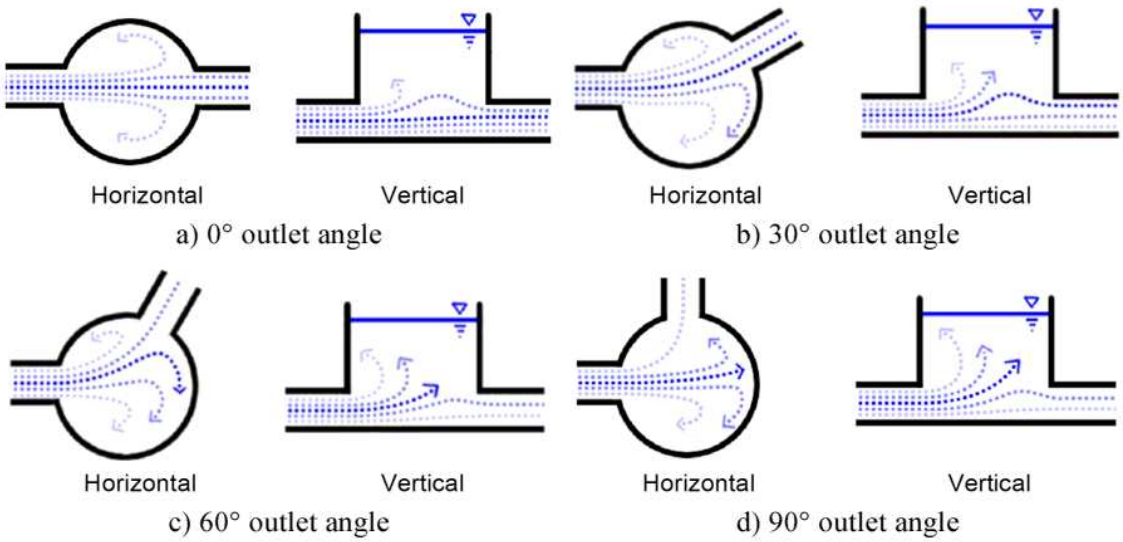

Figure 2.15: Diagram of potential path of jet. Flow is left to right, (Sonnenwald et al., 2011)

2.3.6 Manhole Modelling Software

The first computer models to describe the hydraulics of sewerage systems emerged in the 1970s. The two earliest models were Storm Water Management Model (SWMM), developed by the US EPA (United States Environmental Protection Agency), and Wallingford Storm Sewer Package (WASSP), developed by Hydraulic Research, Wallingford. The aims of these models were to provide insights into the hydrodynamic performance of existing drainage networks and to plan sewer rehabilitation and new systems.

Most models are based on accepted mathematical relationships between physical parameters. The ability of these models to accurately describe the contribution of the physical characteristics of a sewerage network on the mixing of solutes is limited by lack of measurements quantifying the dominant

mechanisms (Rutherford, 1994), they are based on the assumption that full mixing occurs within manholes which recent research has shown to be incorrect as most had no mixing but simply advection.

Furthermore, greater environmental concern and tighter environmental constraints have led to the development of water quality models. These models are incorporated within existing hydrodynamic models to predict the transport of dissolved substances and sediments, and assess sewer flow quality. The ambition of this development is to predict the operation and response to any proposed change of both the contributing systems and the receiving environment (Guymer and O'Brien, 1995). With greater environmental concern, sewerage system network models become a useful aid in deciding the most cost-effective scheme among a number of proposals.

Mark et al. (1996), demonstrated an example of the use of the water quality model to predict the transport of industry loadings in a sewer network of Ljubljana (Slovenia) under dry weather flow conditions. Their work considered conservative pollutants and therefore the complex biological and chemical processes of the pollutants during transport in the sewers could be neglected. The final calibrated model provided good simulations of the selected pollutant (ammonium) concentration, including temporal variations at several locations within the system.

The transport of dissolved substances in sewerage systems involves two processes, which are advection and dispersion. However, some water quality models transport the pollutants only by advection, such as SWMM and

HydroWorks (now InfoWorks); they use the advection dispersion equation whilst ignoring the dispersion effects caused by the urban drainage components. There are others which also account for the effects of dispersion, such as MOUSE TRAP (DHI, 2000).

Recently, Guymer and Stovin (2011), showed that a deconvolution approach derived from systems theory may be applied to identify, from laboratory data, the CRTDs associated with surcharged manholes. Archive laboratory data were re-analyzed to demonstrate that the solute transport characteristics of a surcharged manhole with straight-through inflow and outlet pipes over a range of flow rates and surcharge depths may be modelled using just two dimensionless CRTDs, one for pre-threshold and the other for post-threshold surcharge depths. The model combines the derived manhole CRTDs with a standard (Gaussian) pipe dispersion model to provide temporal solute concentration profiles that are independent of both scale and the ratio of the pipe and manhole diameters. Recent research by Stovin et al. (2013) was carried out to validate its application to differences in size and shape of manhole.

2.4 Energy Loss in Manholes

2.4.1 Determination and Application

Various methodologies have been postulated for evaluating losses at manholes and other flow junctions. The energy loss method is based on laboratory

research and does not apply when the inflow pipe invert is above the water level in the access hole.

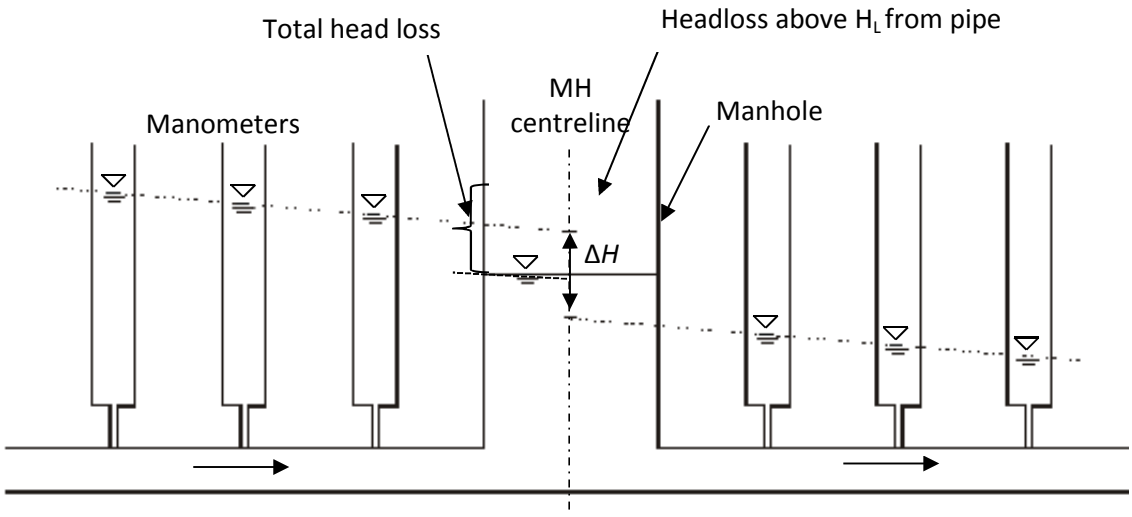

Figure 2.16: Schematic diagram of headloss measurement across manhole

The energy loss encountered going from one pipe to another through an access hole is commonly represented as being proportional to the velocity head of the outlet pipe. Using K to represent the constant of proportionality, the Headloss, ΔH, is approximated by equation 2.20.

$$\Delta H = K\left(\frac{V_0^2}{2g}\right) \qquad (2.20)$$

In the hydraulic design of urban drainage systems, equations of mass continuity and energy conservation are important. The headloss at a manhole, ΔH can therefore be obtained as the difference between the two energy grade lines when projected to the centre of the manhole (Fig 2.16). The energy loss co-efficient, K_e is defined as follows:

$$K_e = \frac{\Delta E}{V_d^2 / 2g} \quad (2.21)$$

Where V_d: the cross-sectional mean flow velocity in the downstream pipe, g: the gravitational acceleration.

The Manual Energy Loss Method described above resulted from preliminary experimental and analytical techniques that focused on relatively simple manhole layout and a small number of inflow pipes. Researchers however are attempting to find ways to cater for more complex arrangement. Other methods to determine a more suitable way for analysis of complex access holes (i.e., with many inflow pipes) have been developed. One of these complex methods, referred to as the Composite Energy Loss Method, is implemented in the FHWA storm drain analysis and design package HYDRA (HYDRAIN, 1996). Details on the method are described in the HYDRA program technical documentation and the associated research report. This complex minor loss computation approach focuses on the calculation of the energy loss from the inflow pipes to the outflow pipe. The methodology can be applied by determining the estimated energy loss through an access hole given a set of physical and hydraulic parameters. Computation of the energy loss allows determination and analysis of the energy grade line and hydraulic grade line in pipes upstream of the manhole.

A lot of flood-analysis models have already been developed in construction consulting companies, universities and public research organizations. Some flood-analysis models, such as MOUSE, Info Works and SWMM have been generally used all over the world. Each formula describing the energy loss at a

manhole in a storm sewer is, however, different from each software application, and consequently the results of simulation of prediction on inundation, flood area and water depth on the ground surface in urban areas are also different.

Arao and Kusuda (2005), explains that flood hazard maps are useful for inhabitants to evacuate in flood. However, flood hazard maps with water depth obtained by numerical simulation are not always correct enough to evacuate them in flood. One of the reasons is that the energy loss at sewer manholes isn't properly taken into consideration in the calculation of the energy-grade lines in storm sewer pipes.

Arao and Kusuda (2005), therefore proposed a new formula on energy loss at a two-way circular drop manhole with an inflow pipe and an outflow pipe. The formula expresses the energy loss coefficient, K_E under surcharged flow as a function of non-dimensionalised independent variables and shape factor as shown in equation 2.22. It was assumed that the pipe slope is mild, and pipe and manhole are circular in shape.

$$K_{E=} f\left(\frac{D_m}{D_d}, \frac{D_u}{D_d}, \frac{y}{D_d}, \frac{S}{D_d}, \frac{\theta}{180}, manhole\ base\ shape\right) \quad (2.22)$$

Where D_m is the diameter of manhole, D_u is the diameter of upstream pipe, D_d is the diameter of downstream pipe, y is the water depth in manhole above the outlet pipe invert, S is the level difference between the upstream and downstream pipes, and θ is the angle between the upstream and downstream pipes.

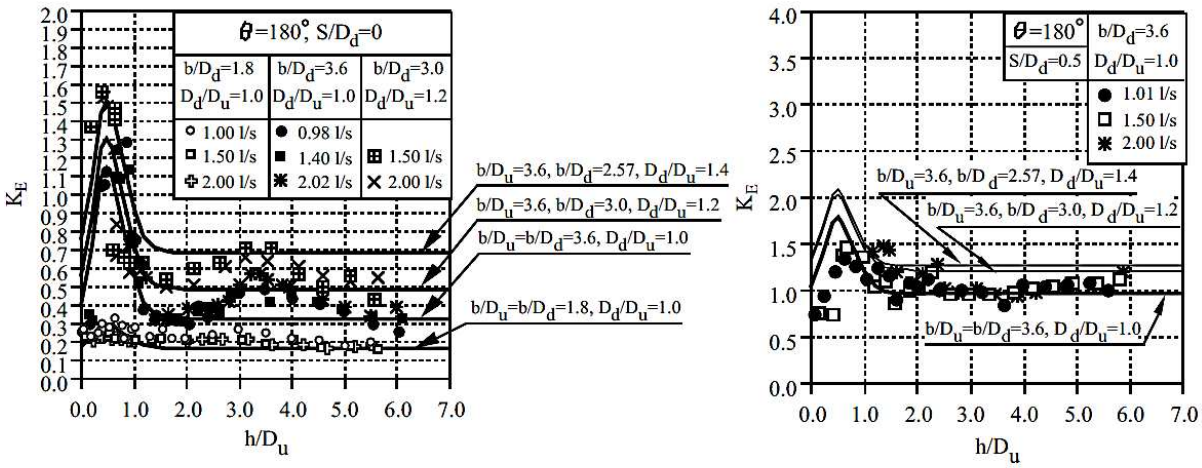

a) K_E (180 degrees, S/D_d=0) **b)** K_E (180 degrees, S/D_d=0.5)

Figure 2.17: Comparison of experimental results and calculated values by proposed equation, Arao and Kusuda (2005).

For a manhole with a straight pipe, the energy loss coefficient K_E from the proposed equation was compared with the experimental results as shown in Fig 2.17. For $b/D_d = 1.8$ and $S/D_d = 0$, the calculated values are within an error of $\pm$ 50% of the measured ones. When $h/D_u > 4.0$, the difference between the calculated and measured values is small, and the measured values reach constant, 0.16. For b/D_d =3.6 and $h/D_u < 1$, the energy loss increases considerably. The calculated values of energy loss are within an error of $\pm$ 20% of the measured values. When $D_d/D_u = 1$ or $D_d/D_u = 1.2$, and h/D_u is from 2.5 to 4.5, the measured energy loss coefficient, K_E fairly increases and this result is out of the range. For S/Dd =0.5, when $h/D_u < 2.5$, the difference of those values is large. When $h/D_u > 2.5$, the calculated values are within an error of $\pm$ 20% of the measured values.

However, because manholes can often have more than two pipes, Arao et al. (2011) carried out further experiments on energy losses at three-way circular drop manholes based on the same assumptions that pipe slope is mild, and pipe and manhole circular in shape and a modified formula which is more accurate than that in Urban Drainage Design Manual (USA, 2001) was proposed. They concluded that for a three-way manhole, the energy loss considerably changes due to the ratio of the diameter between the inflow pipes and an outflow pipe, the ratio of flow rate between those pipes, the water depth in a manhole, and drop gaps between those pipes.

On the other hand the energy loss due to the drop between the lateral and downstream pipes at a three-way circular drop manhole is rather small. They concluded that the proposed formula brings more precise flood hazard maps for disaster prevention as calculated energy loss coefficients by the proposed formula in both straight through and lateral pipes reproduce their laboratory measured results (Arao et al., 2011).

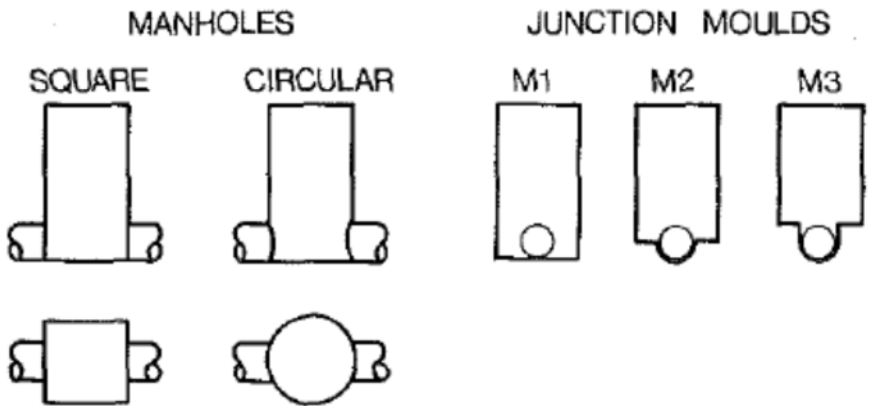

Figure 2.18: Sewer Pipe Junctions tested by Marsalek (1984)

2.4.2 Effect of Manhole Structural Configuration

Several studies have been carried out on head losses at sewer junctions. Sangster (1958) and Archer et al. (1978) studied straight flow-through junctions with identical inflow and outflow pipe diameters for two particular geometries. In both studies, the head loss coefficient was found to be constant for a wide range of velocities and depended only on junction geometry. Marsalek (1984), focused on the effects of junction geometry on head losses in the pressurized flow region, varying junction geometry by using three arrangements in square and circular manholes and by varying the ratio of the manhole size to the pipe diameter for one selected arrangement. The arrangement is shown in Fig. 2.18, with M1, M2, and M3 representing mould 1-3 respectively. He treated the sewer junction manhole loss as the sum of a sudden expansion and sudden contraction loss. The experimental results for the different geometries indicate that the losses at the straight-flow-through junctions are considerably smaller than the combined expansion-contraction loss. This finding follows from the fact that the main body of the stream crossing the junction remains more or less intact. Only the outlying parts undergo changes in trajectories, which lead to energy losses. The junctions with benching inside the manhole (M2 and M3) produced the lowest losses. The head loss obtained compared favourably with that obtained by Archer et al. (1978) and Sangster (1958). He came to the conclusion that the head losses at straight –flow-through junctions are proportional to the velocity head. The coefficient of proportionality, the head loss coefficient was constant with a given geometry

and with manhole benching extending to the crown; the loss coefficient was reduced to 0.12-0.15 from 0.21-0.32 obtained in un-benched manhole.

Archer et al. (1978), conducted laboratory experiments on circular and rectangular manholes with benching; their results suggested that the variations of head loss coefficient between the two types of manholes were not significant but that rectangular manholes tended to have lower energy loss than circular manholes. The effects of benching within manholes have been shown to introduce a large influence on the recorded energy loss coefficient, examined square and circular manholes with different benching arrangements (no benching, half pipe depth benching and full depth benching). The study found that the unbenched manholes had double energy loss compared with those with full depth benching. This observation also agreed with the experimental results of Johnston and Volker (1990). Benching could prevent the swirling within the manholes and reduce energy loss at low surcharge depths.

Saiyudthong (2003), study results showed that the energy loss was higher when there was a change in pipe direction in manhole structures. For instance, the energy loss coefficient for a benched manhole with 60^{o} deflection, i.e. the difference in the angle of the pipes, was approximately six times the value for a benched manhole of the same diameter with no pipe deflection (Archer et al., 1978, Saiyudthong, 2003).

2.4.3 Effects of Surcharge

Pedersen and Mark (1990), described the velocity distribution for a free jet in a study of head losses in surcharge manholes and showed from Albertson et al. (1950) , that the zone of flow establishment extends for a distance of 6.2 times the diameter of the inlet pipe.

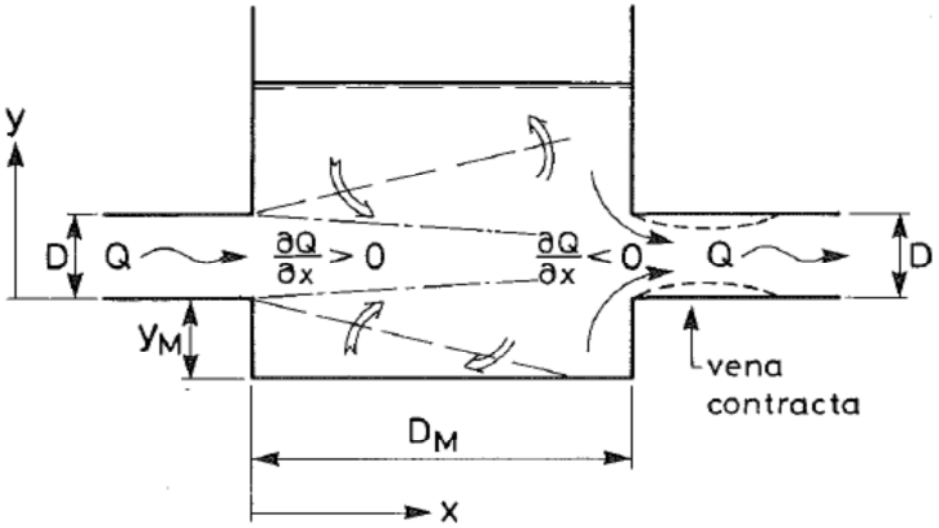

Figure 2.19: Sketch of flow circulation in circular manhole, Pedersen and Mark (1990)

They explained that the inspection of the flow pattern in a circular manhole had revealed that the inflowing water behaves like a submerged jet, which entrains water from the ambient fluid and increases the stream wise discharge through the manhole.

During steady state conditions, the outflow from the manhole equals the inflow, and hence the surplus discharge is rejected from the main flow before it leaves the manhole. The entrained water is accelerated on account of the kinetic

energy of the through-flowing water, and similarly is the energy of the surplus discharge lost in the manhole as well. The energy transformation in this persistent pumping mechanism is directly related to the entrance head loss in the manhole. At the outlet from the manhole, the water is accelerated through a vena contracta in the outlet pipe, and hence an ordinary expansion loss is encountered downstream the vena contracta (Fig 2.19).

By use of a simple jet theory for submerged jets entrance head loss was evaluated. The exit head loss is calculated by use of the Carnot-formula combined with an experimentally determined contraction coefficient ψ. Coefficient ψ is nearly a constant (around 0.6-0.7) with a weak dependency on the effective flow area in the manhole. The latter has been determined as the area in the jet that has an integrated discharge of Q (Pedersen and Mark, 1990).

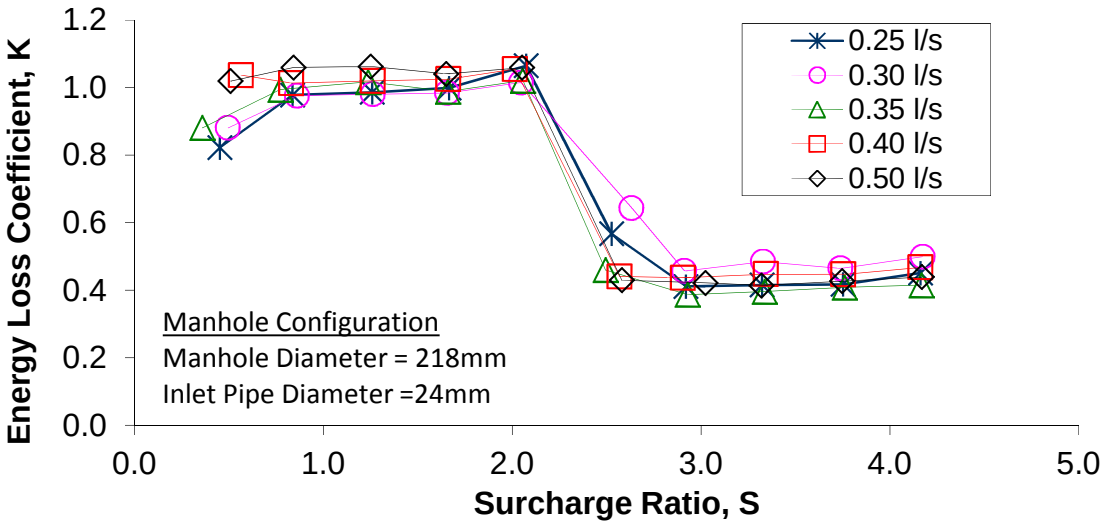

Figure 2.20: Variations of energy loss coefficient with surcharge ratio for the 218mm diameter manhole, (Lau, 2007)

The variations of energy loss coefficient with surcharge ratio for a 218 mm diameter manhole studied by Lau (2007) and Lau et al. (2008), is shown in Fig. 2.20. The surcharge ratio *"S"* is the ratio of the surcharge depth to the manhole diameter. A sharp transition of the energy loss coefficient between the lower and higher surcharge volume is evident at a surcharge ratio of between 2.0 and 2.5. At surcharge ratios below the threshold ratio, but above $S = 0.7D$, energy loss coefficients appear to increase slightly as a function of surcharge ratio. After the transition, the coefficient values are reduced by half compared with the values in the pre-threshold region, yielding a coefficient value of around 0.45. At the lowest surcharge ratio considered in Figure 2.20, there are several data points that fall below the linear trend, with values less than 0.9. This phenomenon was similarly observed by Arao and Kusuda (1999)and Arao and Kusuda (2005) as shown in Fig 2.17a , in the range of 0 to 0.5 surcharge ratio, their data suggests that energy loss coefficients increased rapidly with surcharge; beyond this region, the rate of increase began to flatten off until the hydraulic transition point, marked by a sudden drop in the energy loss coefficient value, was reached. The relationship between energy loss coefficient and surcharge ratio observed in the post-threshold region of Fig. 2.20 matches the experimental findings of Arao and Kusuda (1999). Immediately after the hydraulic transition, the coefficient values drop significantly to around 0.45 and remains constant thereafter. This value appears to be consistent between the two sets of data, with the exception of the lowest discharge considered in Arao and Kusuda (1999)(0.48 l/s), for which the values of the energy loss coefficient are consistently lower than at other discharges.

However, threshold depth for the hydraulic transition from Lau (2007) was S =2.5D while that of Arao and Kusuda (1999) was S =1.0D. This reflects the fact that the two studies have considered manholes with different manhole diameter to pipe diameter ratios. Guymer et al. (2005) suggested that the threshold depth varies as a linear function of the manhole diameter to pipe diameter ratio, and that the value of the threshold depth can be approximately predicted by reference to jet theory. Regression through the origin gives the threshold surcharge depth, $s' = 0.258\phi m$.

2.5 Summary

Mixing within the urban drainage system especially at manholes is complex. Although various studies have been carried out on effects of surcharge variations, pipe sizing and directions, benching, size and shapes of manhole, on mechanisms such as Mixing, Energy loss, Sedimentation, Longitudinal dispersion and Peak Concentration change, the results have not often been generalised due to limitations in the amount of data available for each study. The models used in the analysis of the data collected have also been continually developed to cater for the processes within the manhole; however more is needed to be done to create a robust and more versatile tool in urban drainage predictions and design.

There is limited information about the hydraulics within a square manhole as most research has been carried out using circular manholes. Due to the

advantages presented in using a square manhole over circular manhole, it is necessary to understand the hydraulic processes within this shape of manhole and incorporating this in sewer modelling software. The quest to properly acquire the required data can therefore not be underestimated.

3 Experimental Setup for Manhole Study

3.1 Overview of Experimental Facility

The experimental facility, depicted in Fig. 3.1, consists of a square manhole centrally placed along a horizontally-aligned 50 mm internal diameter and 6.1 m long Perspex pipe each end, serving as inlet and outlet respectively. The pipe extends on opposite sides of the manhole to create a straight through flow. The depth of water in the pipe was controlled with a sluice gate situated at its downstream end, allowing for the creation of different surcharge depths. A flow system consisting of a meter and pump was used to feed the setup, with water continuously recirculating from a sump with dimensions 2.0 x 2.0 x 1.0 m. Turner Designs CYCLOPS-7 fluorometers were used to measure tracer concentrations within the system, with two placed on the inlet pipe and two on the outlet pipe, resulting in a maximum measuring distance of 4.43 m. Four manometer tapings were placed both upstream and downstream to determine the head loss across the system. At different flow rates and surcharge depths, data was collected with a computerised system. Three flow rates (0.71 l/s, 1.17 l/s, 1.64 l/s) were considered. Each of these instruments is discussed further within this chapter.

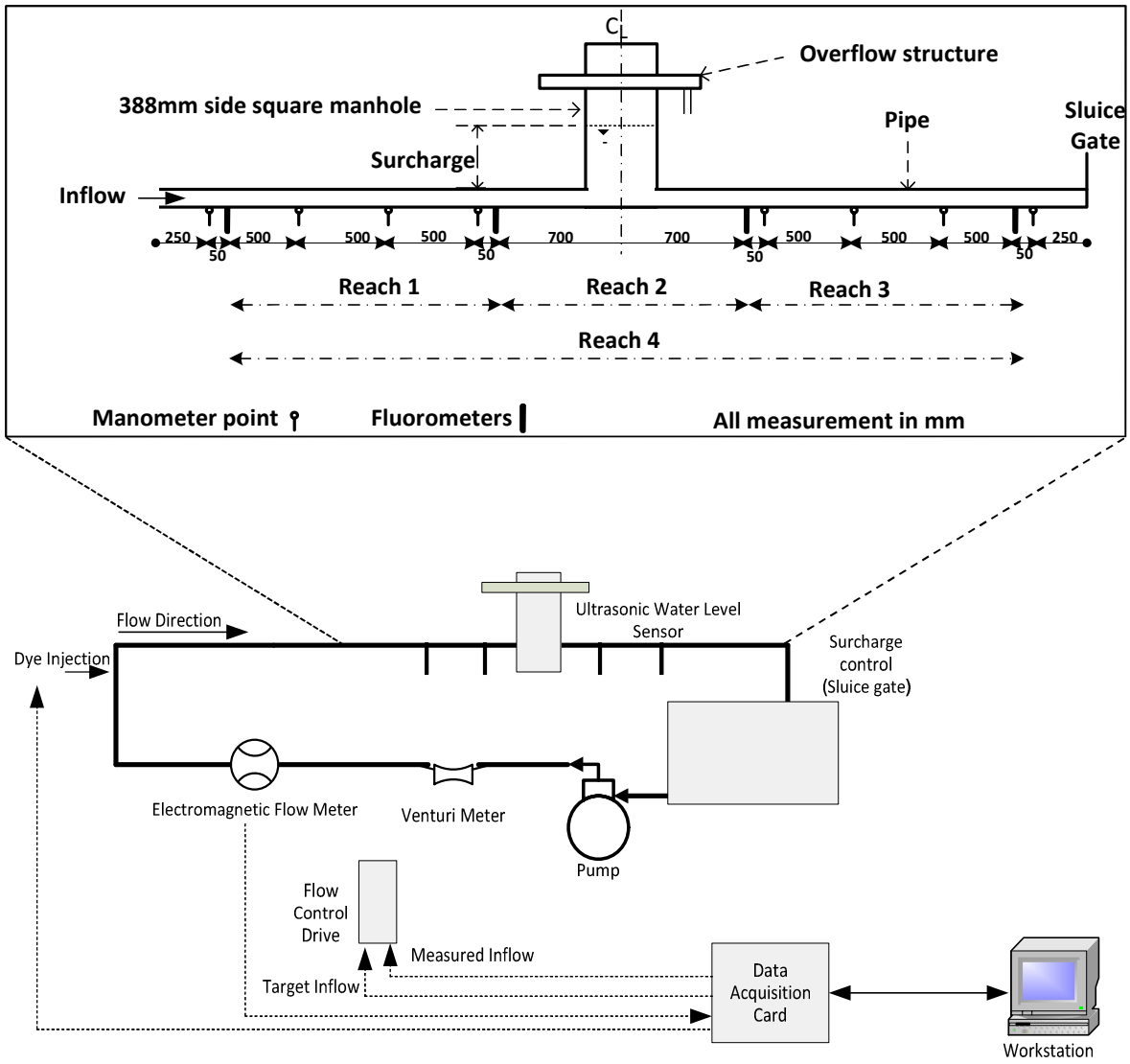

Figure 3.1: Laboratory Set up showing large manhole installation

Two different sizes of manhole were used. One has side dimensions of 388 mm by 388 mm to create a manhole length to pipe diameter ratio of 7.8, and is referred to as large manhole. The other has side dimensions of 150 mm by 150 mm to create a manhole length to pipe diameter ratio of 3.0, and is referred to as small manhole. These referrals are based on the classification studies presented by Stovin et al. (2013). The dimensions of this manhole were within

those stipulated in the Florida Department of Transportation (2000) Handbook and create a platform for similar comparison with previous studies on circular manholes by Stovin et al. (2010a), Jones (2011) and Stovin et al. (2013).

3.1.1 Data Acquisition

Data was acquired on the Warwick water manhole rig using matlab codes. The Rig uses two National Instruments USB-6009 data acquisition cards. The first card is used to log upstream and downstream concentrations from four separate fluorometers. This card also sends output voltages proportional to a target and measured flow rate to a proportional-integral-derivative (PID) controller, governing the rate of flow through the rig. The second card records flow rate and also sends a 5 V signal at specified times which is used to control a dye injection system. All analogue inputs are measured in 'differential' mode on the cards.

3.1.2 Flow Measurement and Control

A flow meter was installed on the outlet pipe from the sump, which measures the discharge entering the pipe. The flow meter comprises of an electromagnetic Sitrans FM MAGFLO MAG 5100W and MAG 6000 transmitter, both manufactured by Siemens (Siemens AG, 2006). Faraday's law of Induction is the principle behind the meter: the fluid acts as a conductor moving through a

magnetic field, inducing a voltage which is directly proportional to the velocity of the fluid.

A Proportional Integral Derivative (PID) controller was wired to the pump. A target flow rate is sent to the drive, along with the present, measured flow rate from the electromagnetic flow meter. The drive calculates the difference between the target and measured flow rates to give an error, e (t). The pump speed is then adjusted based on the size of the error term, as follows:

$$Correction(t) = K_p e(t) + K_i \int_0^t e(\tau) d\tau + K_d \frac{de}{dt} \qquad (3.1)$$

Where *correction(t)* is the correction signal sent to the pump at time *t*, K_p is the proportional control coefficient, *e(t)* is the error term, or difference between the target flow rate and the measured flow rate, K_i is the integral control coefficient, τ is a dummy integration variable, and K_d is the derivative control coefficient. The particular controller used was a Control Techniques Commander SKB 3400055, purchased specifically for the project (Control Techniques Drives Ltd., 2006). Current and target flow rates were sent to the drive every 0.1 s via MATLAB code and the National Instruments data acquisition card discussed previously (Section 3.1.1). The rate at which the current and target flow rates were sent to the drive could not be increased without hindering the data acquisition process.

3.1.3 Calibration of flow

The flow within the system was manually calibrated to determine the actual flow in and out of the system and the accuracy of the flow meter at the time of the experiment. A calibrated volumetric collection tank was used to collect water from the outlet and the overflow, while a stop watch was used to record the time when the proposed volume was collected. For each flow rate, two measurements were taken and at least ten repeats of each to ensure accuracy. The first was to check the outflow volume i.e. when all the flow comes through the outlet pipe. The other, when there is an overflow, was to check the outlet volume from the overflow structure and the outlet pipe. The result of the calibration is shown Fig. 3.2.

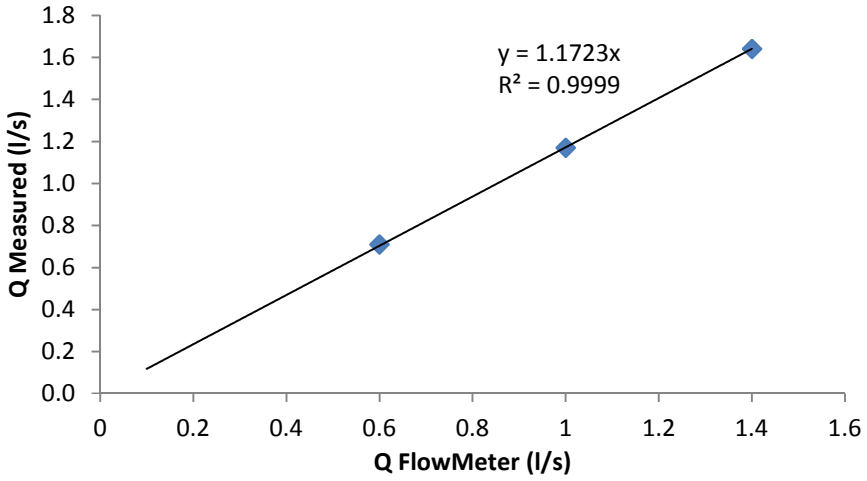

Figure 3.2: Calibration of flow meter

Figure 3.3: Laboratory manometer and Vernier calliper set-up

3.1.4 Headloss Measurement

A system of manometer tubes, stilling tubes and digital Vernier calliper was used to take the pressure measurements. Eight manometer tubes were fitted along the length of the pipe, four on each side of the manhole. The four tubes were located at a distance of 500 m from each other with the closest to the manhole being 556 mm and 675 mm from the entrance/exit of the manhole for the large and small manhole respectively.

Each manometer tube is extended into a large diameter stilling tube. These tubes are 600 mm in height. The eight stilling tubes are attached in a row across a board above which a movable digital Vernier calliper is fitted. The Vernier calliper is lowered into each stilling tube to measure the level of water (Fig 3.3). For this experiment, measurements were taken in millimetres to the nearest 0.01 mm. To ensure accuracy of measurement, the calliper is zeroed before each

reading is taken. For each flow rate, the height of water at the eight points are measured and recorded. This is repeated three times, to ensure the values are an accurate reflection of the true value.

3.1.5 Dye Concentration Measurement

Four Turner Designs CYCLOPS-7 fluorometers were used to measure dye concentrations. Two were placed upstream and downstream at a distance of 700 mm the centre of the pipe and the other two a further 1500 mm from them, with their tip flush with the base of the pipe. Turner Designs CYCLOPS-7 Submersible Fluorometer is an accurate single channel detector that can be used for different applications. The instrument was used to detect dye fluorescence for each dye tracing experiment carried out. It was integrated into a multi-parameter system as shown in Fig 3.4 and 3.5, to obtain its power and to deliver an output voltage to the system data logger, which is proportional to the concentration of the fluorophore, particle or compound of interest. When calibrated with a standard of known concentration, the CYCLOPS-7 output voltage can be correlated to provide data of the actual concentration of the target fluorophore which in this case was a fluorescent dye Rhodamine WT, (Turner Designs, 2007).

The fluorometers have three gain settings; X1, X10 and X100 which refer to the sensitivity adjustment of the sensor. As the gain increases, the sensitivity increases and the measurement range decreases. All three gain settings can be

used but only one gain setting can be used at a time. For the experiments, the X10 gain provided the appropriate sensitivity for the range 0-100 ppb. If working in very low concentration applications (<5 ppb Rhodamine WT), the X100 gain is recommended or if very high concentrations are expected (>80 ppb rhodamine WT) the X1 gain is recommended.

Figure 3.4: Fluorometer indicator light and multi-parameter system

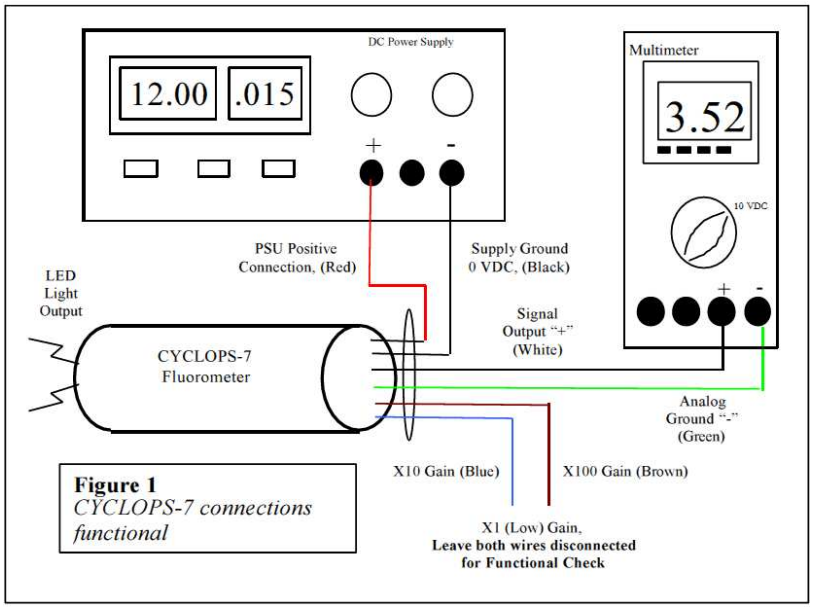

Figure 3.5: Schematic diagram for multi parameter system for cyclops-7 fluorometers, Turner Designs (2007)

Fluorescence is temperature sensitive. As the temperature of the sample increases, the fluorescence decreases. For greatest accuracy, the calibration and experiments were carried out within the temperature range of 17.7 $\pm$ 3.5 ^{o}C.

3.1.6 Calibration of Fluorometers

Calibration of the fluorometers was carried out with Cyclops in-situ to obtain equations that represent their voltage readings in response to change in concentration. Different sets of calibration were done to cater for pipe flows without the manhole installed as well as when the manhole was installed. However the same calibration procedure was used in both cases.

The sump was filled with approximately 2.5 m^3 of clean water. Rhodamine WT was used as the tracer for the experiment. The neat Rhodamine WT dye was estimated to have a concentration of 10^9 parts per billion. 5µl of neat dye was mixed with the sump to create a sump with concentration of 2 parts per billion (ppb). To ensure that the sump was properly mixed, the system was allowed to run for about 20 minutes at a high flow rate.

After this a sample was taken from the sump and its concentration was measured using a different 10AU Fluorometer and recorded, this was done to determine the accurate concentration of dye within the sump also. The rig was then allowed to run for 10 min with the inserted fluorometers taking readings. These readings were logged within the computer attached to the rig. The process above was repeated for each 20 ppb increase in sump concentration

until the voltage measurements from the fluorometers were close to 5 volts. The data logged from each sump concentration was analysed. It was observed that the calibration results changed with time as shown in Fig 3.6 and 3.7. This can be due to the temperature difference at the times and prolonged use of the Cyclops in fluid. Therefore a new calibration was done before each new batch of experiments was carried out. Below are examples of these changes with dates.

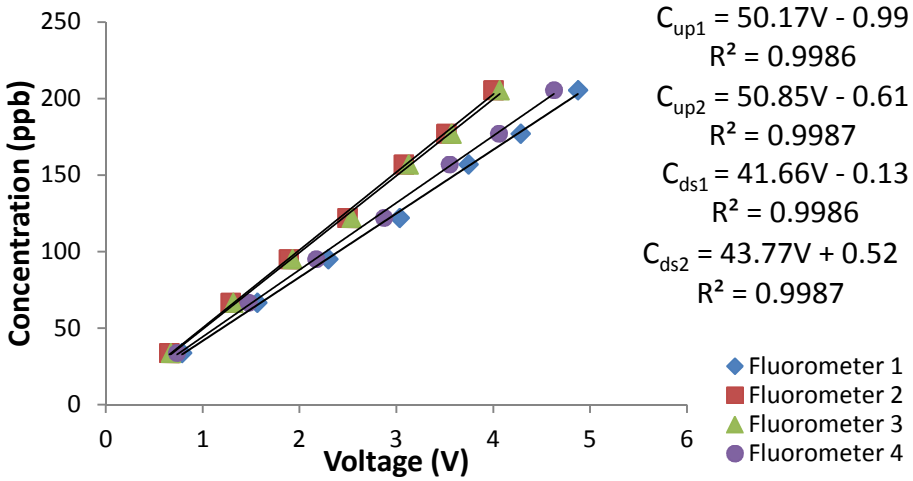

Figure 3.6: Calibration results of four fluorometers on 14/11/2013.

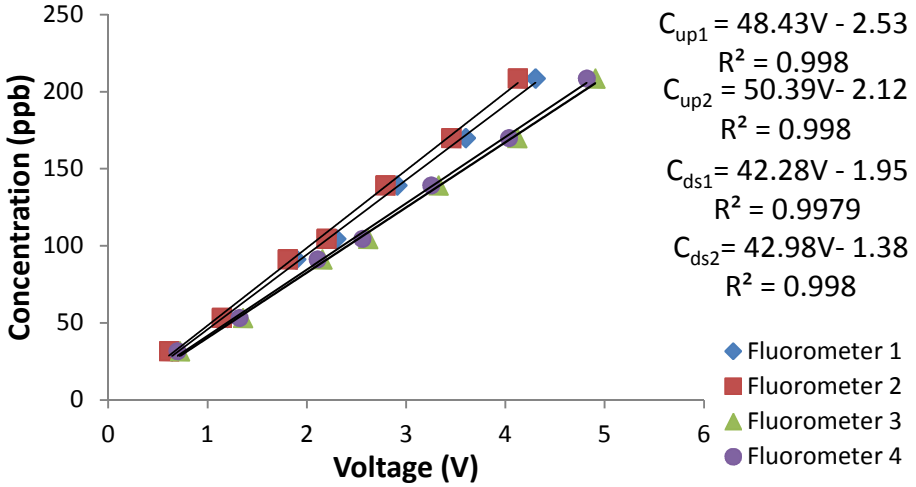

Figure 3.7: Calibration results of four fluorometers on 21/02/2014.

3.1.7 Dye Injection

A dye injection system that would create a steady injection and repeatability is needed since repeat experiments would be carried out. A Watson Marlow 505Di peristaltic pump provided controlled injections of Rhodamine WT for all of the dye trace experiments (Watson-Marlow Bredel Pumps, n.d.). Two 313D pump heads were fitted to the peristaltic pump to minimise pulsing, and these drew fluid from a 10 litre dye sump. For each injection a 5 V signal of different durations (2-15 seconds depending on type of experiment) was sent to the peristaltic pump at a specified time using the same MATLAB code and data acquisition card used to acquire data. The 5 V signal was input directly to the remote control port on the pump and forced it to run at 300 rpm for the specified duration of the signal. When the pump was stopped, a non-return valve ensured additional dye did not continue to seep into or out of the pipe system.

The injection point was fitted at a distance of 1.55 m before the first Cyclops which allows some mixing before fluorescence detection. Air bubbles trapped within the injection system are let out before any experiment so that the correct amount of dye goes into the system with the duration specified.

The dye sump was made to a concentration of 2000 to 6000 ppb depending on the type of measurement carried out and the flow rate. For overflow experiments, a less concentrated sump is used but injections are performed over a longer duration of 15 seconds.

The dye used for this experiment was Rhodamine WT. It is a reddish dye with a maximum excitation wavelength of 555 nm and a maximum emission wavelength of 580 nm (Smart and Laidlaw, 1977). The fluorometers used in this study generate excitation light with wavelengths around 555 nm. Emitted light in the 580 nm range is detected by the fluorometers, and the intensity of the light detected is proportional to the concentration of Rhodamine WT in solution.

3.1.8 Overflow Measurements

The overflow experiment required an addition at the top of the manhole. A thin plate, sharp edged weir was fitted around the top of the manhole (730 mm above the soffit of the pipe) to allow the water overflow steadily over the top into a stilling basin. The stilling basin was made of perplex and had dimension of 570 mm by 500 mm. It is 115 mm deep and collects the overflowing water. The basin is fitted with a trough which conveys the water into the sump for mixing and recirculation. A fluorometer is placed inside the trough to record the fluorescence corresponding to the dye concentration at the overflow. The fluorometer is of the same specification and settings as those used along the pipe. The schematic diagram of the overflow setting is shown in Fig 3.8.

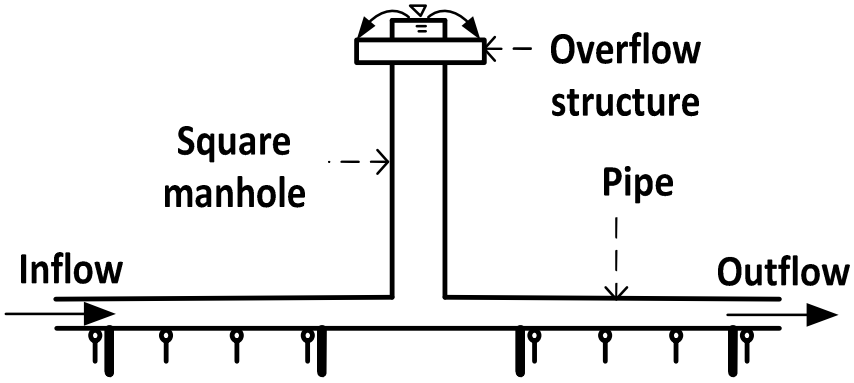

Figure 3.8: Schematic diagram of the overflow structure.

3.2 Types of Laboratory studies

The experiments carried out during this research are subdivided into the following:

- Pipe Flow Study (chapter 4)
- Square Manhole Study (chapter 5)
- Overflow Study (chapter 5)

They are however summarised within this section.

3.2.1 Pipe Flow Study

This study was aimed at investigating the dispersion of tracer within a straight pipe. Full flowing conditions at different flow rates were investigated. The headloss along the flow was recorded and analysed. The trace data recorded was analysed using various methods and compared to existing research. Orifice

plates were also introduced along the length of flow and for each flow rate, their effect on dispersion coefficient was quantified. Each experiment was carried out several times to ensure accuracy and an attempt to describe the relationship between the headloss and dispersion coefficient was carried out.

3.2.2 Square Manhole Study

Two sizes of manhole were used in this study as mentioned earlier, utilising the same procedures. Experiments were carried out to investigate tracer movement within the manhole over three different flow rates and a range of surcharges. To create different surcharge levels, the water level within the manhole was increased by closing the sluice gate at the outlet end of the pipe. The effect of these increases on the head loss was also studied. More surcharge levels were created with the larger manhole than the smaller one, because a 1 mm step closing of the sluice gate results in greater depth of water within the smaller manhole than evident within the larger manhole.

3.2.3 Overflow Study

The study was aimed at observing and understanding the movement of the tracer when an overflow occurs, particularly caused by the split in concentration at the outlet and overflow. Overflow study was carried out for

both the large and small manhole. Two conditions of overflow were investigated. One when the outlet is completed blocked and all the flow into the manhole goes out through the overflow. To achieve this, the sluice gate was completely closed. The other was when the flow into the manhole goes out through a split between the outlet pipe and the overflow. To create this condition, several positions of the sluice gate were considered until a desirable opening that allows for overflow conditions at all the flow rates was achieved.

3.2.4 Visualization of Experiment

Photographs and videos of the experiments were carried out for record purposes as well as acting as an aid to understanding the pattern of flow. Red food dye was used as a tracer because of the large amount that would be needed for good visibility and to avoid toxic and health hazards that might arise from using too much Rhodamine WT while disposing of the sump waste water. The food dye was diluted to a concentration of 1:6 and injected at a pulse of 4 seconds.

A spot light was used to create better illumination, with white card used to black out sides where rays of light might be reflected to the water within the manhole. For each experiment, two video cameras were used to record the dye movement within the manhole; one records the plan view, while the other records the side elevation. The cameras were kept in place with the use of tripod stands. Both cameras were connected to a computer to start the recording automatically and

the images are displayed simultaneously on the screen. The recordings are time stamped which helps in splitting the entire recording into smaller recordings based on flow rate and surcharge levels.

This procedure was repeated twice for every flow rate and several water depths that represent the range of surcharge level considered in the actual experiments.

4 Pipe Mixing Study

4.1 Experimental Specifications

The pipe mixing study was undertaken using the flow rig described earlier in section 3.1. To adapt the rig for this study, the manhole was removed and was replaced by a straight pipe as shown in Fig. 4.1. The aim of this study was to determine longitudinal dispersion within the pipe when there is a clear pipe and when an orifice plate has been fixed along the flow path. Data from the fluorometers located at the upstream and downstream of the rig were logged at a frequency of 30 Hz. Several flow rates were considered. Each flow rate was repeated five times and the temperature within the sump throughout the experiment was recorded. The data was analysed using various models in a bid to accurately describe the physical processes, especially focusing on dispersion and an attempt to relate the headloss to dispersion coefficient.

The experiments were as follows:

Experiment 1: Carried out on the straight pipe within the rig. Four manometer tappings were placed on both the upstream and downstream ends of the pipe. Pressure at these points at different flow rates was recorded. The aim of this experiment is to determine the effect of head loss on travel time and dispersion in a straight pipe.

Experiment 2: The same set up as above was used. The difference in this case was the introduction of an orifice plate midway between the upstream and downstream end of the pipe. Two different diameters of orifice plate (35 mm

and 25 mm) were used. The aim of this experiment was to determine the change in pressure, travel time and dispersion due to the presence of the orifice plate.

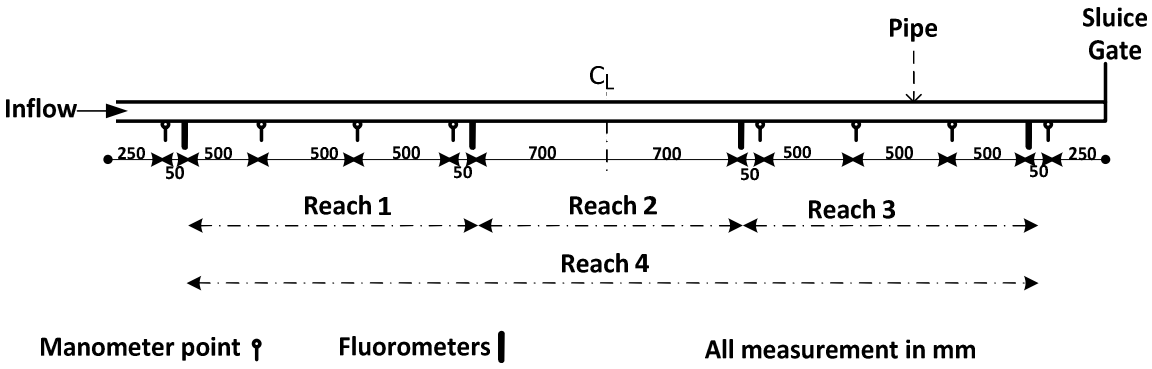

Figure 4.1: Experimental set up for flow in straight pipe

4.1.1 Dye Concentration and Injection

Neat Rhodamine WT was mixed with water to create a standard concentration of between 800 and 1000 ppb. A dye injection pump was fixed to the rig such that it injects dye at some distance before the upstream fluorometer. Using Matlab codes the dye was injected at 60s after the start of each experimental run for a 2s duration. The same process was repeated for each repeat run of flow rate. The injected dye then disperses with the flow along the pipe from the upstream to the downstream end.

4.1.2 Flow Rate Measurement

Full pipe flow experiments were carried out between flows of 0.6 l/s and 2.0 l/s with 'no orifice' inserted along the line of flow. An end control sluice gate was

fixed to the outlet of the pipe to create full pipe conditions at 0.6 l/s. Each flow rate was carried out for duration of 180s with an initial and final wait time of 10s and was repeated for four times.

Table 4.1: Reynolds Number obtained in system at flows studied

Flow Rate (m^3/s)	0.0006	0.0008	0.0010	0.0012	0.0014	0.0016	0.0018	0.0020
Reynolds Number	13521	18028	22535	27042	31549	36056	40563	45070
Theoretical Friction Factor	0.028	0.026	0.024	0.023	0.022	0.022	0.021	0.020

4.1.3 Orifice Plate

The orifice plate acted as constriction in the line of flow. At this point the area of flow is reduced leading to an increase in velocity. There were four manometer positions before the orifice plate and they are referred to as upstream while the four manometer positions after the orifice plate are referred to as downstream. For the 35 mm orifice plate, flow rates between 0.6 l/s and 2.0 l/s were studied while for the 25 mm orifice plate, flow rates of 0.6 l/s to 1.0 l/s were studied. It was visually observed that the jet created by the constriction dissipated after about 0.70 m downstream.

4.1.4 Reynolds Number

The values of Reynolds number and friction factor is shown in Table 4.1. The flow in the pipe was turbulent with the Reynolds number obtained having

values of 13,521 at 0.6 l/s flow rate and 45,070 at a flow rate of 2.0 l/s. In order to validate the laboratory result against expected theoretical values of friction factor, the Moody's diagram was used. The theoretical values of friction factor were obtained by applying the Reynolds's number of the flow, and the roughness factor k for Perspex pipe which is 0.00025 mm in the Moody's chart which gave values ranging from 0.028 at 0.6 l/s to 0.02 at 2.0 l/s. The average of the values was 0.023.

4.2 Pre-Processing of Data

All tracer data recorded was subjected to some pre-processing steps to identify the actual trace data that represents the observations required. These steps were carried out using MATLAB codes which allow for repeatability and takes far much less time than using excel or by manual calculation. The steps are explained below.

4.2.1 Background Concentration Removal

Data logged into the computer was in volts. The equation derived from the calibration of fluorometers was applied to each voltage recorded to obtain the instantaneous quantity of dye in parts per billion (ppb). The time taken to run each experiment was recorded in seconds.

An apparent or real fluorescence background in water samples taken for dye analysis can cause several problems in tracer studies. It may mask very low concentrations of the tracer or cause apparent recoveries to be in excess of 100% in quantitative work. The two major sources of background are natural fluorescence and suspended sediment.

It is likely the water flowing through the pipe has background fluorescence from previous experiments, it was therefore necessary to remove the fluorescence present in the water. This initial fluorescence could be from the water in the sump, dye already present in the system or the combination of both from the trace data. For each experimental run, an initial wait time of 10 seconds was allowed and dye injection at 60 seconds from start. To determine the background concentration value using MATLAB codes, the average of the readings between the 11^{th} second to the 60^{th} second was taken as the background concentration. A matrix of this mean value was created and removed from the matrix of the measured data to obtain a background concentration free data set. The same procedure was repeated for each experimental run.

4.2.2 Start and End Point Determination

Voltage output from fluorometers was logged through the duration of each experiment. This implies that data was recorded before the first trace of dye reached the upstream fluorometer and after the last trace left the downstream fluorometers. If the data was plotted directly it would consists of long tails of

very low concentrations, and in analysis it will significantly alter the variance and dispersion coefficient results. Therefore for each run, the data trace representing the period between the first arrival and departure from each fluorescent measuring point needed to be determined. To achieve these, the method described by Hart (2013) was adopted. The method defines the start and end locations as a point at which the signal drops below a certain percentage of the profile's peak concentration. The approach adopted was to define the start and the end locations as the point at which ten consecutive data points fell below a certain percentage of the peak. The goal of choosing what percentage of the peak to use is to find a value that incorporates the whole concentration profile, whilst minimising the amount of background scatter included. For this experiment, cut off values of 1.0% and 3.0% of the peak concentration was used as determinant of the start and end point.

Table 4.2: Average Mass Recoveries due to Cut-off Point

Q (l/s)	0.6	0.8	1.0	1.2	1.4	1.6	1.8	2.0
Cut Off (%)	Mass Recovery (%)							
1.0	103	103	103	101	102	101	101	101
3.0	99	100	102	100	100	100	100	100

For each of these, the mass recovery was calculated as means of determining the accuracy of the obtained trace. Table 4.2 shows the average mass recovery of four repeats for both cut-off points. At 1.0%, the mass recovery was over 100% at all flow rates but at 3.0%, 6 out of 8 of the mass recoveries were equal to 100%. 3.0% of the peak concentration was therefore used as the cut-off value to determine the start and end point of the trace.

4.2.3 Filtering and Grouping

The data recovered from the above process sometimes contain outliers within them. These are data that are significantly out of place, mostly negative values. A matlab code was written to identify these outliers, remove them and replace them with new values. The new values are an interpolation of the value before and after the outlier. In places where there are two or more consecutive outliers, the program searches wider and performs double interpolation with positive values bordering the outliers.

Data recordings were taken at a frequency of 30 Hz. Figure 4.2 shows an example of concentration data before and after pre-processing.

The data was grouped according to the flow paths and measuring distances. The distances are referred to as 'Reaches'. The classification is listed below and in Fig 4.1.

1. Reach 1: Upstream 1 to Upstream 2
2. Reach 2: Upstream 2 to Downstream 1
3. Reach 3: Downstream 1 to Downstream 2
4. Reach 4: Upstream 1 to Downstream 2

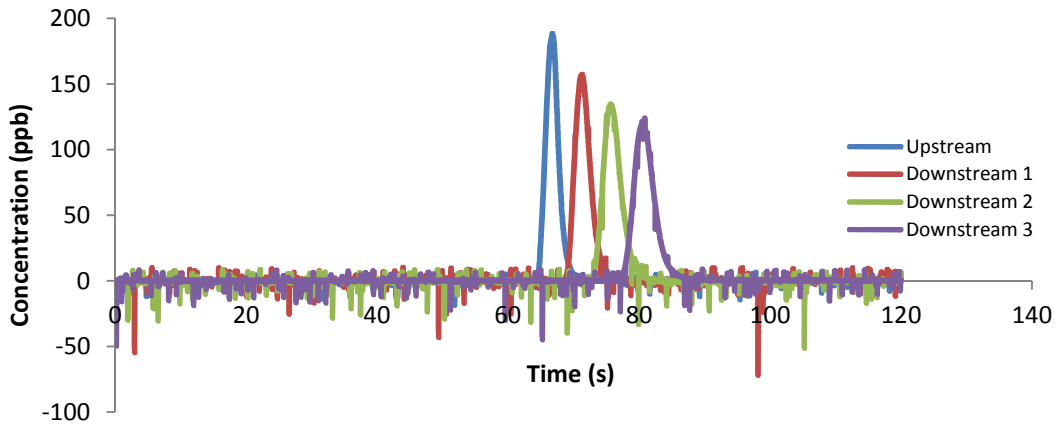

(a) Raw Data

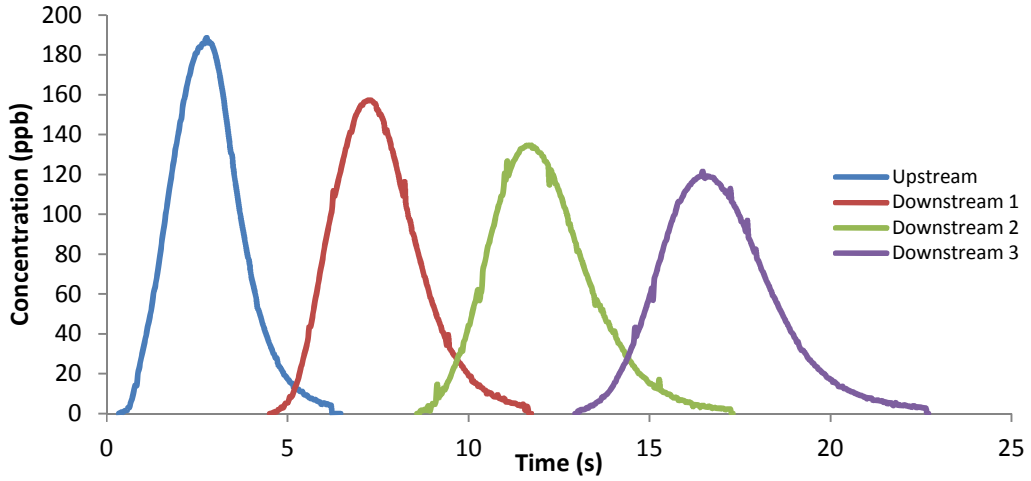

(b) Data after pre-processing

Figure 4.2: Sample concentration profile plot

4.3 Headloss

Each manometer position described previously had a tube that was connected to a stilling cylinder which had a larger diameter than the tube. The height of the

water in the stilling cylinder was measured using an automated calibrated calliper.

4.3.1 No Orifice Flow

For flow rates ranging from 0.6 l/s to 2.0 l/s, the height of water in the manometer tubes was measured and recorded. This was repeated four times for each flow rate (deviation of $\pm$0.003m) and the average value was used as the representative height of water at that flow rate. The head loss in the pipe was defined as a difference in pressure between two distances along the length of a pipe. For each flow rate, the height of water at the eight manometer positions was plotted against the location/position of the manometer positions as shown in Fig. 4.3. The gradient of each which represents headloss/length (h_f/l) was obtained and subsequently the headloss by multiplying the value with the length of the measuring distance. The headloss values ranged from 0.014m at 0.6 l/s to 0.106m at 2.0 l/s for the full length of pipe (4.5 m). The values obtained were plotted against the discharge and also the velocity head given by $\frac{V^2}{2g}$ where v is the velocity of flow and g is the acceleration due to gravity as shown in Fig 4.4. Substituting the obtained values and parameters in the Darcy-Weisbach equation gave a friction factor value of 0.023 which agrees with the theoretical value obtained using Reynolds number. This implies that the head loss occurring in the pipe is solely due to friction along the wall of the pipe. The R-squared (R^2) values denoting goodness of fit of the h_f/l plots are shown in Table 4.3.

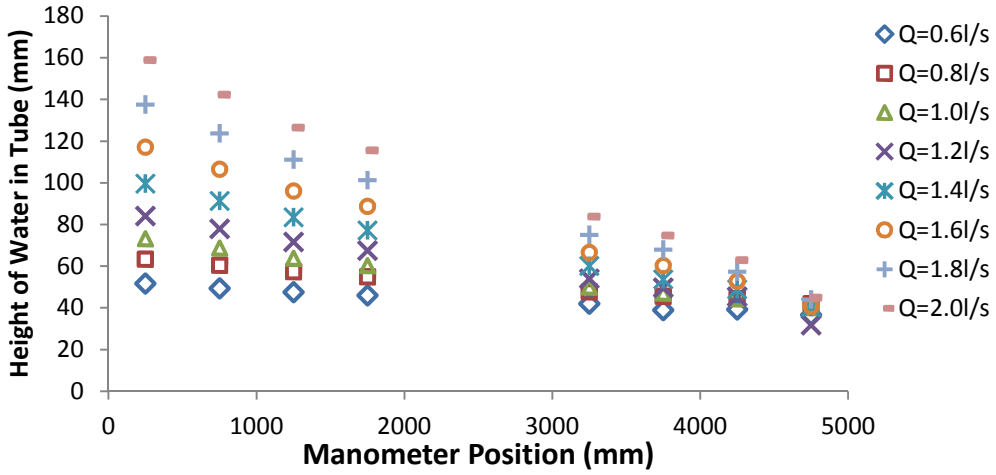

Figure 4.3: Height of water in manometer measured along length of pipe

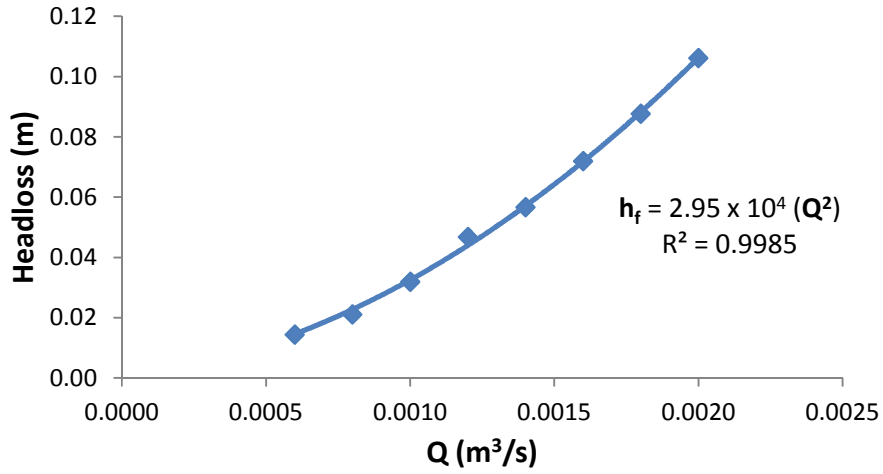

(a) Flow rate Q

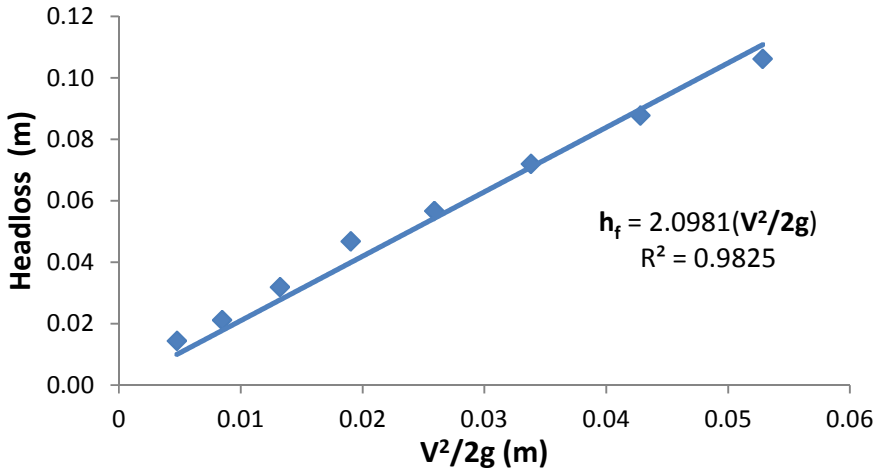

(b) Velocity head

Figure 4.4: Headloss variation with head in no orifice flow

Table 4.3: Goodness of fit of Hydraulic Grade line

Q (l/s)	0.60	0.80	1.00	1.20	1.40	1.60	1.80	2.00
R^2	0.988	0.993	0.995	0.978	0.996	0.995	0.994	0.993

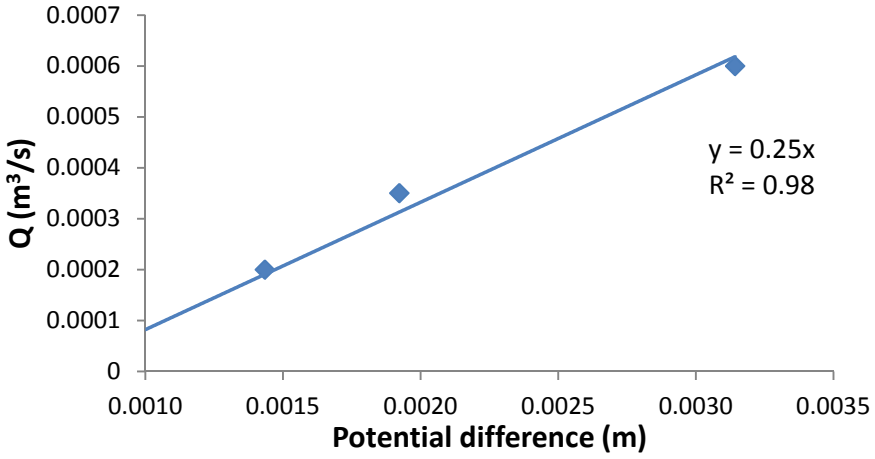

Figure 4.5: The slope of the pipe

- Water surface slope S =δy/δx = 0.25

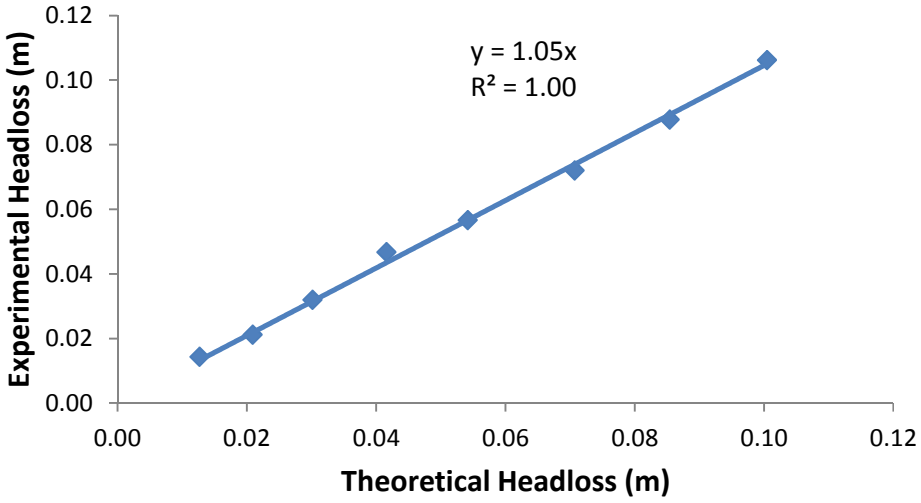

Figure 4.6 Comparison of measured and calculated headloss, no orifice flow

Daisy-Weisbach relates the pressure difference or head loss due to friction along a pipe as

$$h_f = f_D \cdot \frac{L}{D} \cdot \frac{V^2}{2g} \tag{4.1}$$

$$h_f = \frac{8 f_D L Q^2}{g \pi^2 D^5} \tag{4.2}$$

The horizontal slope of the pipe was determined using the potential difference as shown in Fig. 4.5. An attempt was made to predict the theoretical value of the headloss using the slope of the graph (Fig. 4.5), the velocity head and the frictional factor. A plot of the experimental and theoretical value is shown in Fig. 4.6. It can be concluded that the plots and measurements are reliable and comply with Darcy-Weisbach theory.

4.3.2 35 mm orifice Plate

For each flow rate, the height of water at the eight manometer positions was plotted against the manometer positions as shown in Fig. 4.7. The presence of an orifice plate along the line of flow causes a sudden reduction in area, leading to entry and exit losses. It was observed that there was a build-up of pressure at the upstream end of the pipe before the orifice plate; this is evident in the values recorded at the upstream manometers as they were considerable higher than those measured without the orifice plate in place. Values of measured head of water varied from a minimum of 0.026 m at the downstream to a maximum of 0.068 m upstream at 0.6 l/s and a minimum of 0.043 m to a maximum of 0.359 m at 2.0 l/s. The total head loss in the pipe at each flow rate, which is the

combination of frictional losses as well as losses across the orifice plate, was obtained by inserting the distances at the beginning and the end of the pipe into the equations of the best fit lines at the upstream and downstream respectively, and obtaining the head difference. The total headloss changes with discharge are shown in Fig. 4.8.

To obtain the losses across the orifice plate, plots of the height of water in the upstream manometers against the manometer positions as well as the height of water in the downstream manometers against the manometer positions was plotted on the same graph. The gradient of each plot was projected to the position of the orifice plate and the difference in height was calculated as the head loss across the orifice plate. The variations of the total headloss and the headloss across the orifice plate with the velocity head is shown in Fig. 4.9. It shows that the orifice plate contributed significantly to the headloss across the entire system.

Figure 4.10 show the comparison of the experimental value with the theoretical value of headloss within the system was calculated (Som and Biswas, 2008), using

$$Q = C_d A_0 \sqrt{2gH} \tag{4.3}$$

Where $$C_d = \frac{1}{1.7 - \frac{A_0}{A}} \tag{4.4}$$

Where Q = Inflow, C_d=Discharge coefficient, A_0=Area of orifice opening, A= Cross sectional area of pipe, g=Acceleration due to gravity, H=Headloss

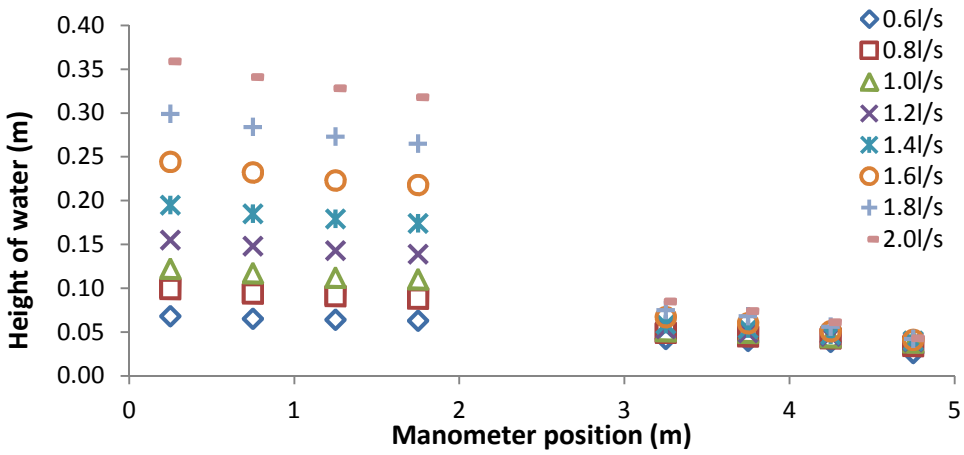

Figure 4.7: Height of water in manometers along pipe, 35 mm orifice plate

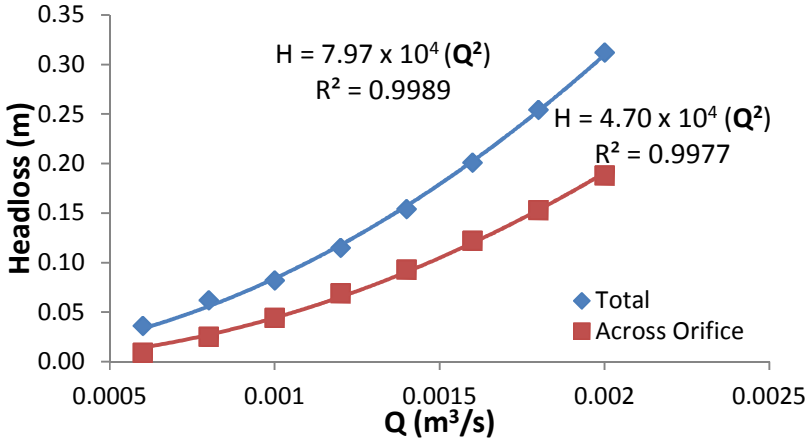

Figure 4.8: Variation of total headloss with flow rate, 35 mm orifice plate

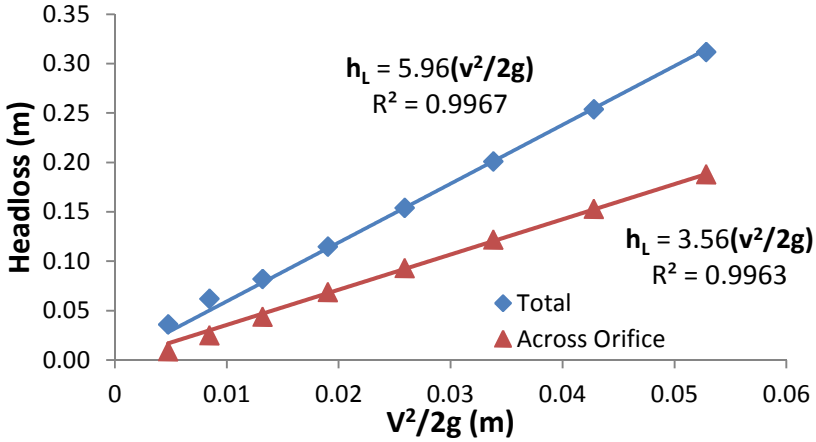

Figure 4.9: Variation of headloss with velocity head across 35 mm orifice plate

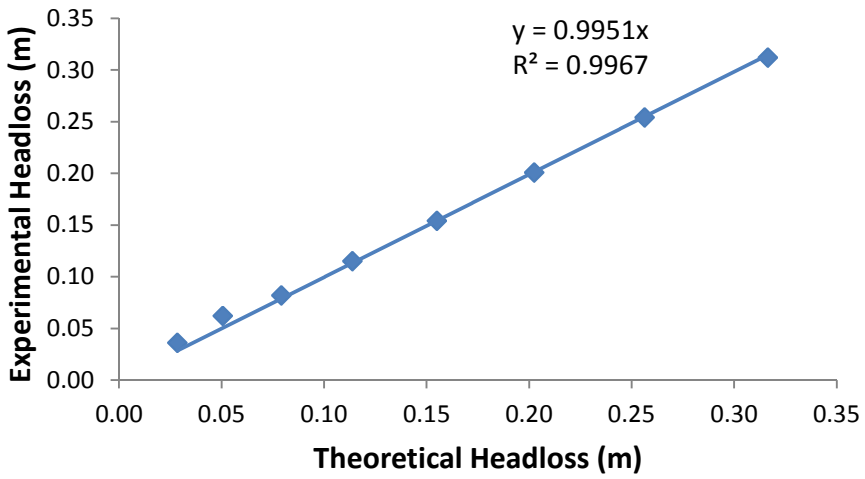

Figure 4.10: Comparison of measured and calculated headloss (Eqn. 4.3), 35 mm orifice plate

4.3.3 25 mm Orifice Plate

A 25mm orifice plate was used to replace the 35mm orifice plate at the same position, in order to compare the effect a smaller diameter will have on the flow. Using the same eight manometers as described under flow in straight through pipe, head loss measurement were taken for flow rates of 0.6 l/s, 0.8 l/s and 1.0 l/s. Only three flow rates could be measured because at higher flow rates, there was a build-up of pressure at the upstream end of the pipe before the orifice plate and the resultant height of water at the manometer tubes would result in spills with the existing laboratory system.

The same process of analysis as for the 35mm orifice plate was carried out. For each flow rate, the height of water at the eight manometer positions was plotted against the manometer positions as shown in Fig. 4.11. Here a greater drop in height of water was obvious between the upstream and downstream

manometers. Values recorded varied from a minimum of 0.026m at the downstream to a maximum of 0.181m upstream at 0.6 l/s and a minimum of 0.037m to a maximum of 0.432m at 1.0 l/s. The total headloss changes over the full length of pipe (4.5 m) with discharge are shown in Fig. 4.12.

The variations of the total headloss and the headloss across the orifice plate with the velocity head is shown in Fig. 4.13. It shows that the orifice plate contributed significantly to the headloss across the entire system.

Figure 4.14 shows the comparison of the experimental value of headloss with the theoretical value of headloss within the system was calculated using equation 4.3.

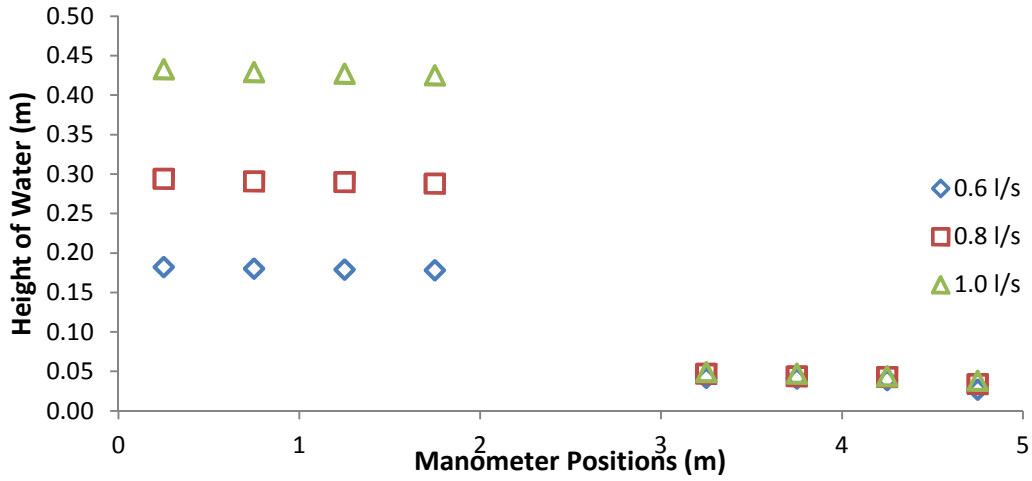

Figure 4.11: Height of water at the eight manometers, 25mm Orifice plate

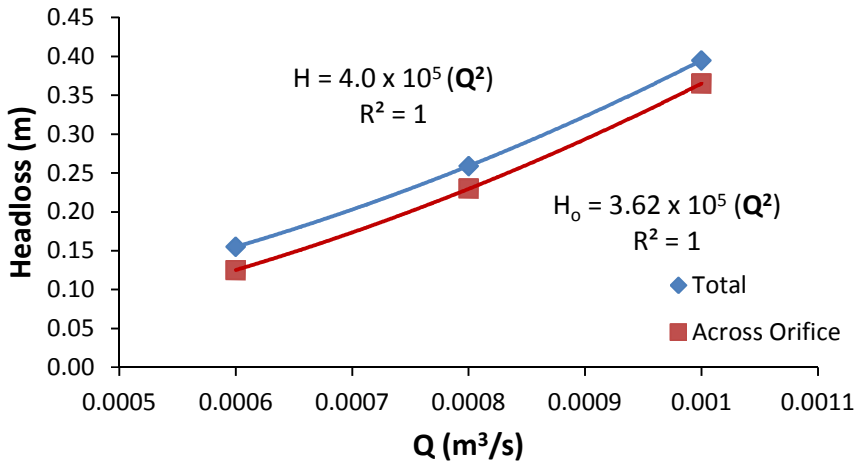

Figure 4.12: Variation of headloss with flow, 25mm Orifice Plate

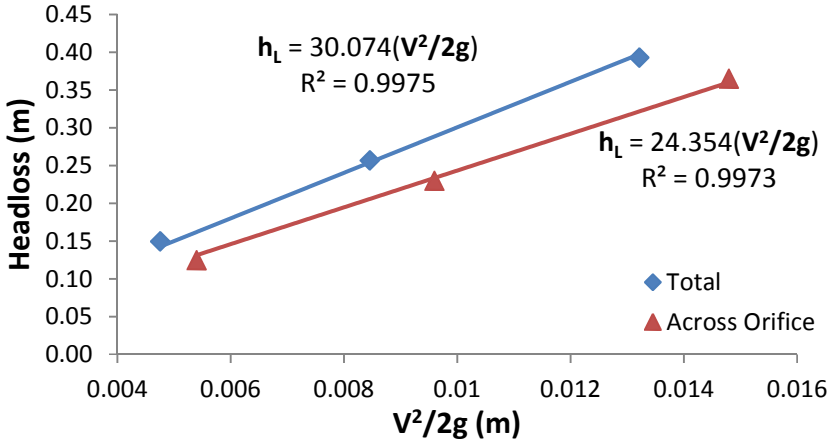

Figure 4.13: Variation of headloss with velocity head, 25mm Orifice Plate

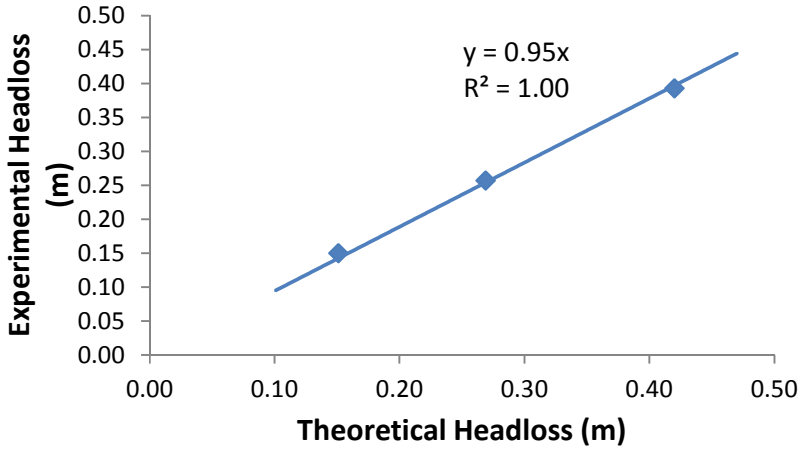

Figure 4.14: Comparison of measured and calculated headloss (Eqn.4.3), 25 mm orifice plate

4.4 Mass Recovery

The mass recovery ratio for the solute tracing experiment which signifies the amount of dye input recovered at the downstream end was high with values ranging from 93% to 108% (Fig.4.15). For the no orifice flow, and the orifice plate insertions considered, the average values of mass recovery ranged between 98% and 102%. This implies that the amount of dye injected upstream was transported and fully recovered downstream along the length of pipe.

4.5 Optimisation using Advection-Diffusion Equation (ADE)

The optimised ADE analysis uses the data recorded at the upstream measuring point to predict the downstream profile. This predicted profile is then compared to the recorded downstream data and the goodness of fit, measured by the R-squared value is calculated. Fig 4.16 shows sample concentration distribution profiles for all three types of experiment carried out. The profile shows the actual trace after background removal and the determination of start and end points. Fig. 4.16a &b represents data at 2.0 l/s while Fig. 4.16c represents data at 1.0 l/s (highest flow rate). The downstream curves are almost Gaussian in shape as expected of a pipe flow. The downstream peak is also slightly attenuated. However the prediction accurately fits the downstream profile. The ADE dispersion parameter obtained by the application of the ADE model to the laboratory data produced predictions with excellent R^2 values. The R-squared values ranged from 0.991 to 0.999 with a majority having values of 0.999. The

closer the R-squared value is to 1.0, the more accurate the ADE analysis has been able to predict the behaviour of the flow downstream. A summary of the results is presented in Table 4.4.

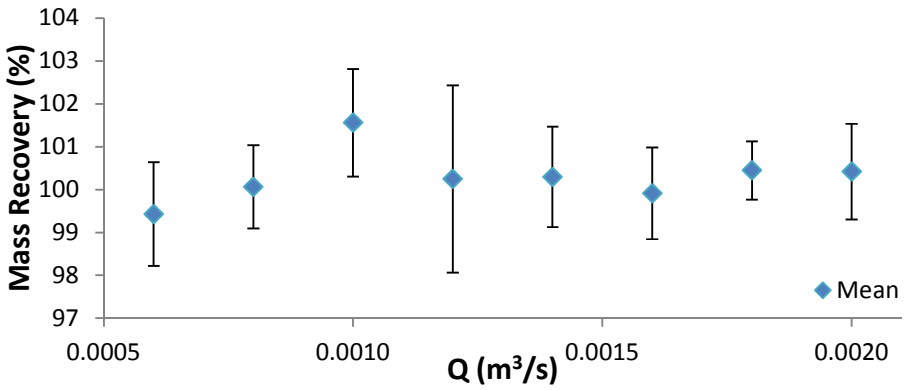

(a) Full pipe flow

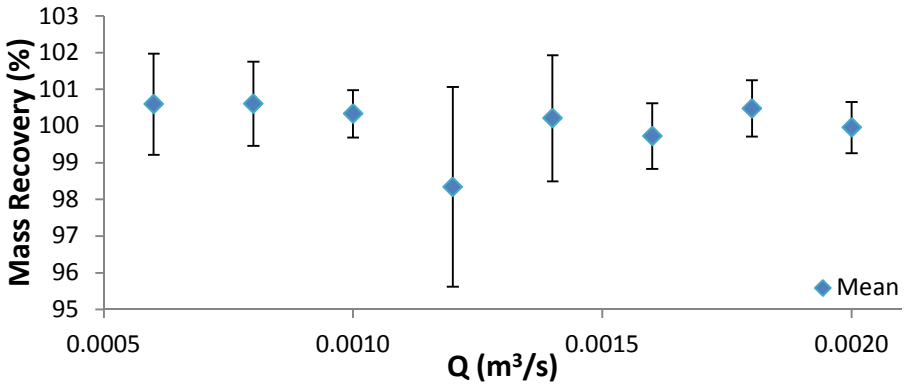

(b)35 mm orifice plate

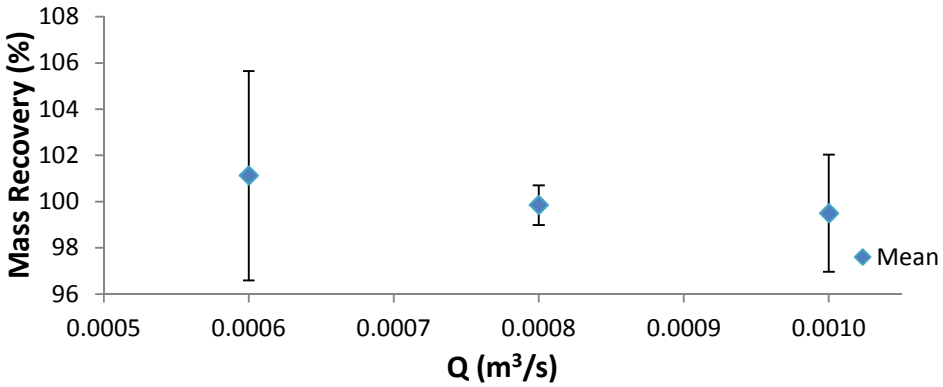

(c)25 mm orifice plate

Figure 4.15: Mass recovery values across length of pipe

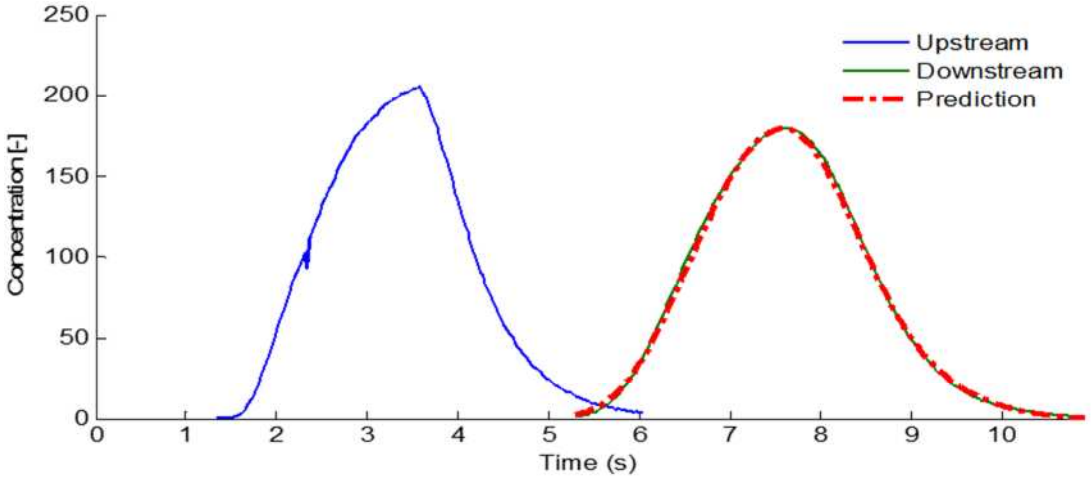

(a) No orifice flow, Q = 2.0 l/s

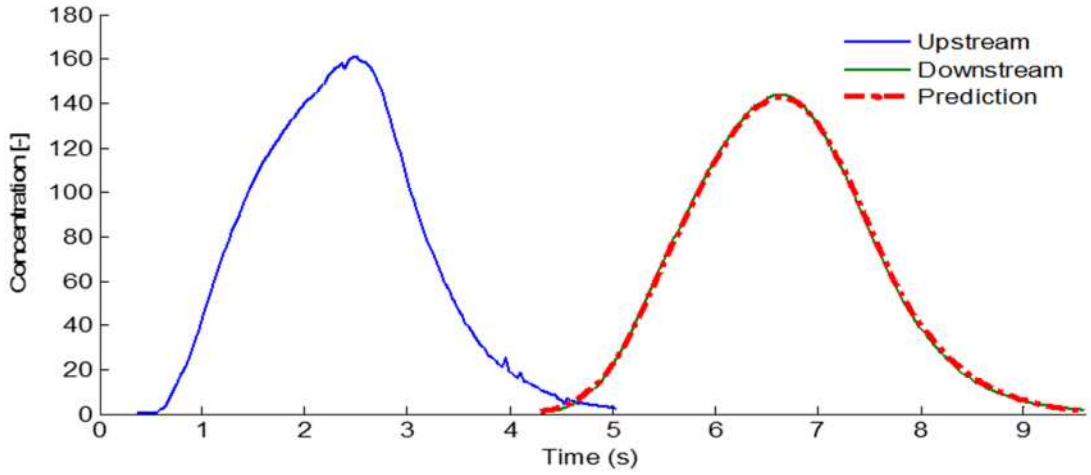

(b) 35 mm orifice plate, Q = 2.0 l/s

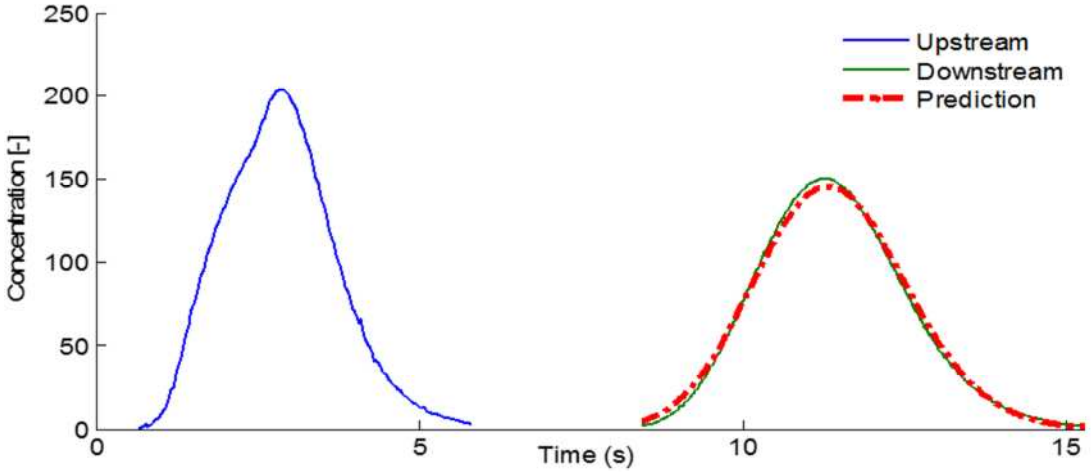

(c) 25 mm orifice plate, Q = 1.0 l/s

Figure 4.16: Sample concentration profile distributions, with ADE downstream prediction (Reach 2); (a) Q= 2.0 l/s, (b) Q=2.0 l/s, (c) Q=1.0 l/s

Table 4.4: Summary from dye tracing analysis

			Reach 1				Reach 2				Reach 3				Reach 4			
	Q (l/s)	Q (m^3/s)	MB (%)	$\bar{t}$ (s)	Dxx (m^2/s)	R^2	MB (%)	$\bar{t}$ (s)	Dxx (m^2/s)	R^2	MB (%)	$\bar{t}$ (s)	Dxx (m^2/s)	R^2	MB (%)	$\bar{t}$ (s)	Dxx (m^2/s)	R^2
No Orifice	0.6	0.0006	100	4.7	0.0040	0.996	98	4.4	0.0043	0.997	101	4.8	0.0044	0.997	99	13.9	0.0045	0.993
	0.8	0.0008	99	3.5	0.0045	0.997	100	3.3	0.0056	0.998	101	3.7	0.0063	0.998	100	10.5	0.0058	0.998
	1.0	0.001	101	2.8	0.0049	0.997	100	2.7	0.0055	0.997	102	2.9	0.0077	0.999	103	8.5	0.0060	0.998
	1.2	0.0012	99	2.4	0.0048	0.998	98	2.2	0.0107	0.999	103	2.4	0.0078	0.999	100	7.1	0.0078	0.999
	1.4	0.0014	99	2.1	0.0090	0.998	101	1.9	0.0121	0.999	101	2.1	0.0097	0.999	101	6.1	0.0102	0.999
	1.6	0.0016	101	1.8	0.0080	0.997	99	1.7	0.0119	0.999	100	1.8	0.0129	0.999	100	5.3	0.0103	0.999
	1.8	0.0018	100	1.6	0.0052	0.999	100	1.5	0.0161	0.999	101	1.6	0.0139	0.999	101	4.7	0.0118	0.999
	2.0	0.002	99	1.4	0.0132	0.999	101	1.4	0.0173	0.999	101	1.5	0.0187	0.999	101	4.3	0.0148	0.999
	Q (l/s)	Q (m^3/s)	MB (%)	$\bar{t}$ (s)	Dxx (m^2/s)	R^2	MB (%)	$\bar{t}$ (s)	Dxx (m^2/s)	R^2	MB (%)	$\bar{t}$ (s)	Dxx (m^2/s)	R^2	MB (%)	$\bar{t}$ (s)	Dxx (m^2/s)	R^2
35mm Orifice	0.6	0.0006	99	4.6	0.0032	0.996	102	4.3	0.0050	0.998	100	4.8	0.0041	0.998	101	13.7	0.0044	0.992
	0.8	0.0008	99	3.5	0.0062	0.997	102	3.2	0.0063	0.998	100	3.7	0.0061	0.999	101	10.5	0.0063	0.997
	1.0	0.001	100	2.8	0.0052	0.998	101	2.7	0.0096	0.999	100	2.9	0.0074	0.999	101	8.4	0.0075	0.996
	1.2	0.0012	95	2.3	0.0071	0.998	101	2.2	0.0109	0.999	100	2.5	0.0093	0.998	97	7.0	0.0094	0.996
	1.4	0.0014	100	2.0	0.0069	0.998	98	1.9	0.0136	0.998	102	2.1	0.0111	0.999	100	6.1	0.0102	0.999
	1.6	0.0016	100	1.7	0.0079	0.999	99	1.7	0.0158	0.999	101	1.9	0.0118	0.999	99	5.3	0.0124	0.999
	1.8	0.0018	100	1.6	0.0081	0.997	101	1.5	0.0173	0.999	100	1.6	0.0138	0.999	101	4.7	0.0132	0.999
	2.0	0.002	99	1.4	0.0100	0.998	100	1.3	0.0187	0.999	101	1.5	0.0171	1.000	100	4.3	0.0137	0.999
	Q (l/s)	Q (m^3/s)	MB (%)	$\bar{t}$ (s)	Dxx (m^2/s)	R^2	MB (%)	$\bar{t}$ (s)	Dxx (m^2/s)	R^2	MB (%)	$\bar{t}$ (s)	Dxx (m^2/s)	R^2	MB (%)	$\bar{t}$ (s)	Dxx (m^2/s)	R^2
25mm Orifice	0.6	0.0006	96	4.6	0.0046	0.993	100	4.3	0.0056	0.993	107	4.9	0.0042	0.994	102	13.8	0.0053	0.992
	0.8	0.0008	100	3.5	0.0051	0.999	99	3.2	0.0080	0.998	101	3.7	0.0049	0.998	100	10.5	0.0064	0.996
	1.0	0.001	97	2.9	0.0070	0.996	103	2.6	0.0095	0.997	100	3.0	0.0078	0.999	99	8.5	0.0083	0.998

4.5.1 No Orifice Flow

4.5.1.1 Travel Time and Velocity

The travel time between the two measuring points ranged from 13.9s to 4.25s as flow rate increased. The values decreased as the flow rate increased but increased as the reach distances increased. To fit a straight line to represent the relationship between the travel time values and the flow rate, the travel time values were plotted against the inverse of the flow rate as shown in Fig 4.17. The slope of the graph is 0.0084 m^3.

The velocity calculated using the travel time obtained from the moment area method ranged from an average value of 0.319 m/s at flow rate of 0.6 l/s to an average value of 1.044 m/s at a flow rate of 2.0 l/s. As expected, for each flow rate, the average value of the velocities at reach 1, 2 and 3 represented by U_{ave} was equal to the velocity value at reach 4 which represents the total length between the first and last fluorescent measuring points. This implies that data collected over reach 4 can accurately give an overview of fluid flow behaviour in the system. In addition for all flow rates, the average value of the velocities (U_{ave}) was compared with the velocity of the system calculated using the flow rate and the cross sectional area of the pipe, U_{bar}. It was observed that the velocity values obtained by the travel time method was slightly higher than the velocity values obtained by cross sectional area. The plot comparison in Fig.4.18 shows that U_{ave} is about 2.6% higher than U_{bar}.

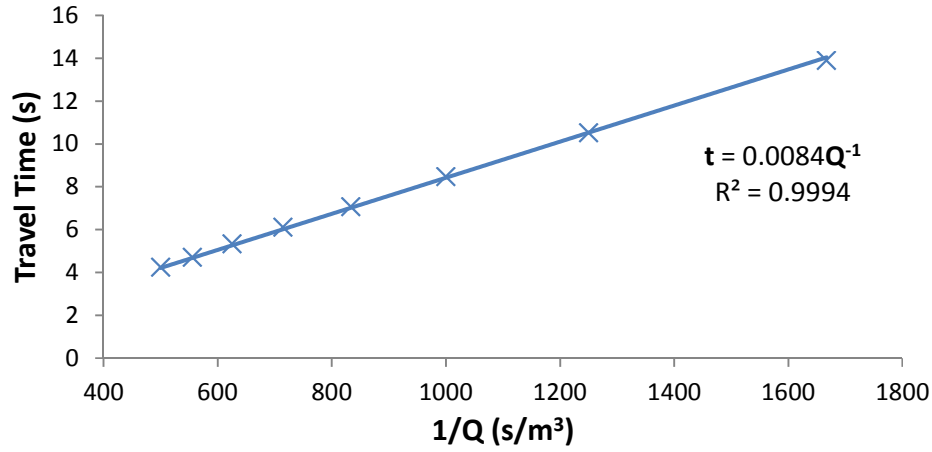

Figure 4.17: Variation of travel time with flow rates using ADE, no orifice flow

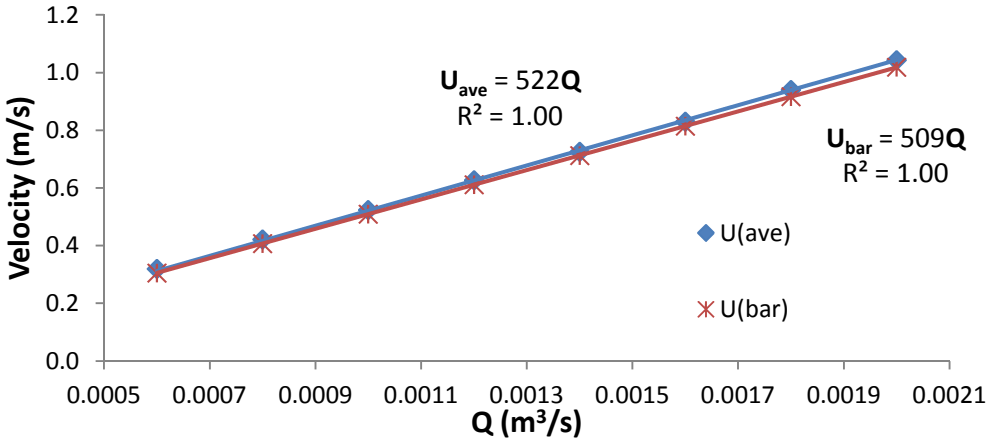

Figure 4.18: Variation of velocity with flow rates using ADE, no orifice flow

4.5.1.2 Dispersion

The values of longitudinal dispersion coefficient obtained from ADE varied from 0.0040 m^2/s obtained at reach 1 for 0.6 l/s and 0.0187 m^2/s obtained at reach 3 at 2.0 l/s (Fig.4.19). However across the total measuring length, the dispersion coefficient was 0.0042 m^2/s for 0.6 l/s, and 0.0148 m^2/s for 2.0 l/s. As Taylor (1954) predicted (Eqn. 2.4), a linear trend of increase in dispersion coefficient values as the flow rate increased was observed. At each flow rate, the dispersion coefficient values in reach 1 and 2 were close in value but the values at reach 3

were significantly higher than reach 1 and 2. This could be because at this reach the cloud of tracer dye left in the pipe are in very small quantities per length of pipe. Similarly, as with the velocity results, the average of the dispersion coefficient values at reach 1, 2 and 3 was equal to the value of dispersion at reach 4. An average of these dispersion coefficient values was therefore used to represent the dispersion occurring within the system (Fig. 4.20).

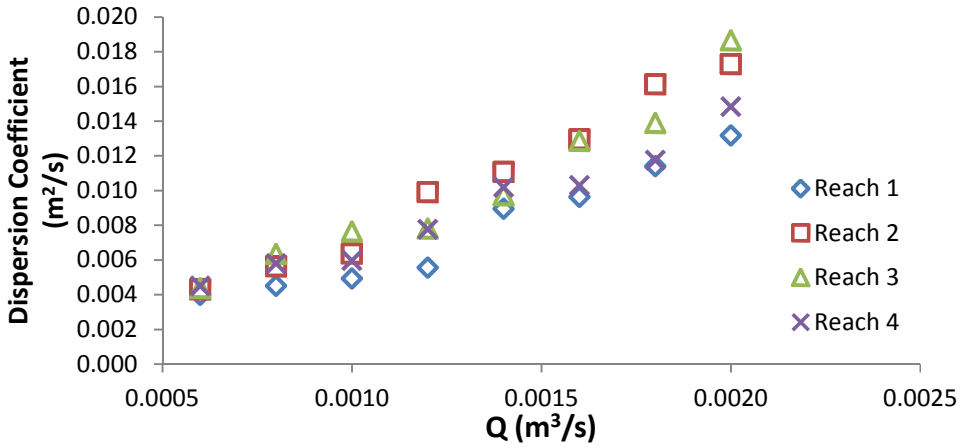

Figure 4.19: Variation of dispersion coefficient across each reach using ADE, no orifice flow

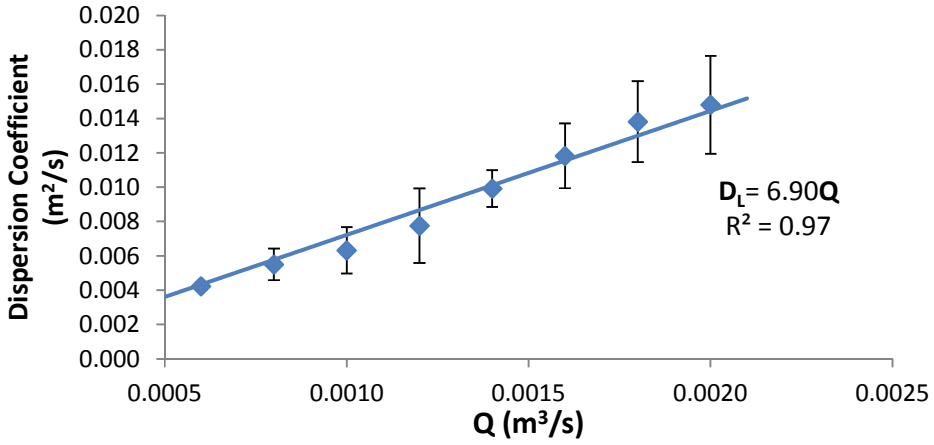

Figure 4.20: Variation of dispersion coefficient with flow using ADE, No orifice flow

Verification

The values of dispersion coefficient obtained from the trace data were verified against the theoretical value of dispersion coefficient that is expected by the application of Taylor's theory (Taylor, 1954), which defines Dispersion coefficient D_L as

$$D_L = 10.1\ au^* = 10.1a\bar{u}\sqrt{\frac{f_L}{8}} \qquad (4.5)$$

Where a= radius of pipe (m), u*= shear velocity (m/s), $\bar{u}$=velocity of flow (m/s), f_L = friction factor.

The theoretical values of "f_L" were obtained by applying the Reynolds's number of the flow, and the roughness factor k for Perspex pipe which is 0.00025mm in the Moody's chart. The f_L values ranging from 0.028 at 0.6 l/s to 0.02 at 2.0 l/s as shown in Table 4.1. These values were used to calculate the theoretical value of dispersion coefficient for the pipe. From the laboratory head loss measurement, the head loss in the pipe was plotted against the velocity head (Fig. 4.4), the gradient of the slope was applied to Eqn. 4.1 to obtain the friction factor which was 0.23. This value equals the average of the theoretical values obtained. The expected theoretical values and the experimental values of dispersion coefficient are plotted in the Fig. 4.21. Comparison of the results shows that the experimental results were slightly higher by 2.5% with a goodness of fit of 0.9372. It can be concluded that for the given laboratory set-up, the Taylor's prediction is a good representation of experimental values.

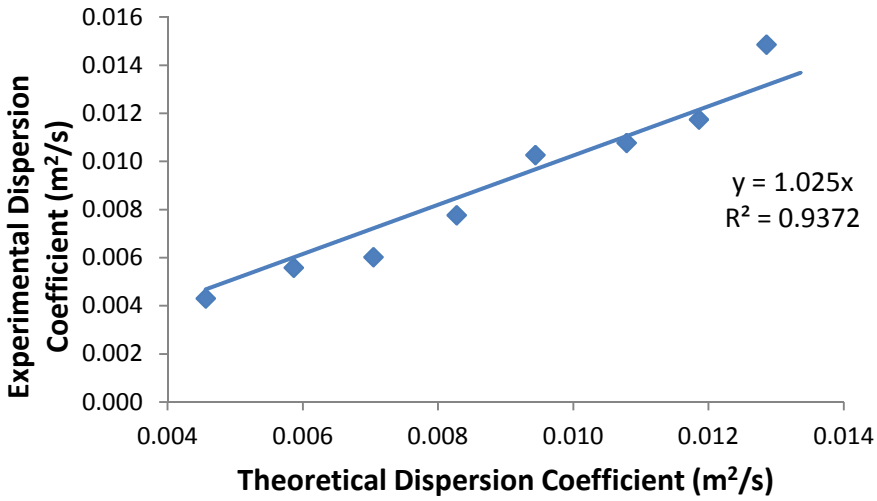

Figure 4.21: Comparison of Experimental and Theoretical dispersion coefficient, no orifice flow

4.5.2 35 mm Orifice Plate

4.5.2.1 Travel Time and Velocity

The travel time from ADE application between the two measuring points ranged from 13.718s to 4.268s as flow rate increased. The values decreased as the flow rate increased. To fit a straight line to represent the relationship between the travel time values and the flow rate, the travel time values were plotted against the inverse of the flow rate as shown in Fig. 4.22a. The slope of the graph is 0.0083 which is 0.0001 lower than a flow without orifice plate implying that overall, the presence of the plate slightly reduces the travel time.

Velocity obtained from travel time along the length of pipe as well as across the orifice plate was calculated from trace results. As for the no orifice flow, for each

flow rate, the average value of the velocities at reach 1, 2 and 3 represented by U_{ave} was equal to the velocity value at reach 4 which represents the total length between the first and last fluorescence measuring points. This implies that data collected across reach 4 can accurately give an overview of fluid flow behaviour in the system. The average velocity along the length of pipe was 0.325 m/s for 0.6 l/s and 1.042 m/s for 2.0 l/s. On the other hand the velocity across the orifice (Reach 2) was slightly higher with values of 0.329 m/s for 0.6 l/s and 1.062 m/s for 2.0 l/s. In addition for all flow rates, the average value of the velocities (U_{ave}) and the velocity across the orifice plate ($U_{orifice}$) was compared with the expected velocity of the system calculated using the flow rate and the cross sectional area of the pipe represented by U_{bar}. It was observed that the velocity values obtained by travel time method were slightly higher than the velocity values obtained by cross sectional area. The plot comparison in Fig. 4.22b shows that this difference is about 3.2% for total length and 4.7% across the orifice plate (Reach 2). The presence of the orifice plate reduces the cross sectional area, and because of flow continuity, velocity increases. It is important to note that the flow along the pipe wasn't of uniform velocity due to change in area. The relationship between the flow rates and the velocities due to continuity (U_{bar}), velocity due to travel time (U_{ave}) and velocity across orifice plate ($U_{orifice}$) is shown in Fig. 4.22b.

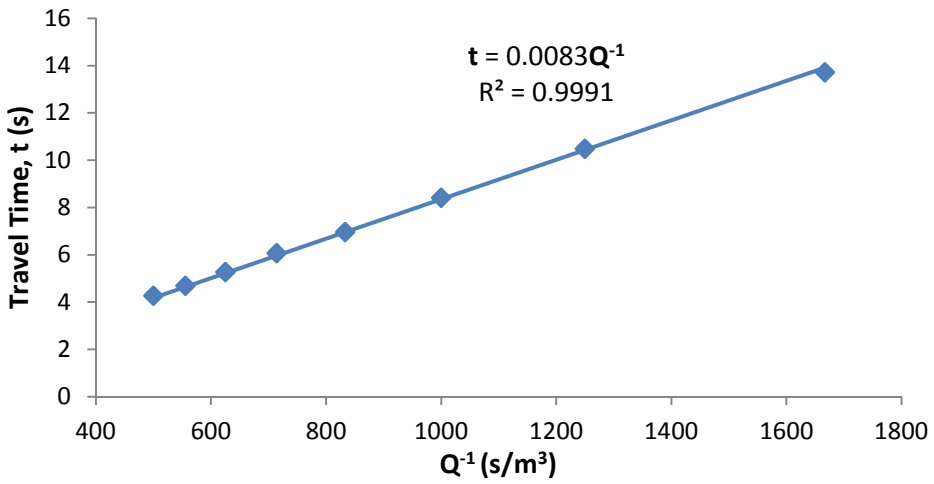

(a) Travel Time

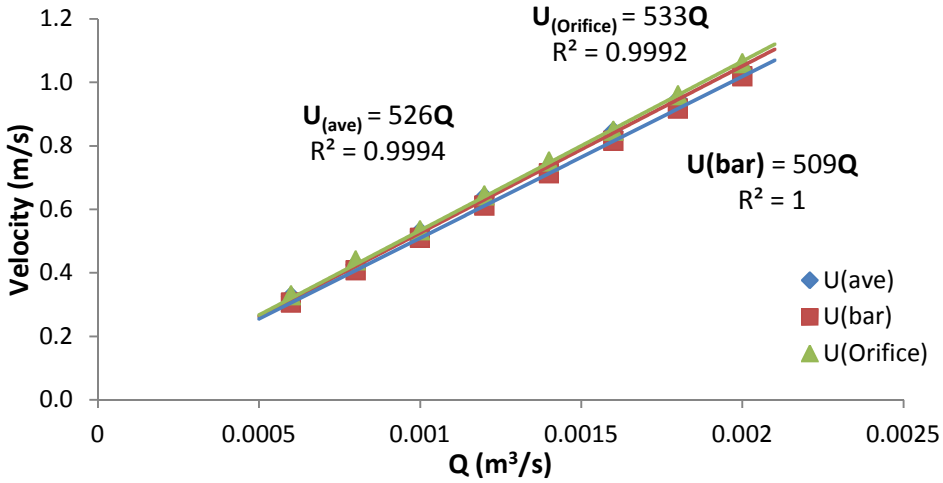

(b) Velocity

Figure 4.22: Variation of travel time and velocities with flow rate using ADE, 35 mm Orifice Plate

4.5.2.2 Dispersion

The average of four repeat tests obtained was used as a representative value of dispersion coefficient at each flow rate. The values of dispersion coefficient varied from an average value of 0.0032 m^2/s at reach 1 for 0.6 l/s to an average value of 0.0171 m^2/s at reach 3 for 2.0 l/s (Fig. 4.23). Dispersion in reach 1 was

the lowest of all the reaches because reach 1 is close to the injection point with minimal mixing occurring whereas reach 3 and 4 had similar values of dispersion. The highest values of dispersion coefficient was at reach 2 due to the presence of the orifice plate. It was observed that the value of dispersion coefficient increased as the flow rate increased.

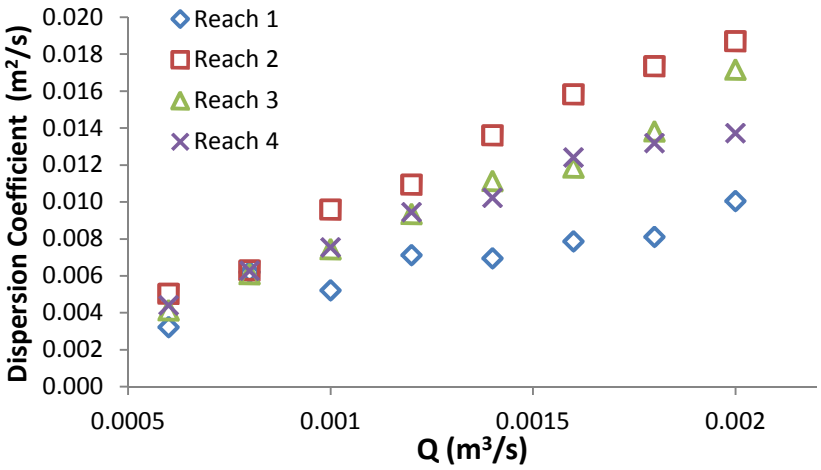

Figure 4.23: Variations of dispersion coefficient at each reach using ADE, 35mm orifice plate

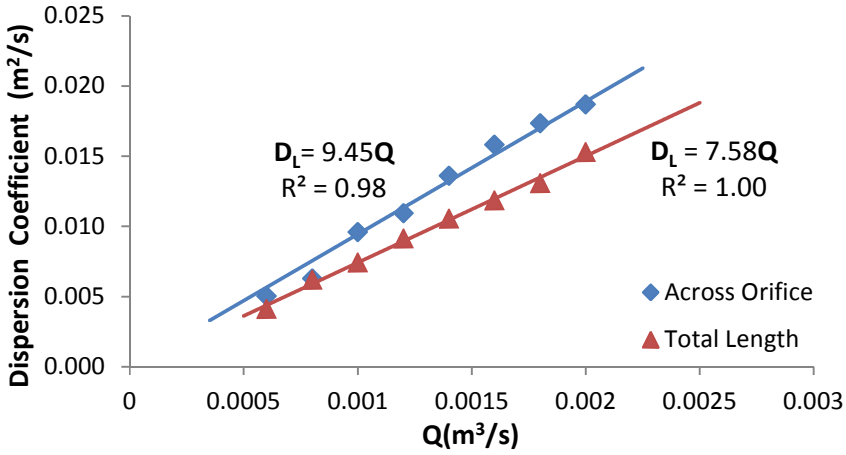

Figure 4.24: Variation of dispersion coefficient with flow rate along total length and across orifice plate using ADE, 35mm Orifice plate

The value of dispersion coefficient obtained across the orifice plate was higher than the dispersion coefficient across the total length of the pipe as shown in Fig. 4.24. Both values were however higher than those obtained when the orifice plate was not inserted (Fig. 4.19 & Fig. 4.20). It was noted that the jet created by the orifice contributes to the increase in the velocity along the pipe.

This can be explained using equation (4.5) which shows that dispersion coefficient D_L is dependent on both the radius and the velocity. The reduction in area leads to more transverse velocity variation and less cross sectional uniform velocity subsequently leading to an increase in dispersion.

4.5.3 25mm Orifice Plate

4.5.3.1 Travel Time and Velocity

The travel time obtained by the ADE method when a 25 mm orifice plate was inserted along the line of flow has values of 13.83 s for 0.6 l/s and 8.49 s for 1.0 l/s. Only three flow rates (with orifice in) can be accommodated by the laboratory set-up. A plot of these values against the inverse of flow rate gave a slope of 0.0084 (Fig 4.25a). The value of the slope is the same as that obtained for no orifice flow. Limitations of test procedures meant only low flows are tested; there is no clear indication that at higher flow rates, the slope might be different. However it is a significant representation of the movement of tracer along the pipe.

For each flow rate, the average value of the velocities at reach 1, 2 and 3 represented by U_{ave} was equal to the velocity value at reach 4 which represents the total length between the first and last fluorescence measuring points. This implies that data collected at reach 4 can accurately give an overview of fluid flow behaviour in the system. In addition for all flow rates, the average value of the velocities due to travel time (U_{ave}) and the velocity across the orifice plate ($U_{orifice}$) was compared with the velocity (due to continuity) of the system calculated using the flow rate and the cross sectional area of the pipe represented by U_{bar}. It was observed that the velocity values obtained by travel time method were higher than the velocity values obtained by cross sectional area by 4.1 % and 7.5% across the orifice (Fig 4.25b). It is important to note that the flow along and across the pipe wasn't of uniform velocity due to change in area.

4.5.3.2 Dispersion

The average of four repeat data obtained was used as a representative value of dispersion coefficient at each flow rate. The values of dispersion coefficient varied from an average value of 0.0046 m^2/s at reach 1 for 0.6 l/s to an average value of 0.0095 m^2/s at reach 2 for 1.0 l/s (Fig 4.26). It was observed that the value of dispersion coefficient increased as the flow rate increased as predicted by Taylor's theory; with the dispersion coefficient across the orifice plate being higher than that across the length of the pipe (Fig.4.27).

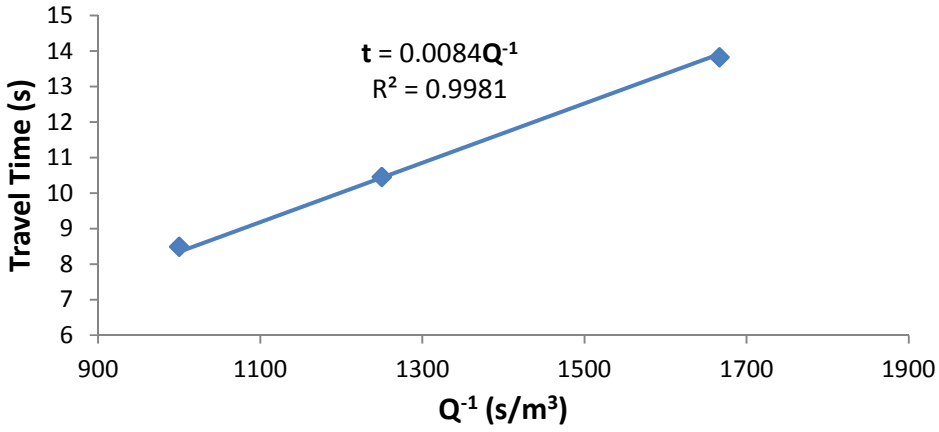

(a) Travel Time

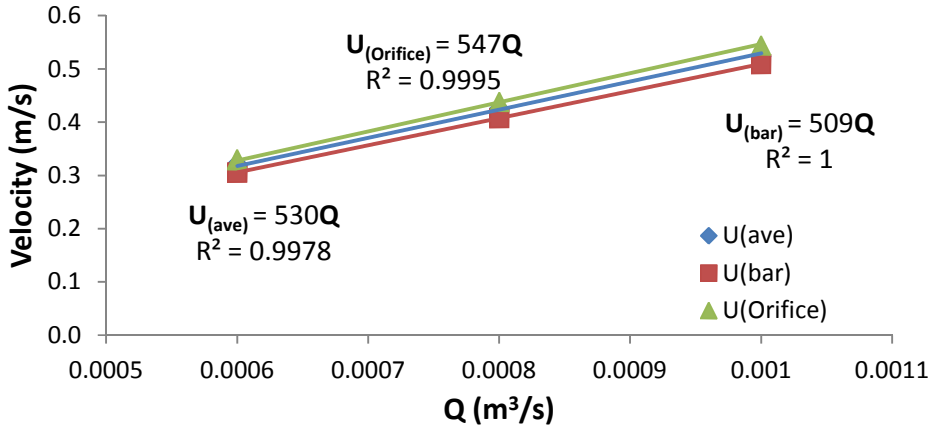

(b) Velocity

Figure 4.25: Variation of travel time and velocities with flow rate using ADE, 25 mm Orifice Plate

*$U_{(ave)}$ = Velocity of dye, U(bar) = Q/A, U(orifice) = Velocity across orifice

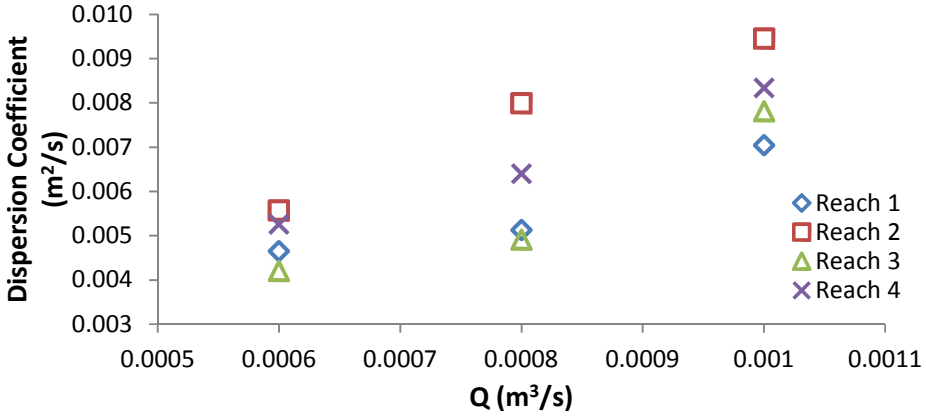

Figure 4.26: Variations of dispersion coefficient at each reach using ADE, 25mm orifice plate

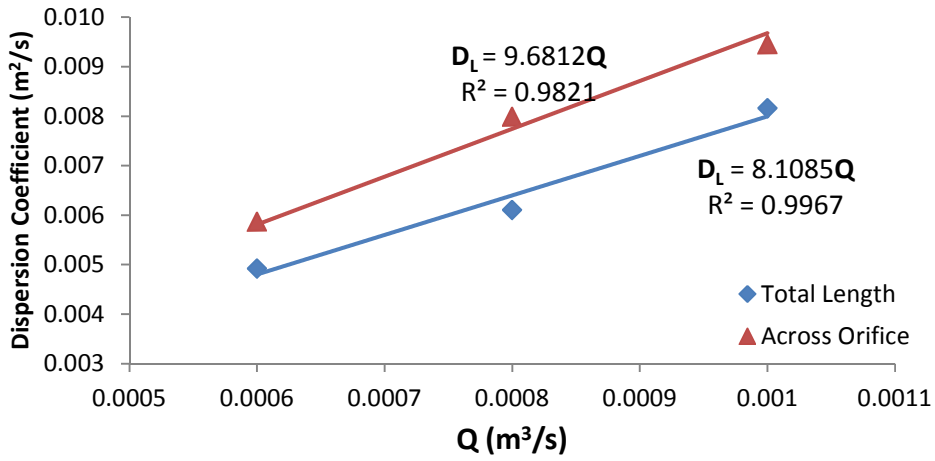

Figure 4.27: Variation of dispersion coefficient with flow rate along total length and across orifice plate using ADE, 25mm Orifice plate

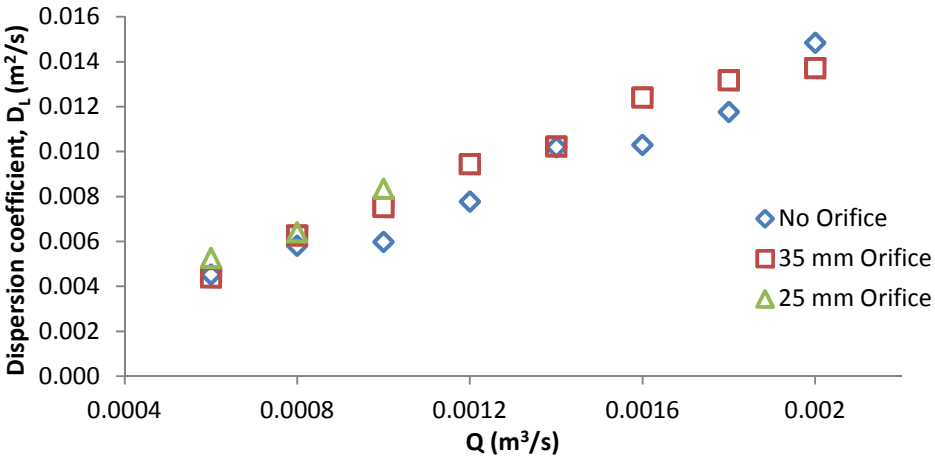

Figure 4.28: Dispersion coefficient values at different conditions of flow, ADE

In comparison with dispersion in no orifice pipe, there was an increase of 17.5% along the length of pipe and 40% across the orifice plate. This difference can be attributed to the change in area created by the orifice plate which reduces the area of flow by half.

A comparison of the dispersion coefficient along the total length of pipe for the different conditions of flow is shown in Fig. 4.28. The values had standard deviations ranging in between 0.0006 and 0.0014.

An initial investigation by this study shows that the presence of an orifice plate in the line of flow increases the dispersion across the region where it is positioned; however the effect is reduced across the total length of pipe (Fig 4.28). The smaller the diameter of the orifice plate, the larger the dispersion coefficient occurring within the system.

4.6 Cumulative Residence Time Distributions (CRTDs)

The temporal concentration distribution data was also analysed using the Deconvolution software by Stovin et al. (2010b) to obtain the Residence Time Distribution (RTD) and predict a downstream profile distribution. Fig. 4.29 shows a sample concentration distribution profile for all three types of experiment. The downstream concentration profiles are almost Gaussian in shape and the prediction adequately fits the downstream profile for all three types of experiments. The goodness-of-fit of the predictions were measured and the CRTDs were obtained. The travel time was normalised as a product of actual travel time and flow rate divided by the volume of flow to give a non-dimensional comparison. Fig. 4.30-4.32 shows the average of four repeats CRTDs for each flow rate at the actual and normalised time for the three types of experiment carried out. At actual time, the CRTDs all have a steep rise but with

the rise starting at different times. However when the time is normalised by multiplying individual time by flow rate (Q)/Volume (V), the curves collapse into one implying that with they can be represented by a single curve. The travel times when 10% of the mass (t_{10}), 50% of the mass (t_{50}) and 90% of the mass (t_{90}) had passed through was obtained for both the actual and normalised time as shown in Table 4.5-4.7. A plot of the t_{50} travel time against the reciprocal of the flow rate gave the same slope and equation for predicting time (t) as that obtained using ADE. The values were 0.0084 s^2/m^3 for no orifice flow and 0.0083 s^2/m^3 for flows through 35mm orifice and 25mm orifice respectively. As the percentiles increased, normalised time increased (i.e. $t_{90}>t_{50}>t_{10}$), however, the values only have slight deviation with increase in flow rate at these percentiles, as well as across the three types of experiment. For example for 0.6 l/s, 10% of the mass had passed through at normalised time of 0.87, 0.86 and 0.87 respectively for no orifice flow, 35 mm orifice plate and 25 mm orifice plate respectively.

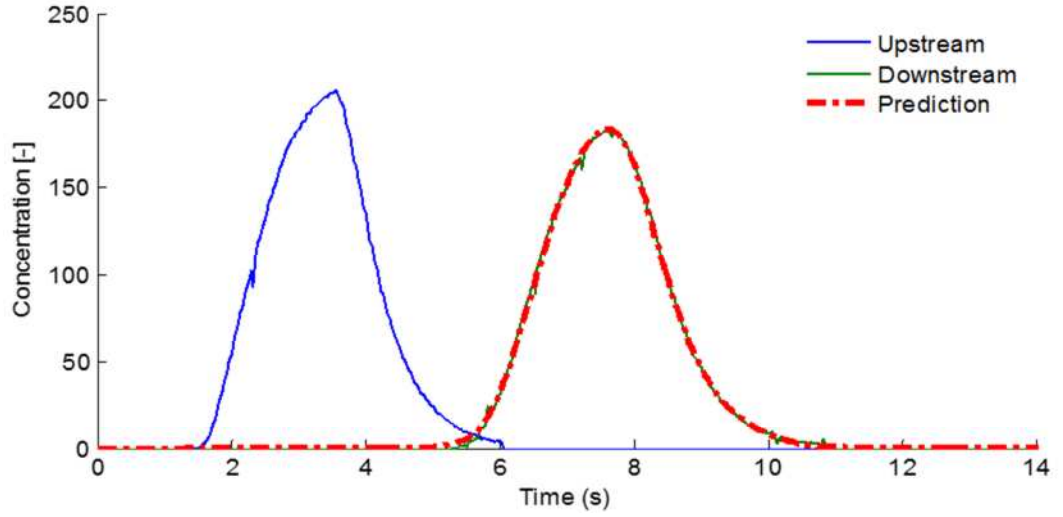

(a) No orifice flow

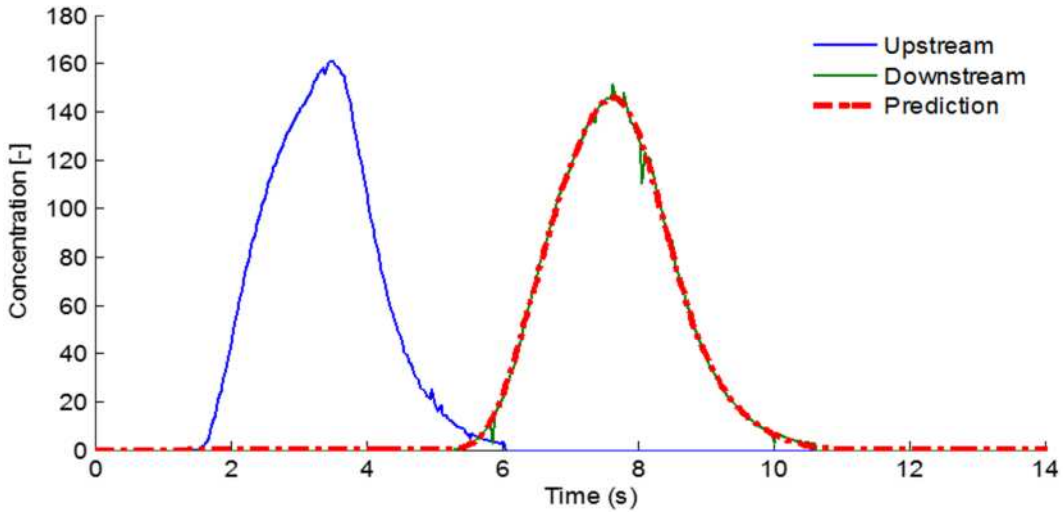

(b) 35 mm orifice plate

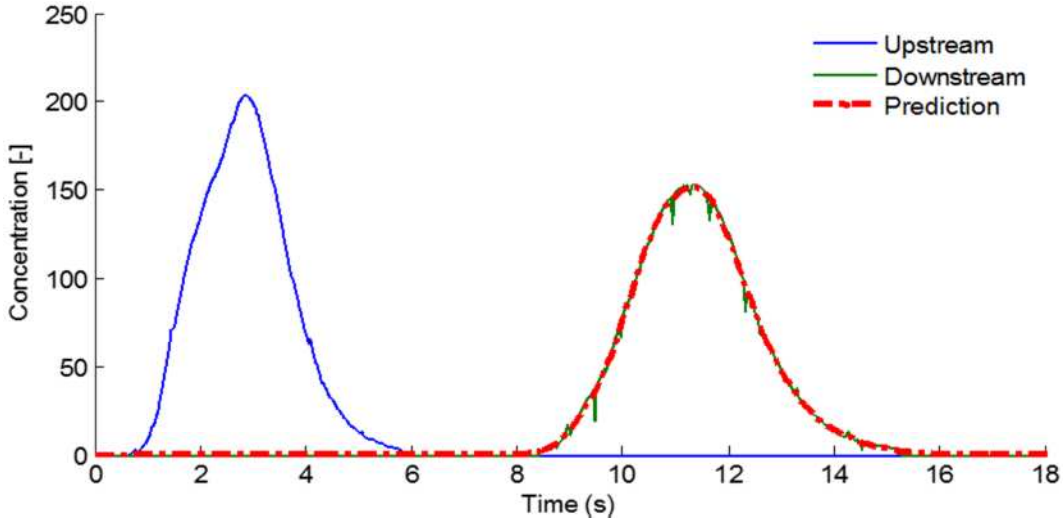

(c) 25 mm orifice plate

Figure 4.29: Sample concentration distribution profile using deconvolution (Reach 2); (a) Q= 2.0 l/s, (b) Q=2.0 l/s, (c) Q=1.0 l/s

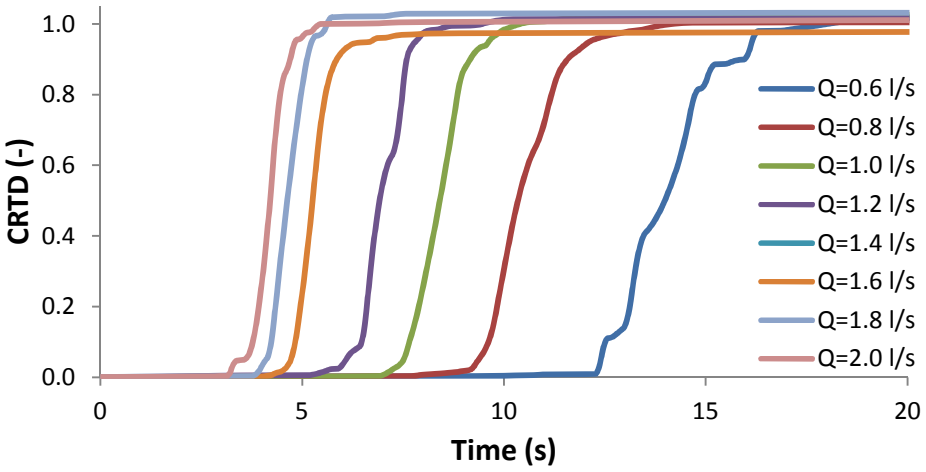

(a) CRTDs at actual time

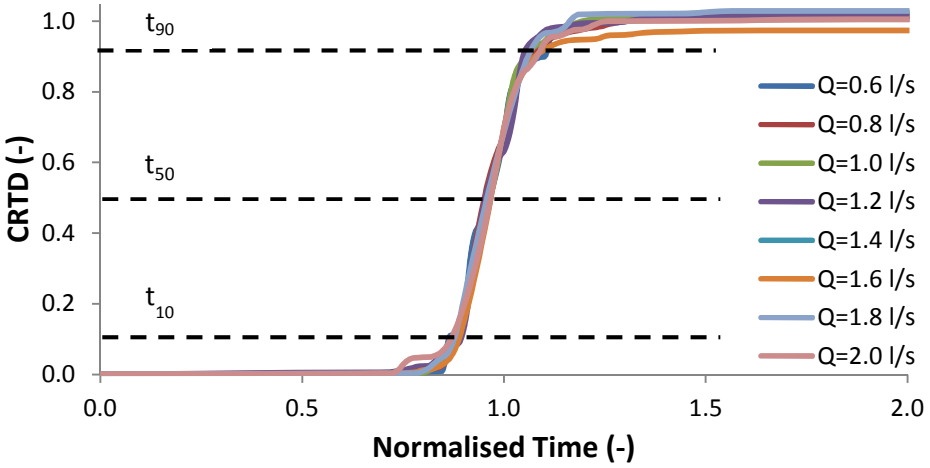

(b) CRTDs at normalised time

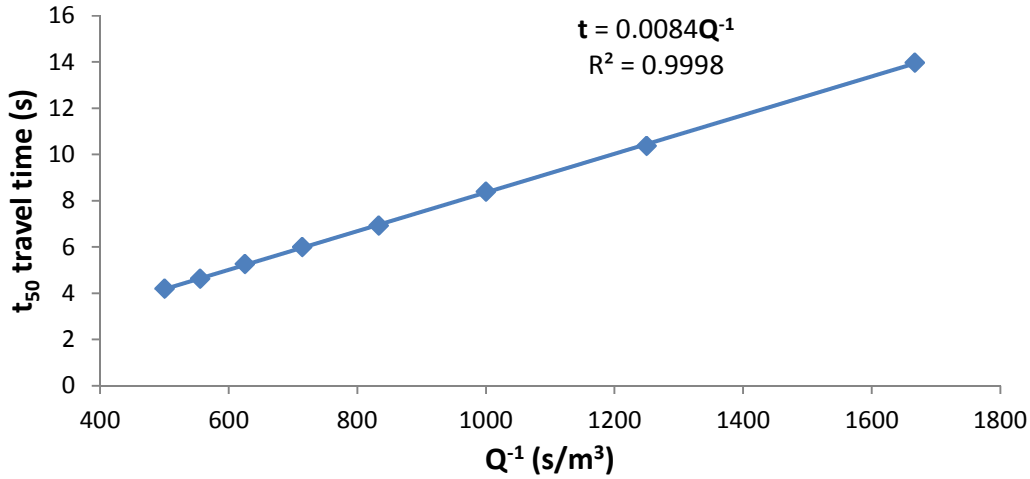

(c) Travel Time

Figure 4.30: Results from deconvolution of no orifice flow data

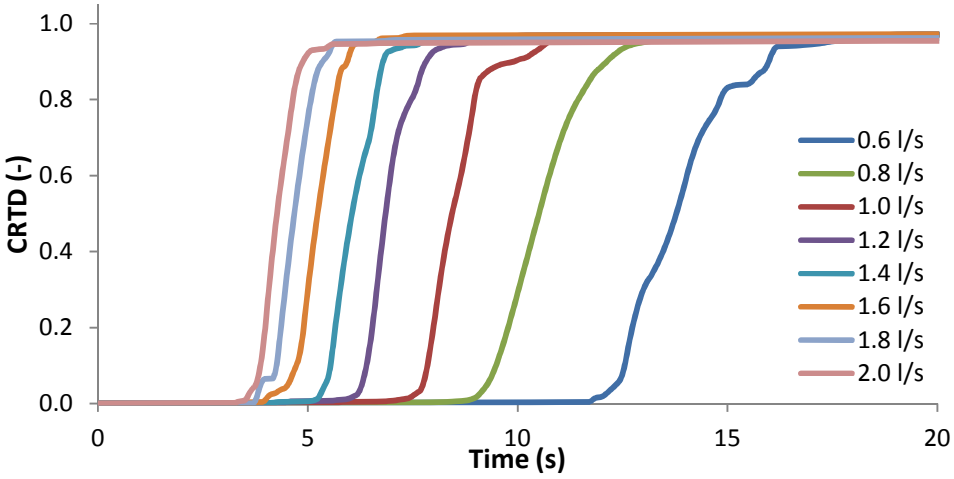

(a) CRTDs at actual time

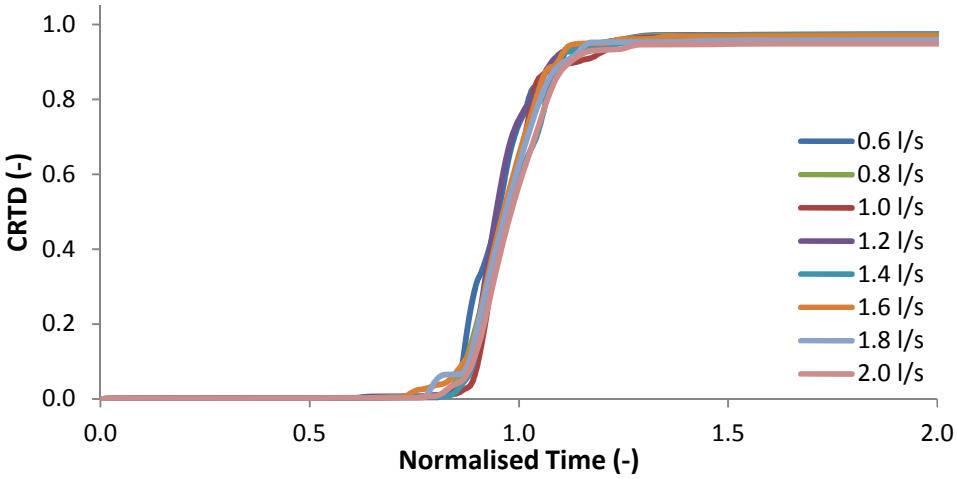

(b) CRTDs at normalised time

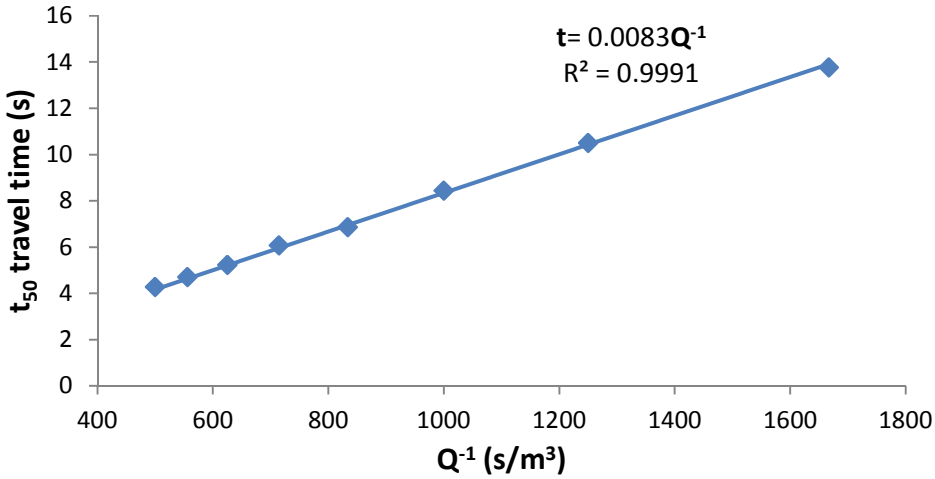

(c) Travel Time

Figure 4.31: Results from deconvolution of 35 mm orifice plate data

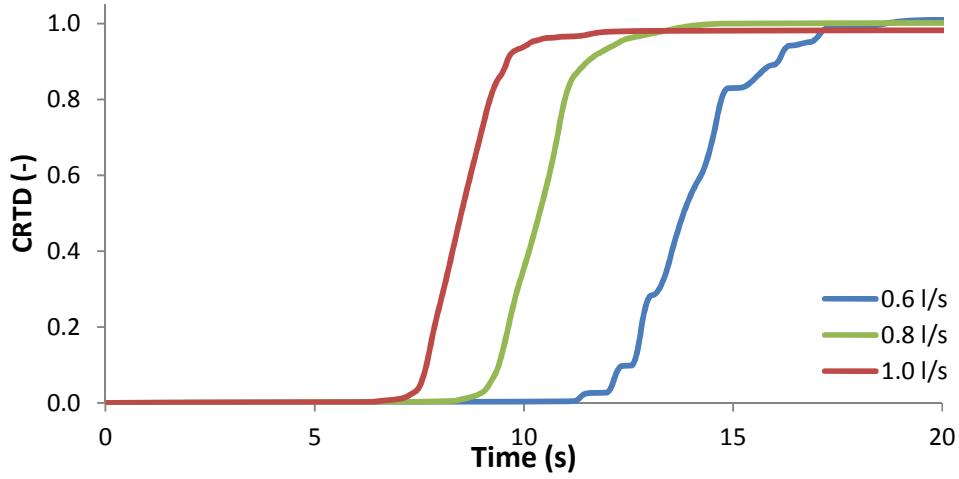

(a) CRTDs at actual time

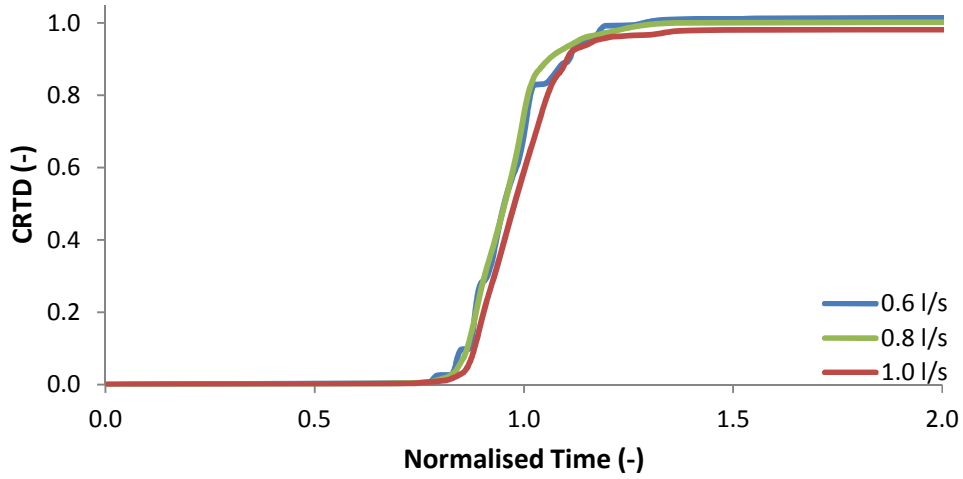

(b) CRTDs at normalised time

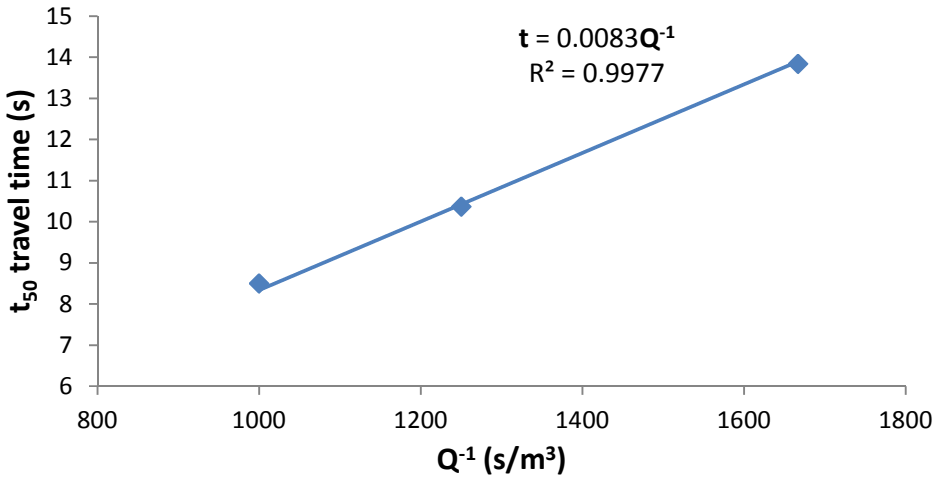

(c) Travel Time

Figure 4.32: Results from deconvolution of 25 mm orifice plate data

Table 4.5: Actual and Normalised travel time for no orifice flow

Q (l/s)	Time t (s)			Normalised Time t_n		
	Percentile			Percentile		
	t_{10}	t_{50}	t_{90}	t_{10}	t_{50}	t_{90}
0.60	12.53	13.97	15.97	0.87	0.96	1.10
0.80	9.63	10.37	11.60	0.89	0.95	1.07
1.00	7.67	8.40	9.17	0.88	0.97	1.05
1.20	6.47	6.93	7.60	0.89	0.96	1.05
1.40	5.47	6.00	6.60	0.88	0.97	1.06
1.60	4.83	5.27	5.87	0.89	0.97	1.08
1.80	4.23	4.63	5.13	0.88	0.96	1.06
2.00	3.77	4.20	4.70	0.87	0.97	1.08

Table 4.6: Actual and Normalised travel time for 35 mm orifice plate

Q(l/s)	Time t (s)			Normalised Time t_n		
	Percentile			Percentile		
	t_{10}	t_{50}	t_{90}	t_{10}	t_{50}	t_{90}
0.6	12.53	13.77	15.97	0.86	0.95	1.10
0.8	9.50	10.50	12.13	0.87	0.97	1.12
1.0	7.87	8.43	9.90	0.90	0.97	1.14
1.2	6.40	6.87	7.83	0.88	0.95	1.08
1.4	5.53	6.07	6.80	0.89	0.98	1.09
1.6	4.73	5.23	5.93	0.87	0.96	1.09
1.8	4.27	4.70	5.37	0.88	0.97	1.11
2.0	3.88	4.27	4.90	0.89	0.98	1.13

Table 4.7: Actual and Normalised travel time for 25 mm orifice plate

Q (l/s)	Time t (s)			Normalised Time t_n		
	Percentile			Percentile		
	t_{10}	t_{50}	t_{90}	t_{10}	t_{50}	t_{90}
0.6	12.60	13.83	16.10	0.87	0.95	1.11
0.8	9.40	10.37	11.53	0.86	0.95	1.06
1.0	7.67	8.50	9.60	0.88	0.98	1.07

4.7 Relationship between Headloss and Dispersion

4.7.1 Headloss and Dispersion along the length of pipe.

The relationship between the measured headloss and the dispersion coefficient values obtained from (i) theory and (ii) the laboratory data is investigated. From theory , the dispersion coefficient can be obtained from equation 4.5, (Taylor, 1954). The square of dispersion coefficient can therefore be written as

$$D_L^2 = 12.75a^2V^2f_L \tag{4.6}$$

Where a = radius of pipe (m), V=velocity of flow (m/s), f_L = friction factor, hence

$$f_L = \frac{D_L^2}{12.75a^2V^2} \tag{4.7}$$

Headloss can be obtained from Darcy's equation

$$h_f = f_L \times \frac{L}{D} \times \frac{V^2}{2g} \tag{4.8}$$

Substituting for the value of friction factor shows that

$$H/L = 0.002a^{-3}D_L^2 \tag{4.9}$$

Where H= headloss, L= Length

To establish the relationship between headloss and dispersion coefficient values from the laboratory result, the logarithm of the coefficient of dispersion was plotted against the logarithm of the ratio of headloss to length as shown in Fig. 4.33a. The plot shows that the log D_L is approximately twice (1.6) the value of log H/L. To verify this application, the square of the values of D_L were plotted against H/L for the no orifice pipe flow condition as shown in Fig. 4.33b.

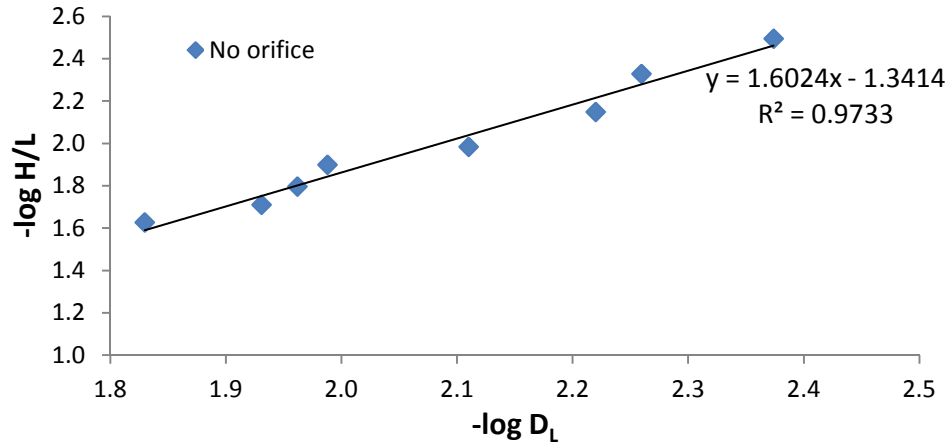

(a) Log D_L against Log H/L

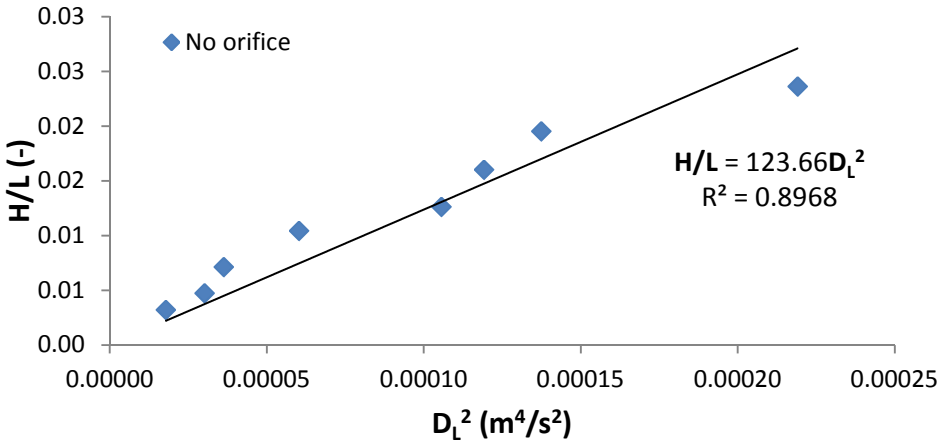

(b) D_L^2 against H/L

Figure 4.33: Relationship between headloss and dispersion coefficient from pipe data

The slope of the graph was obtained by fitting a line to the plots. From Fig. 4.33b,

$$H/L = 124D_L^2 \tag{4.10}$$

Substituting the values of a (= 0.025 m) in eqn. 4.9 gives

$$H/L = 128D_L^2 \tag{4.11}$$

Since the theoretical value is almost equal to the laboratory value, it can be concluded that the relationship between the headloss and dispersion coefficient in a straight pipe can be calculated using eqn. 4.9.

4.7.2 Relationship between Additional Headloss and Dispersion Coefficient due to Orifice Plate

This section develops a relationship between the headloss and the dispersion coefficient due to the presence of an orifice plate across a pipe. From the laboratory results, (refer to Fig. 4.8, Fig. 4.12, Fig. 4.20, Fig. 4.24, Fig. 4.27 respectively) the following predictions were obtained.

Headloss H_0 due to 35 mm orifice can be obtained by

$$H_{O35} = 47029Q^2 \tag{4.12}$$

Headloss H_0 due to 25 mm orifice can be obtained by

$$H_{O25} = 362006Q^2 \tag{4.13}$$

Dispersion coefficient D_L due to pipe can be obtained by

$$D_L = 6.90Q \tag{4.14}$$

Dispersion coefficient D_L due to 35 mm orifice and pipe can be obtained by

$$D_{L35+P} = 9.45Q \tag{4.15}$$

Dispersion coefficient D_L due to 25 mm orifice and pipe can be obtained by

$$D_{L25+P} = 9.68Q \tag{4.16}$$

Therefore additional dispersion coefficient due to the 35 mm orifice plate would be

$$D_{L35} = (9.45 - 6.90)Q \tag{4.17}$$

$$D_{L35} = 2.55Q \tag{4.18}$$

And additional dispersion coefficient due to the 25 mm orifice plate would be

$$D_{L25} = (9.68 - 6.90)Q \quad (4.19)$$

$$D_{L25} = 2.78Q \quad (4.20)$$

It was observed from the equations above that there is a large difference between the headloss at 35mm orifice plate and the 25mm orifice plate whereas the dispersion coefficient values are very close. It can be argued that an average valued equation of dispersion coefficient can be used for both orifice plates, but in the case the relationship is developed using the two equations.

From eqn. 4.18,

$$Q = \frac{D_{L35}}{2.55} \quad (4.21)$$

Substituting for Q in eqn. 4.12 gives

$$H_{O35} = 7232D_L^2 \quad (4.22)$$

From eqn. 4.20,

$$Q = \frac{D_{L25}}{2.78} \quad (4.23)$$

Substituting for Q in eqn. 4.13 gives

$$H_{O25} = 46841D_L^2 \quad (4.24)$$

The relationship between the multiplying factor for the dispersion coefficient and the orifice diameter was obtained by calculating and plotting a graph of the logarithm of both values. These are shown in Table 4.8 and Fig. 4.34.

Table 4.8: Relationship between slope and diameter

slope (s^2/m^3)	a (m)	log slope	log a	a^{-5} (m^{-5})
7232	0.0175	3.859258	-1.75696	609269947
46841	0.0125	4.670626	-1.90309	3.277E+09

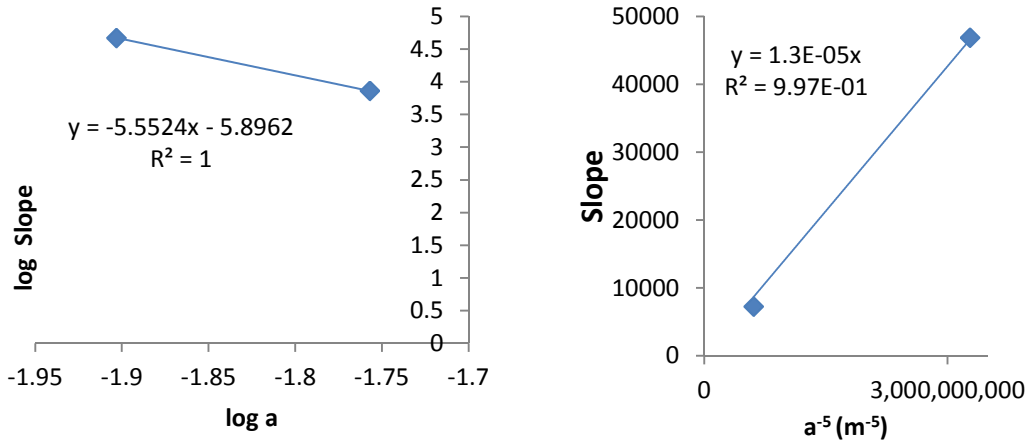

Figure 4.34: Relationship between additional dispersion and headloss

The relationship between the additional headloss and dispersion coefficient due to the presence of an orifice plate can therefore be written as

$$H = C_{HD_L}.a^{-5}.D_L^2 \qquad (4.25)$$

where

H = Headloss (m)

C_{HDL} = Headloss-Dispersion Constant = 1.3 x 10^{-5} (m^2s^2)

a= Radius (m)

D_L = Dispersion coefficient (m^2/s)

Equation 4.25 is recommended to determine the headloss or dispersion coefficient when an orifice plate is present given one of the headloss or dispersion coefficient is known. However there is a need to further develop this relationship for a wider range of orifice diameters.

4.8 Summary

Table 4.9 and 4.10 summarises the relationship between the parameters studied across the three types of experiments i.e. headloss, flow rate, velocity head, velocity, travel time and dispersion coefficient.

The measured headloss along the length of pipe increased with flow rate as well as with the introduction of an orifice plate. An increase of approximately five fold was observed when the orifice plate was changed from 35 mm to 25 mm. A comparison of the measured and calculated value of headloss for all three types of experiment showed a good fit with an error of about $\pm$ 0.01 m.

For the range of flow rates in this study, a fitted Advection Diffusion Equation (ADE) method of analysis was able to predict the downstream concentration to a very high goodness of fit with an exception to the lowest flow rate of 0.6 l/s, Re = 13521. Though the lowest goodness of fit observed at this flow rate was 0.992, it falls within the acceptable range. A similar experiment carried out by Jones (2011) indicated that the optimised ADE parameters still did not fully replicate the mixing processes occurring within the pipe at flow rates lower than 0.72 l/s. Although there was a noticeable increase in the velocity and dispersion coefficient across the entire length of pipe when the orifice plates are introduced; there was little or no change in the travel time relationship with flow rate. This can be as a result of the diameter of pipe being significantly less than the length of pipe (Diameter: Length = 1:88.6).

The deconvolution method produced predictions that closely fit the measured downstream data. The travel time obtained from this method was the same as

that observed from the method of moment's analysis of the measured data. There was no significant change with the three experiments. The presence of the orifice plate didn't contribute to change in the shape of the CRTD along the length of the pipe, but all collapsed into a single profile with normalised time. A comparison of all CRTDs for the three scenarios (Fig. 4.35) shows that all the graphs also formed a single profile. In comparison, the deconvolution approach produced a better fit than the ADE predictions with R_t^2 values all over 0.997 (Fig. 4.34).

Table 4.9: Relationship between headloss, flow rate and velocity head

Parameter	Pipe	35mm Orifice Plate	25mm orifice Plate
Headloss H_o Across orifice plate		$3.56(V^2/2g)$ ($R^2 = 0.9963$)	$24.35(V^2/2g)$ ($R^2 = 0.9973$)
Headloss H_o Across orifice plate		$47029(Q^2)$ ($R^2 = 0.9977$)	$362006(Q^2)$ ($R^2 = 1.0$)
Total Headloss H Along full length pipe	$29546(Q^2)$, $2.10(V^2/2g)$ ($R^2 = 0.9825$)	$79691(Q^2)$ ($R^2 = 0.9939$)	$400572(Q^2)$ ($R^2 = 0.9947$)

Table 4.10: Relationship between hydraulic parameters and flow

ADE Analysis			
Parameter	Pipe	35mm Orifice Plate	25mm orifice Plate
Travel time t (s)	$0.0084Q^{-1}$ ($R^2 = 0.9994$)	$0.0083Q^{-1}$ ($R^2 = 0.9991$)	$0.0084Q^{-1}$ ($R^2 = 0.9981$)
Velocity, t/x (m/s) (Reach 4: Along Pipe)	522Q ($R^2 = 1.000$)	526Q ($R^2 = 0.9994$)	530Q ($R^2 = 0.9978$)
Velocity (m/s) (Reach 2: Across orifice plate)		533Q ($R^2 = 0.9992$)	547Q ($R^2 = 0.9995$)
Dispersion coefficient K (m^2/s) (Reach 4: Along pipe)	6.90Q ($R^2 = 0.9669$)	7.58Q ($R^2 = 1.000$)	8.11Q ($R^2 = 0.9967$)
Dispersion coefficient K (m^2/s) (Reach 2: Across orifice)		9.45Q ($R^2 = 0.9832$)	9.68Q ($R^2 = 0.9821$)
Deconvolution			
Parameter	Pipe	35mm Orifice Plate	25mm orifice Plate
Travel time t (s)	$0.0084Q^{-1}$ ($R^2 = 0.9998$)	$0.0083Q^{-1}$ ($R^2 = 0.9991$)	$0.0083Q^{-1}$ ($R^2 = 0.9977$)

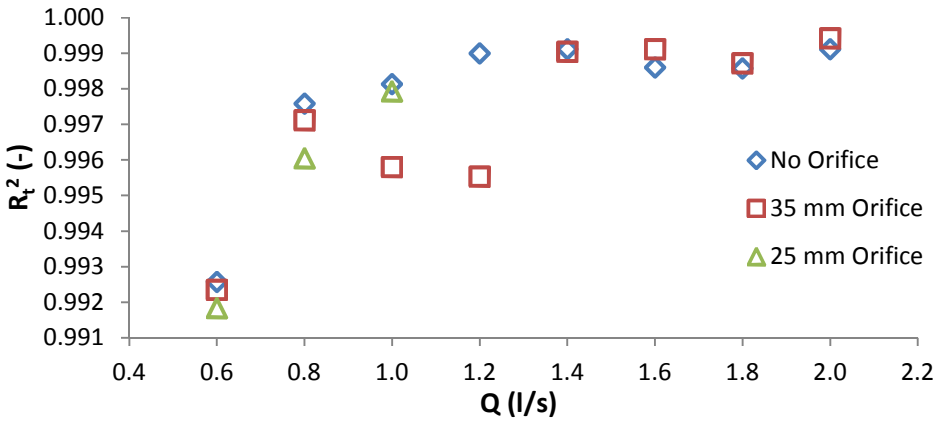

(a) ADE predictions

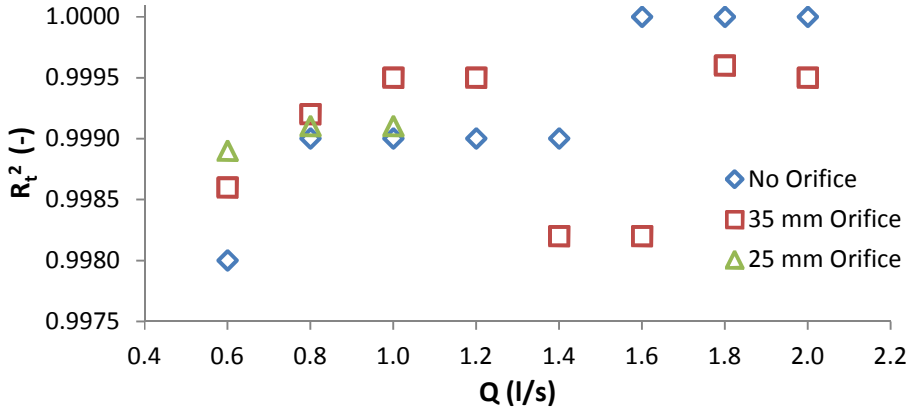

(b) Deconvolution

Figure 4.35: Measure of goodness of fit of predictions

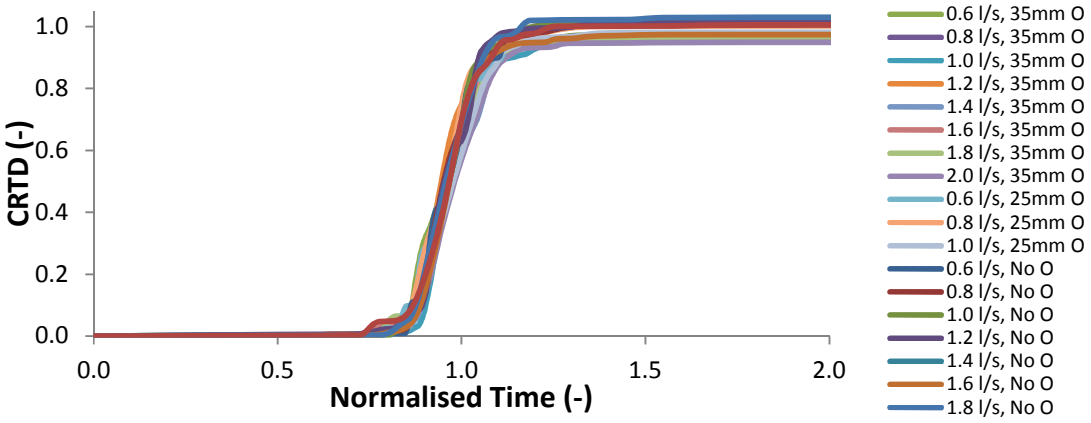

No O = No Orifice, 35mm O = 35mm Orifice, 25mm O = 25mm Orifice

Figure 4.36: Combination of CRTDs for No orifice, 35mm and 25mm Orifice Plate

5 Manhole Mixing Studies

5.1 Surcharged Square Manhole

5.1.1 Surcharge Depths

Two manholes, namely large and small, were considered and the results presented. The manhole described as large has dimensions 388 x 388 x 700 mm, while the small manhole has dimensions 200 x 200 x 700 mm, both fitted with a 50mm diameter pipe. This results in a ratio of manhole length to pipe diameter $L_m/D_p = 7.76$ for the large manhole and $L_m/D_p = 3.0$ for the small manhole. For both large and small manhole, three flow rates (0.71 l/s, 1.17 l/s, 1.64 l/s) were investigated , 11 and 8 surcharge depths, s, the difference between the height of water in the manhole and the soffit of the pipe, were considered respectively as shown in Fig. 5.1 and Fig. 5.2. At the higher flow rates, the lowest surcharge depth obtained was higher than the first surcharge depth for lower flow rates because higher flow rates resulted in higher heads of water. However effort was made to obtain similar surcharge depths across the flow rates to aid comparison. Each experiment is classified according to the ratio of the surcharge to manhole side length s/L_m and the ratio of surcharge to pipe diameter s/D_p for easy comparison with previous studies such as those by Jones (2011) and Stovin et al. (2013).

5.1.2 Headloss Measurement

The headloss at a manhole, ΔH is defined as the difference in pressure head between the extrapolated upstream and downstream hydraulic grade line. The results for the three flow rates considered are shown in Fig. 5.3 and Fig. 5.4. The result in Fig. 5.3 show that higher headloss occurred at lower surcharge which reduces as the surcharge increases. At low surcharge depths, the incoming jet interacts violently with the free surface, causing a significant flow exchange and consequently high headloss. As the surcharge increases, the effect is reduced hence a reduction in the headloss.

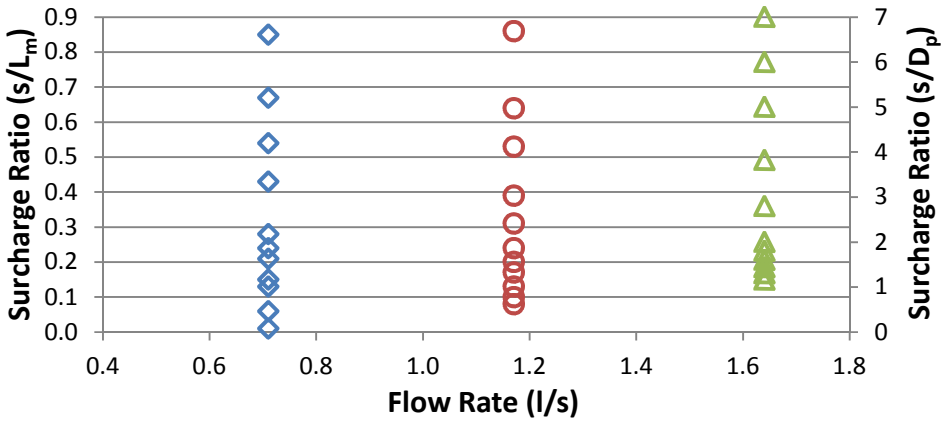

Figure 5.1: Surcharge ratios investigated for large manhole.

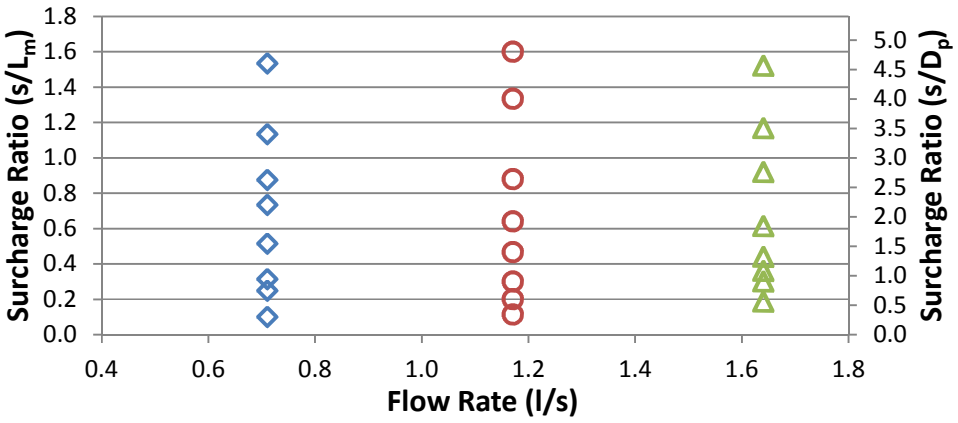

Figure 5.2: Surcharge ratios investigated for small manhole.

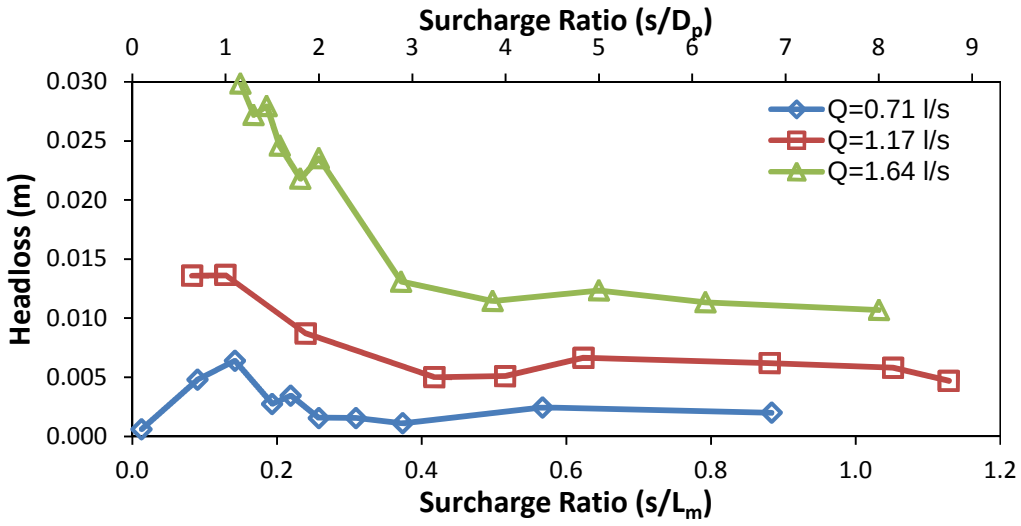

Figure 5.3: Headloss across large manhole

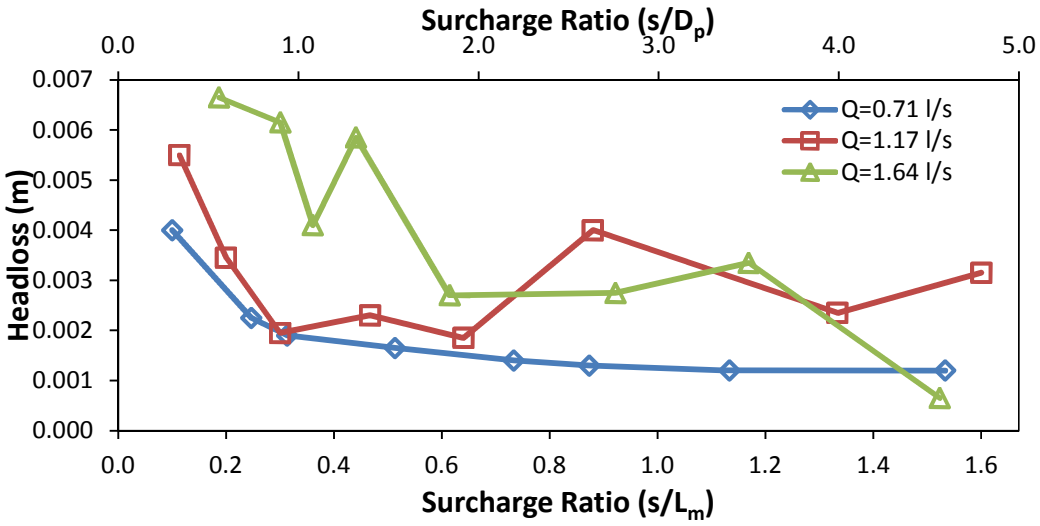

Figure 5.4: Headloss across small manhole

The relationship between the measured headloss and the energy loss coefficient is described by Urban Drainage Manual (2011) as

$$\Delta H = K\left(\frac{V_0^2}{2g}\right) \qquad (5.1)$$

Fig. 5.5 and Fig. 5.6 show the energy loss coefficient K, values for the large and small manhole respectively.

For the large manhole (Fig. 5.5), a significant drop in the energy loss coefficient occurs after $s/L_m > 0.20$ equivalent to $s/D_p > 2$, with the values becoming almost constant across all flow rates considered. However at lower surcharge depths before this limit, the coefficient value rose to about 2.5 times the constant value before decreasing. This is because at the lower surcharge depths, the incoming jet interacts more with the surface than at higher surcharge depths where the incoming jets passes through the flowing section of the manhole. For 0.71 l/s, at 5 mm surcharge, which can be described as very low, with a surcharge ratio of $s/L_m = 0.08$ equivalent to $s/D_p = 0.64$, the inflow jet passes straight into the outlet pipe with little mixing occurring hence the lower headloss and consequently energy loss coefficient.

The same pattern of energy loss coefficient increase and subsequent decrease with almost constant values were also observed for circular manholes by Lau (2007), Arao et al. (2011), and Jones (2011). Arao et al. (2011), explained that when the ratio of surcharge to downstream pipe diameter is smaller than 1, the energy loss coefficients increased due to horizontal vortices which corresponds to the manhole diameter.

On the other hand, the small manhole (Fig. 5.6) doesn't exhibit the same pattern. There is an initial drop in the value of K, followed by an almost constant value for each flow rate.

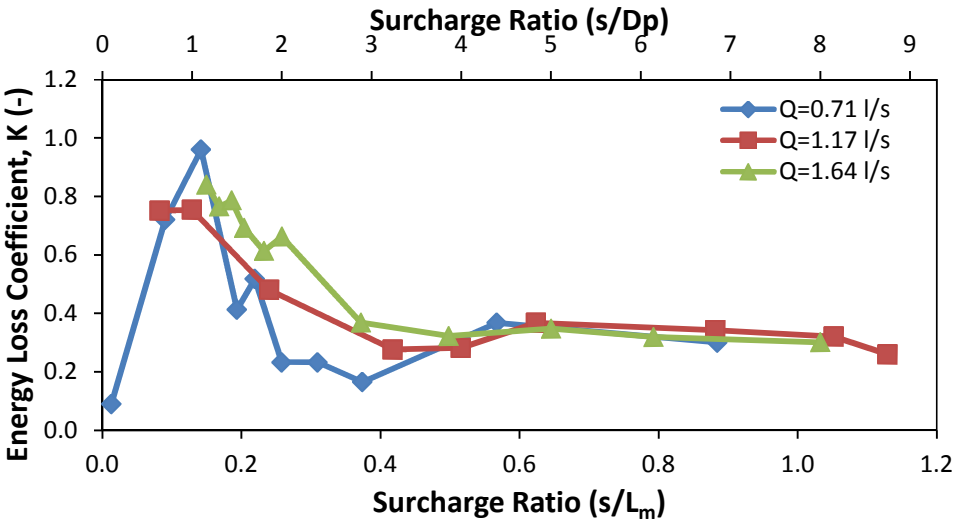

Figure 5.5: Energy Loss Coefficient across the large manhole

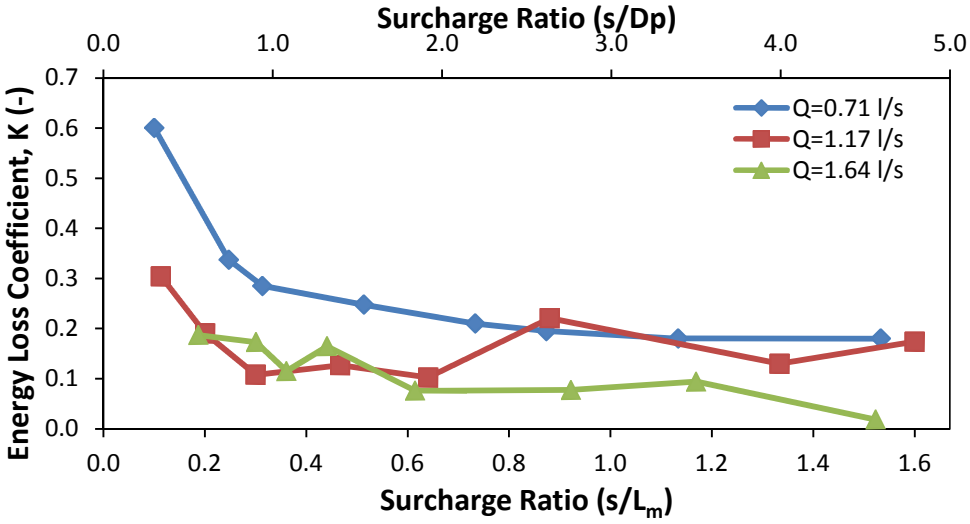

Figure 5.6: Energy Loss Coefficient across the small manhole

The pressure loss coefficient K_p is defined as

$$K_p = K + 1 - \left(\frac{V_*}{V_d}\right)^2 \qquad (5.2)$$

Where V_* is the cross sectional mean velocity in the inflow pipe while V_d is the cross sectional mean velocity in the downstream pipe.

For this study, the inlet and outlet pipe diameter is equal and creates a straight through flow, therefore $V_*=V_d$, therefore the pressure loss coefficient is equal to the energy loss coefficient i.e. $K_p = K$.

Comparison with previous studies

Table 5.1 and Table 5.2 show the average value of the energy loss coefficients obtained in this experiment. This is done in a bid to compare present results with published ones.

A comparison of five algorithms from different authors for determining manhole pressure change coefficients was presented by O'Loughlin and Stack (2002). An extract of the result is shown in the Table 5.3. The study concluded that the methods were not strictly comparable because of different levels of coverage which may or may not include conditions such as part full pipe flow, pipe drops and alignment amongst others.

The application of some of these theoretic methods of estimation (O'Loughlin and Stack, 2002) to the present study gave the following values: Mills=0.5, Hare=0.3, FHWA= 0.42. A comparison of the theoretical values to the experimental values suggest that the Hare method predicts the K values after the s/Dp >2 (Table 5.1) better, whilst the Mills and FHWA better predict the overall average value of 0.46.

Table 5.1: Average Energy Loss Coefficient values for Large Manhole

	Average K values with standard deviation		
Q (l/s))	**$s/L_m < 0.258$ ($s/D_p < 2$)**	**$s/L_m > 0.258$ ($s/D_p > 2$)**	**All**
0.71	0.54 ± 0.33	0.26 ± 0.08	0.40 ± 0.26
1.17	0.66 ± 0.16	0.31 ±0.04	0.42 ± 0.20
1.64	0.73 ± 0.08	0.33 ± 0.03	0.55 ± 0.22
All Data	0.64 ± 0.23	0.30 ± 0.06	0.46 ± 0.23

Table 5.2: Average Energy Loss Coefficient values for Small Manhole

	Average K values with standard deviation		
Q (l/s))	**$s/L_m < 0.258$ ($s/D_p < 2$)**	**$s/L_m > 0.258$ ($s/D_p > 2$)**	**All**
0.71	0.37 ± 0.16	0.19 ± 0.01	0.28 ± 0.14
1.17	0.17 ± 0.08	0.17 ± 0.05	0.17 ± 0.07
1.64	0.14 ± 0.05	0.06 ± 0.04	0.11 ± 0.06
All Data	0.23 ± 0.23	0.14 ± 0.07	0.19 ± 0.12

Table 5.3: Comparison of Fitted and Estimated manhole pressure change coefficients, (O'Loughlin and Stack, 2002)

Case	**K_p Coefficients**				
	Charts	**Mills**	**Hare**	**Parsell**	**FHWA**
One inlet pipe, straight-through flow, no grate flow (Missouri Chart 3)					
$-D_u/D_o = 1.0$, submergence ratio = 0.5	-	-	-	-	0.53
$-D_u/D_o = 1.0$, submergence ratio = 1.5	0.12	0.5	0.3	0.46	0.17
$-D_u/D_o = 1.0$, submergence ratio = 3.0	0.12	0.5	0.3	0.28	0.32

*D_u= Diameter of upstream pipe, D_o= Diameter of outlet pipe

Marsalek (1984), observed that for a non-benched square manhole with sides 0.344 m x 0.344 m and a smaller manhole of sides 0.241 m x 0.241 m, with a straight through pipe of 0.152m, the headloss coefficients ranges from 0.21-

0.32. The investigation however was limited to a ratio of manhole width to pipe diameter ($\emptyset_m/\emptyset_p$) $\leq$ 2.26. Sangster (1958), discovered that for a ratio $\emptyset_m/\emptyset_p$ greater than 2, only minor changes occurred to the coefficient while no changes occurred when the ratio is greater than 2.5. The large manhole considered in this study has a length to pipe diameter ratio of 7.76 and the average value of the energy loss coefficient obtained at surcharge depths to pipe ratio $>$ 2 is 0.30 which falls within the range confirming a lack of change as manhole width to pipe diameter ratio increases.

Headloss studies in square manholes by Marsalek (1984) recorded headloss values less than 0.01m at $\frac{V_0^2}{2g}$ values less than 0.05, similar to those recorded in this study. He obtained mean values of headloss coefficient for a similar set-up to be 0.323 with 95% confidence limits between 0.302-0.344. He further explained that the losses at a straight through flow junction are considerably smaller than the combined expansion-contraction loss because the main body of the stream crossing the junction remains more or less intact.

Pedersen and Mark (1990), proposed a simple function to determine the value of K based on a shape factor. The function was generated by a combination of results from previous researchers as well as the new results they got for, manhole length to pipe diameter ratios $D_M/D \leq 4$. The function is presented as

$$K = \zeta\left(\frac{D_M}{D}\right) \qquad (5.3)$$

Table 5.4: Shape Factor (Pedersen and Mark, 1990)

Shape	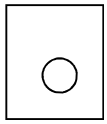	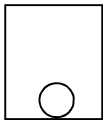	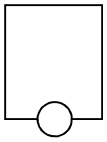	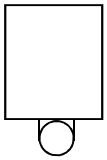	$D_m/D \leq 4$
ζ	0.24	0.12	0.07	0.025	

Applying Equation 5.3 to the present study, using a shape factor of 0.12, gives the value of K as 0.36 for the small manhole with $D_M/D = 3$. This is higher than the coefficient obtained from this experimental result which gave an average of 0.19 (Table 5.2). This could be because the pipe in the Pedersen and Mark (1990) study is slightly above the bottom of the manhole. A shape factor of 0.07 however presents a closer coefficient result of 0.21, though the pipe entrance is not flush with the bottom of the manhole as well. The results from this present study however prove that for a square manhole, the headloss coefficient can be predicted and falls within the ranges earlier proposed by other authors.

5.1.3 Flow Visualization

The surcharges filmed for each flow rate are presented in Table 5.5. A repeat of each was carried out to ensure reproducibility. A side elevation and plan view of the dye transport for 1.17 l/s and varying surcharge is shown in Fig. 5.7-Fig. 5.8 for the large and small manhole respectively. The flow direction is from left to right. All others can be found in Appendix A.

For the large manhole, it was observed that for low-surcharge conditions, surcharge 70-110 mm, examined using dye visualisation, there was an initial straight jet, after which the flow direction of rotation became clockwise before spreading anti-clockwise towards the exit wall, resulting in mixing.

However in a few, the flow fields went anti-clockwise before spreading clockwise. This deviation in flow field direction was also noticed by Jones (2011). She stated that the dye visualisation study is too small to firmly conclude whether there is a preferred direction of rotation in the low-surcharge zone but it implies that either clockwise or anticlockwise rotation may be assumed and that once the direction of rotation has been chosen it is not prone to change. Lau et al. (2008) stated that for both Particle Image Velocimetry (PIV) measurements and CFD simulations of a 218 mm diameter circular manhole under low-surcharge conditions, the flow did not always rotate in the same direction.

Table 5.5: Surcharges at which visualization was carried out

Manhole	Large	Small
Q (l/s)	Surcharge (mm)	Surcharge (mm)
0.71	72	60
	145	150
	160	190
	340	240
1.17	86	70
	145	140
	212	210
	290	290
1.64	108	85
	142	110
	290	150
		210

The same pattern is however evident in all three flow rates (Appendix A), suggesting that the flow profile is more dependent on surcharge than flow rate. The visualization study also shows dead zones occurring at the corners of the manhole.

For the large manhole, as the surcharge increases a transitional change occurs in the flow field (Fig. 5.7). The pattern of the flow field slightly deviates from that observed for the low surcharge to a more evident centralised straight jet.

For high surcharge flow, a straight central jet is evident in the plan views. This is also evident in the small manhole (Fig. 5.8). Almost symmetrical recirculating volumes on either side of the jet carry a proportion of the dye up towards the water surface and back towards the inlet pipe, where it is re-entrained by the jet. This leads to a dead zone being created at the top volume of the manhole. This retains the dye, resulting in a long period before all the dye exits the manhole. The jet appears stable; its position is constant in the plan views at each time shown in Fig. 5.7. This high-surcharge flow field was also noticed in the circular manhole study by Jones (2011). Overall, for the small manhole at low surcharge, a large portion of the dye went through the manhole as a straight jet.

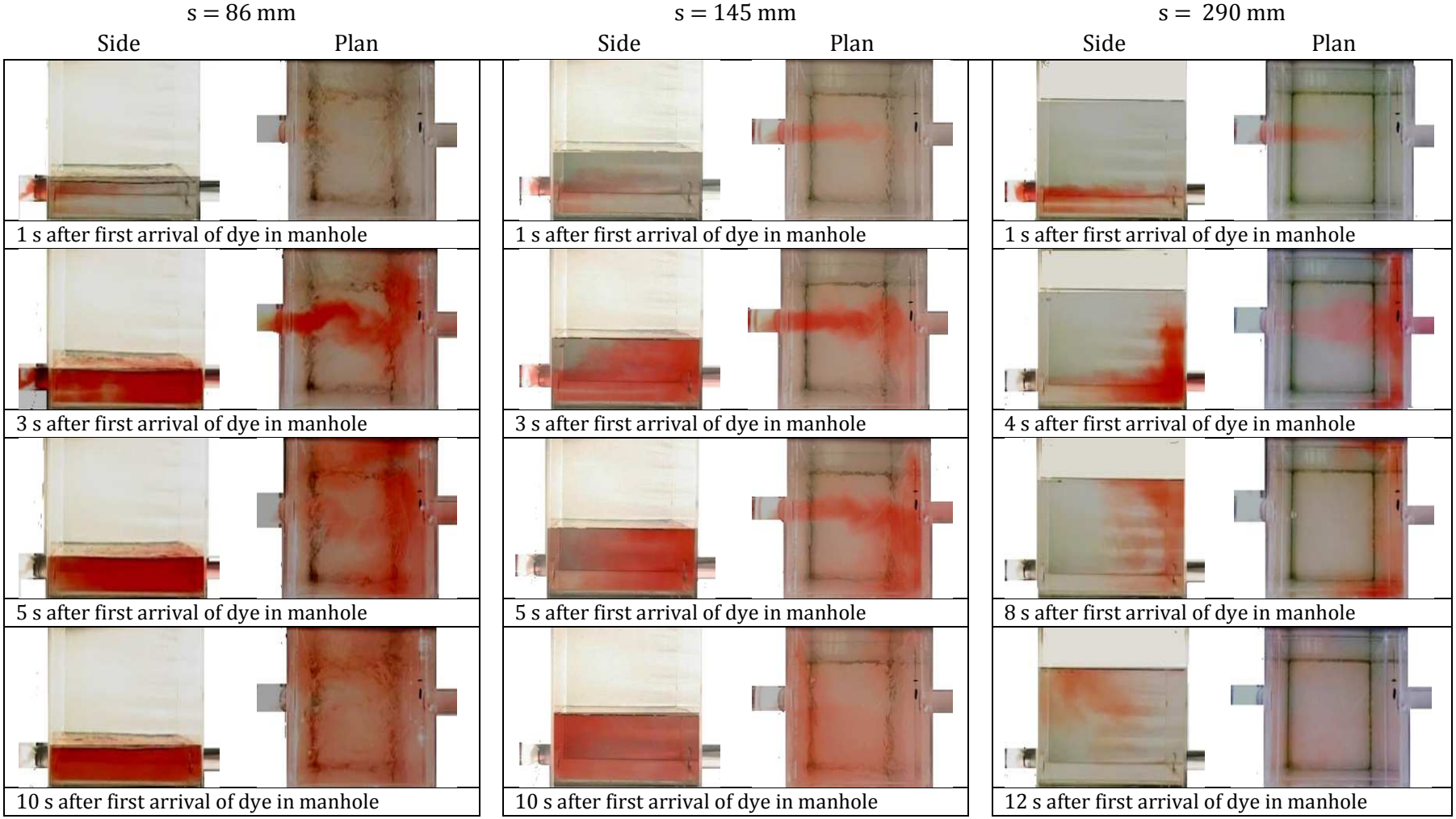

Figure 5.7: Flow pattern for 1.71 l/s, large manhole at different surcharge levels

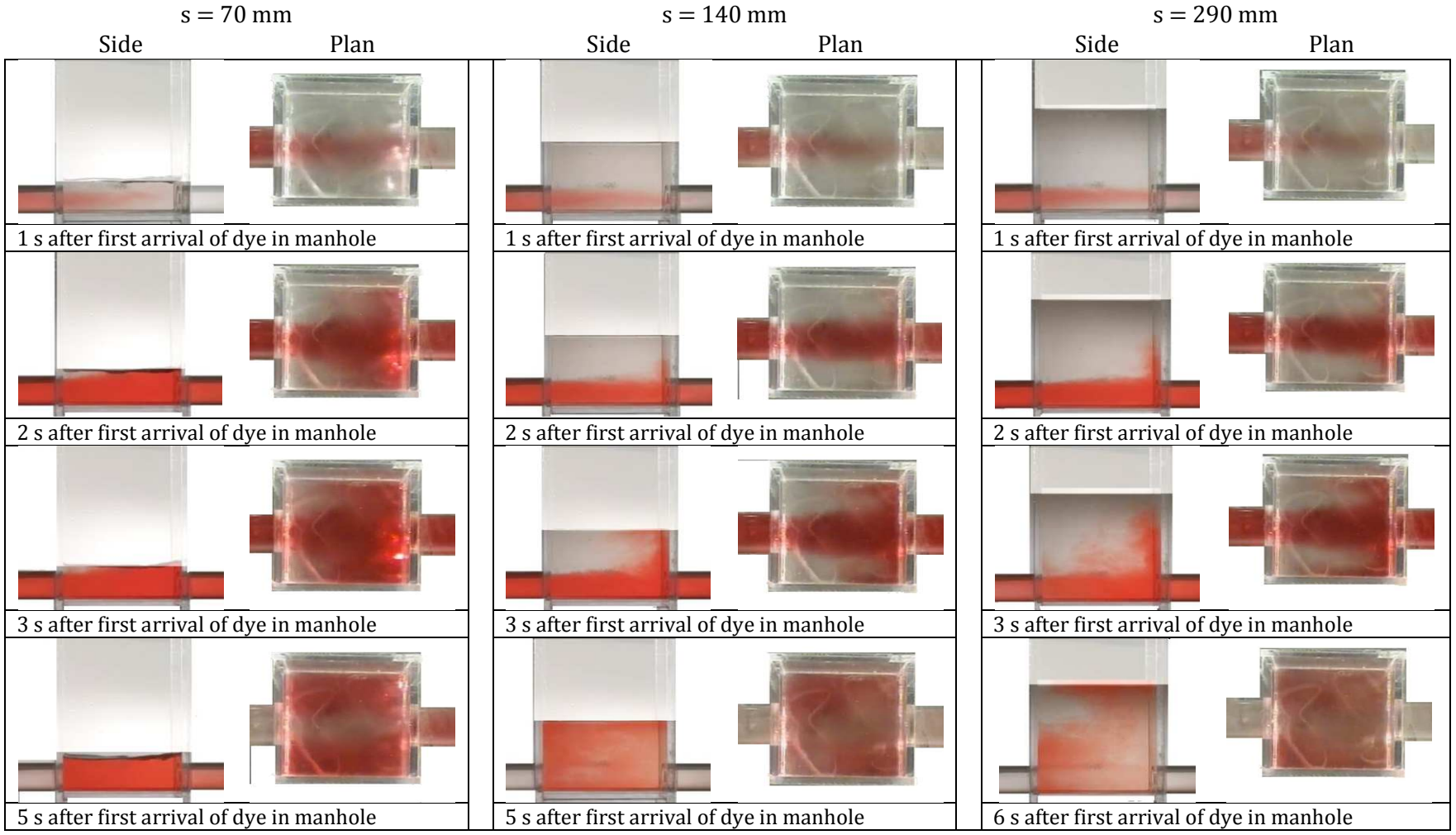

Figure 5.8: Flow pattern for 1.71 l/s, small manhole at different surcharge levels

5.1.4 Analysis of Measured Concentration Profiles

5.1.4.1 Comparison of Traces

Five repeat trace injections were carried out for each flow rate and surcharge level considered. Fig. 5.9 and Fig. 5.10 shows sample plots as surcharge increases at 1.17 l/s flow rate for both the large and the small manhole. The figures show the repeatability of the experiments. The upstream profiles were all Gaussian-like. On the other hand, the downstream profiles were dependent on the size of the manhole as well as the surcharge depth. For the large manhole, at low surcharge depths, the peak concentration is greatly attenuated to about 37% of the upstream peak with a greater spread towards the tail. As the surcharge increased, the attenuation of the peak concentration reduces with the concentration returning to zero much quicker. At very high surcharge depth as shown in Fig. 5.9(c), the downstream profile is similar to that of a free flowing pipe, suggesting that the tracer didn't mix within the manhole volume but was dispersed longitudinally across the manhole. A more Gaussian-like profile was evident across the small manhole, although decay in the downstream tail can be seen in the lower surcharge it soon quickly disappears as the surcharge increases. No significant attenuation was evident between the upstream peak and the downstream peak concentrations. The concentration profile change across the small manhole therefore suggests that the tracer is being transported longitudinally along the manhole with little or no mixing occurring. A compilation of all the downstream profiles is shown in Fig. 5.11 to highlight the changes occurring at the downstream tail as surcharge and flow rate increases across both manholes.

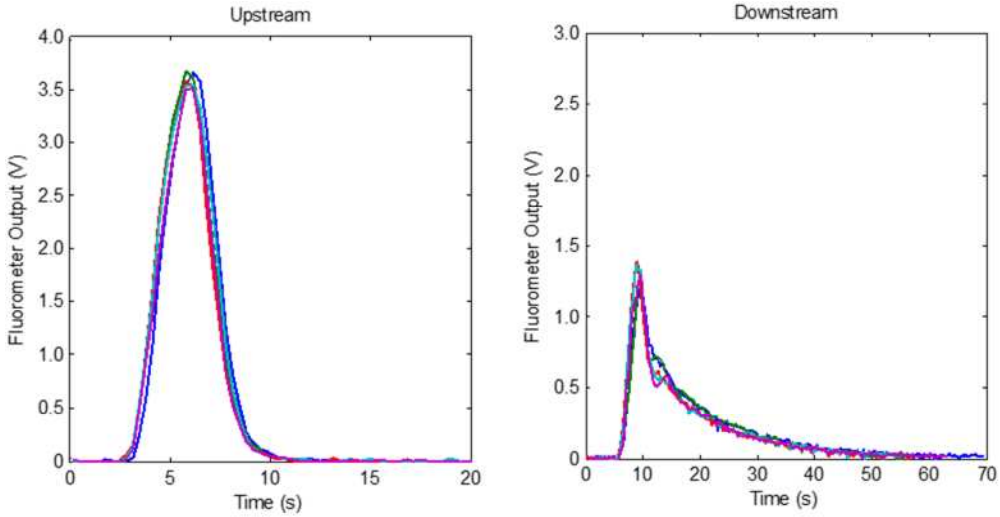

(a) Surcharge 32 mm

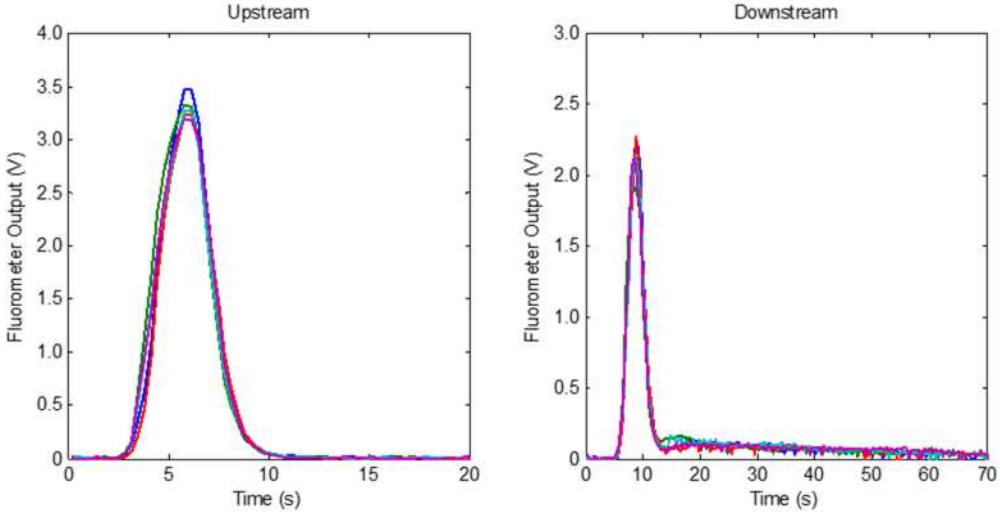

(b) Surcharge 92 mm

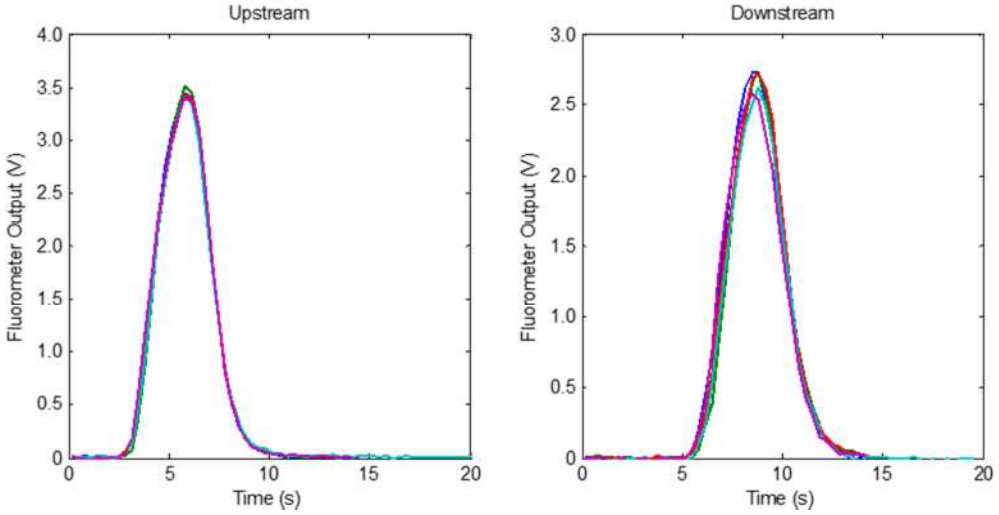

(c) Surcharge 335 mm

Figure 5.9: Comparison of repeat traces measured at 1.17 l/s for large manhole

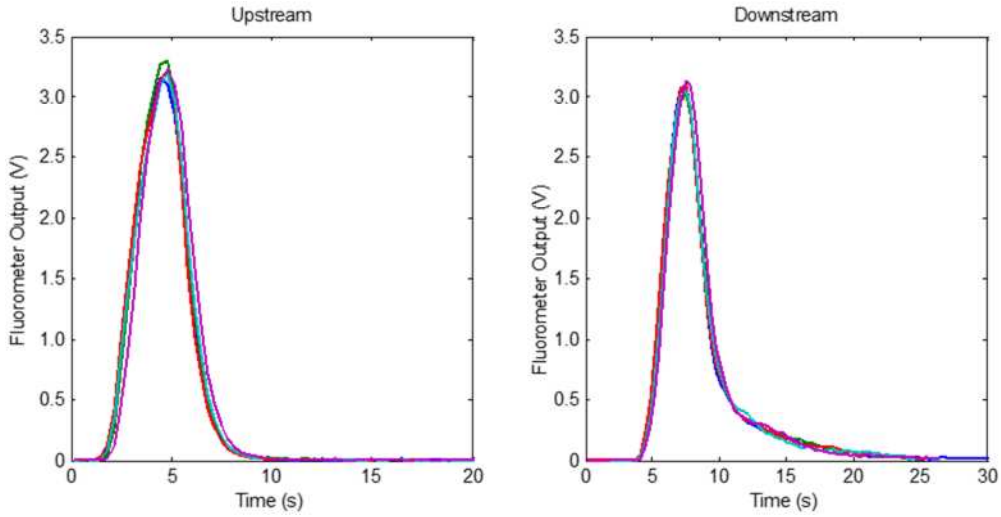

(a) Surcharge 17 mm

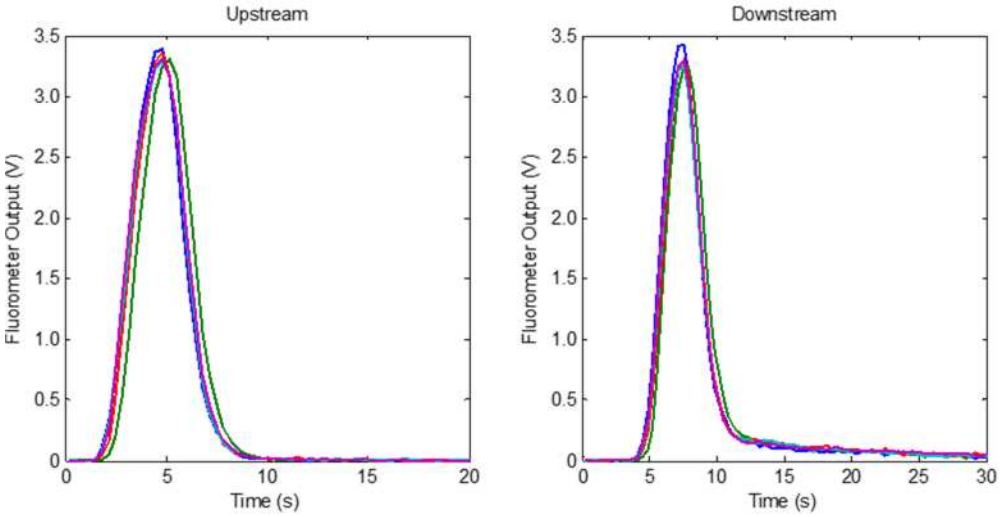

(b) Surcharge 70 mm

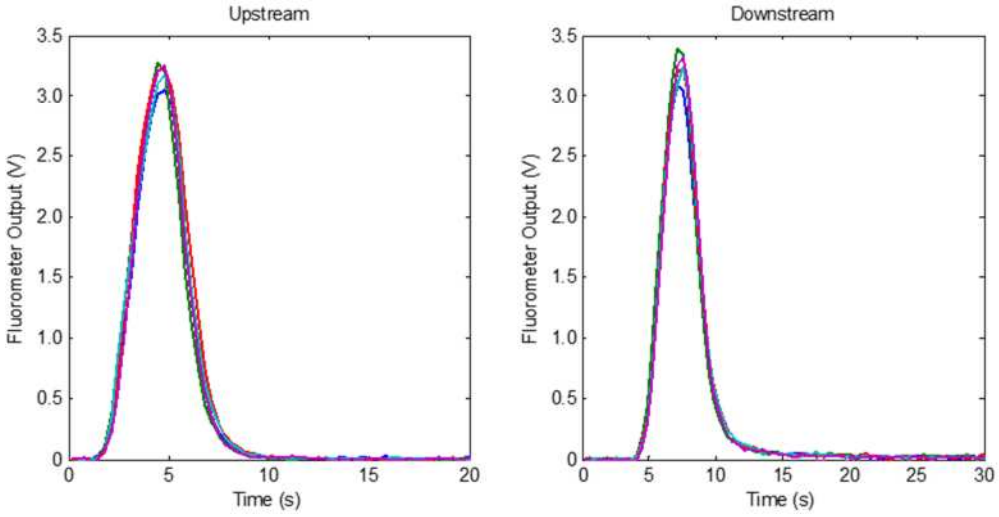

(c) Surcharge 240 mm

Figure 5.10: Comparison of repeat traces measured at 1.17 l/s for small manhole

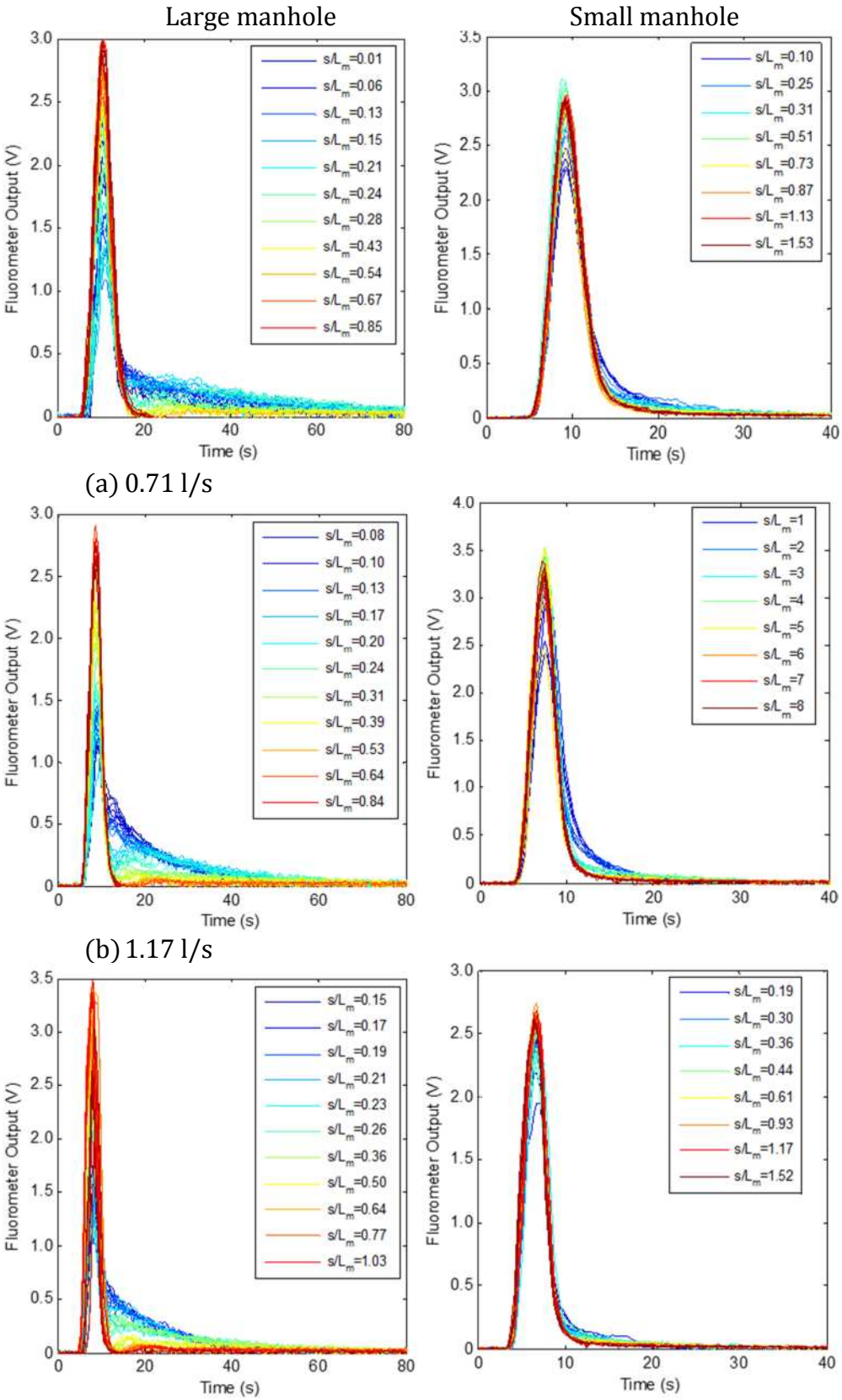

(a) 0.71 l/s

(b) 1.17 l/s

(c) 1.64 l/s

Figure 5.11: Downstream profiles with surcharge for large and small manhole

5.1.4.2 Mass Balance

Readings were taken using four fluorometers and classified as follows;

Distance between fluorometer 1 and 2: Reach 1 (Straight pipe before manhole)

Distance between fluorometer 2 and 3: Reach 2 (Across manhole)

Distance between fluorometer 3 and 4: Reach 3 (Straight pipe after manhole)

Distance between fluorometer 2 and 4: Reach 4 (Across manhole to downstream2)

The mass balance is the ratio of the total mass of dye measured downstream to the total mass of dye measured upstream. For this experiment, concentration profiles were collected over a period of 180 seconds after injection of dye at a sample rate of 30 Hz. Background concentration was taken as the average of the data recorded before first injection of tracer. To ensure that the actual trace profile is obtained, cut-off points were applied to the start and end of the recorded data. The cut-off point was taken as a percentage of the maximum temporal concentration recorded. They are important as it allows checks on mass recovery of dye between the measurement locations as well as identifying the signal, the period between which dispersion parameters are determined.

For the three flow rates measured, all the mass balance values were above 75% (Fig. 5.12). It was observed that a cluster of high surcharge recoveries occurred when $s/D_p \leq 2.0$. However at $s/D_p > 2.0$, the mass balance values decreased. This is because as surcharge increases, there is more manhole volume; the tracer dye therefore travels into and is sometimes trapped within the upper

volume of the manhole. This results in a delayed release of the pocket of dye to the outlet in very low concentrations over a long period.

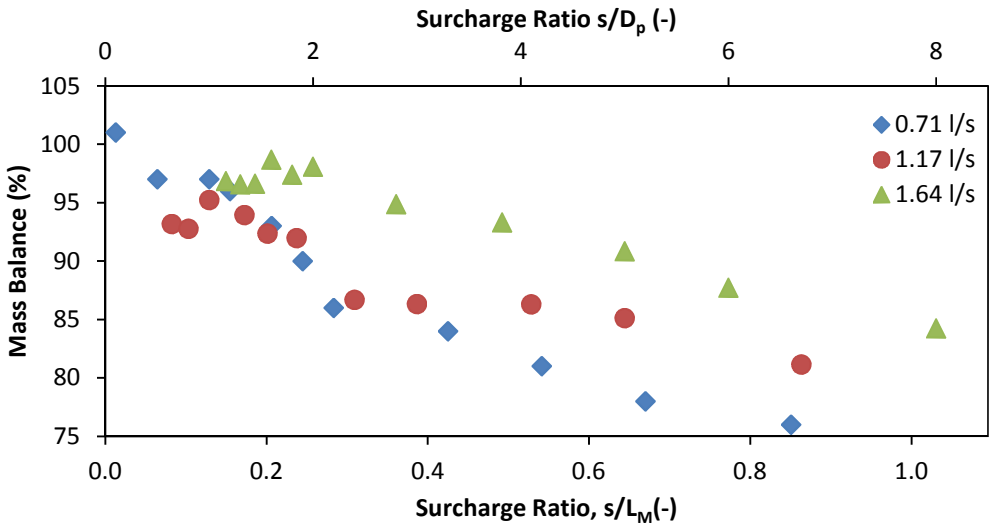

(a) Across manhole (Reach 2)

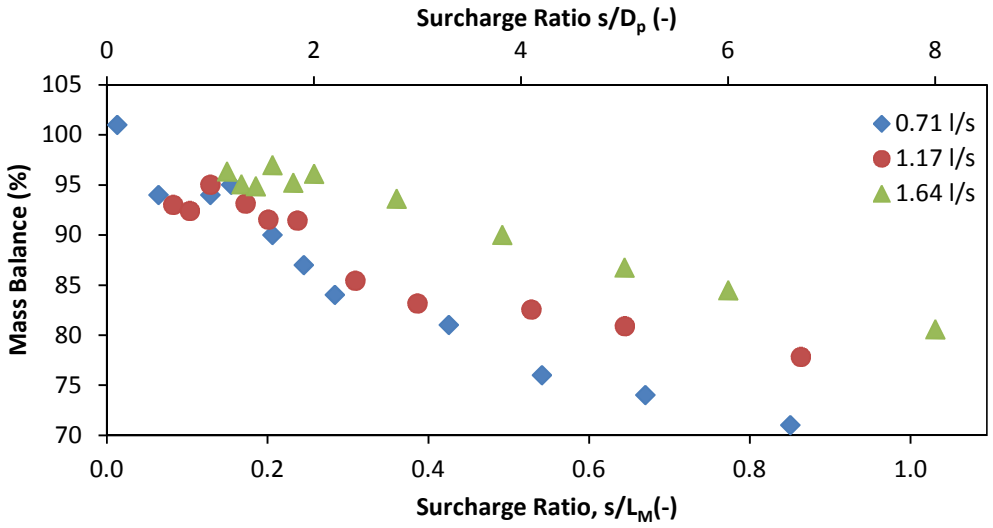

(b) Across manhole to downstream2 (Reach 4)

Figure 5.12: Mass balance values across large manhole

As the flow rate increased, there was an increase in recovered dye. This can be as a result of better mixing occurring at higher flow rates resulting in a more consistent amount of dye per unit area. Results across the manhole (Fig 5.12a and Fig 5.13a) were better than results further downstream (Fig 5.12b and Fig 5.13b). The mass recovery at lower surcharge ratios, were higher than those of the higher surcharge ratios. A similar pattern was observed by Jones (2011).

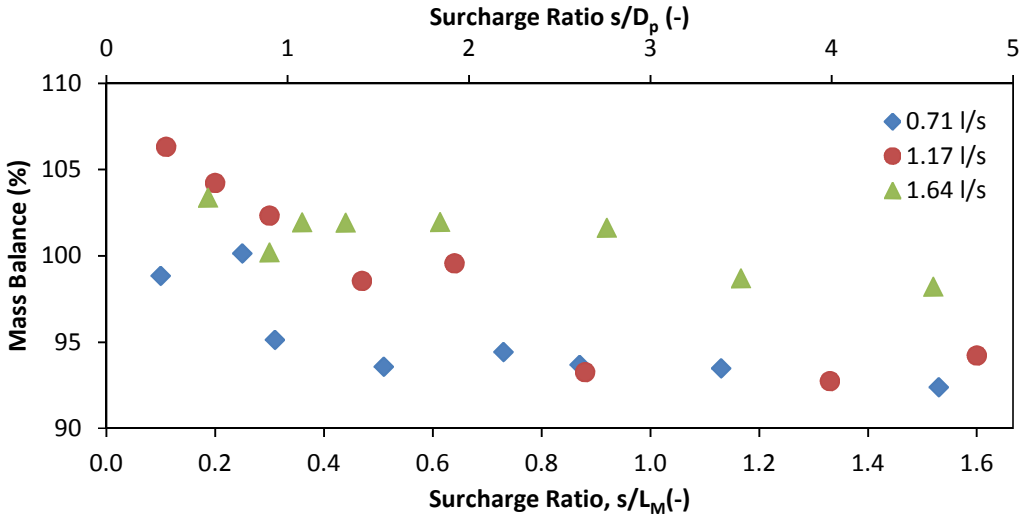

(a) Across manhole (Reach 2)

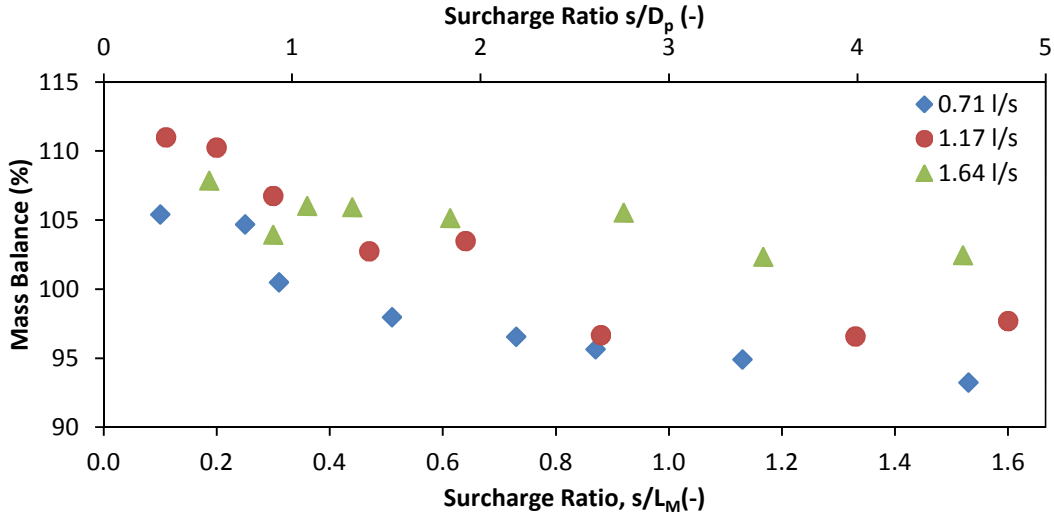

(b) Across manhole to downstream2 (Reach 4)

Figure 5.13: Mass balance values across small manhole

5.1.4.3 Travel Time

Travel times obtained by the standard method of moment analysis are shown in Fig. 5.14 and Fig. 5.15. Travel times for the large manhole for all three flow rates (Fig. 5.14) exhibited an initial rise, followed by a sharp drop after a surcharge ratio of 0.2 before descending at almost a constant rate after a surcharge ratio of 0.4. Travel times for the small manhole did not change significantly as the surcharge ratio increased (Fig. 5.15a).

At 0.71 l/s, a higher value was recorded between a surcharge ratio of 0.01 and 0.8 after which it was almost constant. This confirms that more mixing was occurring at the low surcharge depths as evident in the downstream concentration profiles of the low surcharges. Fig. 5.15b shows a plot of the average travel times against the inverse of flow rate.

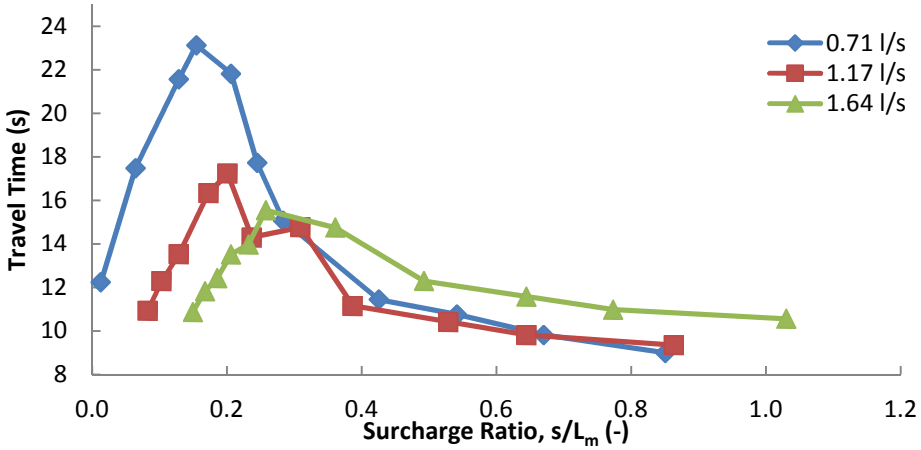

Figure 5.14: Travel time at all flow rates for large manhole

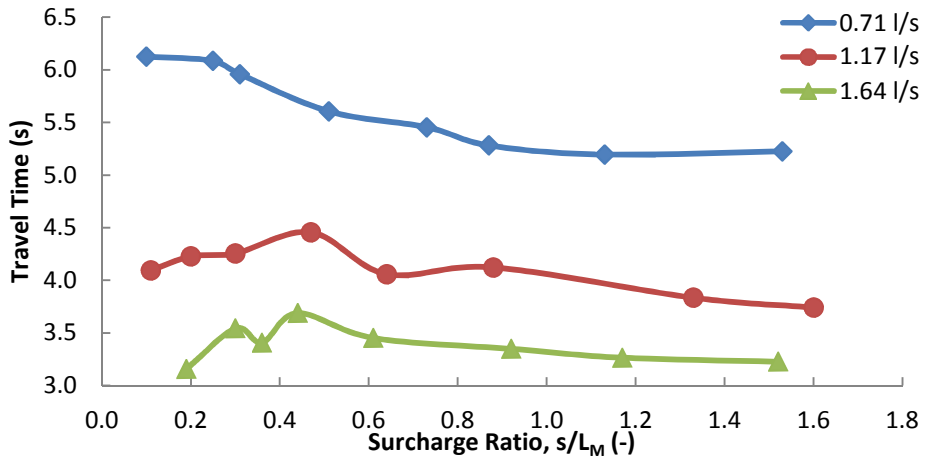

(a) Travel time against surcharge

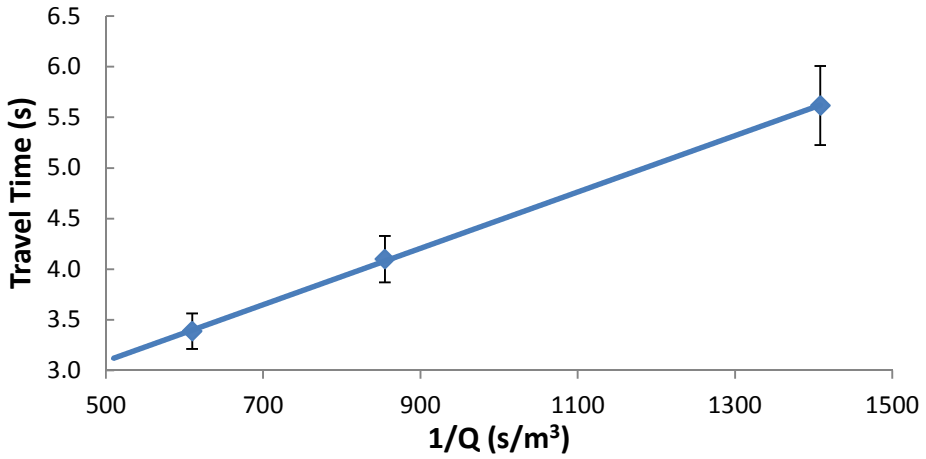

(b) Travel time against inverse of Q

Figure 5.15: Travel time at all flow rates for small manhole

5.1.5 Cumulative Residence Time Distribution

5.1.5.1 Deconvolution Software

A deconvolution technique, Sonnenwald et al. (2015), was used to produce the RTD and subsequently the CRTDs across the manhole (Reach 2) for both the large and small manhole data. The software does not need the user to provide linear calibrations of Cyclops; the measured data was therefore input without

pre-processing. Sensitivity analysis on a subset of the data led to a 'normal' distribution of 20 sampling points and a limit of 150 iterations being applied to both manhole data. The goodness of fit (using R_t^2) of the predicted downstream concentration profile from deconvolution was calculated and is shown for all repeats and flow rates in Fig. 5.16(a) for large manhole and Fig. 5.16(b) for small manhole.

Fig. 5.16(a) shows a range of values between 0.9570 and 0.9996. The values however show a general decline across the entire flow rate around the surcharge ratio of 0.2, before increasing, to a near constant value for each surcharge and flow rate after a surcharge ratio of 0.3. For 4 out of the 120 (3%) data points plotted for the small manhole, a decrease was also noticed around a surcharge ratio of 0.3 though it was not pronounced and does not occur for the 1.17 l/s flow rate. The mean R_t^2 value for the large manhole is 0.9858 and for the small manhole is 0.9979. This shows that deconvolution can accurately predict the transfer function and produce the downstream concentration profile across a square manhole. Samples of the deconvolution results are shown in Fig. 5.17 and Fig. 5.18. It shows the worst and best predictions of the downstream data; the RTDs as well as the CRTDs. For the large manhole, the worst prediction was R_t^2 of 0.9570 occurring at 0.71 l/s, surcharge ratio of 0.13 while the best prediction was R_t^2 of 0.9988 occurring at 1.17 l/s, surcharge ratio of 0.86. However for the small manhole, the worst prediction was R_t^2 of 0.9721 at 1.64 l/s, surcharge ratio 0.44 and the best prediction occurred at R_t^2 of 0.9996 at 1.17 l/s, surcharge ratio 0.11.

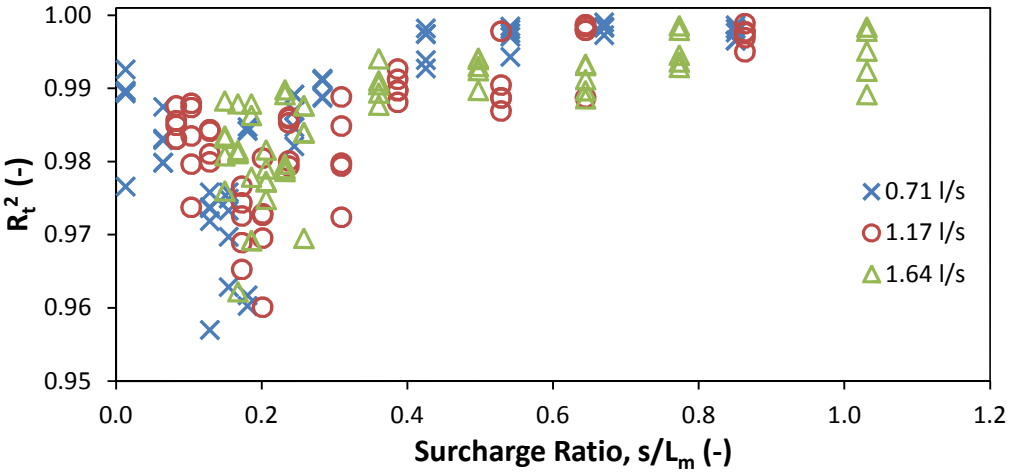

(a) Large manhole

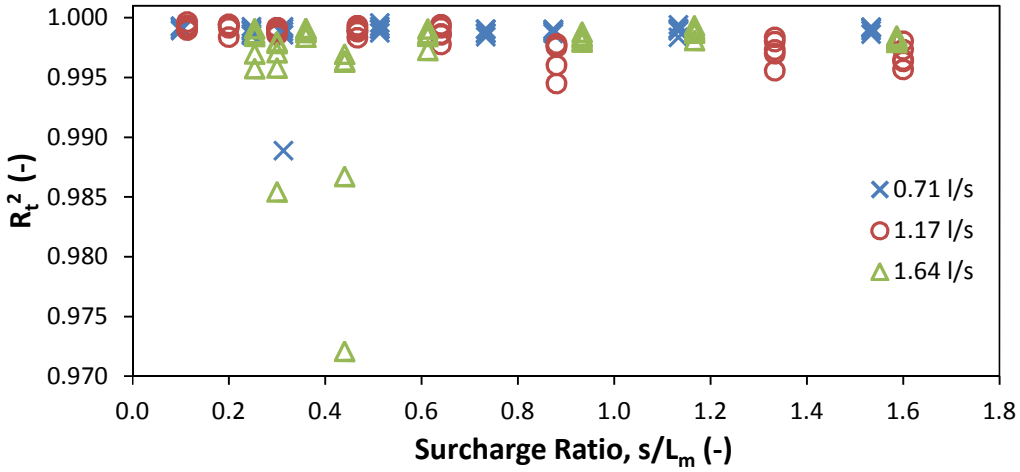

(b) Small manhole

Figure 5.16: Measure of goodness of fit of predicted downstream profile

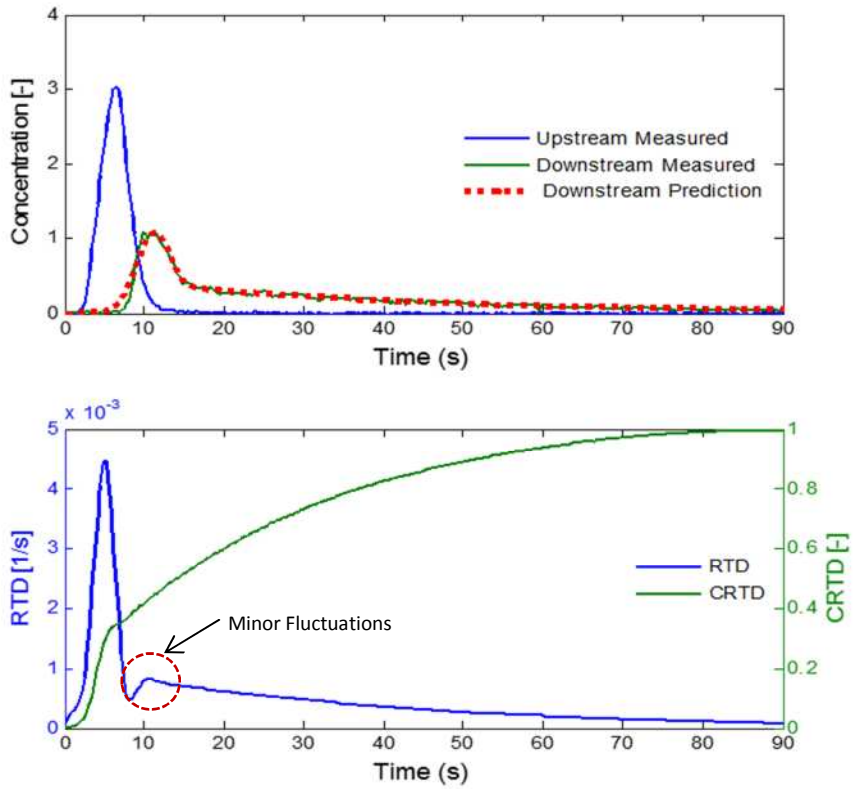

(a) Worst Prediction, $R_t^2 = 0.9570$ at 0.71 l/s surcharge ratio 0.13

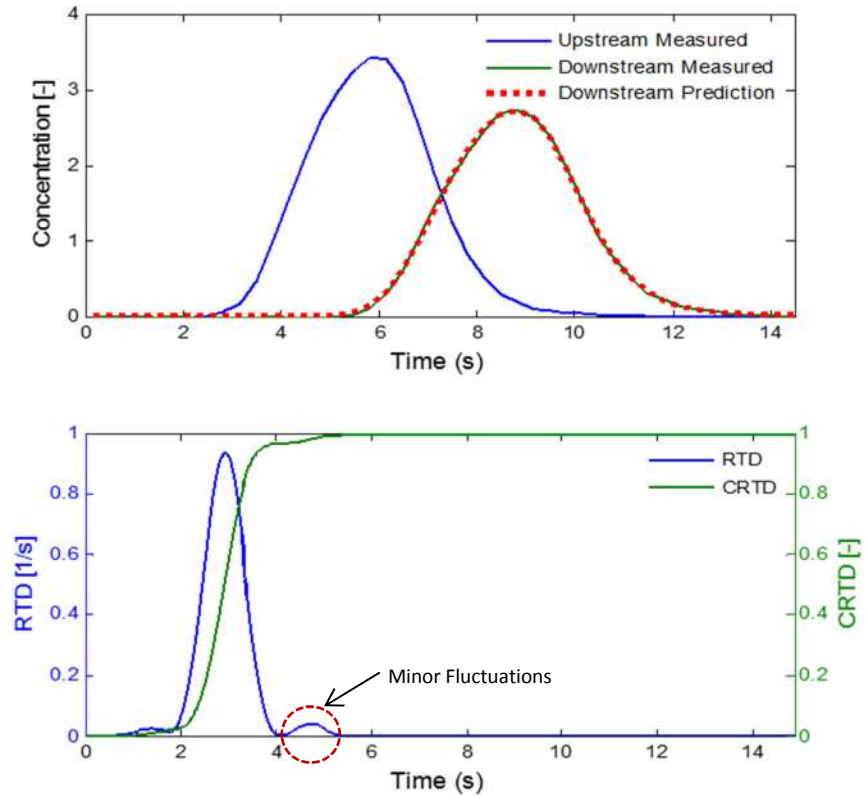

(b) Best Prediction, $R_t^2 = 0.9988$ at 1.17 l/s surcharge ratio 0.86

Figure 5.17: Sample deconvolution results for large manhole

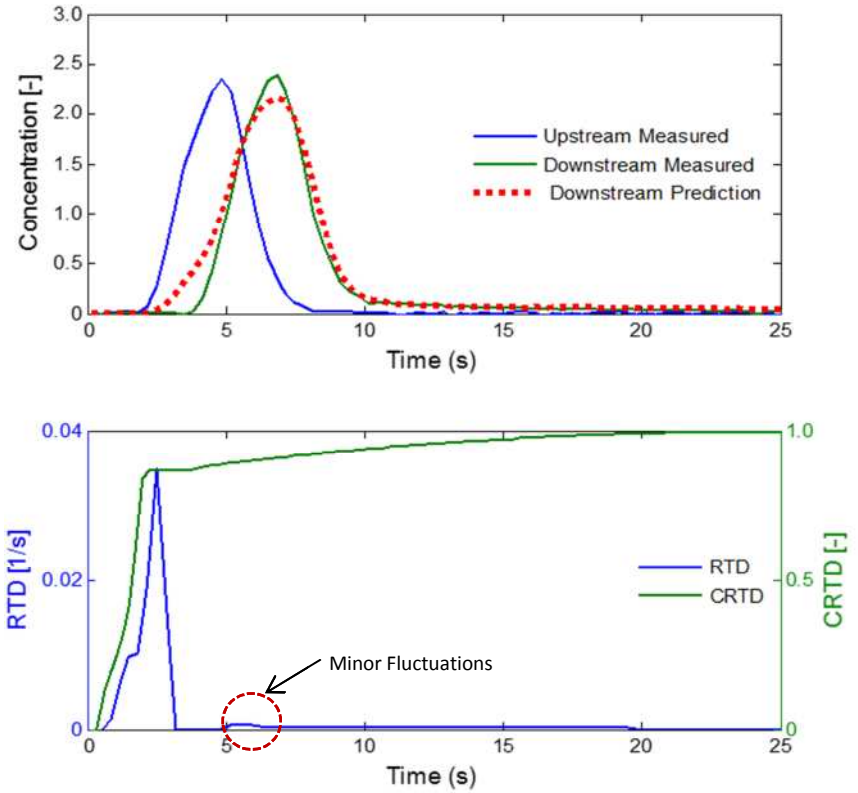

(a) Worst prediction, $R_t^2 = 0.9721$ at 1.64 l/s, surcharge ratio 0.44

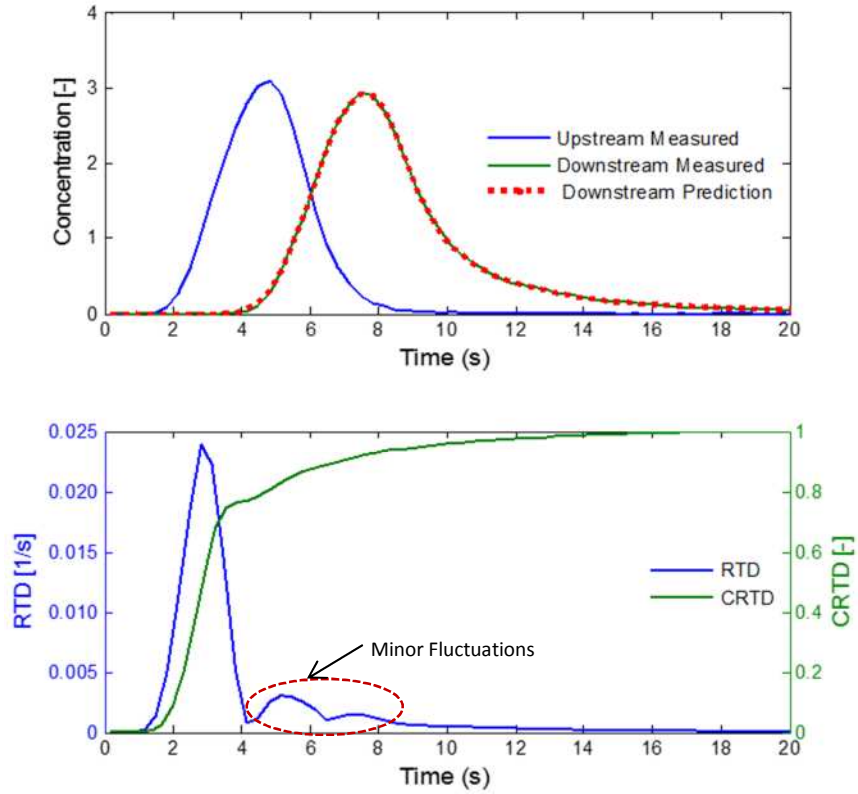

(b) Best prediction, $R_t^2 = 0.9996$ at 1.17 l/s, surcharge ratio 0.11

Figure 5.18: Sample deconvolution results for small manhole

Fluctuations are often present in deconvolved RTDs, highlighting a potential issue with the use of maximum entropy deconvolution. Sonnenwald et al. (2015), incorporated steps in the software produced to reduce this fluctuations, resulting in smoother RTDs. The effect is evident in the minor fluctuations exhibited in the RTDs, the smoother RTDs and the lack of fluctuations in the CRTDs as shown in Fig. 5.17 and Fig. 5.18. However, the fluctuations noticed can actually be secondary peaks which are results of recirculation in the system.

5.1.5.2 Normalised Time

In a bid to create a universal level of comparison for the data and existing studies, the time was normalised by the ratio of the flow rate to the volume of water between measuring points. The mean CRTDs from five repeats, classified according to the ratio of the surcharge to manhole side length (s/L_m), were compiled for each flow rate and are shown in Fig. 5.19 and Fig. 5.20 for the large and small manhole respectively. A compilation of the individual CRTDs at actual and normalised time can be found in Appendix B.

CRTDs for the large manhole have distinct change in shape as the surcharge increases. They show evidence of short circuiting as well as mixing. The short circuiting mass fraction increases with increase in surcharge and can be inferred from the CRTD plots by looking for the point at which the steep incline ceases. This increase is shown in Fig. 5.21. At low surcharges, the curves rise steeply initially before changing direction projecting a long tail. The curves suggest a short circuiting jet of 30% to 40% of the mass across the manhole with a recirculation that promotes mixing of the remaining mass. These curves

however collapse into one at normalised time. At the high surcharge depths, the CRTDs are mainly a steep line with a slight curve (short tail) between the 85th and 90th percentile indicating that most of the tracer short- circuited through the manhole as a straight jet with a minimal amount of dispersion occurring. For 1.64 l/s, the percentage of dye within the upper manhole volume at high surcharge is higher than those of 1.17 l/s and 0.71 l/s because the higher flow rates results in more turbulence which in turn results in swifter movement of tracer across all planes within the manhole. At normalised time the CRTDs across the manhole separate into two distinct groups with a few of the CRTDs remained in between. The CRTDs lying in between behave partly like both classifications of low and high surcharges with a greater leaning towards the high surcharge CRTDs.

A comparison of the CRTDs across the three flow rate (Fig. 5.19a-c) suggests that the normalised CRTDs are less dependent on flow rate than on surcharge. At a very low surcharge level measured at 0.71 l/s, $s/L_m = 0.01$, (Fig. 5.19a), the CRTD lie between the lower surcharged CRTDs and those of the higher surcharged CRTDs, both at actual and normalised time. This difference was classified for the observations from circular manholes by Jones (2011) where the CRTD had a similar shape as the high surcharge CRTDs. Jones (2011), described that with full flowing pipe, but low-surcharge conditions, the incoming jet showed varying degrees of deflection from the pipe centreline. At low surcharges (0 to 10 mm) similar to that obtained in this present study for 0.71 l/s ($s/L_m = 0.01$), the jet appeared to short-circuit the manhole, deflecting only slightly. At a higher surcharge (35 to 40 mm) the jet was more curved, and

more complete mixing was seen to take place in the manhole. This flow condition was attributed to the Coanda effect, which is the tendency of a fluid to be attracted to a nearby surface. Jones (2011), found that surcharge was more important than flow rate for the range of Reynolds numbers covered ($6152 \leq Re \leq 33194$). The changes in CRTDs across the surcharge range away from the low surcharge curve became evident at a surcharge ratio of $0.24L_m$.

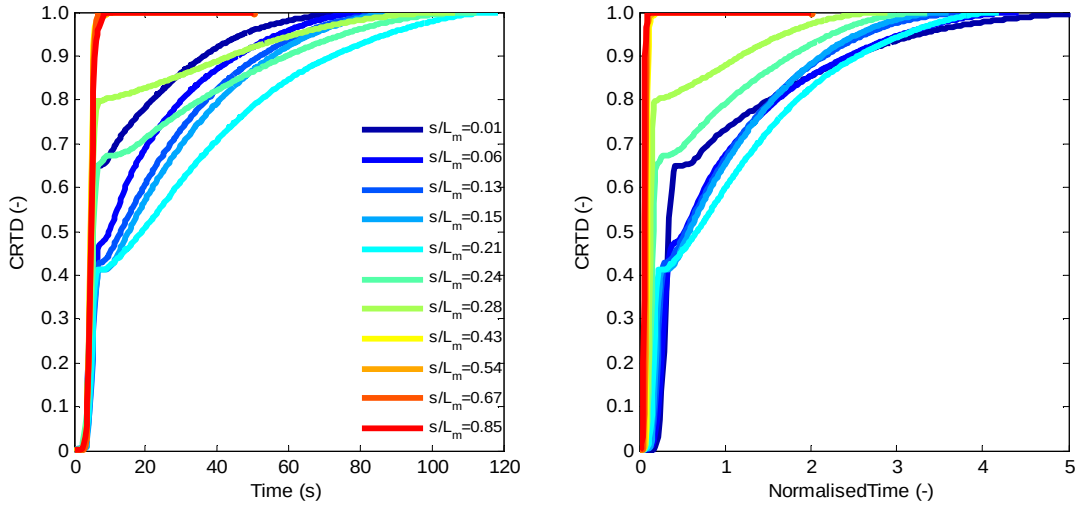

(a) Q= 0.71 l/s

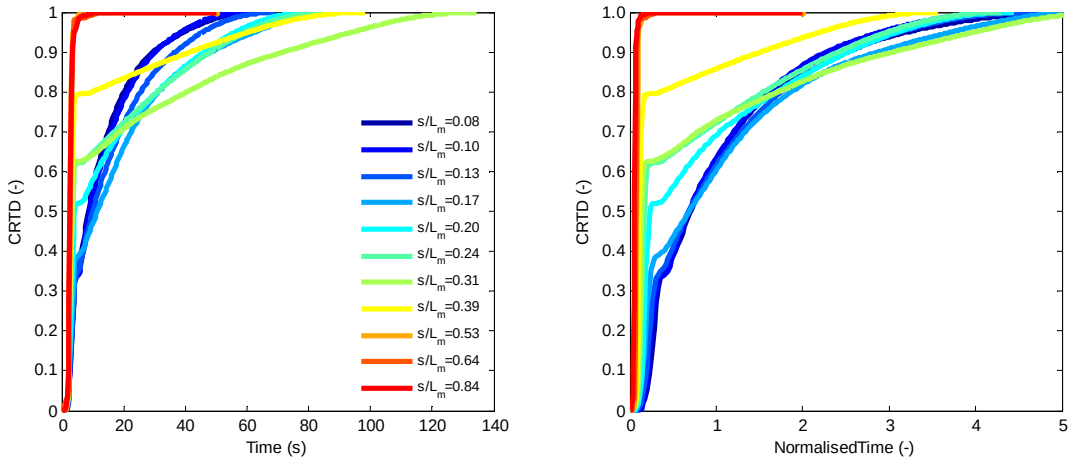

(b) Q=1.17 l/s

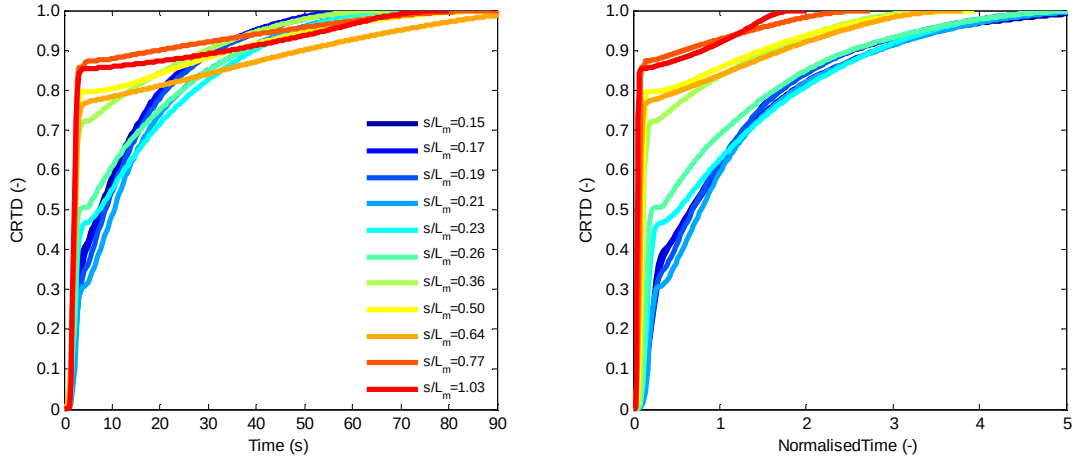

(c) Q=1.64 l/s

Figure 5.19: Compiled average CRTD for large manhole

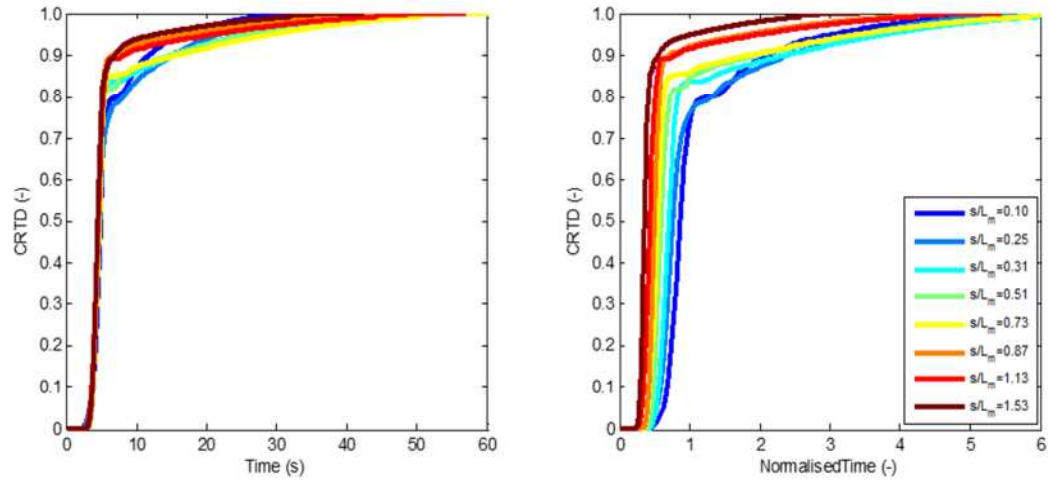

(a) Q=0.71 l/s

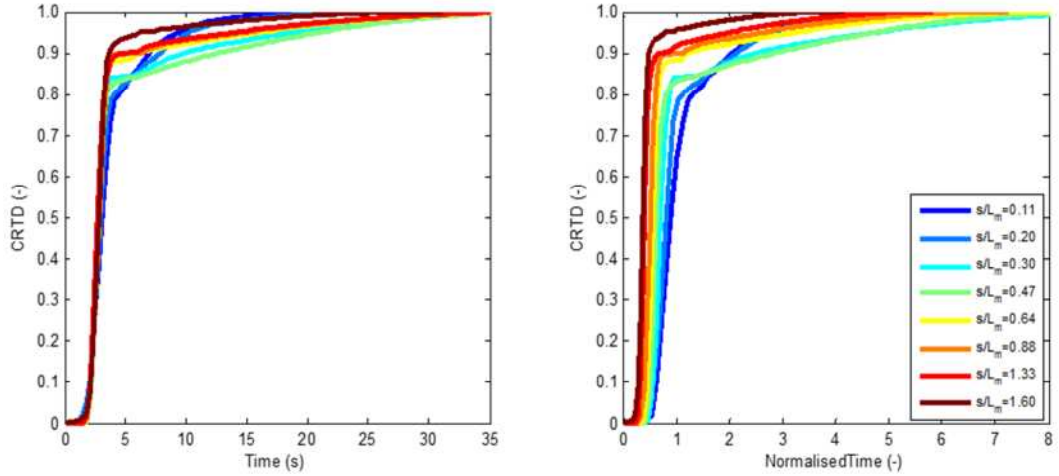

(b) Q=1.17 l/s

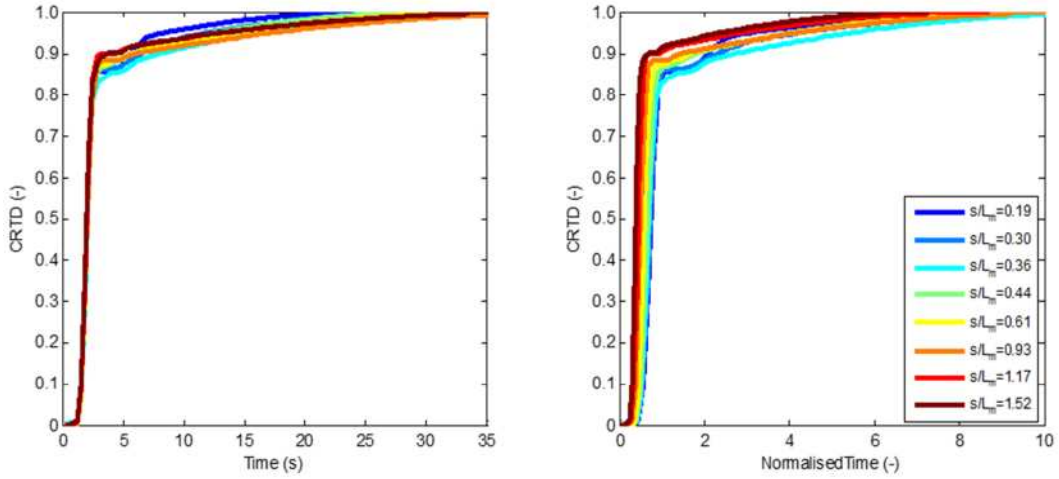

(c) Q=1.64 l/s

Figure 5.20: Compiled average CRTDs for small manhole

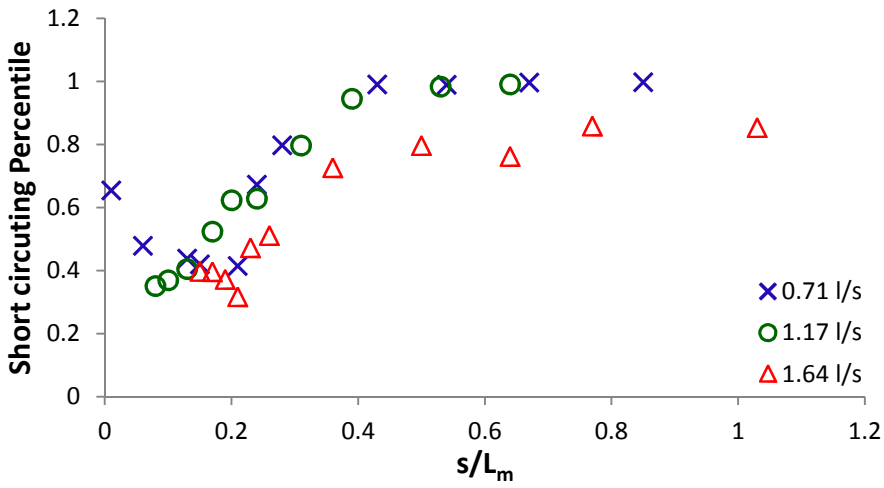

Figure 5.21: Percentage of mass short-circuiting

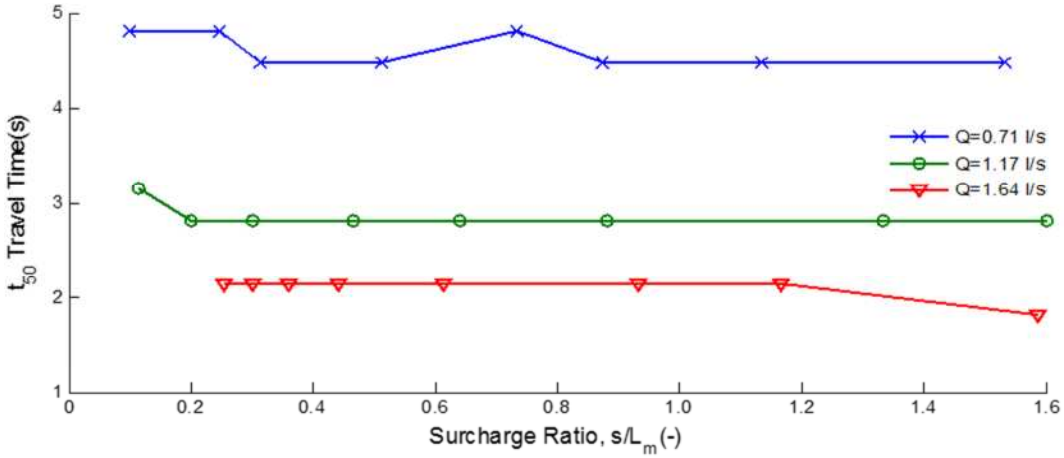

(a) Actual Time

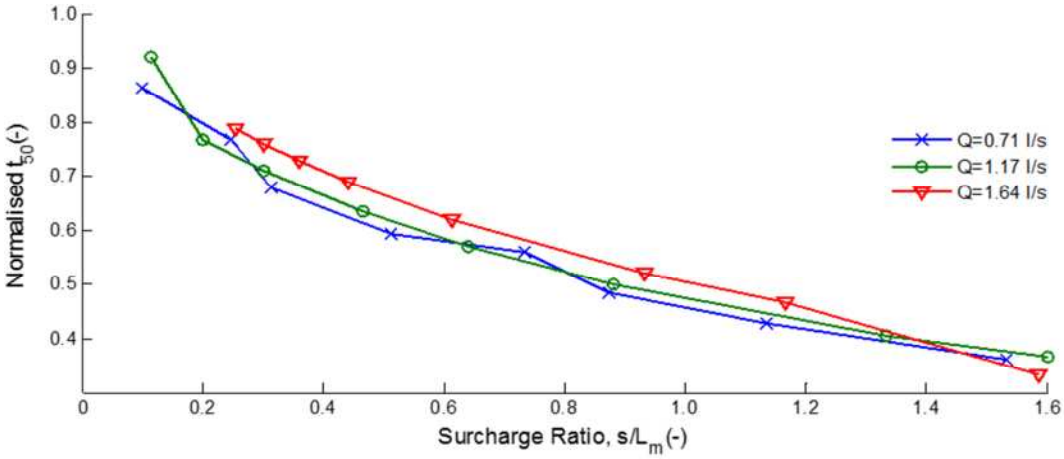

(b) Normalised Time

Figure 5.22: Travel time across large manhole

Although the shape of the manhole in this present study is square, studies on circular manhole by Lau et al. (2008), Stovin et al. (2010b) and Jones (2011), observed the same hydraulic profiles at low and high surcharges suggesting a threshold level in terms of the ratio of surcharge to manhole diameter.

A different mechanism however occurs within the small manhole (Fig. 5.20). The CRTDs both at actual and normalised time do not exhibit a significant change in shape as surcharge increased. The CRTDs exhibit a steep curve from 0 to approximately 80th percentile before changing direction. At normalised time, the CRTDs show evidence of the effect of pipe travel times and slight shifts as surcharge increased. The trend suggests that the hydraulics within the small manhole is similar to that obtained within a pipe. A CFD study by Stovin et al. (2013) on a series of circular manhole with manhole diameter to pipe diameter ratio greater than 1.5 but less than 4.4 shows that the flow field is characterized by short-circuiting throughout the full range of surcharged depth with no distinct threshold level. The results from this study of the small manhole, therefore confirm existing theory that the ratio of pipe size to manhole size is important in determining the hydraulics within a manhole.

5.1.5.1 Travel Time

Median travel times across the large manhole initially increased with increase in surcharge, before decreasing after a surcharge ratio of 0.17-0.24, followed by a constant value (Fig. 5.22). This trend occurred at all flow rates. At normalised time however, the t_{50} values began to close up across flow rate between a surcharge ratio of 0.24 and 0.40, after which similar values were recorded

irrespective of flow rate. A similar trend was observed in Stovin et al. (2013) where the CFD modelled data sets showed an increase with surcharge up to a surcharge of $s/\Phi_P = 0.2$, after which there was a sharp drop in t_{50} values to a low, constant value.

Short-circuiting parameters for the large manhole are shown in Fig. 5.23. Fig. 5.23a shows a decline in the value of t_{10}/t_{90} at $s/L_m < 0.2$ after which there is an increase. On the other hand the t_{50}/t_{10} parameter (Fig. 5.23b) showed a rise in value until $s/L_m = 0.20$ after which an almost constant value across all flow rate was obtained as surcharge increased. This goes to confirm the suggestion by Bennett (2012) that a change in transition of fluid behaviour in a large surcharge circular manhole occurs in the range $0.20 \leq s/D_m \leq 0.27$.

The trend in the large manhole was different from the small manhole as t_{50} travel times along the small manhole (Fig. 5.24), were almost constant with each flow rate as surcharge increased, although they reduced with increase in flow rate. At normalised time however, the normalised t_{50} times reduced with increase in surcharge ratios with a constant slope across all flow rate.

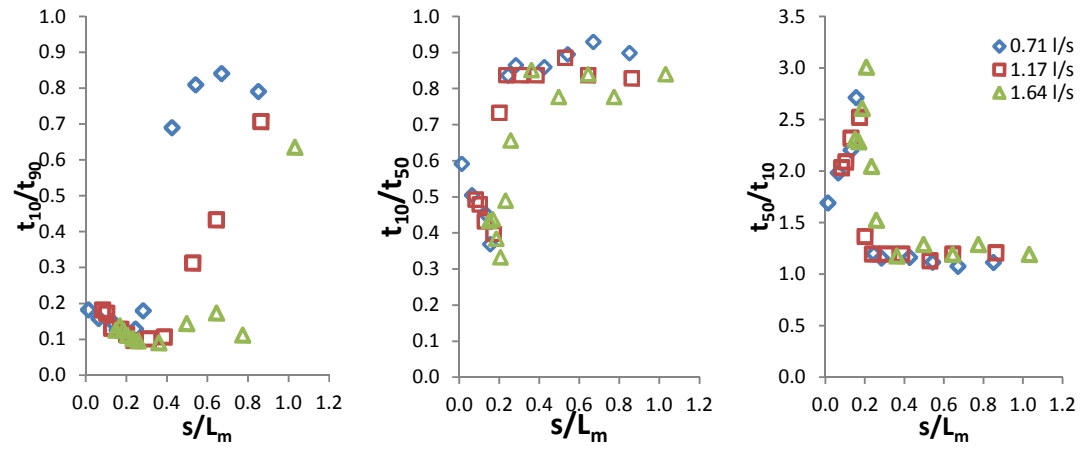

(a) t_{10}/t_{90} (b) t_{10}/t_{50} (c) t_{50}/t_{10}

Figure 5.23 : Short circuiting parameters in large manhole

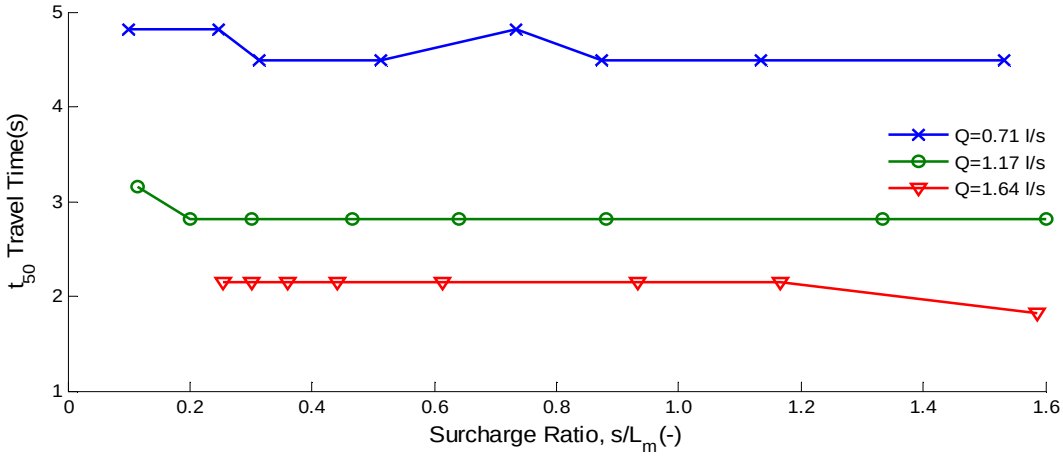

(c) Actual Time

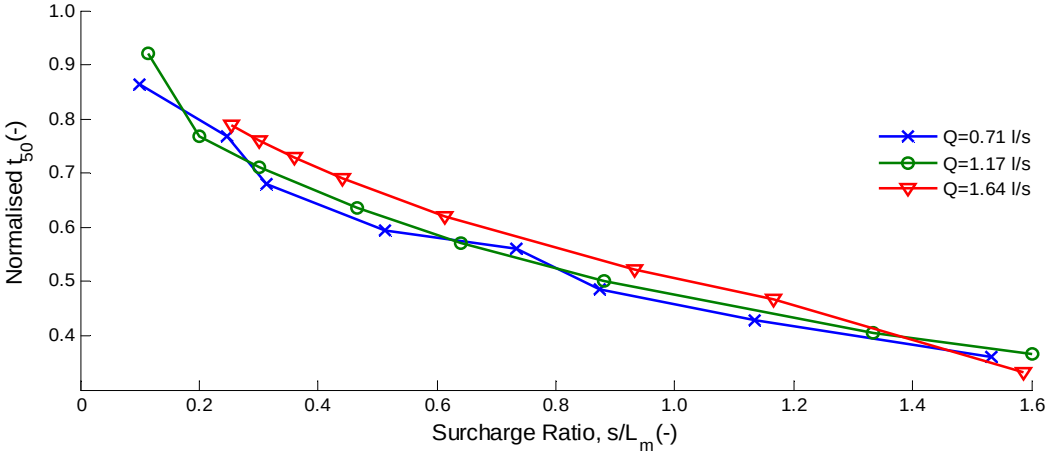

(d) Normalised Time

Figure 5.24: Travel time across small manhole

5.1.5.2 Evidence of Threshold Level in Large Manholes

The results indicate that as the surcharge increases, there is a point of significant change in the headloss (Fig. 5.3), energy loss coefficient (Fig. 5.5), mass balance (Fig. 5.12), travel time (Fig. 5.14), CRTDs (Fig. 5.19) as well as the short-circuiting ratios presented in Fig. 5.23. At surcharge levels below $0.24L_{m,}$ a similar pattern exists. Between surcharge depth $0.24L_m$ and $0.39L_m$, a different pattern of transition exists which becomes more consistent after $0.39L_m$ irrespective of flow rate. It can therefore be noted that there exists a threshold level in large square manholes (i.e. L_m/D_p=7.76) and that this threshold level can be obtained at $0.24L_m$. Guymer et al. (2005), studied four sizes of manhole with a pipe diameter, Φ_p = 88 mm. The data presented suggested that the threshold surcharge depths for the 800, 600, 485 and 385 mm Φ_m manholes were approximately 220, 156, 121 and 90 mm respectively. Regression through the origin gives a general relationship for the threshold surcharge depth, $s' = 0.258\ \Phi_m$. Guymer et al. (2005) proposed that the threshold depth was linked to the jet expansion described by Albertson et al. (1950). If the surcharge depth exceeds $\Phi_m/5$, then the diffusion region will not break the surface and the upper dead zone, characteristic of the above-threshold hydraulic regime, will result. Conversely, if $s < \Phi_m/5$, then the diffusion region will break the free surface within the manhole, leading to the chaotic, well-mixed, hydraulic regime associated with below-threshold surcharge depths. They went ahead to suggest a longitudinal diffusion zone growth rate of 1 in 4, which probably reflects the fact that the jet is confined by the base of the manhole, enhancing the vertical diffusion rate upwards into the manhole's surcharge volume. If this is the case,

then it would be consistent to assume that the length of the jet core will be reduced below the theoretical distance of 6.2 Φ_p (550 mm). This may explain why, although less prominent, evidence of the threshold was detected in the 485 and 385 mm manholes, despite them being smaller than 550 mm (6.2 Φ_p). Lau et al. (2008), suggested a threshold level between 2.0Φ_p (0.220Φ_m) and 2.5 Φ_p (0.275Φ_m) based on sharp changes noticed in the headloss and travel time values of the data recorded as surcharge increased. A study of the same scale of manhole as this present study (Φ_m = 388 mm, Φ_p = 50 mm) although circular by Jones (2011), suggested the threshold lies at 2.0D_p (0.258D_m) while Sonnenwald (2014) suggested this same threshold level of 0.258D_m for a circular manhole of manhole to pipe diameter of 4.4.

The small square manhole (i.e. L_m/D_p = 3.0) does not exhibit this significant transition as the surcharge increases as shown in the headloss (Fig. 5.3), energy loss coefficient (Fig. 5.5), mass balance (Fig. 5.12), travel time (Fig. 5.14) and CRTDs (Fig. 5.19). Stovin et al. (2013), conducted a CFD study of surcharged manholes and observed that the hydraulic threshold previously identified in Guymer et al. (2005) and Lau et al. (2008) for surcharged manholes is only evident in systems with large Φ_m/Φ_p ratios. In smaller-diameter manholes the incoming jet tends to bridge the distance across the manhole such that short-circuiting effects dominate, irrespective of surcharge level. Stovin et al. (2013), found that the critical Φ_m/Φ_p ratio was Φ_m/Φ_p = 4.4. They suggested that since many manholes found in practice have Φ_m/Φ_p ratios of less than 4.4; their mixing characteristics can be assumed to be equivalent to a pipe.

5.1.5.3 Modelling of Surcharge CRTD

Guymer and Stovin (2011), modelled a data set obtained from a surcharged manhole effectively into two dimensionless CRTDs, each of which corresponds to an alternative hydraulic regime. A comparison of the laboratory results to this model is shown in Fig. 5.25. For large manhole, pre threshold CRTDs (Fig. 5.25a), the model agreed with the present data between 0 and 50^{th} percentile after which it predicts that the 90% of the data would pass through earlier than it actually happened with the present data. For post threshold large manhole data (Fig. 5.25b), the model only fits the lower limit of $0.24 \leq s/L_m \leq 0.39$. The post-threshold curves from the present study, at $s/L_m > 0.39$ (Fig. 5.25c), have a similar shape to the model but with a higher steepness. It shows that 60% of the dye passes through in a straight jet (0.1 normalised time) as opposed to the present data that has an average of 80% of the dye passing through as jet.

An alternative approach to modelling of the large manhole data was suggested by Jones (2011) which considered percentile based and time based methods to model the data for circular manhole. It found that the time based model was more plausible and closely matched that predicted by Guymer and Stovin (2011). This approach was implemented to model the CRTDs from the large and small square manhole. The percentile based model considers the average time taken to achieve specified percentiles for each CRTD while the time based model considers the average percentile of mass at specific time steps. Fig. 5.25(c) shows that although the percentile based model was representative of the result, it doesn't adequately fit the data for both pre and post threshold

CRTDs after the 90th percentile. The time based model however adequately fitted both the pre and post threshold data. It can therefore be used as a modelling tool for predicting mixing properties within a square manhole. A copy of the model is in the Appendix C.

Fig. 5.26(a) shows the comparison of the Guymer and Stovin (2011) and the small manhole CRTDs. Although the model is for post threshold CRTDs as exhibited by the small manhole, the model does not perfectly fit the data. The inadequacy of this model to adequately fit the data could be as a result of the different shape of manhole, or the difference in flow mechanism occurring in the small manhole as the model was postulated using a large manhole data. In a circular manhole, the entire cross sectional area serves as the mixing zone whereas the corners of a square manhole are likely to be excluded from the core mixing region. However the Taylor's dispersion model (eqn. 2.14), provided a better fit for the CRTDs as shown in Fig. 5.26(a). It observed that the CRTDs for the small manhole at normalised time did not fully collapse into a single profile (Fig 5.26(a)), whereas there is a more concise grouping at the actual time as shown in Fig. 5. 26(b). The time was normalised using the entire volume within the manhole, whereas because of the short distance between the inlet and outlet the pipe, the tracer went though as a jet towards the outlet pipe with little mixing occurring vertical. It can then be suggested that normalising with the pipe volume might produce a single profile. The fitting of the Taylor's dispersion model to the CRTDs further confirms this suggestion.

For all large manhole surcharge CRTD curves, the mass fraction short-circuted (point at which there is a change in slope of curve) was observed along with the normalised time at which they occur. Fig. 5.27 shows a plot of these values. It was observed that at very low surcharge ($s/L_m = 0.01$), the values are high while at low surcharge ratios before the threshold ($s/L_m < 0.24$), the values of mass fraction as well as normalised time were approximately 0.4. However as the surcharge ratio increased beyond the threshold ($s/L_m > 0.24$), the mass fraction short-circuted increased while the normalised time at which the short-circuting occurred decreased.

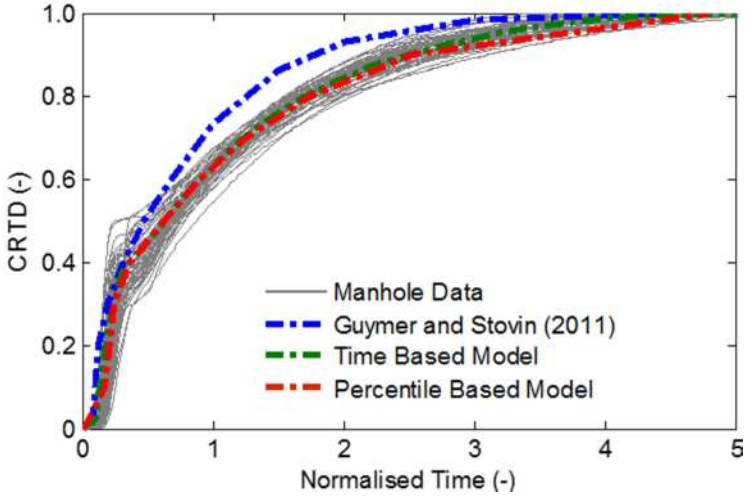

(a) $0 < s/L_m \leq 0.24$, large manhole pre-threshold

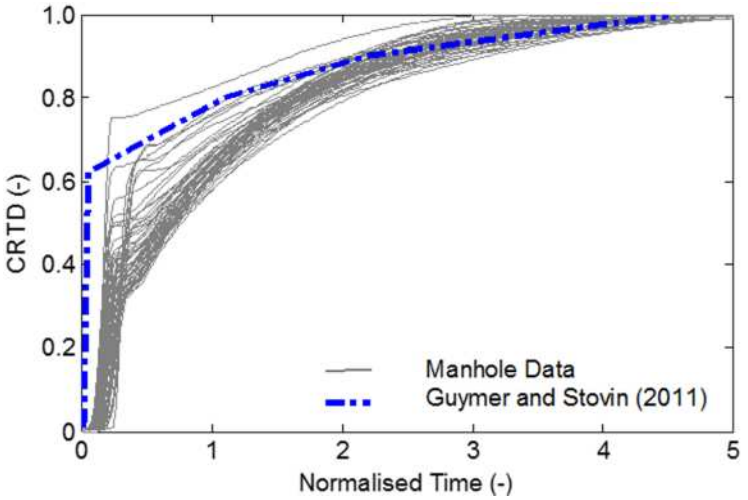

(b) $0.24 < s/L_m < 0.39$, large manhole post-threshold

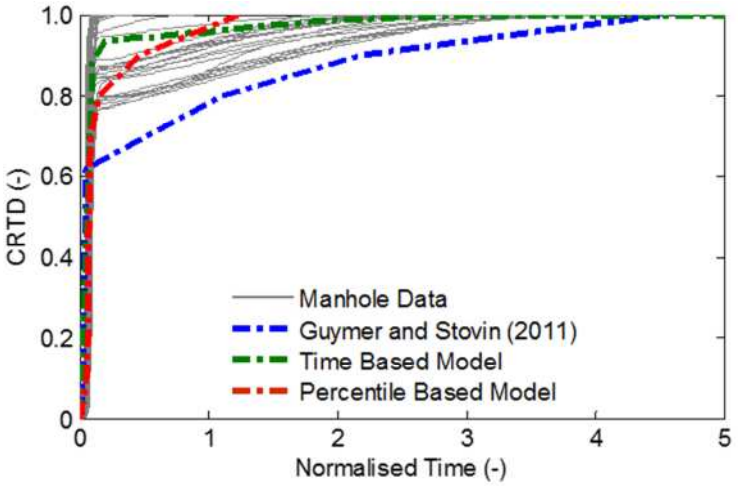

(c) $s/L_m > 0.39$, large manhole post-threshold

Figure 5.25: Comparison of Large Manhole Result with Models

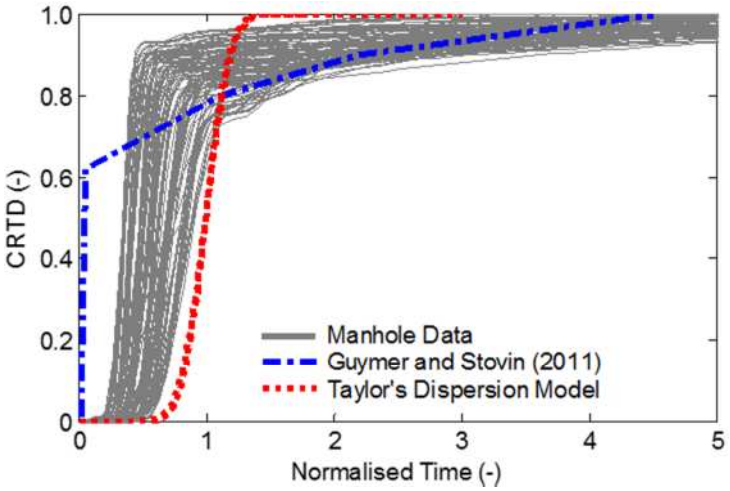

(a) Small manhole data with Stovin and Taylor's model

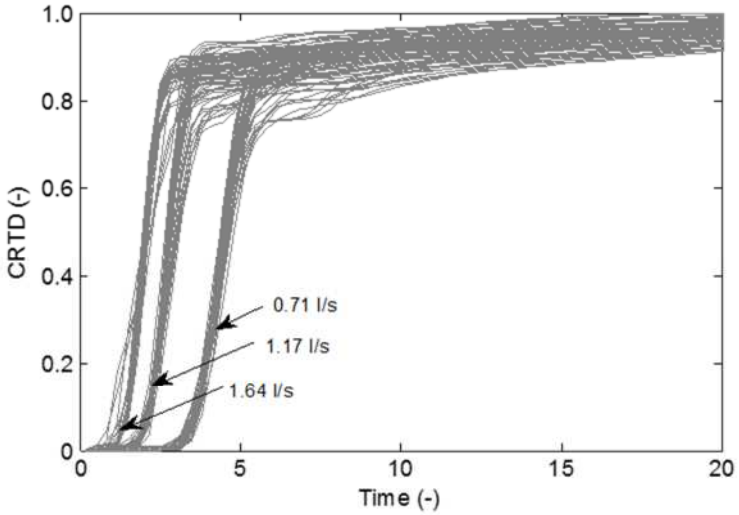

(b) Small manhole data at actual time

Figure 5.26: Small Manhole Results

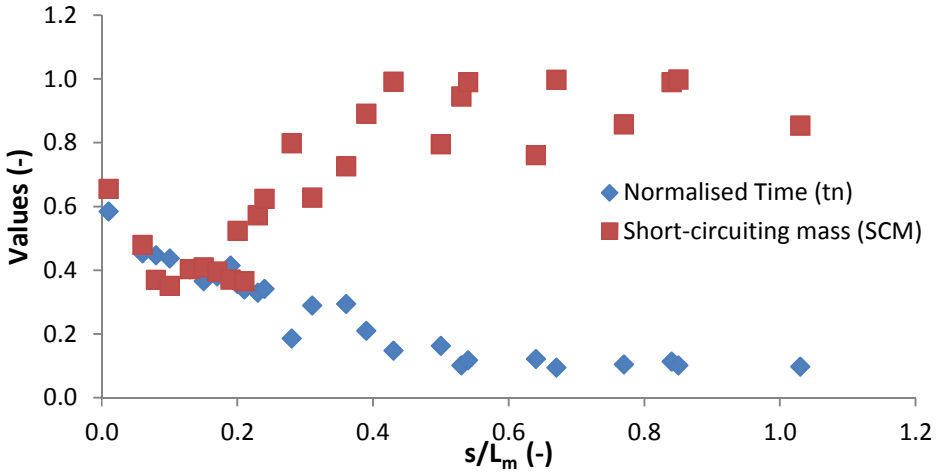

Figure 5.27: Relationship between surcharge ratio and short circuiting

5.2 Manhole Overflow Study

5.2.1 Description of Experiment

The overflow experiment required a modification at the top of the manhole. A weir was fitted around the top of the manhole (Surcharge height = 730 mm) to allow the water to overflow steadily into a stilling basin. The stilling basin was made of perplex glass and had dimension of 570 mm by 500 mm. It is 115 mm deep and collects the overflowing water. The basin is fitted with a trough which conveys the water into the sump for recirculation. A fluorometer is placed inside the trough to record the fluorescence corresponding to the dye concentration at the overflow. The fluorometer is of the same specification and settings as those used along the pipe. The overflow experiment was carried out for three flow rates (0.71 l/s, 1.17 l/s, 1.64 l/s) for both the large and the small manhole. Several combinations of tracer concentration and tracer injection time were carried out. A low concentration of rhodamine WT was injected for duration of 90 seconds and each repeat experiment was carried out for fifteen minutes. The concentration of tracer and the duration of injection used was chosen because they resulted in a good comparison of concentration profile at all measuring point i.e. upstream, overflow and downstream. Two different overflow scenarios were investigated, which is described as one (1) exit and two (2) exits. The first scenario corresponded to when the exit of the pipe becomes blocked and the only exit for the flow is the top of the manhole (Fig. 5.28a). The second scenario is when there is an overflow in combination with a pipe exit (Fig. 5.28b). The downstream end of the pipe is fixed in size, therefore an increase in flow rates results in a considerable increase in the flow towards

the overflow for the two exit scenario. The flow split for the 2 Exit scenario is shown in Table 5.6 and the analysis of the measured data is presented in the ensuing sections.

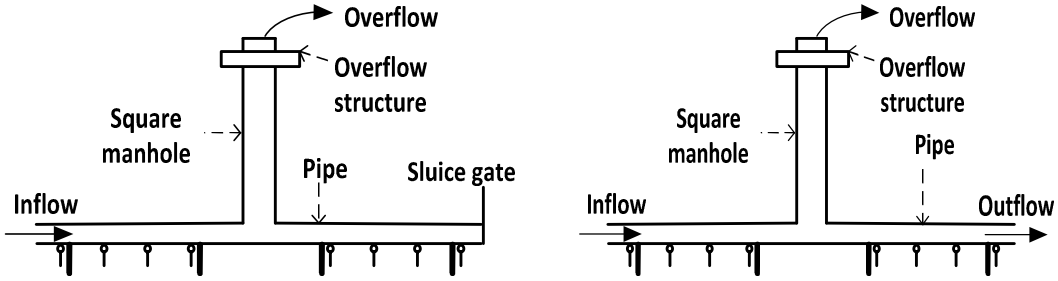

(a) Scenario 1: 1 Exit (b) Scenario 2: 2 Exits

Figure 5.28: Schematic of flow directions for the two overflow scenarios

Table 5.6: Measured outlet flowrates for overflow experiment

2 EXITS	Size	Large Manhole		Small Manhole	
	Q_{in} (l/s)	Q_{out} (l/s)	$Q_{overflow}$ (l/s)	Q_{out} (l/s)	$Q_{overflow}$ (l/s)
	0.71	0.440	0.256	0.49	0.216
	1.17	0.457	0.664	0.67	0.507
	1.64	0.457	1.180	0.589	1.051

5.2.2 Analysis of Measured Data

5.2.2.1 Comparison of Repeat Trace

The overflow experiment was repeated five times for each of the three flow rate (0.71 l/s, 1.17 l/s, 1.64 l/s). Fig. 5.29 -5.30 shows samples of these repeats. It was noticed that all the experiments were repeatable with only slight deviations noticed. Measurements were taken over a fifteen (15) minute period to ensure that the tracer data measurement is a good representation of the system response. Due to the long duration of dye injection, the upstream trace does not

exhibit the Gaussian distribution expected for a pipe. It was however similar to the profile obtained in a range of simple rectangular on-line storage tanks examined by Guymer et al. (2002). On the other hand, the small manhole downstream concentration profiles were similar to Gaussian.

For both one exit and two exit scenarios, overflow peak concentrations for the large manhole ranged between 30%-60% of the inflow peak concentration, increasing as flow rate increases. Measured overflow data profile (Fig. 5.29a-b) shows that the peak tracer concentration in comparison to the upstream peak concentration has been attenuated as it travels between the two measuring points. On the other hand, the small manhole had little attenuation occurring to its peak concentration (Fig. 5.30).

For the two exit experiment, the concentration split was corresponding to the flow split between the two exits. The flow split however exhibited an almost constant flow value going through at the downstream outlet, such that the increase in flow rate had more effect at the overflow outlet. This implies that at lower flow rates more mixing occur and particle mass flux is lower. When two exits flow occurs at 0.71 l/s, the percentage of flow and consequently the flux towards the overflow is low, resulting in an arbitrary flow. The resultant effect of the attenuation is that when an overflow occurs through a manhole of similar dimensions of manhole length to pipe diameter ratio, mixing within the manhole would prevent the same peak concentration of incoming wastewater from overflowing to the surrounding environment.

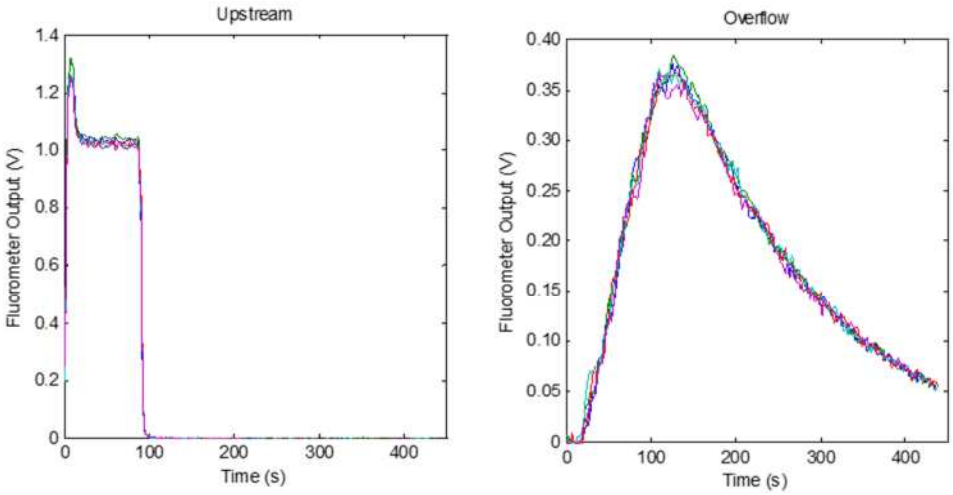

(a) Upstream to Overflow at 0.71 l/s for 1 Exit

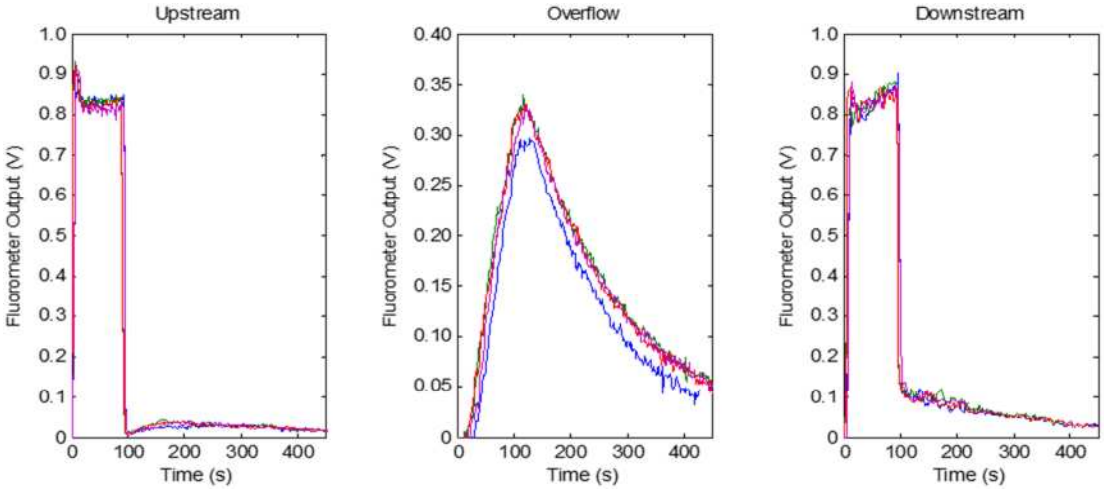

(b) Upstream to Overflow at 1.17 l/s for 2 Exits

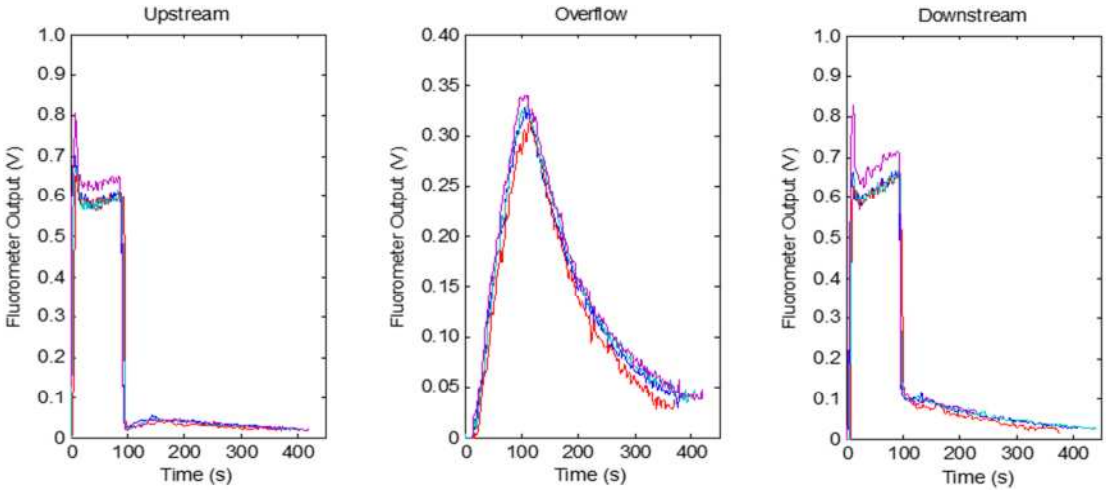

(c) Upstream to Downstream at 1.64 l/s for 2 Exits

Figure 5.29: Sample overfl overflow concentration Profile for large manhole

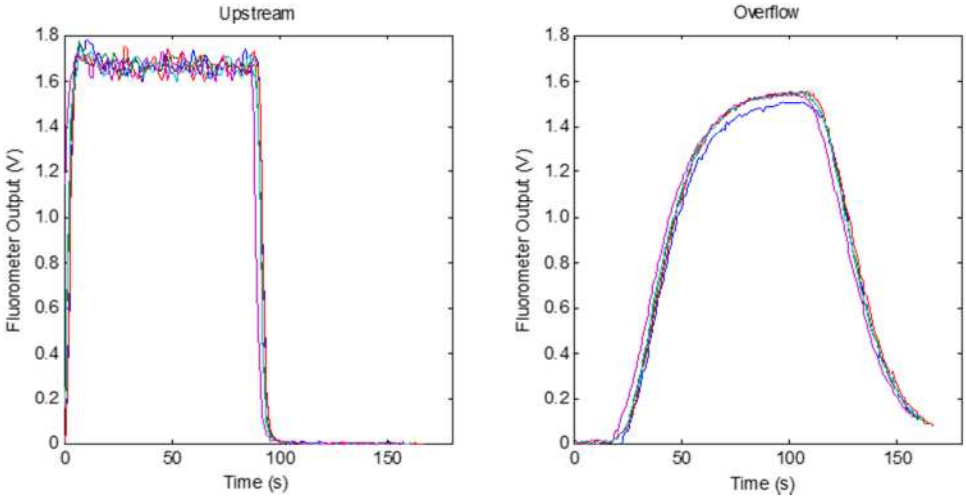

(a) Upstream to Overflow at 0.71 l/s for 1 Exit

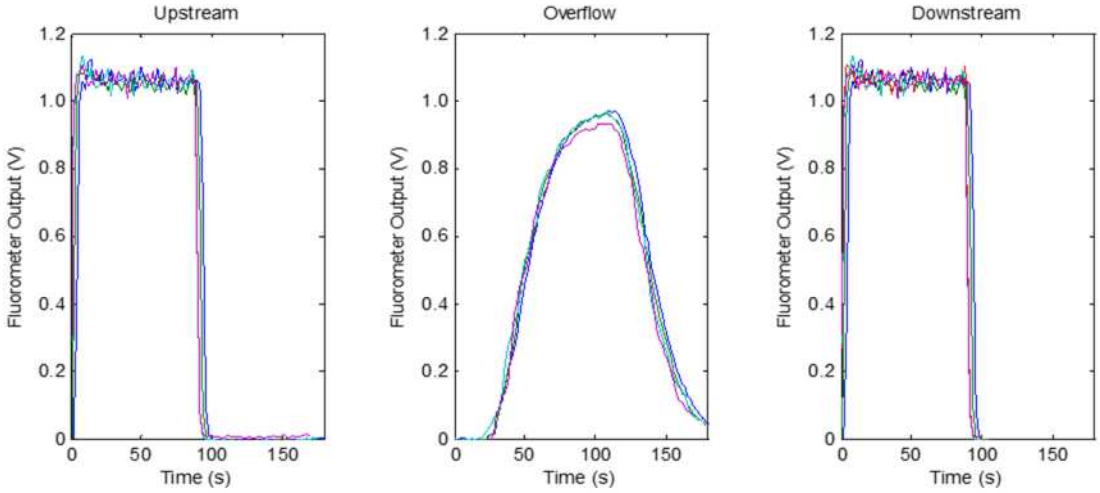

(b) Upstream to Overflow at 1.17 l/s for 2 Exits

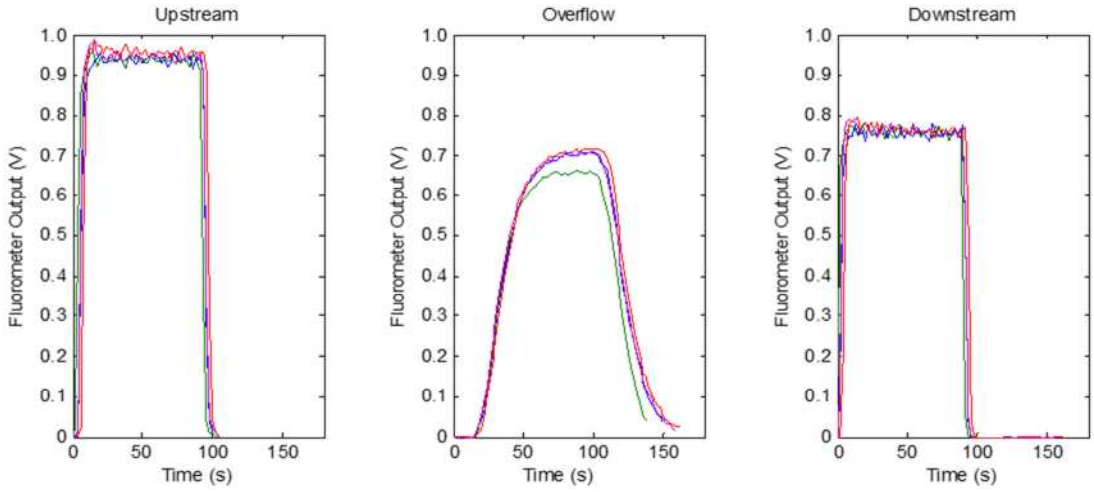

(c) Upstream to Downstream at 1.64 l/s for 2 Exits

Figure 5.30: Sample overflow concentration Profile for small manhole

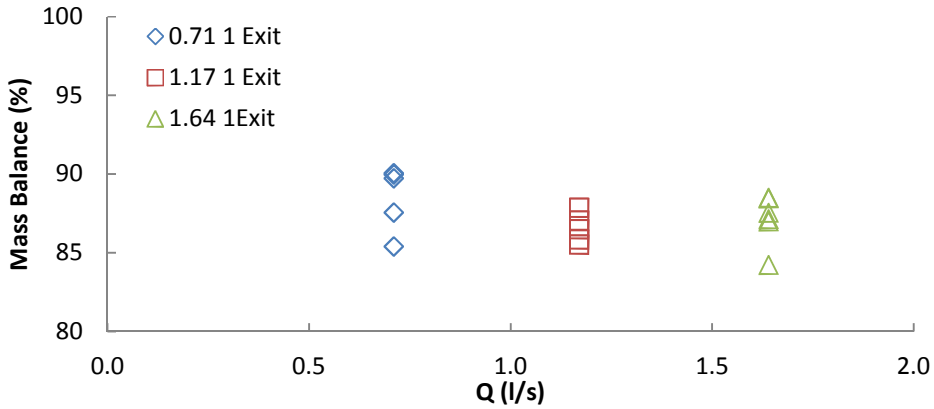

a) Total mass balance for one exits scenario

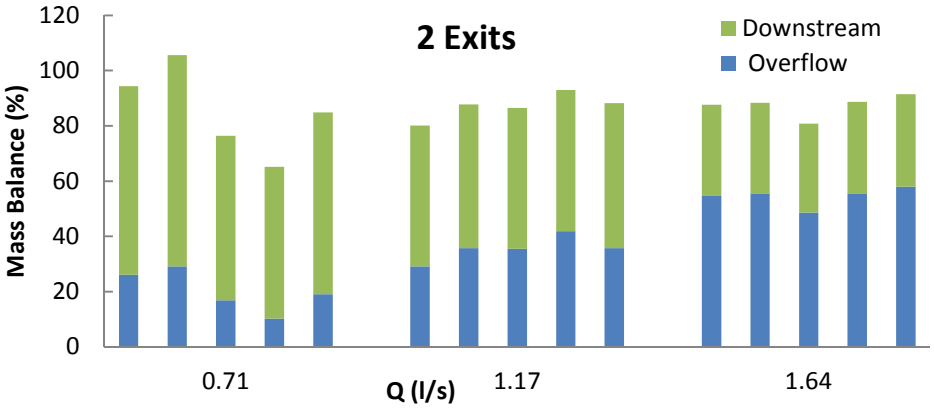

b) Mass balance split in two exit scenario

Figure 5.31: Mass balance values for overflow in large manhole

5.2.2.2 Mass Balance

Figure 5.31 shows the total mass balance values of the overflow measurement for both the one and two exits flow scenarios for the large manhole and Fig. 5.32 for the small manhole. It is observed that the higher values were obtained at higher flow rates with less deviation among the five repeats especially for one exit data. The distribution of the tracer recovered at the overflow and downstream end of the two exit flow is shown in Fig. 5.31(b). The higher the flow rate, the higher the flow split towards the overflow, bearing with it more of

the tracer. Figure 5.31, shows discrepancy between the five repeats at 0.71 l/s, this can be as a result of the low flux towards the overflow at this flow rate.

The small manhole however showed a more consistent mass recovery in both directions for the two exit flow (Fig. 5.32b). The overflow concentration mass increasing as flow rate increases. Comparing both sizes of manhole, the average overflow mass recovery for each flow rate are repeatable but a significant difference exists between the downstream mass recoveries. This is due to the length of the pipe has more dye passes straight downstream in the small manhole than the large manhole.

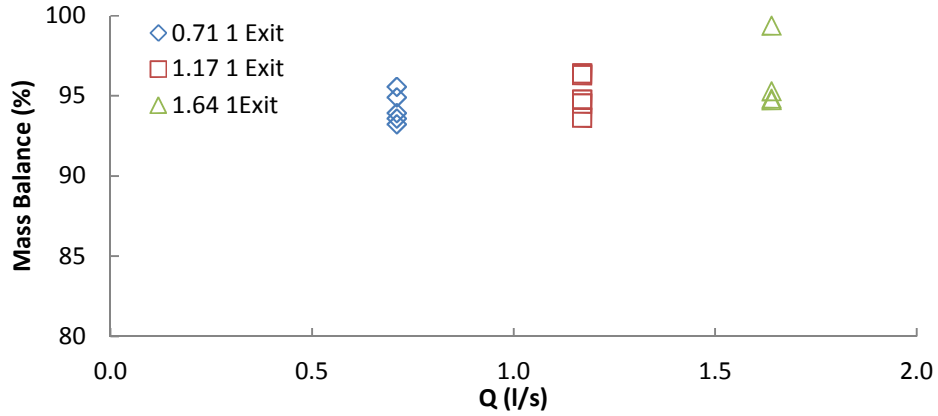

a) Total mass balance for one and two exits scenario

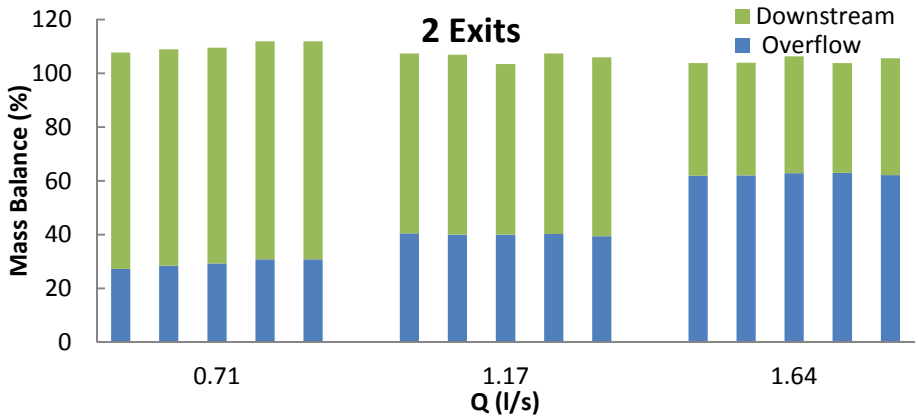

b) Mass balance split in two exit scenario

Figure 5.32: Mass balance values for overflow in small manhole

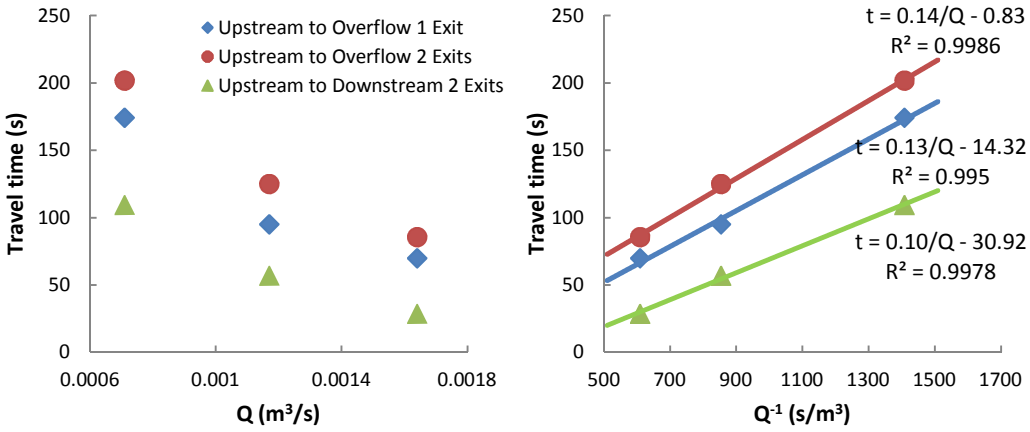

(a) Travel time values for overflow in large manhole

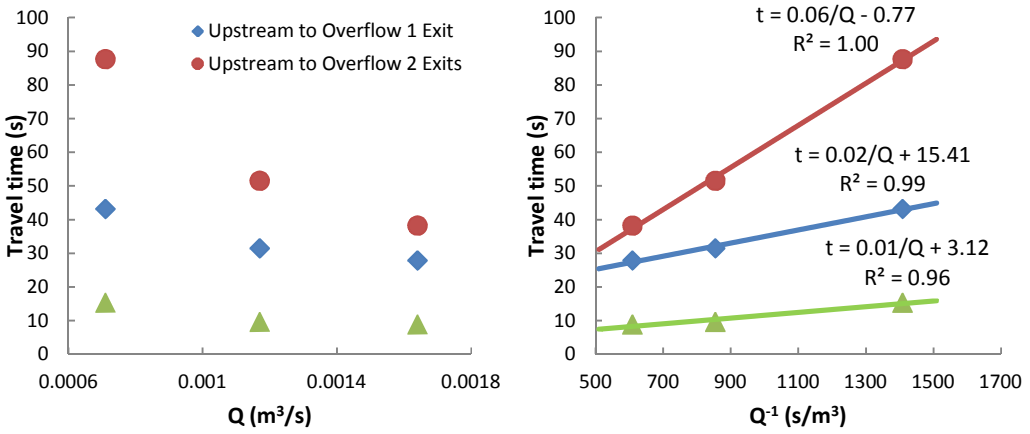

(b) Travel time values for overflow in small manhole

Figure 5.33: Travel time values for overflow in large and small manholes

5.2.2.3 Travel Time

The travel time for both manholes is shown in Fig. 5.33. The travel time decreased with flow rate. When the flow is split, the tracer takes more time before reaching the overflow which is as a result of the reduced flux in that direction. For both manholes however, a similar sequence of the one exit flow having the highest travel time and the two exits flow having the lowest travel time was evident.

5.2.3 Deconvolution

5.2.3.1 Overflow and Downstream Concentration Profile Predictions

Downstream responses for the measured laboratory data were evaluated using the deconvolution tool by Sonnenwald et al. (2015) to derive RTDs and CRTDs from the observed laboratory temporal concentration profile. The predicted laboratory trace was compared to the measured downstream using R_t^2 (Young et al., 1980). The values of R_t^2 obtained are shown in Table 5.7 while the best and worst predictions are shown in Fig. 5.34 and Fig. 5.35 for the large and small manhole respectively. The best prediction was 0.9996 at 1.64 l/s for the large manhole 1 Exit scenario, while the worst was 0.9944 at 1.64 l/s for the 2 Exit scenario. For the small manhole, the best prediction occurred at 0.71 l/s 1 Exit with a goodness of fit value of 0.999 while the worst prediction was at 1.17 l/s with a value of 0.9052. The latter seems to be as a result of poor raw data collection. Overall, the deconvolution tool was able to adequately predict both the overflow and downstream concentration profile.

Table 5.7: Goodness of fit of overflow predictions

Large Manhole	**1 Exit**			**2 Exits**		
Q(l/s)	**0.71**	**1.17**	**1.64**	**0.71**	**1.17**	**1.64**
Trial 1	0.9992	0.9995	0.9965	0.9709	0.9981	0.9993
Trial 2	0.9993	0.9995	0.9992	0.9976	0.9993	0.9944
Trial 3	0.9993	0.9995	0.9996	0.9976	0.9994	0.9984
Trial 4	0.9991	0.9992	0.9996	0.9903	0.9634	0.9993
Trial 5	0.9988	0.8077	0.9965	0.9903	0.9993	0.9993
Average	0.9991	0.9611	0.9983	0.8693	0.9919	0.9981
Small Manhole	**1 Exit**			**2 Exits**		
Q(l/s)	**0.71**	**1.17**	**1.64**	**0.71**	**1.17**	**1.64**
Trial 1	0.9996	0.9998	0.9996	0.9988	0.9998	0.9998
Trial 2	0.9934	0.9998	0.9997	0.9995	0.9994	0.9988
Trial 3	0.9985	0.9998	0.9993	0.9952	0.9052	0.9997
Trial 4	0.9999	0.9997	0.9997	0.9618	0.9959	0.9995
Trial 5	0.9943	0.9998	0.9996	0.9265	0.9976	0.9314
Average	0.9971	0.9998	0.9996	0.9764	0.9796	0.9858

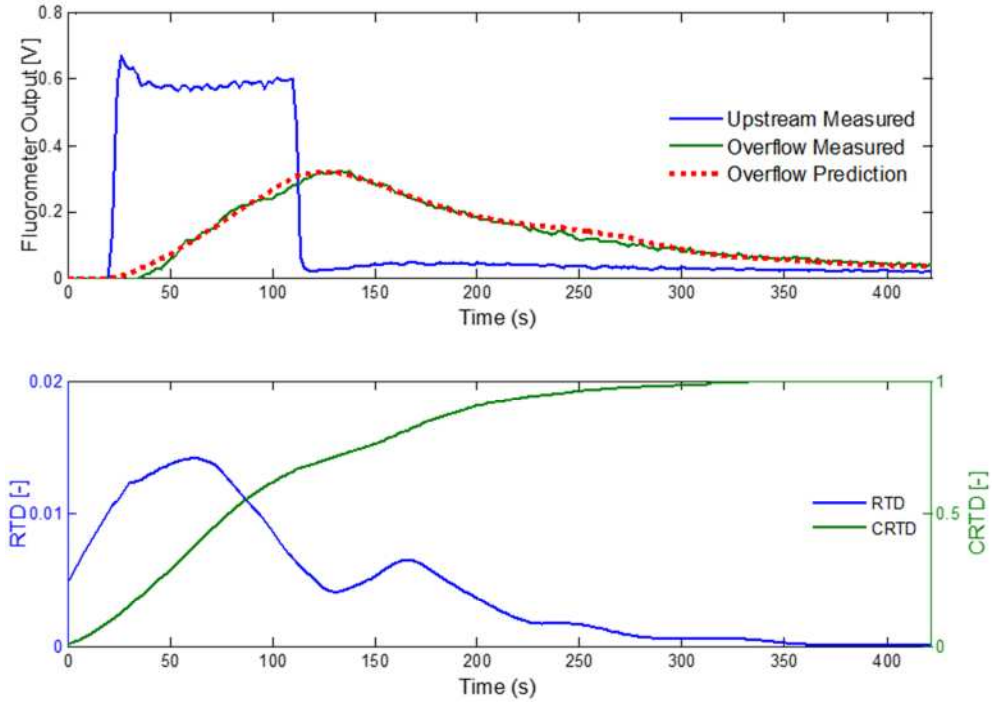

(a) Worst Prediction at 1.64 l/s 1 Exit, R_t^2 =0.9944

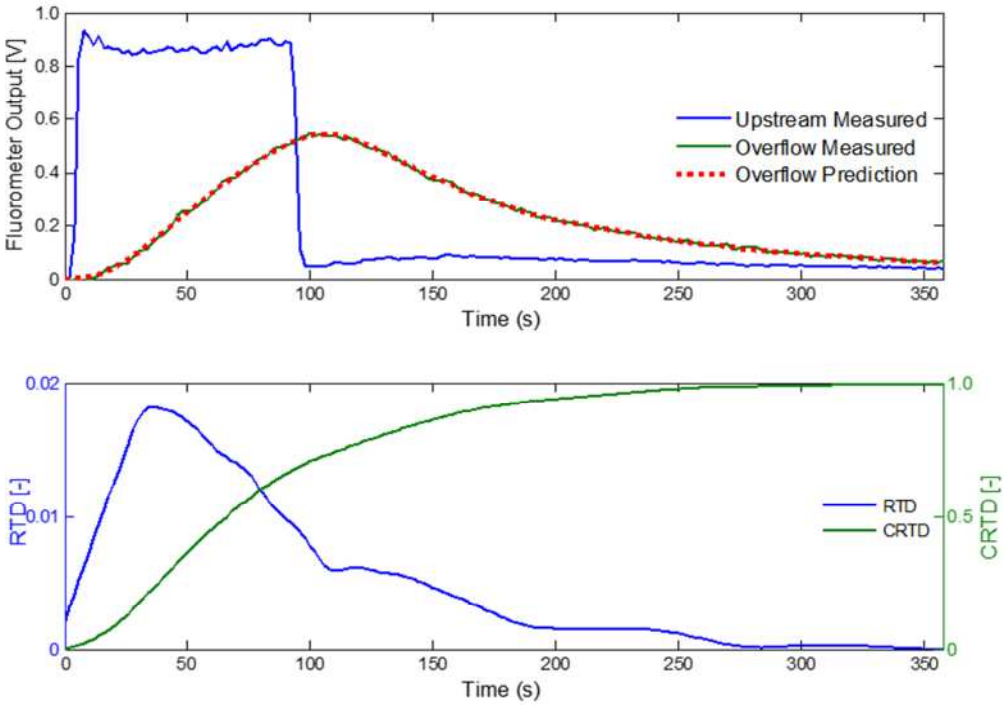

(b) Best prediction at 1.64 l/s 1 Exit, R_t^2 = 0.9996

Figure 5.34: Sample predictions from large manhole overflow

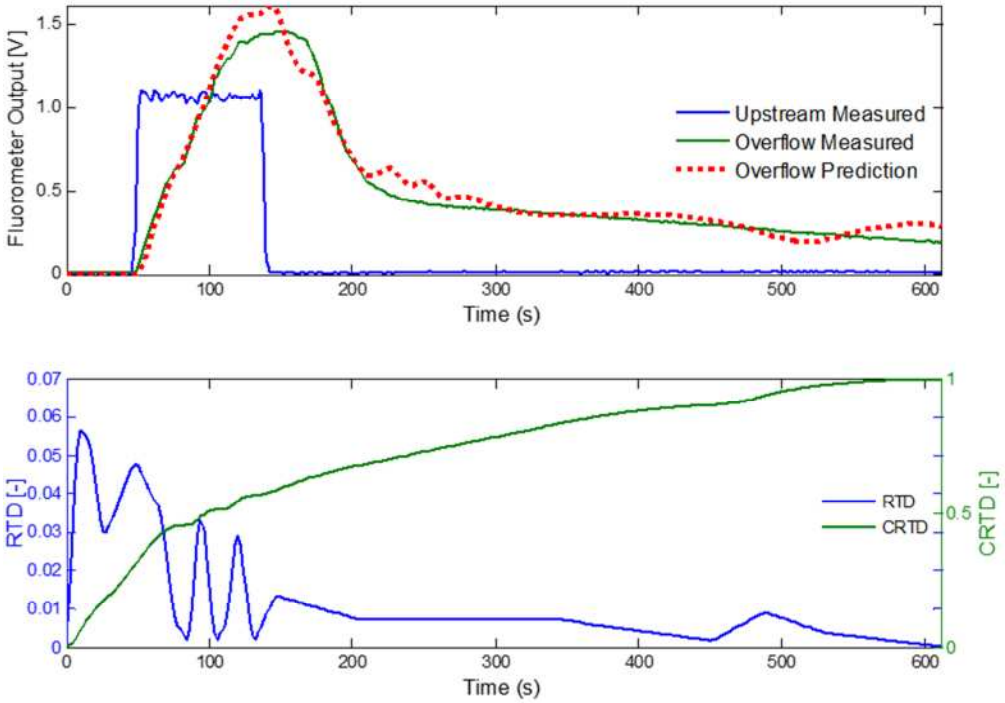

(a) Worst Prediction at 1.17 l/s 2 Exits, $R_t^2 = 0.9052$

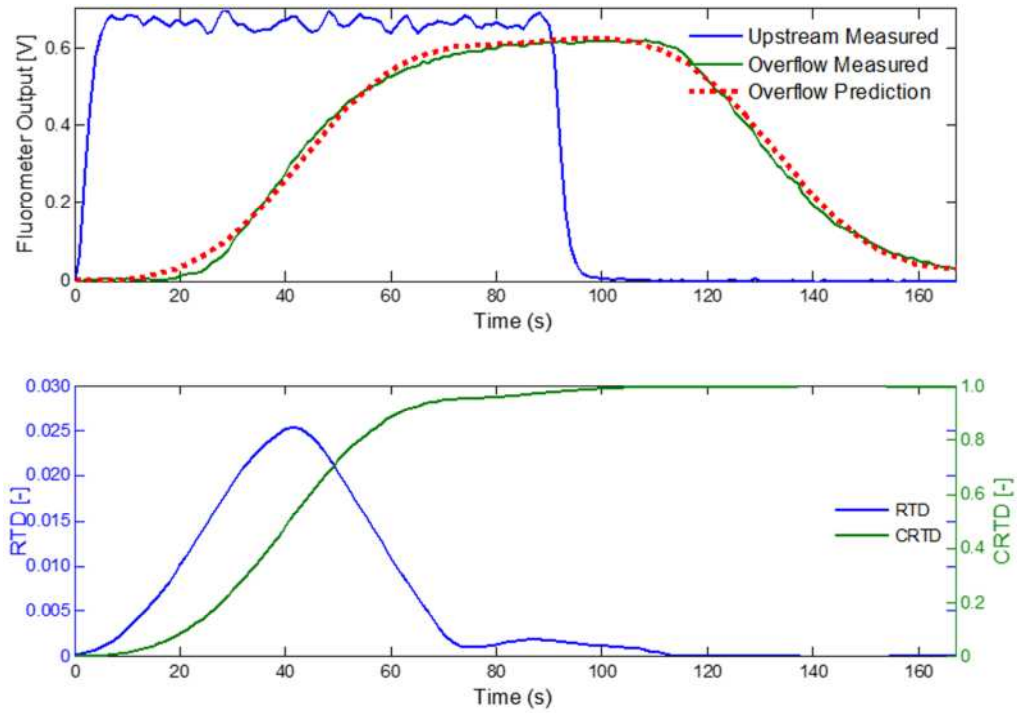

(b) Best prediction at 0.71 l/s 1Exit, $R_t^2 = 0.999$

Figure 5.35: Sample predictions from small manhole overflow

5.2.3.2 Cumulative Residence Time Distribution

Five repeats of each experiment were carried out for both manholes resulting in a total of 60 experiments. Sample plots for each scenario showing the Residence Time Distributions (RTD) and its corresponding Cumulative Residence Time Distributions (CRTD) at 1.17 l/s for large and small manhole is shown in Fig. 5.36 and Fig. 5.37 respectively. The Figures shows the repeatability of the process. Shape of overflow CRTD in both one exit (Fig. 5.36a) and two exit (Fig. 5.36b) experiment is similar to pre threshold CRTD observed in previous studies and is characterised by good mixing while the shape of the CRTD in the outlet pipe for two exit flow as shown in Fig. 5.36(c) is similar to post threshold CRTD in surcharged manhole characterised by straight through flow. A similar flow pattern was recorded, as described in Section 5.1.5 of this study for post threshold manholes. Here, the curves rise steeply initially before changing slope giving an indication that short-circuiting occurs. It is observed that for the two scenarios while considering the three flow rates, the shape of the upstream profile, downstream profile and CRTD are similar, suggesting that the mixing characteristics in an overflowing manhole has more dependence on the shape and size of the manhole than the flow rate (Fig. 5.36).

The time was normalised by multiplying the actual time by the flow rate and dividing it by the volume of water between the measuring points. For each five repeats, mean CRTDs were generated by averaging all the individual CRTDs at the actual and normalised time for a specific configuration. Figure 5.38 and 5.39 show the mean CRTDs for both one exit and two exit overflows for all three flow

rates. It was observed that the CRTDs produced smooth curves. At Normalised time, the individual curves collapse onto a similar curve that can be used to describe the mixing process occurring during the flow.

For the large manhole, the shape of overflow CRTD in both one exit and two exit experiment is indicative of a completely mixed flow which has been observed in fundamental mixing regimes after Danckwerts (1953), Fig. 2.7. However, for the same manhole, at 0.71 l/s 2 Exits flow, the CRTD shape is indicative of dead water. After the split in the flow between the downstream and the overflow at this flow rate, there is low flux towards the overflow. On the other hand, for the small manhole overflow at normalised time, all CRTDs collapsed into an individual curve. The shape of the CRTDs shows a “piston flow” with some longitudinal mixing occurring equivalent to pipe flow.

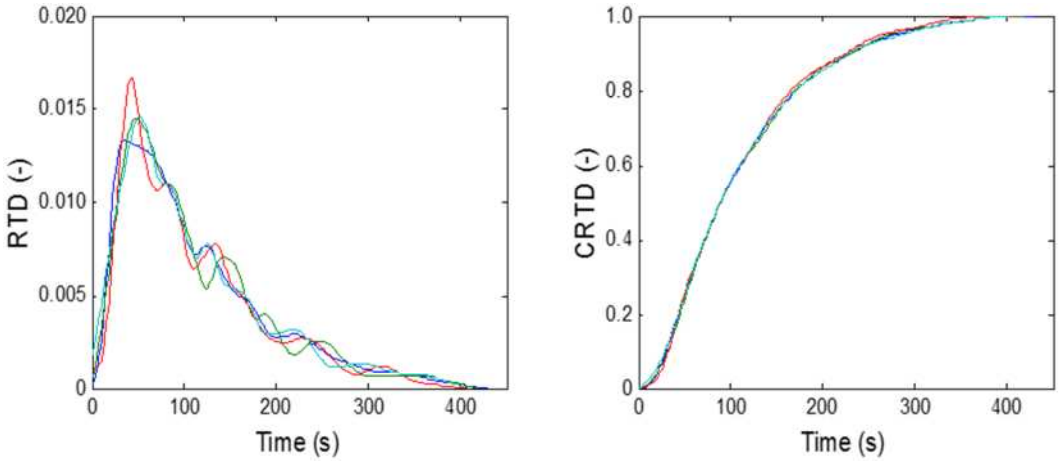

(a) 1 Exit overflow

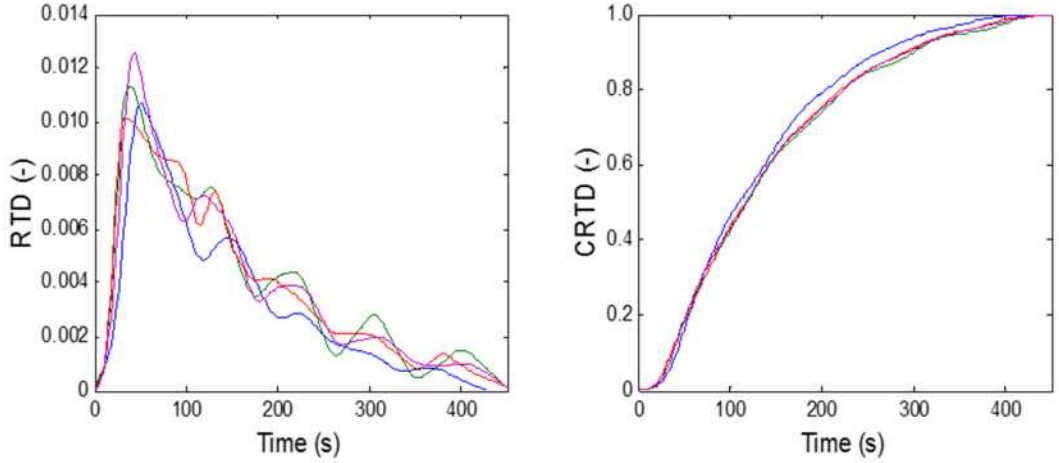

(b) 2 Exit Overflow

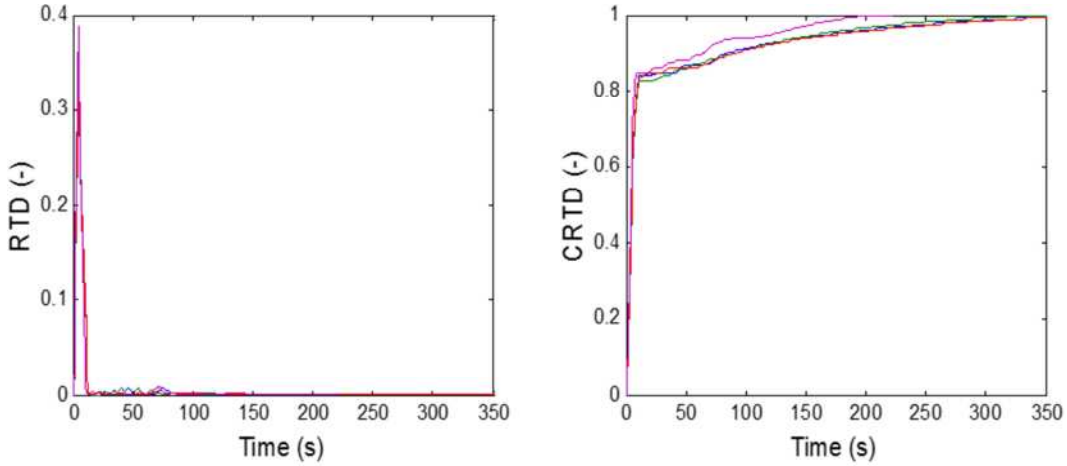

(c) 2 Exit downstream

Figure 5.36: Repeat RTD and CRTD large manhole overflow, Q =1.17 l/s

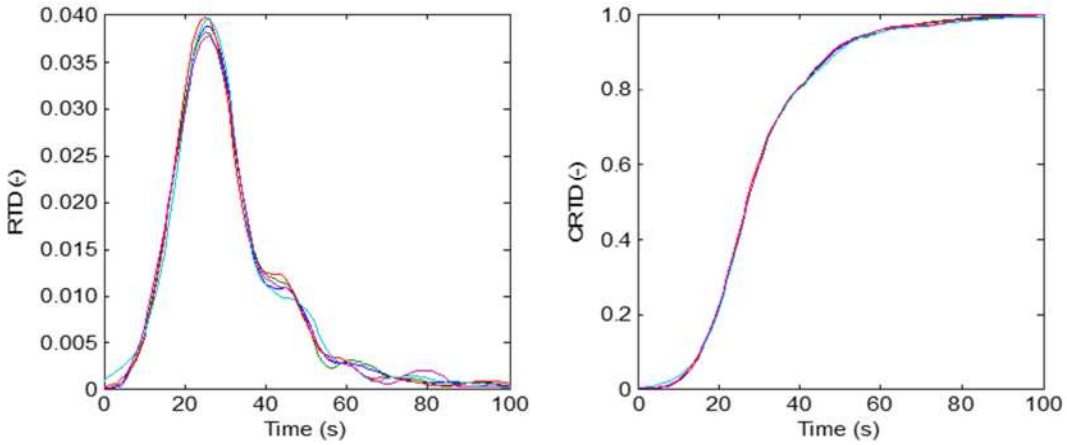

(a) 1 Exit overflow

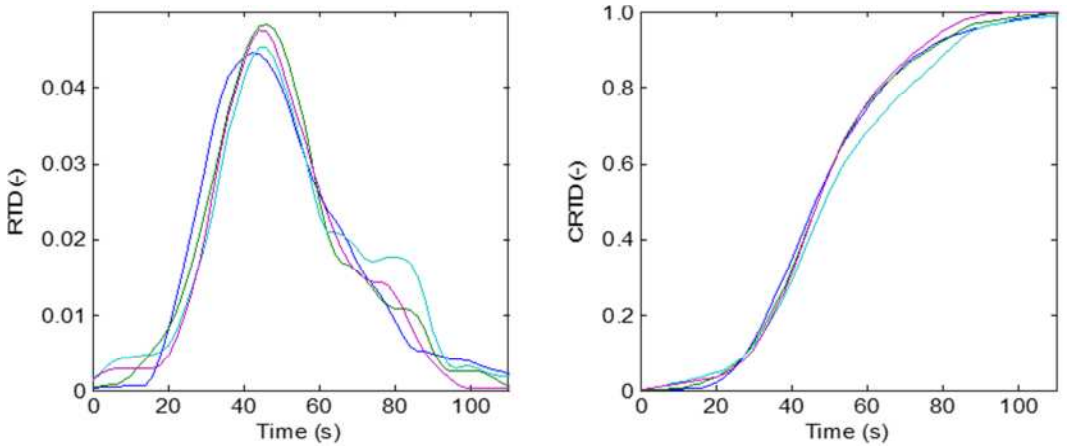

(b) 2 Exit overflow

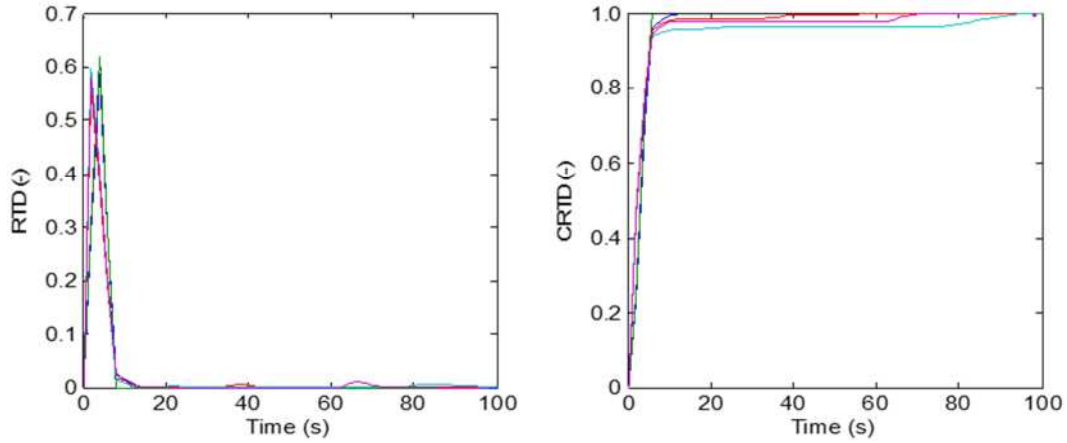

(c) 2 Exit downstream

Figure 5.37: Repeat RTD and CRTD small manhole overflow, Q = 1.17 l/s

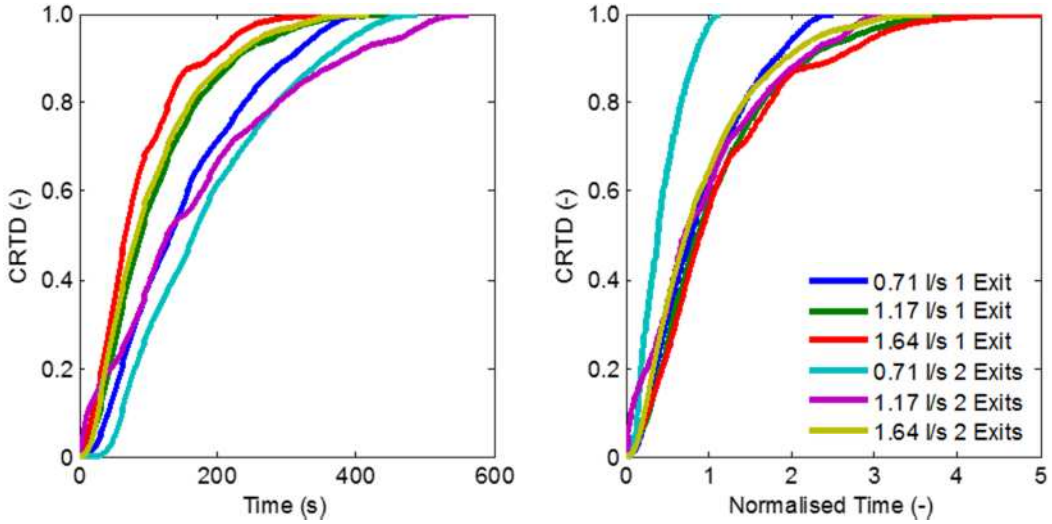

Figure 5.38: Compilation of average curves for overflow large manhole

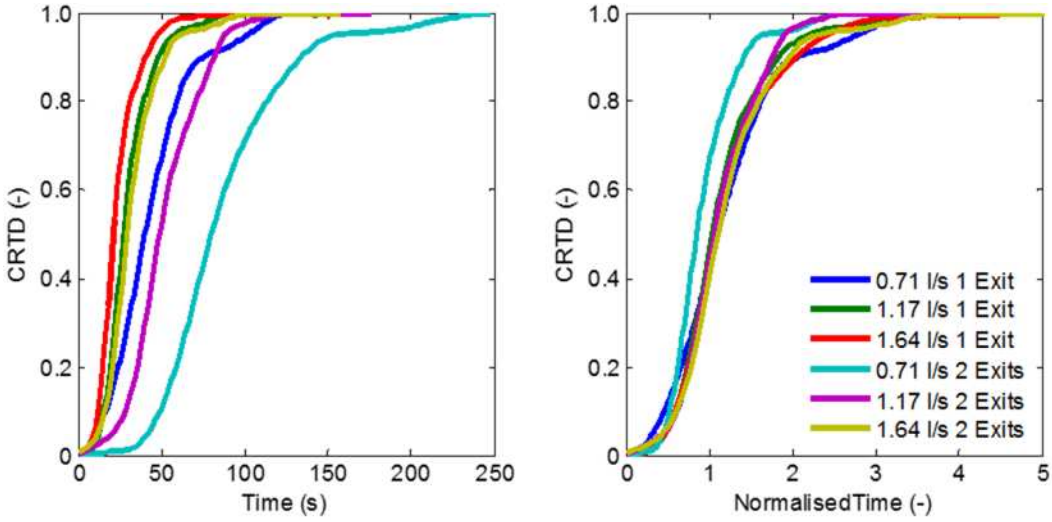

Figure 5.39: Compilation of average curves for overflow small manhole

Table 5.8: T_{50} Travel time for overflow manhole

	Large Manhole				Small Manhole			
Q x 10^{-3} (m^3/s)	1 Exit		2 Exits		1 Exit		2 Exits	
	t_{50} (s)	t_{50n} (-)	t_{50} (s)	t_{50n} (-)	t_{50} (s)	t_{50n} (-)	t_{50} (s)	t_{50n} (-)
0.71	134	0.8	166	0.4	40	1.1	80	0.8
1.17	116	1.1	128	0.7	28	1.1	50	1.1
1.64	68	0.9	84	0.7	22	1.1	30	1.1

5.2.3.3 Travel Time

The t_{50} travel time of the overflow data decreased as flow rates increased for both the 1Exit and the 2 Exit scenario although the values were higher for the latter (Table 5.8). For the large manhole overflow, at normalised time, the t_{50} values for the 1 Exit scenario ranged between 0.95 ± 0.16 while for the two exit scenario, the same value was obtained for 1.17 l/s and 1.64 l/s.

The small manhole on the other hand had the same normalised t_{50} value of 1.1 across both scenarios except for 0.71 l/s. This further reinforces the suggestion that the overflow within the small manhole is similar to the flow within a pipe, since there is very little difference in the volume of water within the measuring volume as the flow rate increased. The lower value of the normalised t_{50} travel time for 0.71 l/s at the 2 Exits scenario for both large and small manhole overflow can be attributed to the low flux occurring towards the overflow exit.

5.2.3.4 Modelling of Overflow CRTD

Guymer and Stovin (2011), proposed a model of two dimensionless CRTDs, one for pre-threshold and the other for post-threshold surcharge depths to demonstrate the solute transport characteristics of a surcharged manhole with straight-through inflow and outlet pipes over a range of flow rates and surcharge depths. A superposition of the proposed model on the results from the large manhole of this study is shown in Fig. 5.40a. It is observed that for both scenarios and three flow rates each, the overflow CRTD was comparable to the 1D model for pre threshold mixing suggested by (Guymer and Stovin

(2011)). The overflow result agrees with the pre-threshold model although there is a deviation between the 0 and 70th percentile. The slight deviation around the model could be as a result of a difference in shape since the model was based on a circular manhole, more research is needed to verify this. An alternative Continuous Stirred Tank Reactor (CSTR) model was introduced (Bennett, 2012). This model fitted better with the CRTDs from the large manhole as shown in Fig. 5.40b, confirming that the flow from the overflow was fully mixed. It can be obtained using

$$MF = 1 - e^{-t/(V|Q)}$$

Where MF = mass fraction (-), t = time(s), v = volume (m^3) and Q = flow rate (m^3/s)

For the small manhole, CRTDs were produced using the CSTR and Taylor's dispersion model (eqn. 2.14) as shown in Fig. 5.40b. It was observed that the CSTR model does not fit the data however the Taylor's dispersion model slightly fits the CRTDs obtained by the deconvolution method. The difference between the Taylor's dispersion model profile and the CRTDs may be as a result of the expansion in diameter from the pipe to the length of the manhole, $Ø_p : L_m = 1:3$. The CRTDs summed up to 1 at normalised time, $t_n = 4.0$, which is approximately 3 times the time taken by the Taylors dispersion model at $t_n = 1.37$.

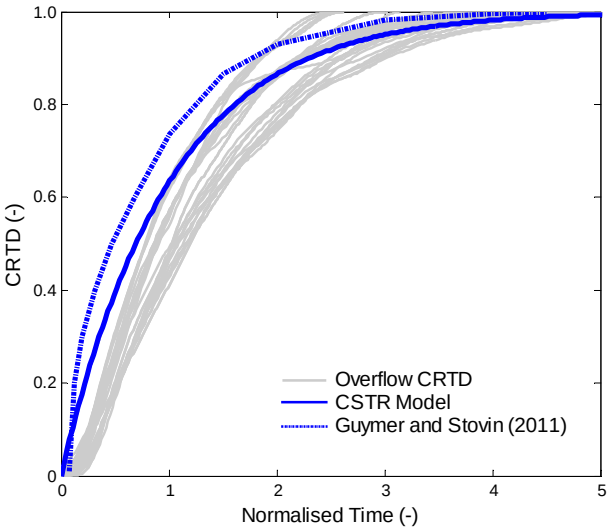

(a) Large manhole overflow CRTDs with CSRT and pre threshold model

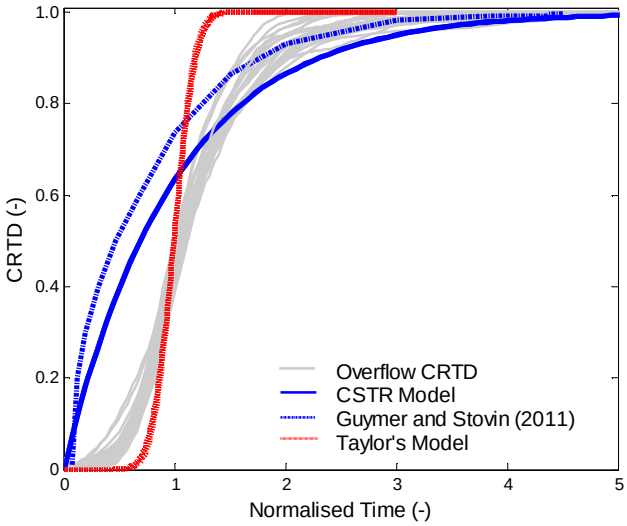

(b) Small manhole overflow CRTDs with existing models

Figure 5.40: Modelling of overflow data

5.3 Summary

The manhole laboratory study was divided into two parts to investigate the mixing and hydraulic properties of (i) a surcharged square manhole and (ii) an

overflowing square manhole. For the two parts, a comparison in size of manhole between a large and small manhole was carried out.

Both the large and small surcharged manhole had hydraulic behaviours similar to those observed in surcharged circular manholes. For the large manhole, the energy loss coefficient increased as surcharge increased until $s/L_m = 0.2$. An almost constant value was obtained afterwards as surcharge increased. The same pattern was noticed for the measured travel time as well as the normalised travel time. CRTDs were obtained by method of deconvolution and this suggests that at low surcharge depths mixing was more prevalent while at high surcharge depths, short-circuiting was more prevalent. For the surcharged small manhole the same hydraulic pattern occurred across the range of surcharge investigated.

There was evidence of a threshold level where a difference in flow and mixing patterns between low and high surcharge depths occurs, in the large manhole at $s/L_m = 0.24$, whereas none was evident in the small manhole.

Overflow studies in the large manhole showed that complete mixing occurred. For this experiment, the peak concentration at the overflow was however attenuated to about 30% of the upstream peak concentration. The CSRT model was able to predict the mixing properties of the overflow. A different property was however observed in the small overflow manhole. CRTDs suggest a piston flow occurring between the upstream and the overflow. There was less attenuation of the peak concentration and little mixing occurring.

6 Conclusions and Future Work

6.1 Conclusions

The aim of this study is to describe the transportation and mixing of solute pollutants through urban drainage systems and the effects of structures such as a square manhole. Flow through a pipe with and without orifice plate insertion was considered. This was to investigate the effect of the orifice plate on hydraulic properties such as headloss and dispersion coefficient while seeking to establish a relationship between the two properties. The change in area effect caused by the presence of the orifice plate has similarities to studies in a manhole which similarly creates a change in area e.g. drop in hydraulic grade line.

Studies were carried out on two square manholes referred to as large (388 mm x 388 mm x 700 mm) and small (150 mm x 150 mm x 700 mm). The hydraulic field and behaviour of the flow through surcharged square manholes were studied and compared in terms of surcharge level, manhole size as well as in comparison to circular manhole. Overflow conditions were also considered in both manholes. Here the change in concentration, flow pattern and effect of change in size was considered.

The study was carried with different flow rates under steady conditions. A summary of the conclusions from this study is listed below.

Pipe Study

1) The experimental results were a good representation of theoretical predictions for dispersion coefficient and headloss for both 'no orifice' and 'orifice inserted' flow.
2) The presence of the orifice plate (35 mm Ø and 25 mm Ø) resulted in an increase in dispersion coefficient as well as headloss.
3) However, the mean travel time along the length of pipe was not affected by the presence of the orifice plate (Diameter: Length = 1:88.6).
4) It was established that the relationship between dispersion coefficient and headloss across the length of a pipe with or without an orifice plate is directly related and can be obtained from the equation 4.11 which included the introduction of a new parameter.
5) A relationship between the additional dispersion coefficient and the additional headloss due to the orifice plate was established.

Manhole Study

1) For a large surcharged manhole, there is an initial increase in the energy loss coefficient as surcharge increases, for $s/L_m < 0.258$ ($s/D_p < 2$), after $s/L_m > 0.258$ ($s/D_p > 2$) a significant drop in the energy loss coefficient occurs with the values becoming almost constant across all flow rates considered. This was however different from the energy loss coefficient from the small surcharged manhole which had an almost linear trend.

The same pattern of energy loss coefficient increase and subsequent decrease with almost constant values were also observed for circular manholes by, Lau (2007), Arao et al. (2011), and Jones (2011).

2) The results from this present study show that for a square manhole, the headloss coefficient can be predicted theoretically and falls within the ranges proposed by other authors.
3) The flow field within a large surcharged manhole is different from that observed within a small surcharged manhole as surcharge increases. The jet within the latter is centralised and goes straight through the manhole, while for the former this only occurs at high surcharge. Low surcharge flow field in the large manhole was characterised by mixing when the flow deviates from the central core as swirls in either direction.
4) RTDs, and subsequently CRTDs, were produced by using a deconvolution technique. Downstream predictions from the method of deconvolution of the measured data produced excellent goodness of fit. At normalised time the CRTDs across the manhole separate into two distinct groups while some of the CRTDs remained in between. The CRTDs lying between behaves partly like both classifications of low and high surcharges with a greater leaning towards the high surcharge CRTDs.
5) At normalised time, the t_{50} values from the large manhole began to close up across flow rate between a surcharge ratio of 0.24 and 0.40, after which the same value was recorded irrespective of flow rate. The change in values noticed from the headloss, mass balance, travel time and the

CRTDs suggests there exists a threshold level in large square manholes (i.e. $L_m/D_p = 7.76$) and that this threshold level occurs at $0.24L_m$.

6) A different mechanism however occurs within the small manhole. The CRTDs both at actual and normalised time do not exhibit a significant change in shape as surcharge increased. T_{50} travel times across the small manhole were almost constant with each flow rate as surcharge increased, although they reduced slightly with increase in flow rate. In line with previous research, no threshold exists in a small manholes and this was confirmed for the square manhole.
7) Measured overflow data profile shows that the peak tracer concentration in comparison to the upstream peak concentration has been attenuated as it travels between the two measuring points. Overflow peak concentration for the large manhole studied ranged between 30%-60% of the inflow peak concentration, increasing as flow rate increases. On the other hand, the small manhole had little attenuation occurring to its peak concentration. For the two exit experiment, the concentration split corresponded to the flow split between the two exits.
8) The shape of overflow CRTD in the large manhole in both one exit and two exit experiment is similar to pre threshold CRTD observed in surcharged manhole while the shape of the CRTD in the outlet pipe for two exit flow is similar to post threshold CRTD in surcharged manholes. For the large manhole, the shape of overflow CRTD in both one exit and two exit experiment is indicative of a completely mixed flow, while that

of the small manhole suggests a piston flow with some longitudinal mixing occurring.

9) An attempt was made to model the CRTDs obtained from this study. A time based model was fitted to the CRTDs from the surcharged large manhole while a CSTR model as well as the 1D model proposed by Guymer and Stovin (2011) was fitted to the overflow large manhole CRTD. The surcharged and Overflow CRTD for the small manhole does not fit previous predictions for manholes but could be modelled using Taylor's dispersion equation.

6.2 Future Work

The following are recommendations for future studies;

1. Develop an analytical method to verify relationship between dispersion coefficient and headloss.
2. Study of flow characteristics and trends due to time varying flows in square Manholes.
3. CFD studies of flow within square manholes in comparison with this laboratory study.
4. Investigating overflow studies at different manhole heights to establish the effect of manhole height on mixing properties of overflows.
5. Investigating headloss changes as overflows occurs in manholes.

References

Albertson, M. L., Dai, Y. B., Jensen, R. A. & Rouse, H. 1950. Diffusion of Submerged Jets. *Trans. Am. Soc. Civ. Eng.,* 136(5)**,** 639-664.

Allen, C. M. & Taylor, E. A. 1923. *The Salt Velocity Method of Water Measurement,* New York, N.Y.: American Society of Mechanical Engineers.

Anderson, S. T., Erichsen, A. C., Mark, O. & Albrechtsen, H. J. 2013. Effects of a 20 Year Rain Event: A Quantitative Microbial Risk Assessment of a Case of Contaminated Bathing Water in Copenhagen, Denmark. *Journal of Water and Health,* 11.

Arao, S. & Kusuda, T. 1999. Effects of Pipe Bending Angle on Energy Losses at Two-Way Circular Drop Manholes. . *8th International Conference On Urban Storm Drainage.* Sydney. Australia.

Arao, S. & Kusuda, T. 2005. Head Loss at Three-Way Circular Drop Manhole and Its Reduction by Improvement in Base Shape. *10th International Conference on Urban Drainage.* Copenhagen/Denmark.

Arao, S., Kusuda, T., Moriyama, K. & Hiratsuka, S. 2011. Energy Loss at Three-Way Circular Drop Manhole under Surcharge Flow. *12th International Conference on Urban Drainage.* Porto Alegre/Brazil.

Archer, B., Bettess, F. & Colyer, P. J. 1978. *Head Losses and Air Entrainment at Surcharged Manholes*: Hydraulics Research Station (Great Britain).

Bean, H. S. 1983. *Fluid Meters : Their Theory and Application Report,* New York: American Society of Mechanical, Engineers Research Committee on Fluid, Meters.

Beer, T. & Young, P. C. 1983. Longitudinal Dispersion in Natural Streams. *J. Environ. Eng. Journal of Environmental Engineering,* 109**,** 1049-1067.

Bennett, P. 2012. *Evaluation of the Solute Transport Characteristics of Surcharged Manholes Using a Rans Solution.* PhD, The University of Sheffield.

Butler, D. & Davis, J. W. 2011. *Urban Drainage,* London [u.a.]: Spon.

Canadian Concrete Pipe Association 2013. *Advantages of Round Manholes over Square and Rectangular Shapes,* www.ccpa.org.

Clean Waterways Program of Frankfort & Franklin County Kentucky 2008. *Sanitary Sewer Overflows*: http://cwffc.org/SanitarySewerOverflows.aspx.

Danckwerts, P. V. 1953. Continuous Flow Systems. *Chemical Engineering Science Chemical Engineering Science,* 2**,** 1-13.

Daniel Measurement and Control Inc 2010. *Fundamentals of Orifice Meter Measurement,* USA: Emerson process Management,.

Dennis, P. M. 2000. Longitudinal Dispersion Due to Surcharged Manholes. *PhD thesis, The University of Sheffield, Sheffield, U.K.*

Falkovich, G. 2011. *Fluid Mechanics a Short Course for Physicists* [Online]. Cambridge; New York: Cambridge University Press. Available: http://www.knovel.com/knovel2/Toc.jsp?BookID=4413.

Fischer, H. B. 1966. *A Note on the One-Dimensional Dispersion Model,* Pasadena, Calif.: W.M. Keck Laboratory of Hydraulics and Water Resources, California Institute of Technology.

Florida Department of Transportation, O. O. D., Drainage Section 2000. Drainage Handbook : Storm Drains.

Gan, G. & Riffat, S. B. 1997. Pressure Loss Characteristics of Orifice and Perforated Plates. *Experimental Thermal and Fluid Science,* 14**,** 160-165.

Guymer, I., Dennis, P., O'brien, R. & Saiyudthong, C. 2005. Diameter and Surcharge Effects on Solute Transport across Surcharged Manholes. *Journal Of Hydraulic Engineering.,* 131**,** 312-321.

Guymer, I. & O'brien, R. 1995. The Effects of Surcharged Manholes on the Travel Time and Dispersion of Solutes in Sewer Systems. *Water science and technology : a journal of the International Association on Water Pollution Research.,* 31**,** 51-59.

Guymer, I. & O'brien, R. 2000. Longitudinal Dispersion Due to Surcharged Manhole. *Journal Of Hydraulic Engineering.,* 126**,** 137.

Guymer, I., Shepherd, W., Dearing, M., Dutton, R. & Saul, A. 2002. Solute Retention in Storage Tanks. *Global Solutions for Urban Drainage.* American Society of Civil Engineers.

Guymer, I. & Stovin, V. R. 2011. One-Dimensional Mixing Model for Surcharged Manholes. *Journal of Hydraulic Engineering,* 137**,** 1160-1172.

Hart, J. R. 2013. *Longitudinal Dispersion in Steady and Unsteady Pipe Flow.* PhD thesis, University of Warwick, U.K.

Hassan, M. N. 1993. Longitudinal Dispersion of Pollutants in Natural Streams - the Aggregated Dead-Zone Approach. *Pertanika J. Sci. & Technol. 1(2): 225-238 (1993)*.

Hobbs, J. M. & Humphreys, J. S. 1990. The Effect of Orifice Plate Geometry Upon Discharge Coefficient. *Journal of Flow Measurement and Instrumentation,* 1**,** 133-140.

Jianhua, W., Wanzheng, A. & Qi, Z. 2010. Head Loss Coefficient of Orifice Plate Energy Dissipator. *Journal of Hydraulic Research,* 48**,** 526-530.

Johnston, A. J. & Volker, R. E. 1990. Head Losses at Junction Boxes. *Journal of Hydraulic Engineering,* 116**,** 326-341.

Jones, A. 2011. *Solute Dispersion across Manholes under Time-Varying Flow Conditions.* PhD Thesis, University of Warwick,Coventry, U.K.

Kashefipour, S. & Falconer, R. 2000. An Improved Model for Predicting Sediment Fluxes in Estuarine Waters. *In Proceedings of the Fourth International Hydroinformatics Conference, Iowa, USA*.

Lau, S.-T. D. 2007. *Scaling Dispersion Processes in Surcharged Manholes.* PhD Thesis, University of Sheffield.

Lau, S., Stovin, V. & Guymer, I. 2008. Scaling the Solute Transport Characteristics of a Surcharged Manhole. *Urban Water Journal,* 5**,** 33-42.

Levenspiel, O. 1972. *Chemical Reaction Engineering,* New York: Wiley.

Madden, F. N., Godfrey, K. R., Chappell, M. J., Hovorka, R. & Bates, R. A. 1996. A Comparison of Six Deconvolution Techniques. *Journal of Pharmacokinetics and Biopharmaceutics Journal of Pharmacokinetics and Biopharmaceutics,* 24**,** 283-299.

Mark, O., Appelgren, C. & Kosir, M. 1996. Water Quality Modelling for the Ljubljana Master Plan. *8th International Conference on Urban Storm Drainage.* Sydney, Australia.

Marsalek, J. 1984. Head Losses at Sewer Juntion Manholes. *Journal of Hydraulic Engineering,* 110**,** 1150-1154.

Marsalek, J. & Greck, B. J. 1988. Head Losses at Manholes with a 90^0 Bend. *Canadian Journal of Civil Engineering,* 15**,** 851-858.

Mcgraw-Hill Concise Encyclopedia of Science & Technology 2005. Mcgraw-Hill Concise Encyclopedia of Science & Technology. *McGraw-Hill concise encyclopedia of science & technology.* New York: McGraw-Hill.

Nash, J. E. & Sutcliffe, J. V. 1970. River Flow Forecasting through Conceptual Models Part I - a Discussion of Principles. *Journal of Hydrology,* 10**,** 282–290.

New Civil Engineer 2010. *Invasion of the Square Manholes*: http://www.nce.co.uk/features/water/invasion-of-the-square-manholes/8606418.article.

O'brien, R. 2000. *Dispersion Due to Surcharged Manhole.* PhD Thesis, Universitry of Sheffield.

O'loughlin, G. & Stack, B. 2002. Algorithms for Pit Pressure Changes and Head Losses in Stormwater Drainage Systems. *Global Solutions for Urban Drainage.*

Pedersen, F. B. & Mark, O. 1990. Head Losses in Storm Sewer Manholes: Submerged Jet Theory. *Journal of Hydraulic Engineering,* 116**,** 1317-1328.

Pipeflow.Co.Uk. 2007. Laminar Flow and Turbulent Flow of Fluids. Available: http://www.pipeflow.co.uk/public/articles/Laminar And Turbulent Flow.pdf.

Rawlings, J. B. & Ekerdt, J. G. 2002. *Chemical Reactor Analysis and Design Fundamentals,* Madison, Wis.: Nob Hill Pub.

Reed, E. C. 1983. *Design and Analysis of Urban Storm Drainage: The Wallingford Procedure. Principles, Methods and Practice*: Hydraulics Research Limited, Howbery Park, Crowmarsh, Wallingford, Oxfordshire.

Reynolds, O. 1883. *An Experimental Investigation of the Circumstances Which Determine Whether the Motion of Water Shall Be Direct or Sinuous : And of the Law of Resistance in Parallel Channels,* [London]: [Royal Society of London].

Rutherford, J. C. 1994. *River Mixing,* Chichester [England]; New York: Wiley.

Saiyudthong, C. 2003. *Effect of Changes in Pipe Direction across Surcharged Manholes on Dispersion and Head Loss.* PhD Thesis, University of Sheffield, U.K.

Sangster, W. M. 1958. *Pressure Changes at Storm Drain Junctions,* Columbia, Mo.: Engineering Experiment Station, University of Missouri.

Smart, P. L. & Laidlaw, I. M. S. 1977. An Evaluation of Some Fluorescent Dyes for Water Tracing. *WRCR Water Resources Research,* 13**,** 15-33.

Som, S. K. & Biswas, G. 2008. *Introduction to Fluid Mechanics and Fluid Machines,* New Delhi: Tata McGraw-Hill.

Sonnenwald, F. 2014. *Identifying the Residence Time Distributions of Urban Drainage Structures from Solute Transport Data Using Maximum Entropy Deconvolution.* PhD Thesis, The University of Sheffield.

Sonnenwald, F., Stovin, V. & Guymer, I. 2015. Deconvolving Smooth Residence Time Distributions from Raw Solute Transport Data. *Journal of Hydrologic Engineering*.

Sonnenwald, F., V.R., S. & I.Guymer 2011. The Influence of Outlet Angle on Solute Transport in Surcharged Manholes. *Proceedings of the 12th International Conference on Urban Drainage.* Porto Alegre/Brazil.

Stefan, H. G. & Demetracopoulos, A. C. 1983. Cells-in-Series Simulation of Riverine Transport. *Journal of Hydraulic Engineering,* 109**,** 135-136.

Stovin, V., Bennett, P. & Guymer, I. 2013. Absence of a Hydraulic Threshold in Small-Diameter Surcharged Manholes. *Journal of Hydraulic Engineering,* 139**,** 984-994.

Stovin, V., Guymer, I. & Lau, S. T. D. 2010a. Dimensionless Method to Characterize the Mixing Effects of Surcharged Manholes. *Journal of Hydraulic Engineering ,New York,* 136**,** 318-327.

Stovin, V. R., Guymer, I., Chappell, M. J. & Hattersley, J. G. 2010b. The Use of Deconvolution Techniques to Identify the Fundamental Mixing Characteristics of Urban Drainage Structures. *Water science and technology : a journal of the International Association on Water Pollution Research,* 61**,** 2075-2081.

Taylor, G. 1953. Dispersion of Soluble Matter in Solvent Flowing Slowly through a Tube. *Proceedings of the Royal Society A: Mathematical, Physical and*

Engineering Sciences Proceedings of the Royal Society A: Mathematical, Physical and Engineering Sciences, 219**,** 186-203.

Taylor, G. 1954. The Dispersion of Matter in Turbulent Flow through a Pipe. *Proceedings of the Royal Society of London. Series A, Mathematical and Physical Sciences,* 223**,** 446-468.

The National Precast Concrete Association 2010. *Precast Concrete Manholes*: The National Precast Concrete Association.

Turner Designs 1994. *Application Note: Fluorescent Tracer Dyes,* 845 W. Maude Ave.,Sunnyvale, CA 94085.

Turner Designs 2007. *Cyclops-7 Submersible Sensors User Manual*: 845 W. Maude Ave.,Sunnyvale, CA 94085.

United States Environmental Protection Agency 2004. *Report to Congress on the Impacts and Control of Csos and Ssos*: U.S. Environmental Protection Agency, Washington, D.C.

Wallis, S. G., Beven, K. J. & Young, P. C. 1989. Experimental Investigation of the Aggregated Dead Zone Model. *ICE Proceedings,* 87**,** 1-22.

Watson-Marlow Bredel Pumps (N.D.) *Watson Marlow Pumps 505di*: Watson-Marlow Bredel Pumps, Falmouth, UK.

Yen, B. C. & Pansic, N. 1980. Surcharge of Sewer Systems. Department of Civil Engineering,University Of Illinois, Urbana, Illinois

Young, P., Jakeman, A. & Mcmurtrie, R. 1980. An Instrumental Variable Method for Model Order Identification. *AUT Automatica,* 16**,** 281-294.

Appendix A

This section shows the visualization results for the large and small manhole at flow rates of 0.71 l/s and 1.64 l/s.

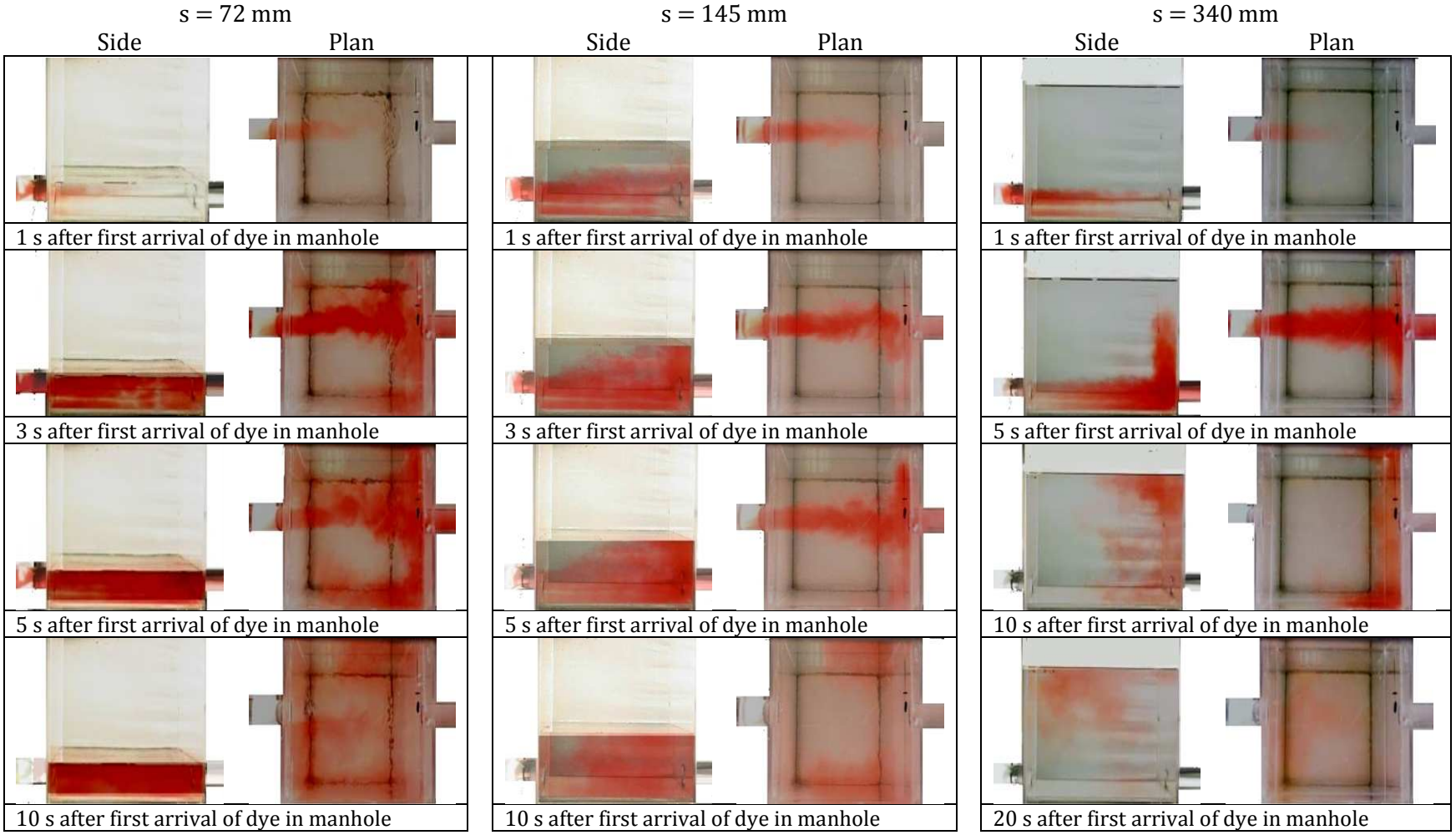

Figure A.0.1: Flow pattern for 0.71 l/s, large manhole at different surcharge levels

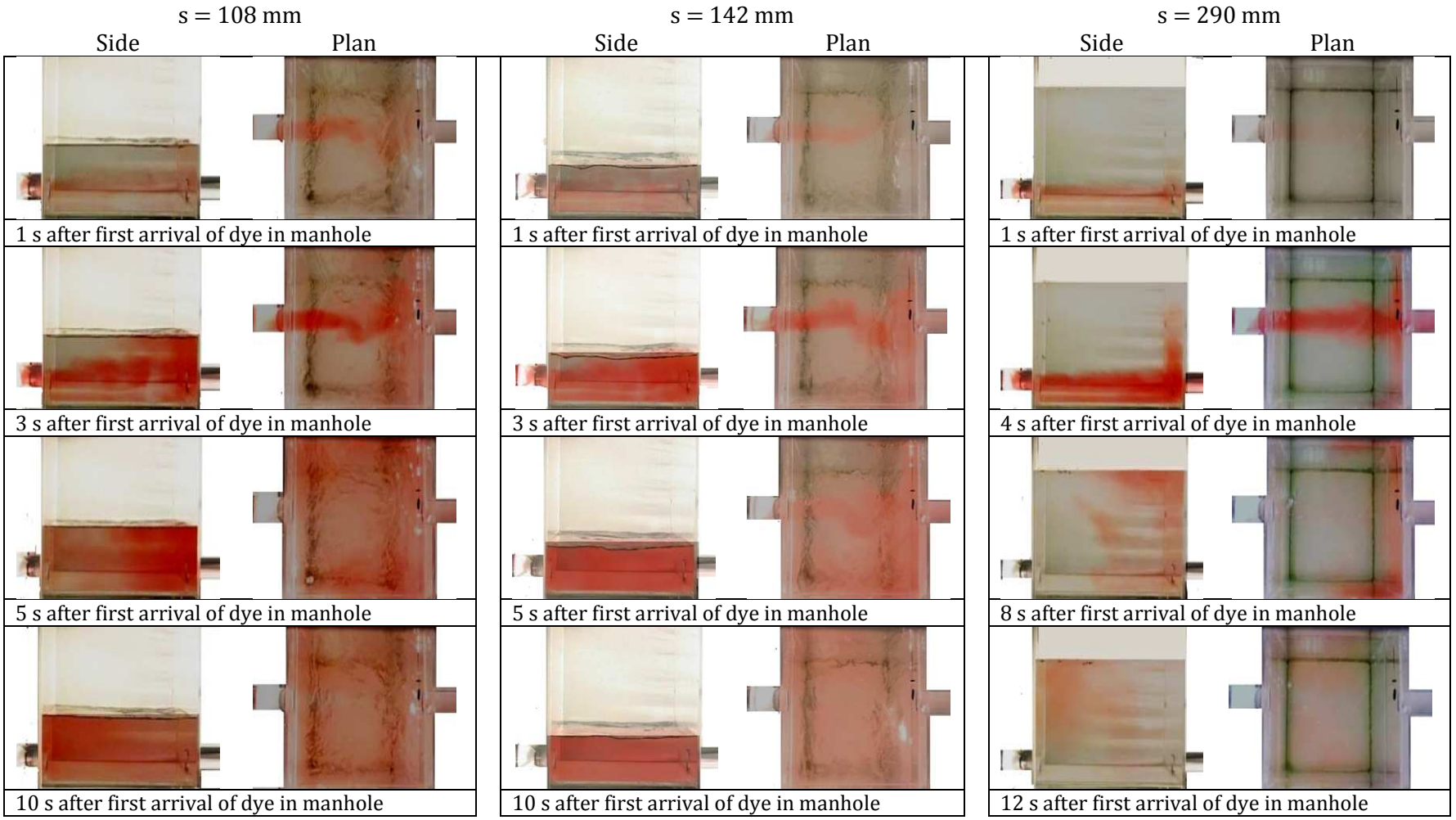

Figure A.0.2: Flow pattern for 1.64 l/s, large manhole at different surcharge levels

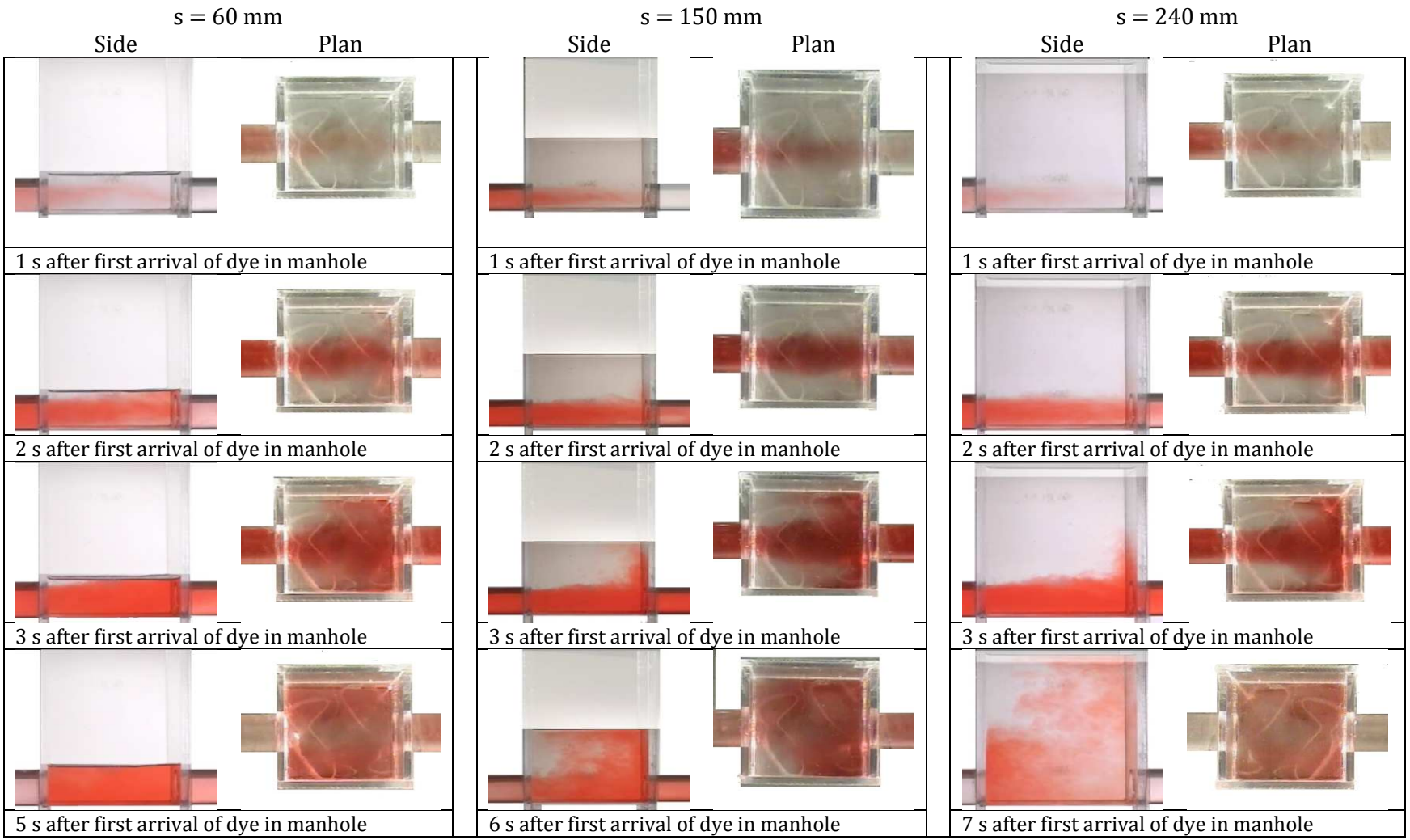

Figure A.0.3: Flow pattern for 0.71 l/s, small manhole at different surcharge levels

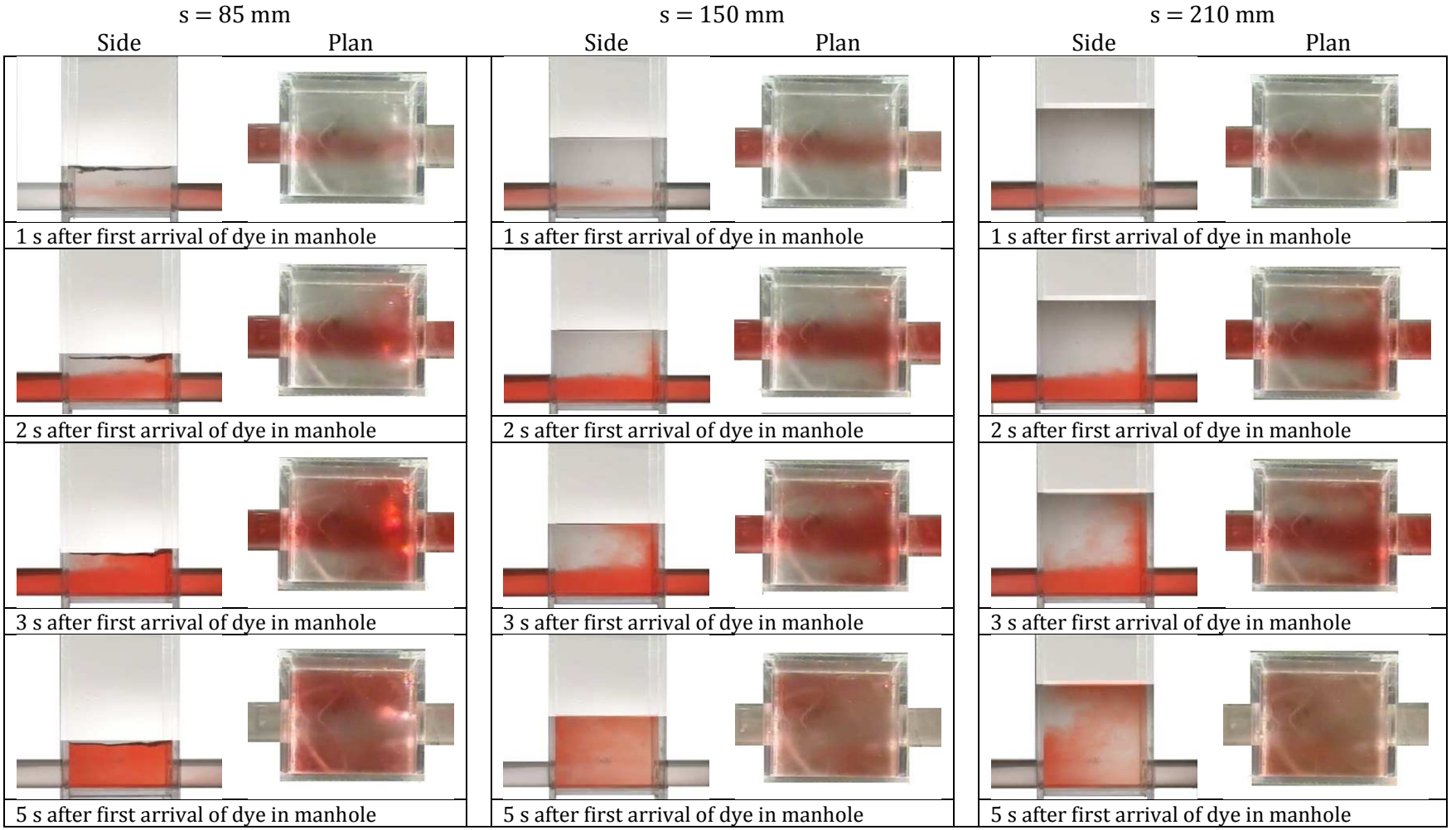

Figure A.0.4: Flow pattern for 1.64 l/s, small manhole at different surcharge levels

Appendix B

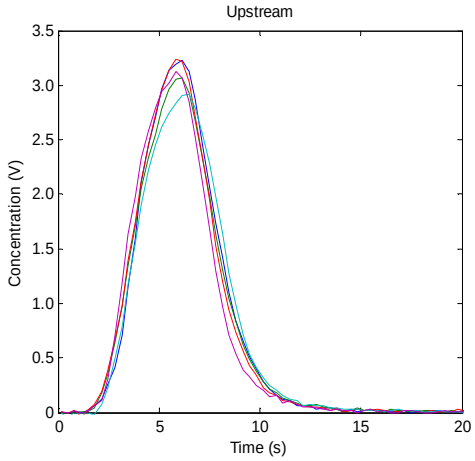

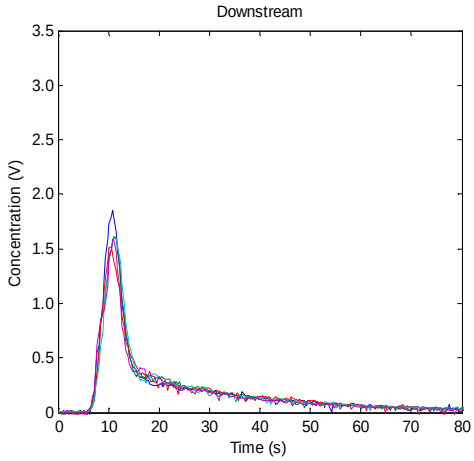

(a) Surcharge 25 mm

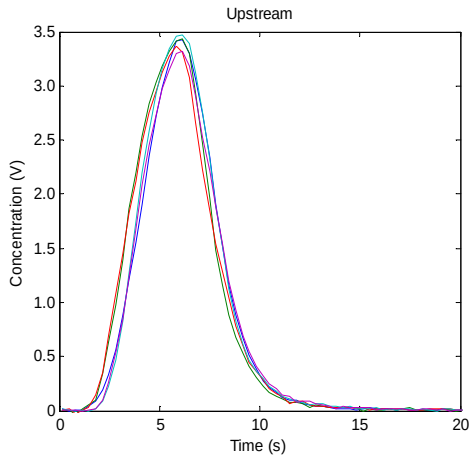

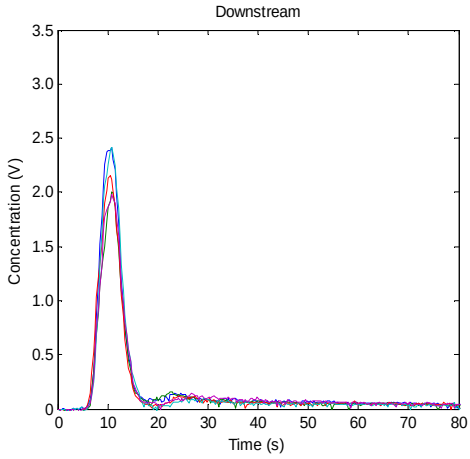

(b) Surcharge 95 mm

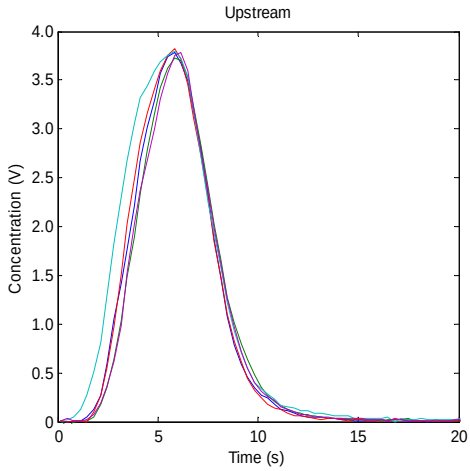

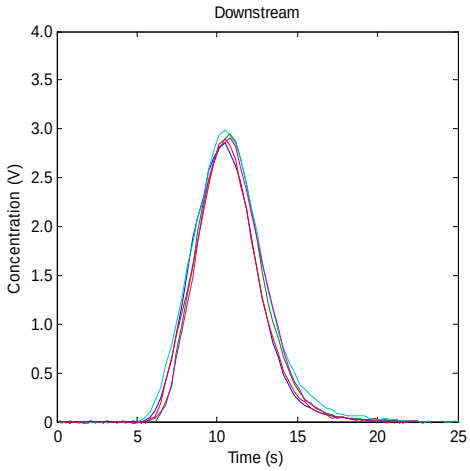

(c) Surcharge 330 mm

Figure B.0.1: Comparison of repeat traces measured at 0.71 l/s for large manhole

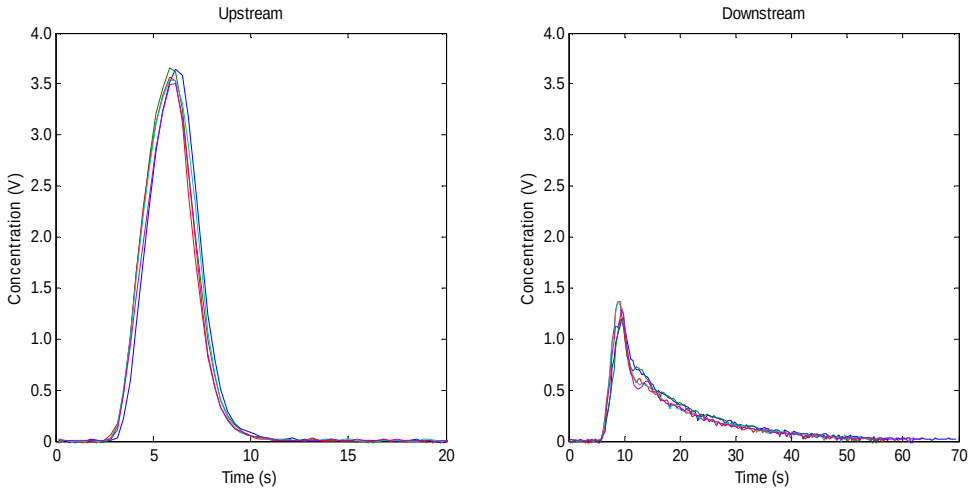

(a) Surcharge 32 mm

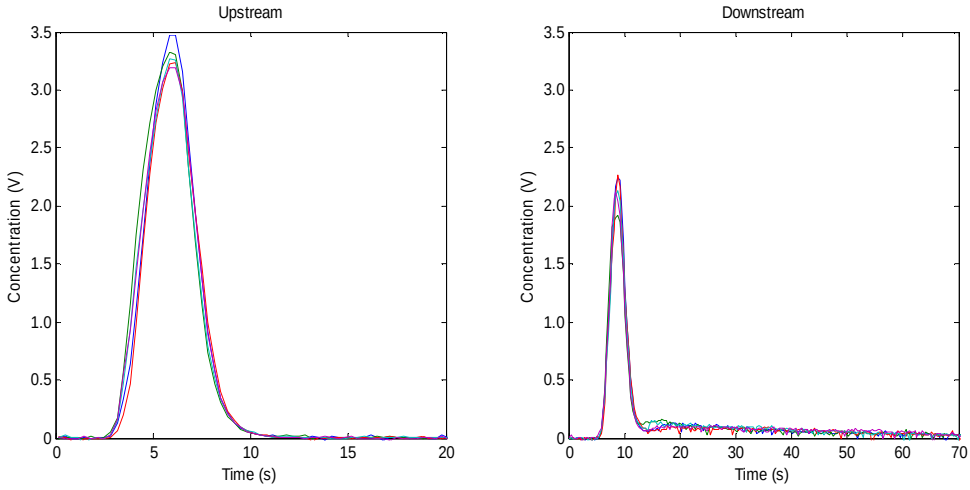

(b) Surcharge 92 mm

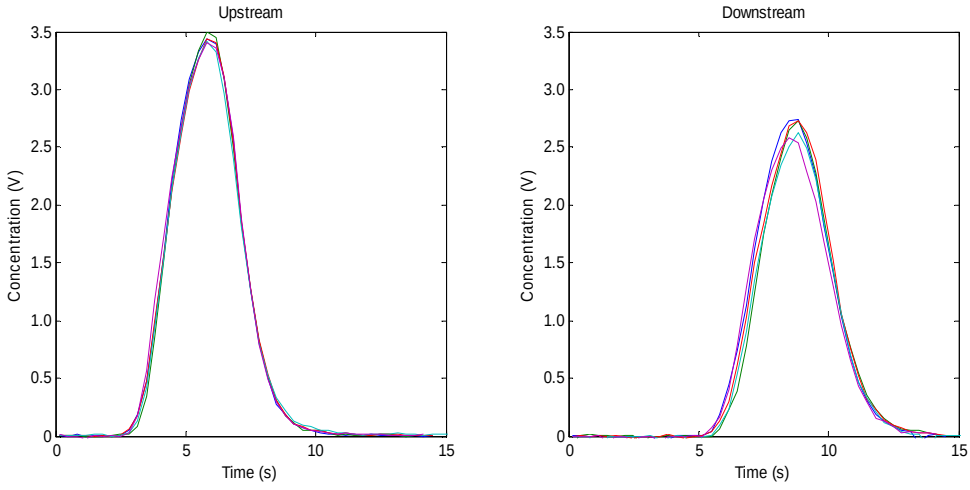

(c) Surcharge 335 mm

Figure B.0.2: Comparison of repeat traces measured at 1.17 l/s for large manhole

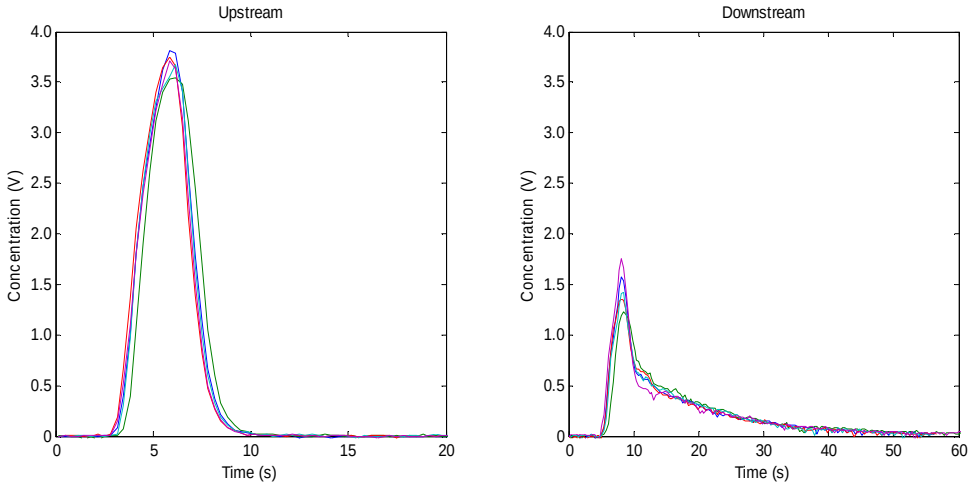

(a) Surcharge 58 mm

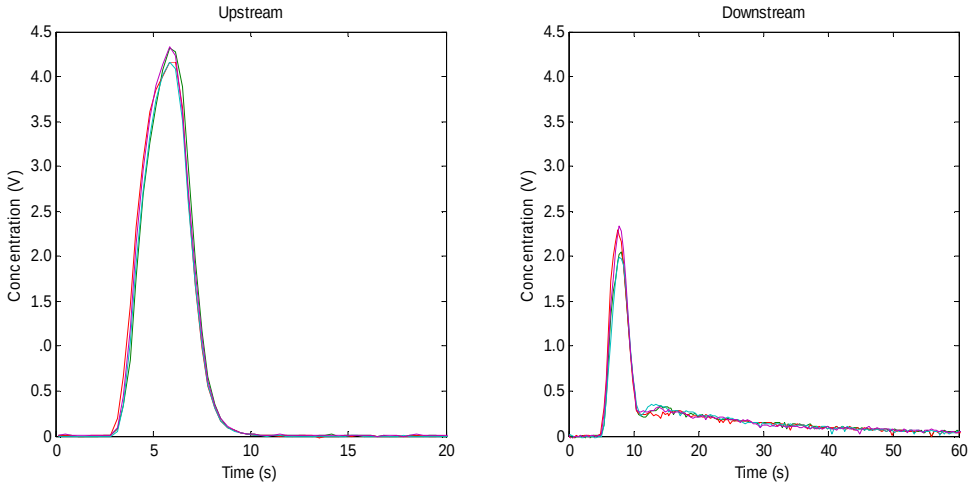

(b) Surcharge 100 mm

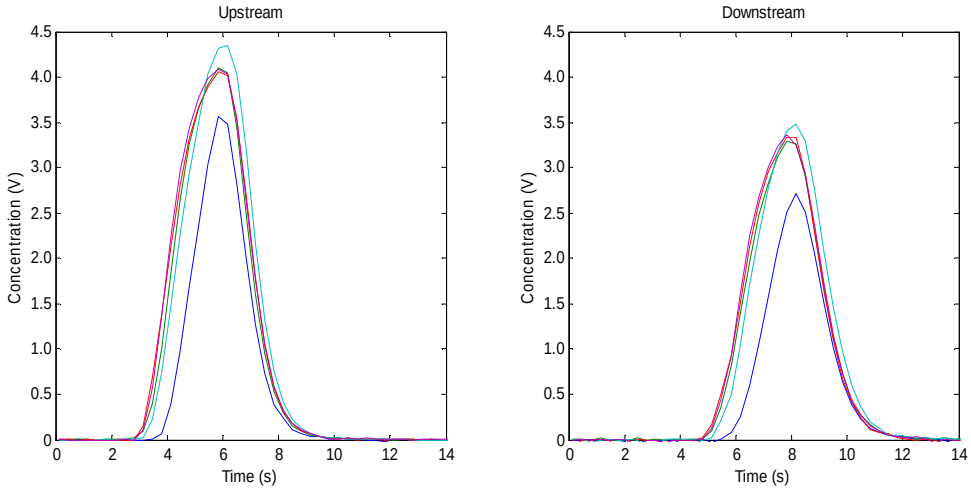

(c) Surcharge 300 mm

Figure B.0.3: Comparison of repeat traces measured at 1.64 l/s for large manhole

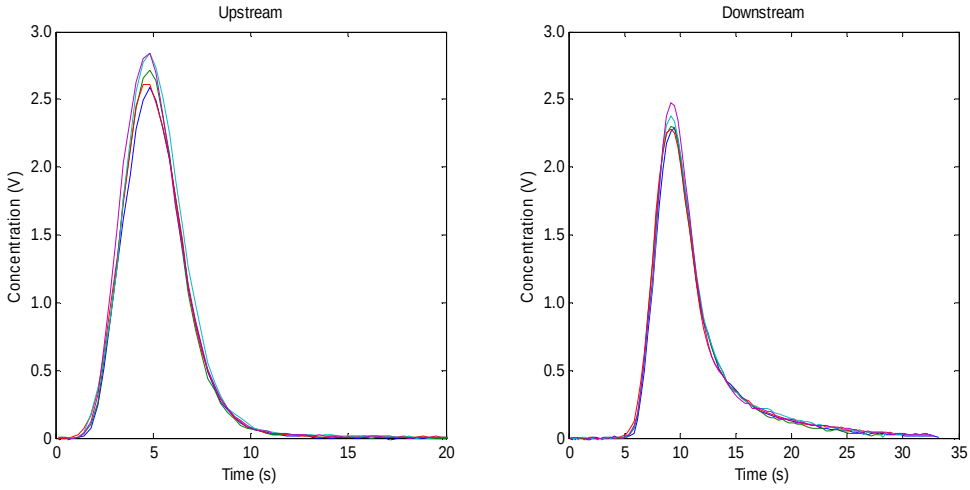

(a) Surcharge 15 mm

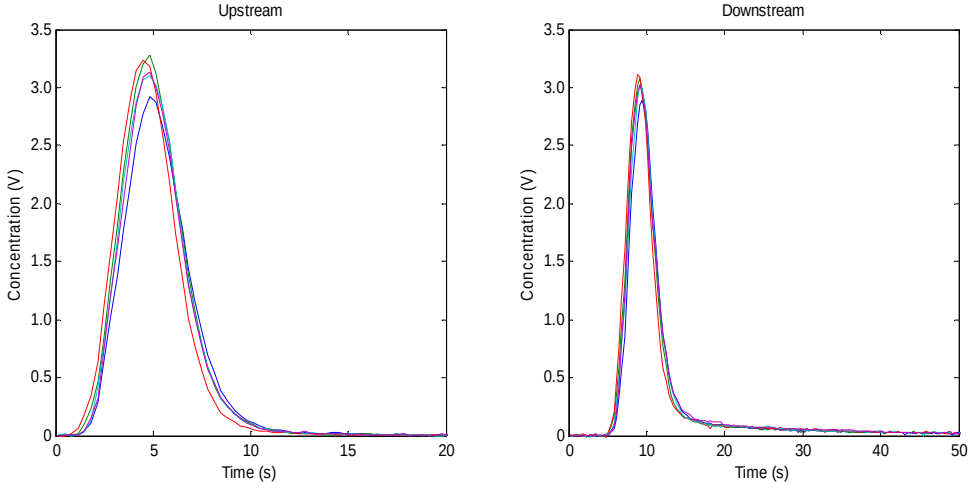

(b) Surcharge 77 mm

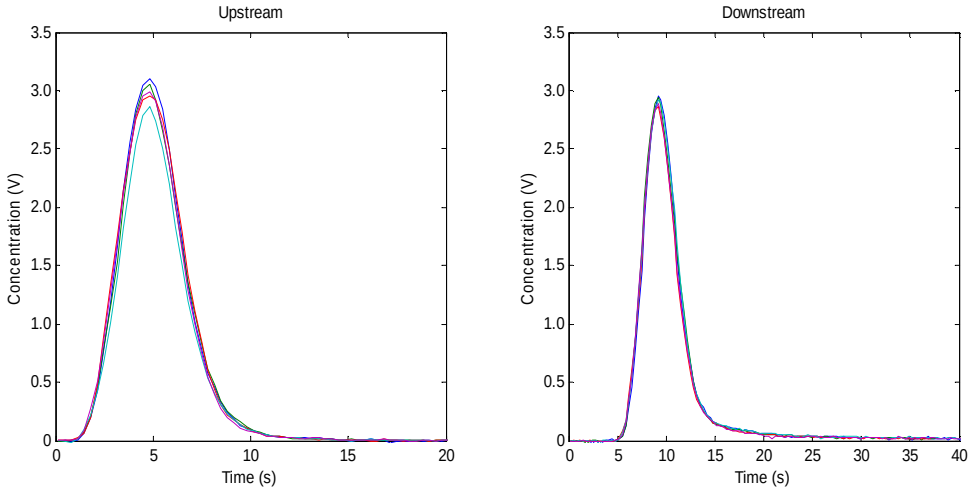

(c) Surcharge 230 mm

Figure B.0.4: Comparison of repeat traces measured at 0.71 l/s for small manhole

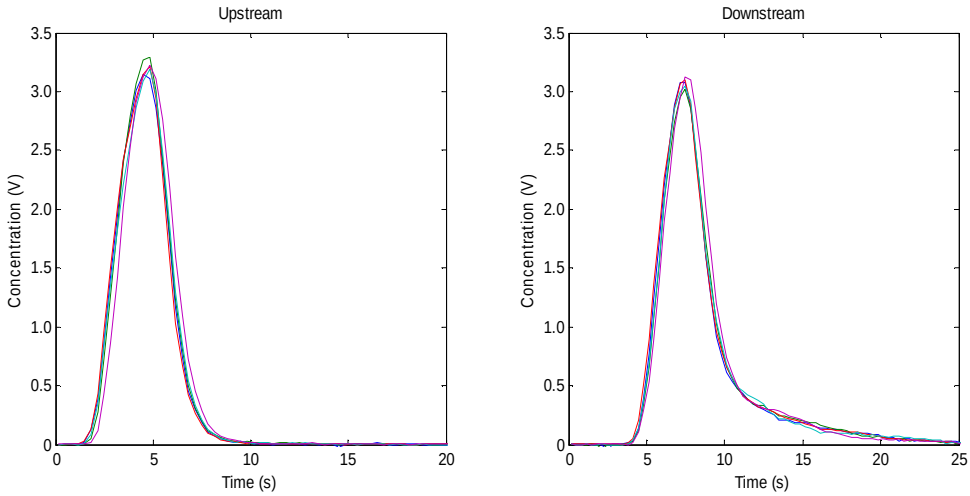

(a) Surcharge 17 mm

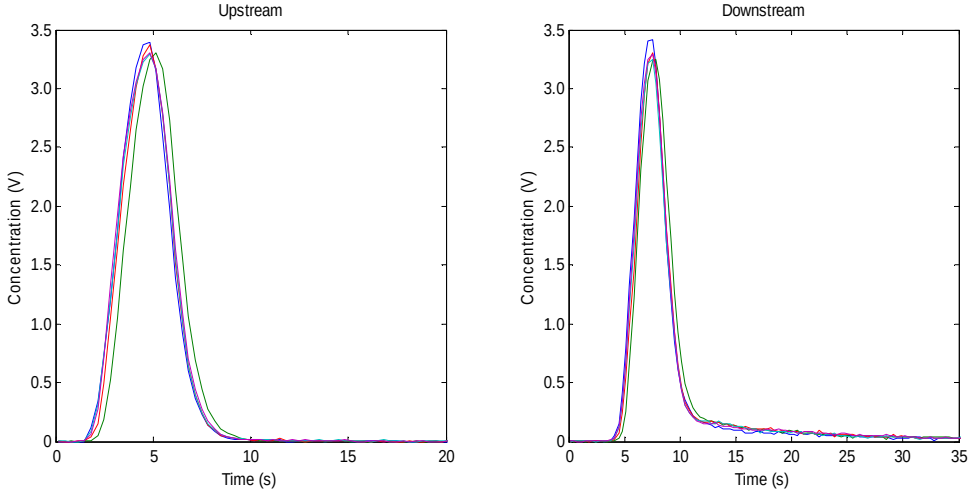

(b) Surcharge 70 mm

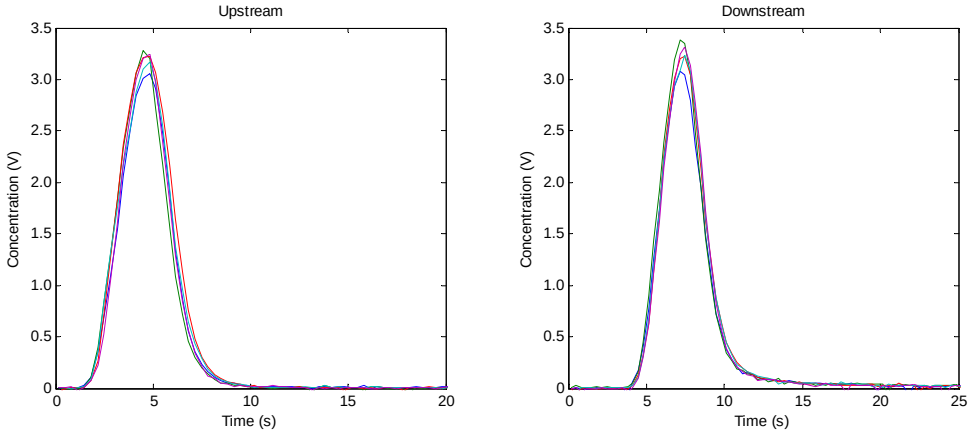

(c) Surcharge 240 mm

Figure B.0.5: Comparison of repeat traces measured at 1.17 l/s for small manhole

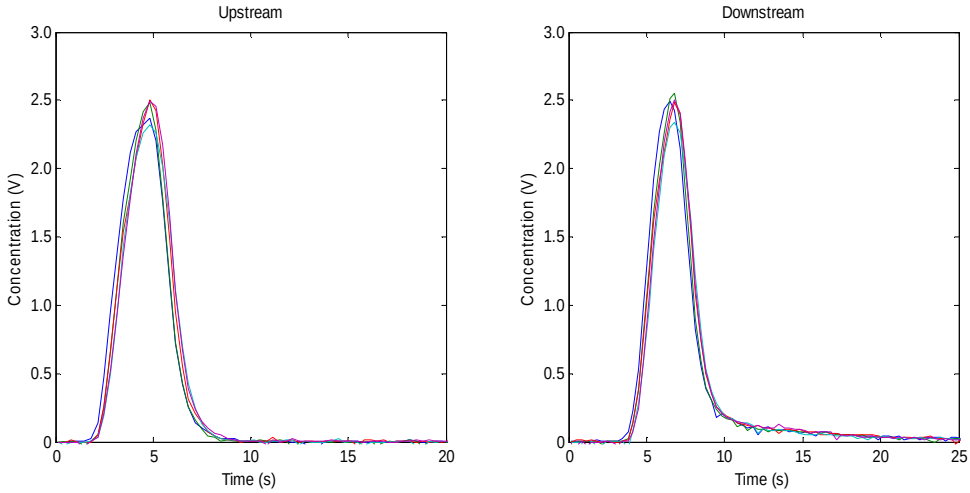

(a) Surcharge 45 mm

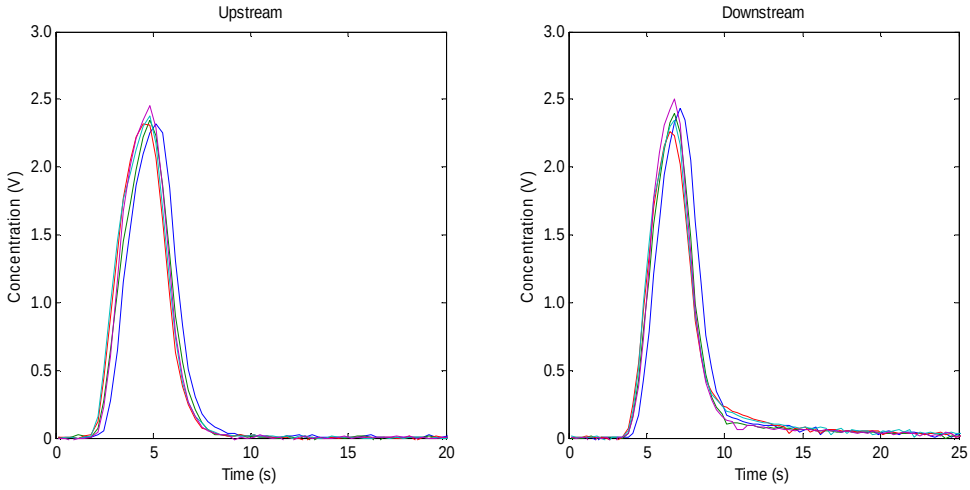

(b) Surcharge 66 mm

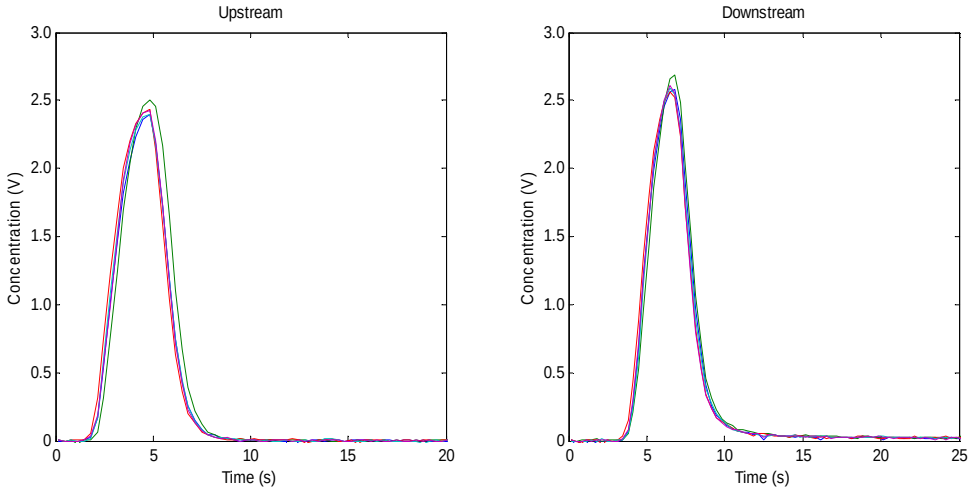

(c) Surcharge 228 mm

Figure B.0.6: Comparison of repeat traces measured at 1.64 l/s for small manhole

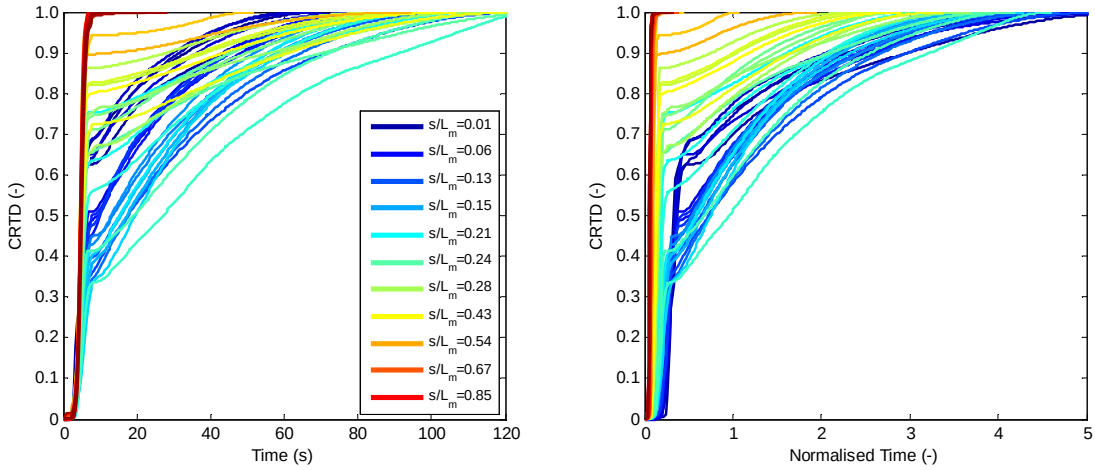

(a) 0.71 l/s

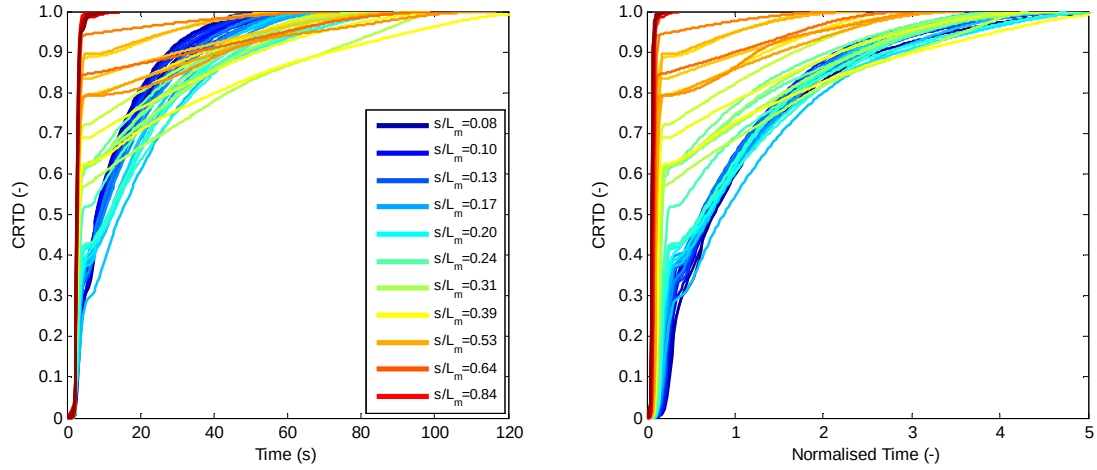

(b) 1.17 l/s

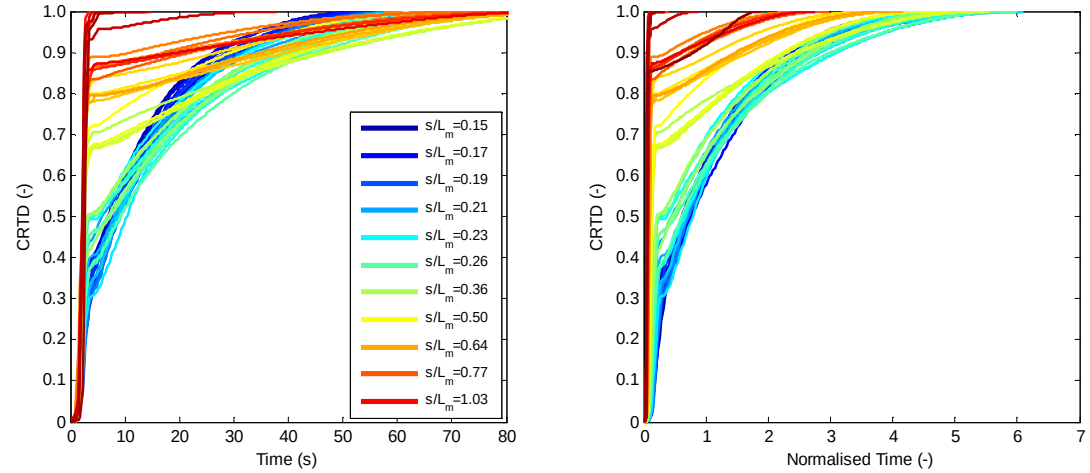

(c) 1.64 l/s

Figure B.0.7: Compiled CRTDs for large manhole

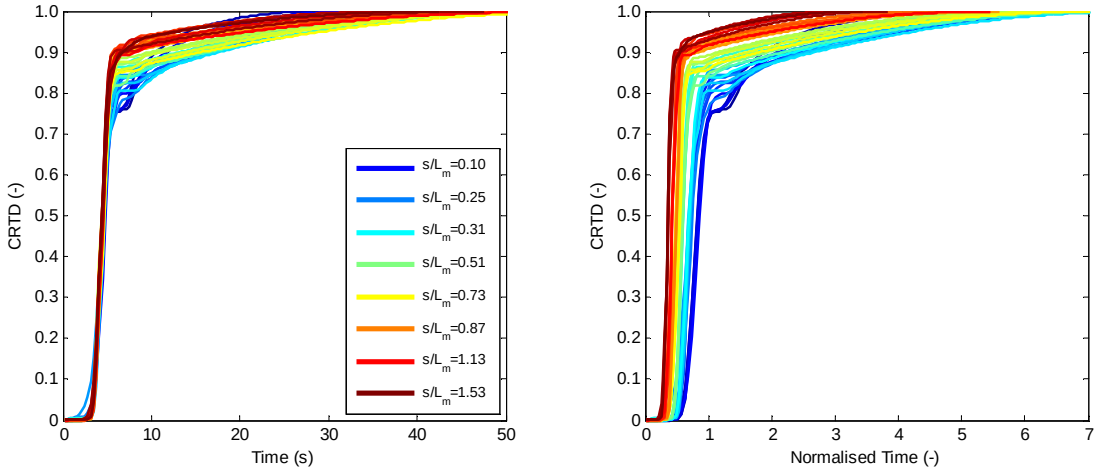

(a) 0.71 l/s

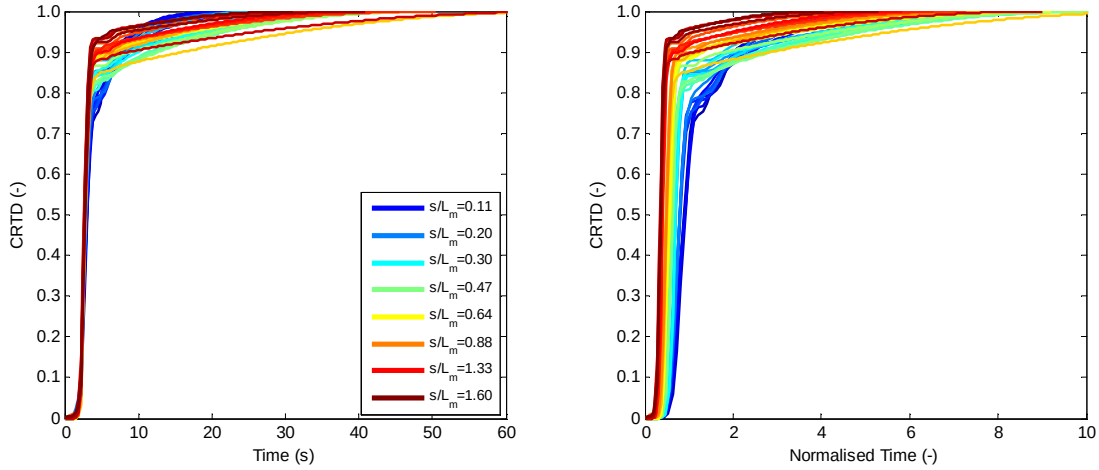

(b) 1.17 l/s

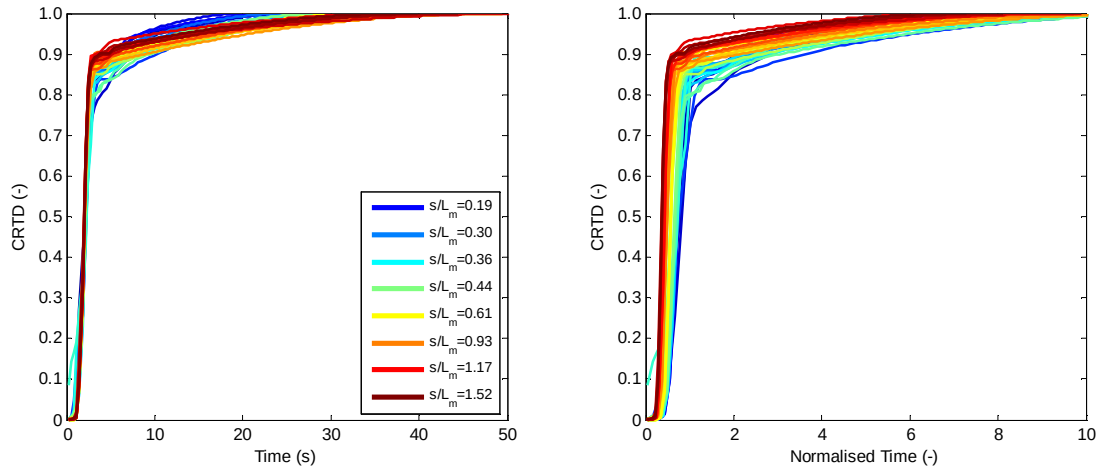

(c) 1.64 l/s

Figure B.0.8: Compiled CRTD for small manhole

Appendix C

Table C.0.1: Percentile travel times for surcharged large manhole across two reaches

Reach 1		Actual Time			Normalised Time			Reach 2		Actual Time			Normalised Time		
0.6 l/s	s/Lm	t10	t50	t90	t10	t50	t90	0.6 l/s	s/Lm	t10	t50	t90	t10	t50	t90
	0.01	3.82	5.15	36.48	0.26	0.35	2.51		0.01	8.15	9.82	43.15	0.44	0.53	2.31
	0.06	4.15	9.82	45.82	0.22	0.52	2.44		0.06	9.15	15.48	50.15	0.40	0.68	2.19
	0.13	4.48	13.15	52.15	0.19	0.55	2.17		0.13	9.15	18.15	57.82	0.32	0.64	2.05
	0.15	4.48	15.15	55.48	0.17	0.58	2.12		0.15	9.15	20.15	60.82	0.30	0.66	2.01
	0.18	4.15	19.15	72.15	0.15	0.68	2.55		0.18	9.15	24.82	73.15	0.28	0.76	2.25
	0.24	3.48	5.48	59.48	0.10	0.16	1.77		0.24	8.48	10.15	66.15	0.22	0.27	1.75
	0.28	3.82	5.15	43.48	0.10	0.14	1.18		0.28	8.48	9.82	47.15	0.21	0.24	1.15
	0.43	3.82	4.48	5.48	0.08	0.09	0.11		0.43	8.15	9.48	11.82	0.15	0.18	0.22
	0.54	3.82	4.82	5.48	0.07	0.08	0.09		0.54	8.48	9.48	10.48	0.14	0.15	0.17
	0.67	3.82	4.82	5.82	0.06	0.07	0.08		0.67	8.82	9.48	10.48	0.12	0.13	0.14
	0.85	3.82	4.82	5.82	0.05	0.06	0.07		0.85	8.82	9.82	11.15	0.10	0.11	0.13

		Actual Time			Normalised Time					Actual Time			Normalised Time		
1.0 l/s	s/Lm	t10	t50	t90	t10	t50	t90	1.0 l/s	s/Lm	t10	t50	t90	t10	t50	t90
	0.08	2.82	8.82	29.48	0.23	0.72	2.40		0.08	5.82	11.82	32.15	0.39	0.80	2.17
	0.10	2.82	9.15	30.15	0.21	0.69	2.26		0.10	5.82	12.15	33.82	0.37	0.77	2.14
	0.13	2.82	10.15	36.82	0.19	0.70	2.52		0.13	5.82	13.48	44.48	0.34	0.79	2.60
	0.17	2.48	11.48	48.15	0.15	0.68	2.87		0.17	5.48	13.82	42.82	0.28	0.72	2.22
	0.20	2.48	4.15	46.15	0.14	0.23	2.54		0.20	5.48	7.48	48.15	0.26	0.36	2.32
	0.24	2.15	3.48	48.15	0.11	0.17	2.41		0.24	5.15	6.15	53.48	0.23	0.27	2.37
	0.31	2.15	3.48	71.82	0.09	0.15	3.04		0.31	5.15	6.15	51.15	0.20	0.24	1.96
	0.39	2.15	3.15	41.48	0.08	0.11	1.51		0.39	5.15	6.15	48.48	0.17	0.21	1.62
	0.53	2.15	2.82	3.15	0.06	0.08	0.09		0.53	5.15	5.82	16.48	0.14	0.16	0.44
	0.64	2.15	2.82	3.48	0.05	0.07	0.09		0.64	5.15	6.15	73.15	0.12	0.14	1.71
	0.86	2.15	2.82	3.48	0.04	0.05	0.07		0.86	4.82	5.82	6.82	0.09	0.11	0.13

		Actual Time			Normalised Time					Actual Time			Normalised Time		
1.4 l/s	s/Lm	t10	t50	t90	t10	t50	t90	1.4 l/s	s/Lm	t10	t50	t90	t10	t50	t90
	0.15	1.82	7.48	31.15	0.16	0.67	2.79		0.15	3.82	8.82	30.48	0.29	0.68	2.35
	0.17	1.82	8.15	30.15	0.15	0.69	2.56		0.17	4.15	9.48	30.15	0.31	0.70	2.22
	0.19	1.82	8.48	31.48	0.15	0.68	2.53		0.19	4.15	10.82	33.48	0.29	0.76	2.35
	0.21	2.15	10.48	37.48	0.16	0.80	2.85		0.21	4.15	12.48	37.48	0.28	0.83	2.50
	0.23	1.82	7.15	39.48	0.13	0.51	2.80		0.23	4.15	8.48	40.82	0.26	0.53	2.57
	0.26	1.82	3.15	37.82	0.12	0.21	2.52		0.26	3.82	5.82	39.82	0.23	0.35	2.37
	0.36	1.48	2.15	29.48	0.08	0.12	1.58		0.36	3.82	4.48	42.15	0.19	0.22	2.06
	0.50	1.48	2.48	35.15	0.06	0.11	1.49		0.50	3.48	4.48	24.15	0.11	0.15	0.79
	0.64	1.48	2.48	49.82	0.05	0.09	1.73		0.64	3.48	4.15	20.15	0.11	0.14	0.66
	0.77	1.48	2.15	19.82	0.04	0.06	0.59		0.77	3.48	4.48	31.15	0.10	0.13	0.89
	1.03	1.48	2.15	34.48	0.03	0.05	0.81		1.03	3.48	4.15	5.48	0.08	0.09	0.12

Table C.0.2: Modelling Surcharge CRTDs

Time based Averaging			
Normalised Time	Low	Intermediate	High
0.0	0.000	0.001	0.007
0.1	0.013	0.125	0.803
0.2	0.162	0.597	0.948
0.3	0.318	0.698	0.951
0.4	0.404	0.710	0.953
0.5	0.452	0.725	0.955
0.6	0.492	0.741	0.958
0.7	0.535	0.757	0.961
0.8	0.575	0.772	0.964
0.9	0.611	0.787	0.966
1.0	0.643	0.801	0.969
1.1	0.674	0.815	0.972
1.2	0.702	0.828	0.974
1.3	0.728	0.841	0.976
1.4	0.752	0.853	0.979
1.5	0.774	0.865	0.981
1.6	0.794	0.876	0.983
1.7	0.813	0.887	0.985
1.8	0.829	0.897	0.986
1.9	0.845	0.907	0.988
2.0	0.860	0.916	0.989
2.1	0.872	0.925	0.990
2.2	0.885	0.933	0.991
2.3	0.896	0.940	0.993
2.4	0.906	0.947	0.994
2.5	0.916	0.954	0.995
2.6	0.925	0.959	0.995
2.7	0.933	0.964	0.996
2.8	0.941	0.969	0.997
2.9	0.948	0.973	0.998
3.0	0.955	0.976	0.998
3.1	0.961	0.980	0.999
3.2	0.966	0.982	0.999
3.3	0.971	0.985	0.999
3.4	0.975	0.987	1.000
3.5	0.979	0.989	1.000

Time based Averaging			
Normalised Time	Low	Intermediate	High
3.6	0.982	0.990	1.000
3.7	0.985	0.992	1.000
3.8	0.988	0.993	1.000
3.9	0.990	0.994	1.000
4.0	0.992	0.995	1.000
4.1	0.993	0.995	1.000
4.2	0.995	0.996	1.000
4.3	0.995	0.997	1.000
4.4	0.996	0.997	1.000
4.5	0.997	0.998	1.000
4.6	0.998	0.998	1.000
4.7	0.998	0.998	1.000
4.8	0.999	0.999	1.000
4.9	0.999	0.999	1.000
5.0	0.999	0.999	1.000

Percentile Based Modelling			
	Normalised Time		
CRTD	Low	inter	High
0.0	0.000	0.000	0.000
0.1	0.242	0.152	0.085
0.2	0.275	0.166	0.093
0.3	0.313	0.178	0.096
0.4	0.430	0.188	0.101
0.5	0.656	0.204	0.105
0.6	0.914	0.272	0.108
0.7	1.237	0.550	0.114
0.8	1.682	1.049	0.166
0.9	2.405	1.950	0.484
1.0	4.497	3.968	1.420